Karlsruher Institut für Technologie

Sources of biogenic volatile organic compounds and organic aerosol particles

Zur Erlangung des akademischen Grades einer

DOKTORIN DER NATURWISSENSCHAFTEN (Dr. rer. nat.)

von der KIT- Fakultät für

Bauingenieur-, Geo- und Umweltwissenschaften des

Karlsruher Instituts für Technologie (KIT)

genehmigte

DISSERTATION

von

M.Sc. Yanxia Li

aus

China

Tag der mündlichen Prüfung: 11.07.2025

Referent: Prof. Dr. Jan Cermak

Korreferent: Prof. Dr. Thomas Leisner

Karlsruhe, den 11.07.2025

Erklärung

Hiermit erkläre ich, dass ich die vorliegende Dissertation, abgesehen von der Benutzung der angegebenen Hilfsmittel, selbständig verfasst habe.

Alle Stellen, die gemäß Wortlaut oder Inhalt aus anderen Arbeiten entnommen sind, wurden durch Angabe der Quelle als Entlehnungen kenntlich gemacht.

Diese Dissertation liegt in gleicher oder ähnlicher Form keiner anderen Prüfungsbehörde vor.

Karlsruhe, im Juni 2025

Yanxia Li

Acknowledgments

First and foremost, I would like to express my sincere gratitude to the China Scholarship Council (CSC) for their generous financial support, which made my PhD studies possible. I am also deeply thankful to the KIT Graduate School for Climate and Environment (GRACE) for providing enriching academic courses and funding my participation in conferences and research stays abroad.

Here, I would like to extend my heartfelt thanks to many people who have supported me along this journey. Above all, I am immensely grateful to my direct supervisor, Dr. Harald Saathoff, for his unwavering guidance and assistance over the past four years. He has always been there to help me overcome challenges, and I will never forget the countless nights we spent repairing the PTR-MS mass spectrometer together. Even after AIDA experiments, he would kindly drive me home. His patience has been instrumental in my growth, and I truly appreciate his understanding, even when I occasionally let my frustrations show. I also owe a great deal to my official supervisors, Prof. Jan Cermak and Prof. Thomas Leisner, for their valuable advice throughout my PhD journey.

A special thanks goes to my dear friend, roommate, and colleague, Yue Meng. Fate brought us together, making our PhD experience more joyful and meaningful. We've shared countless moments, and through them, I've grown in ways I couldn't have imagined. I consider this friendship a reward for striving to be a better person. Indeed, at every stage of life, we meet people who leave a lasting impact, and I'm fortunate to have found such a friend in her.

I am also deeply indebted to my colleagues at KIT. Junwei Song, Linyu Gao, and Hengheng Zhang generously taught me data analysis and instrument operation. Alexander Böhmlander and Tobias Schorr were always eager to share their Python expertise and went out of their way to assist everyone—their kindness was truly inspiring. I also extend my thanks to Xuefeng Shi and Hao Li for their help during my experiments and data analysis. My sincere appreciation goes to Georg Scheurig and Steffen Vogt for their technical support, as well as to our secretary, Susanne Bolz, who patiently resolved countless issues and even took care of the plants in our institute.

Finally, my deepest gratitude goes to my family—especially my father, my cousin (who is like a brother to me), my sister-in-law, and my aunt. Their unwavering support has been my anchor, allowing me to focus on my studies in Germany while they cared for my mother back home. I couldn't have done this without them.

Abstract

Understanding the sources of volatile organic compounds (VOC) and organic aerosols (OA) is crucial for mitigating air pollution and improving public health, as these components significantly influence air quality, human exposure to ultrafine particles, weather, and climate.

Therefore, I studied VOC and OA sources in four field campaigns across three distinct environments—a mountain in summer (Feldberg, Black Forest), an industrial area in summer (Karlsruhe harbor), and an urban street canyon in summer and winter (Munich). By combining online mass spectrometry of VOC, semi-volatile organic aerosol particles (SVOA), and organic aerosol particles (OA) with detailed statistical analysis by positive matrix factorization (PMF). I quantified source contributions, their impacts on air quality, ultrafine particles, and potential aerosol-cloud interaction in these contrasting settings.

The Feldberg site at 1500 m a.s.l. surrounded by the large Black Forest showed relatively low aerosol concentrations due to clean marine air masses from the Atlantic Ocean for 56% of the observation time. Furthermore, the mountain top was in the free troposphere for 88% of the time. This explains also the disconnect between abundant biogenic VOC emissions and limited aerosol formation, with relatively low biogenic contributions to OA due to very low NO_x levels that limited VOC oxidation. The OA composition was dominated by aged biomass burning organic aerosol (BBOA) (35±24%), and with substantial contributions from semi-volatile and low volatile oxygenated organic aerosol (SV-OOA: 24±14%; LV-OOA: 23±14%). Chemical composition of semi-volatile organic aerosol revealed photochemical processing as the dominant formation mechanism (79±18%). VOC measurements showed strong influences from aged anthropogenic (35±15%) and biomass burning emissions (21±12%), alongside with oxidized biogenic compounds (25±16%), demonstrating that this mountain top in the Black Forest receives processed polluted air masses from distant sources via transport in the free troposphere. One substantial pollution event was caused by reginal transport of aged BBOA to the Feldberg and another by transcontinental transport of Canadian wildfire plumes causing high BBOA concentrations enhancing ice-nucleating particle numbers, thus potentially influencing cloud properties.

In Karlsruhe's industrial area at the Rhein harbor, I identified three primary aerosol sources: (1) industrial food processing emissions (41±23% of VOC, 20±9% of OA), (2) industrial phyto-emissions—VOC released from plant processing like in the local paper factory (44±27% of SVOA,

30±15% more oxygenated OA), and (3) biomass burning from wildfires in France (26±21% of SVOA). The influence of wildfire plumes was particularly significant, sometimes overlapping with local landfill emissions. Ultrafine particles at this location showed no correlation with primary sources but were formed as secondary organic aerosol for multiple sources.

Munich's air quality exhibited strong seasonal variations, with biomass burning dominating in winter (Aged: 34 ± 15% and Fresh: 7 ± 3%) and spring (Aged: 32 ± 21% and Fresh: 20 ± 6%), due to emissions from heating and barbecue. Winter also sees high regional background pollution (37 ± 12%), related to stagnant atmospheric conditions. In contrast, summer is characterized by biogenic emissions (24 ± 21%) and photochemically generated low volatile oxygenated OA (25 ± 12%), driven by intensive sunlight and higher plant emissions, while biomass burning contributions are still relatively high (27 ± 18%). Traffic emissions range from 10-15 % throughout the seasons and also cooking emissions (4-10%) remain a small but steady source year-round. Traffic and cooking emissions persistently impact ultrafine particle formation, while biogenic VOCs contribute to their growth typically in early night times of summer. Key mitigation strategies for ultrafine particles should reduce traffic and cooking emissions and select low-terpene vegetation to curb secondary aerosol growths. However, only with addressing the biomass burning sources (barbecue & heating) substantial improvement in air quality can be achieved.

The findings highlight the complex interplay of different sources from local, regional and global origin with biomass burning being the dominant source at all three different locations in southern Germany.

Zusammenfassung

Das Verständnis der Quellen flüchtiger organischer Verbindungen (VOC) und organischer Aerosolpartikel (OA) ist entscheidend für die Minderung der Luftverschmutzung und die Verbesserung der öffentlichen Gesundheit, da diese Komponenten die Luftqualität, die Exposition des Menschen gegenüber ultrafeinen Partikeln, das Wetter und das Klima wesentlich beeinflussen.

Daher untersuchte ich die Quellen von VOC und OA in vier Feldmesskampagnen in drei unterschiedlichen Umgebungen – einem Bergstandort im Sommer (Feldberg, Schwarzwald), einem Industriegebiet im Sommer (Rheinhafen Karlsruhe) sowie einer städtischen Straßenschlucht im Sommer und Winter (München). Durch die Kombination von Online-Massenspektrometrie von VOC, halbflüchtigen organischen Aerosolpartikeln (SVOA) und organischen Aerosolpartikeln (OA) mit einer detaillierten statistischen Analyse durch positive Matrixfaktorisierung (PMF) habe ich die Beiträge verschiedener Quellen von VOC und OA sowie deren Einfluss auf Luftqualität, ultrafeine Partikel und potenzielle Aerosol-Wolken-Wechselwirkungen in diesen kontrastierenden Umgebungen quantifiziert.

Am Feldberg (1500 m ü. NN), umgeben vom ausgedehnten Schwarzwald, waren die Aerosolkonzentrationen relativ niedrige, was auf saubere Meeresluftmassen aus dem Atlantik während 56 % der Beobachtungszeit zurückzuführen ist. Außerdem befand sich der Berggipfel während 88 % der Zeit in der freien Troposphäre. Dies erklärt auch die Diskrepanz zwischen den relativ hohen biogenen VOC-Emissionen und der begrenzten Aerosolbildung mit biogenen Beiträgen aufgrund der sehr niedrigen NO_x-Werte, die die VOC-Oxidation begrenzten. Die OA-Zusammensetzung wurde von gealtertem Biomasseverbrennungsaerosol (BBOA) dominiert (35 ± 24 %) mit erheblichen Beiträgen von halbflüchtigem und schwerflüchtigem oxidiertem organischem Aerosol (SV-OOA: 24±14%; LV-OOA: 23±14%). Die chemische Zusammensetzung des halbflüchtigen organischen Aerosols ergab, dass die photochemische Alterung sein dominierende Entstehungsmechanismus ist (79±18%). Die VOC-Messungen ergaben starke Einflüsse von gealterten anthropogenen Emissionen (35±15%), Biomasseverbrennung (21±12%) und von oxidierten biogenen Verbindungen (25±16%). Dies zeigt, dass Luft auf dem Gipfel des Feldbergs wesentlich durch verschmutzte gealterte Luftmassen aus entfernten Quellen beeinflusst wird. Ein erhebliches Verschmutzungsereignis wurde durch den reginalen Transport gealterter Biomasseverbrennungsaerosole auf den Feldberg verursacht, ein weiteres durch den

transkontinentalen Transport kanadischer Waldbrandfahnen. Dies verursachte hohe BBOA-Konzentrationen, welche die Anzahl eiskeimbildender Partikel erhöhten und somit möglicherweise die Wolkeneigenschaften beeinflussten.

Im Karlsruher Industriegebiet am Rheinhafen habe ich drei wesentliche Aerosolquellen identifiziert: (1) industrielle Emissionen aus der Lebensmittelverarbeitung (41±23% der VOC, 20±9% der OA), (2) industrielle Phyto-Emissionen - VOC, die bei der Verarbeitung von Pflanzen freigesetzt werden, wie z.B. in der örtlichen Papierfabrik (44±27% der SVOA, 30±15% höher oxidierte OA), und (3) Biomasse-Verbrennung durch Waldbrände in Frankreich (26±21% der SVOA). Der Einfluss von Waldbrandfahnen war besonders groß und überschnitt sich manchmal mit lokalen Deponieemissionen. Ultrafeine Partikel zeigten an diesem Standort keine Korrelation mit primären Quellen, sondern wurden als sekundäres organisches Aerosol aus mehreren Quellen gebildet.

Die Luftqualität in München weist starke jahreszeitliche Schwankungen auf, wobei die Verbrennung von Biomasse im Winter (gealtert: 34 ± 15 % und frisch: 7 ± 3 %) und im Frühjahr (gealtert: 32 ± 21 % und frisch: 20 ± 6 %) aufgrund von Emissionen durch Heizen und Grillen dominiert. Im Winter ist auch die regionale Hintergrundbelastung hoch (37 ± 12 %), was auf die stagnierenden atmosphärischen Bedingungen zurückzuführen ist. Im Gegensatz dazu ist der Sommer durch biogene Emissionen (24 ± 21 %) und photochemisch erzeugte schwerflüchtige sauerstoffhaltige OA (25 ± 12 %) gekennzeichnet, die durch intensive Sonneneinstrahlung und höhere Pflanzenemissionen verursacht werden, während der Beitrag der Biomasseverbrennung immer noch relativ hoch ist (27 ± 18 %). Die verkehrsbedingten Emissionen schwanken im Laufe der Jahreszeiten zwischen 10 und 15 %, und auch die Emissionen durch kochen (4 bis 10 %) bleiben das ganze Jahr über eine Kleine, aber stetige Quelle. Verkehrs- und Kochemissionen haben einen anhaltenden Einfluss auf die Bildung ultrafeiner Partikel typischerweise in den frühen Nachtstunden des Sommers, wobei biogene flüchtige organische Verbindungen (VOC) zu deren Wachstum beitragen. Minderungsstrategien für ultrafeine Partikel sollten die Verkehrs- und Kochemissionen reduzieren und Pflanzen mit geringeren Terpenemisssionen für die städtischen Grünanlagen auswählen, um das Wachstum sekundärer Aerosole einzudämmen. Eine wesentliche Verbesserung der Luftqualität kann jedoch nur erreicht werden, wenn die Emissionen aus der Biomasseverbrennug (Grillen und Heizen) deutlich reduziert werden.

Die Ergebnisse verdeutlichen das komplexe Zusammenspiel verschiedener Quellen lokalen, regionalen und globalen Ursprungs, wobei die Verbrennung von Biomasse an allen drei Standorten in Süddeutschland die dominierende Quelle darstellt.

Contents

List of Figures

List of Tables

Abbreviations

AVOC	Anthropogenic volatile organic compounds
AIDA	Aerosol Interaction and Dynamics in the Atmosphere
BVOC	Biogenic volatile organic compounds
BTEX	Benzene, toluene, ethylbenzene and xylene
BBOA	Biomass burning organic aerosol
BC	Black carbon
BLH	boundary layer height
BL	boundary layer
BOA	Biogenic OA
CPC	Condensation Particle Counter
CHARON	Chemical Analysis of aeRosol ONline
CIMS	Chemical ionization mass spectrometer
DMA	Differential mobility analyzer
DCOA	Diesel combustion OA
FIGAERO	Filter Inlet for Gases and AEROsols
FT	Free tropospheric
HOS	highly oxidized species
HR-TOF-AMS	High-resolution time-of-flight Aerosol Mass Spectrometer
HOA	Hydrocarbon-like organic aerosol
H_3O^+	Hydronium ions
ISOPOOH	Isoprene hydroxyhydroperoxide
IEPOX	Isoprene epoxydiol
IHN	Isoprene hydroxy nitrate
I^-	Iodide
IDA	Ionicon Data Analyzer
IFPOA	Industrial food process OA
KIT	Karlsruhe Institute of Technology
LV-OOA	Low-Volatility Oxygenated Organic Aerosol
MVK	Methyl vinyl ketone
MACR	Methacrolein
MPAN	Methacryloyl peroxynitrate
MBTCA	3-methyl-1,2,3-butane-tricarboxylic acid

MOOA	More oxygenated OA
MS	Mass spectrometry
NO_3	Nitrate radicals
NH_3	Ammonia
NR	Non-refractory
NO_2	nitrogen dioxide
OA	Organic aerosol
OH	Hydroxyl radicals
O_3	Ozone
OVOC	Oxygenated VOC
OPC	Optical particle counter
PAHs	Polycyclic aromatic hydrocarbons
PAN	Peroxy acetyl nitrate
PHA	peroxyhemiacetals
PTR-TOF	Proton-transfer-reaction time-Of-flight
PMF	positive matrix factorization
PBL	planetary boundary layer
RH	relative humidity
SMPS	Scanning Mobility Particle Sizer
SO_2	sulfur dioxide
SVOA	semi-volatile organic aerosols
SOA	Secondary organic aerosol
SV-OOA	Semi-Volatile Oxygenated Organic Aerosol
UFP	ultrafine particle
VOC	Volatile organic compounds
VCPs	volatile chemical products
WD	Wind direction
WS	Wind speed

1. Introduction

Aerosols, a mixture of gases and particulate matter, play a crucial role in atmospheric processes, influencing climate, weather patterns, air quality, and human health (Shrivastava et al., 2017; Lee et al., 2023). Organic aerosol (OA) represents a significant fraction of the major components of atmospheric total fine aerosols (20-90%) (Kuang et al., 2020; Chen et al., 2022). Its formation is closely linked to volatile organic compounds (VOC), which undergo atmospheric oxidation through reactions with hydroxyl radicals (OH), ozone (O_3), and nitrate radicals (NO_3). These oxidation processes produce a range of oxygenated volatile and semi-volatile organic compounds, which can subsequently undergo gas-to-particle partitioning, condensation, and heterogeneous reactions, leading to the formation and growth of secondary organic aerosol (SOA). In Europe, SOA accounts for the majority of OA mass, with an average contribution of 71.1% and a range of 43.7% to 100% (Chen et al., 2022). Understanding the sources, transformation, and atmospheric impact of VOC and OA remains a major challenge in atmospheric chemistry.

1.1 Volatile organic compounds (VOC)

1.1.1 Biogenic VOC

Vegetation, particularly trees, releases substantial amounts of biogenic volatile organic compounds (BVOC) into the continental boundary layer. BVOC are predominantly composed of terpenes, highly reactive compounds characterized by one or more C=C double bonds. Terpenes include isoprene (C_5H_8), monoterpenes ($C_{10}H_{16}$), sesquiterpenes ($C_{15}H_{24}$), and diterpenes ($C_{20}H_{32}$) (Li et al., 2020a; Li et al., 2021). The composition of BVOC varies depending on vegetation type and environmental factors such as stress and predation. Between 2001 and 2020, the worldwide annual emission of BVOC reached a total of 835.4 Tg yr^{-1}. Emissions were distributed as follows: isoprene contributed 347.7 Tg yr^{-1} (41.6%), monoterpenes amounted to 184.8 Tg yr^{-1} (22.1%), sesquiterpenes added 23.3 Tg yr^{-1} (2.8%), and all other BVOC species made up 279.6 Tg yr^{-1} (33.5%) (Figure 1) (Dada et al., 2023; Wang et al., 2024b).

BVOC undergo rapid oxidation in the atmosphere, primarily by hydroxyl radicals (OH) during the day and by ozone (O_3) and nitrate radicals (NO_3) at night, leading to the formation of oxygenated VOC (OVOC) and secondary organic aerosol (SOA) (Hamilton et al., 2021; Devault et al., 2022; Dada et al., 2023). The efficiency of SOA formation varies among BVOC; monoterpenes and sesquiterpenes generally exhibit higher SOA yields than isoprene or other

BVOC (Kundu et al., 2017). Recent observational studies estimate that isoprene-derived SOA accounts for approximately 3% of the total SOA mass (Kim et al., 2015; Marais et al., 2016), while modeling studies suggest that isoprene SOA yields range from 4% to 10%, depending on the oxidant. In contrast, monoterpenes exhibit SOA yields of approximately 10% to 20%, whereas sesquiterpenes can exceed 40% (Pye et al., 2010; Fry et al., 2018). Globally, SOA production from BVOC is estimated to range between 2.86 and 97.5 TgC year^{-1} (annual is 49.0 TgC year^{-1}) (Farina et al., 2010; Hodzic et al., 2016). In many regions, SOA from BVOC accounts for a major fraction of the annual global total SOA, typically ranging from 74% to over 95%, depending on environmental conditions and precursor availability (Kelly et al., 2018). SOA contributes one of the largest fractions to total aerosol mass of particles smaller than 1 µm over continental regions (Tsimpidi et al., 2024).

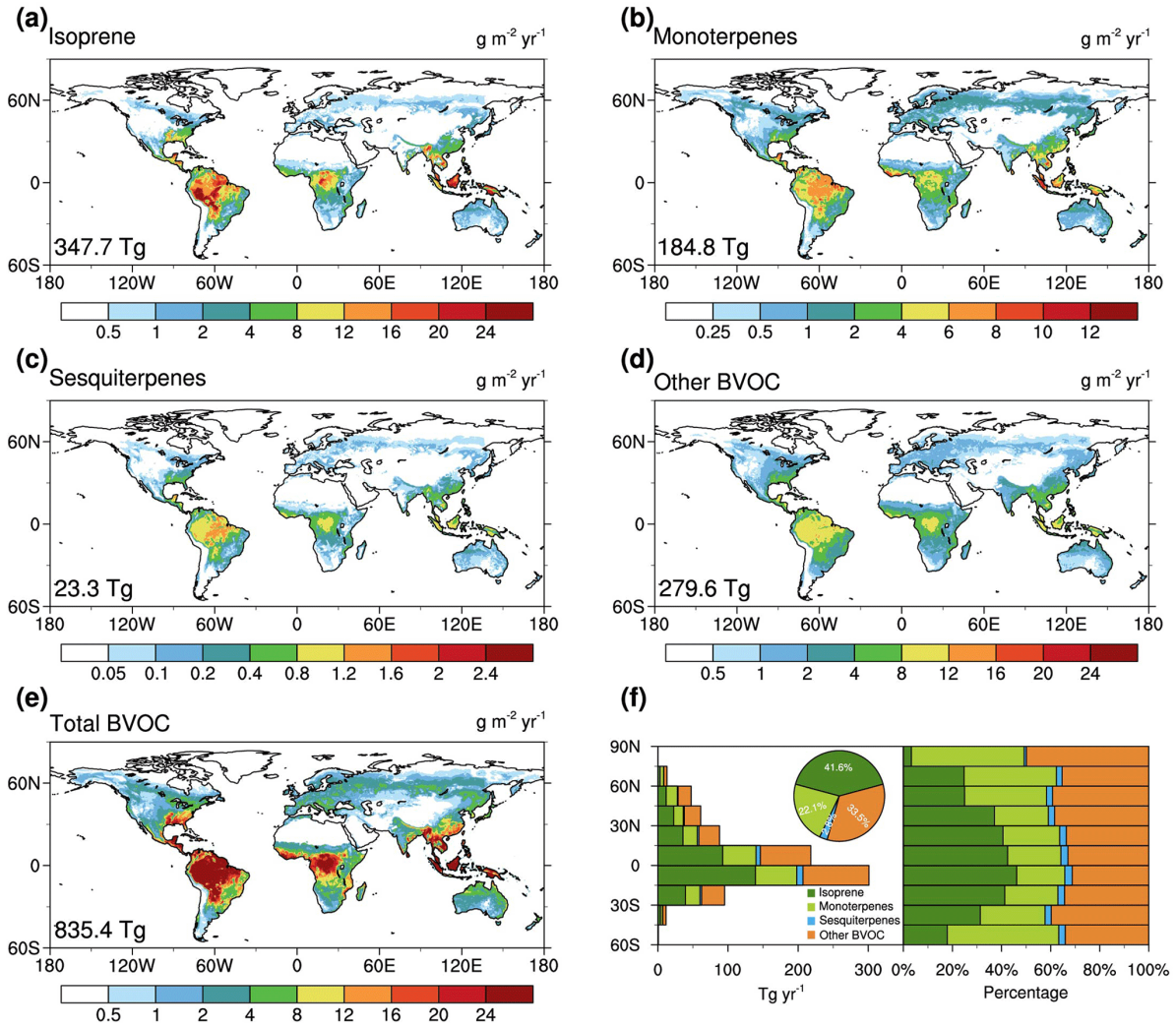

Figure 1. the spatial distribution of mean yearly emission fluxes for BVOCs from 2001 to 2020, including: (a) isoprene, (b) monoterpenes, (c) sesquiterpenes, (d) other BVOCs, (e) the combined total BVOC, and (f) the distribution by latitude (left: the total emissions; right: the proportional contribution of each compound class). A pie chart presents the global percentage share of each BVOC type. Each panel includes the corresponding global annual emission value in its bottom-left corner (Wang et al., 2024b).

1.1.2 Anthropogenic VOC

Vehicular, industrial, and biomass burning emissions are the primary sources of anthropogenic volatile organic compounds (AVOC) in the atmosphere (Kaltsonoudis et al., 2016; Hajizadeh et al., 2018; Mohd Hanif et al., 2021). AVOC emissions (139-163 TgC $year^{-1}$) are significantly lower than BVOC emissions (Von Schneidemesser et al., 2010; Mohd Hanif et al., 2021). Globally, hexanes and higher alkanes were the dominant AVOC (16.53%-17.41%), mainly from mobile, oil and gas, and consumer products. Pentanes (12.88%-13.65%) originated from chemical manufacturing and asphalt, while butanes (10.30%-11.33%) come from transportation and industry. Other AVOCs included toluene, xylenes, benzene, alcohols, ketones, and aldehydes (Figure 2) (Duan et al., 2023). Globally, the annual SOA formation from AVOC was approximately 24.6 TgC $year^{-1}$ (Kelly et al., 2018).

In urban areas, C_6H_6 benzene (5.6 TgC $year^{-1}$), C_7H_8 toluene (6.9 TgC $year^{-1}$), C_8H_{10} ethylbenzene and xylene (4.7 TgC $year^{-1}$) (BTEX) are essential due to vehicular and biomass burning sources and the range of SOA production from aromatics of 2-12 TgC $year^{-1}$ (Henze et al., 2008; Mohd Hanif et al., 2021). Several health risk assessment studies conducted in city centers have indicated that VOCs, particularly BTEX, pose risks to human health and may increase the likelihood of cancer development (Kaltsonoudis et al., 2016; Hajizadeh et al., 2018; Montero-Montoya et al., 2018; Kim et al., 2020; Mohd Hanif et al., 2021).

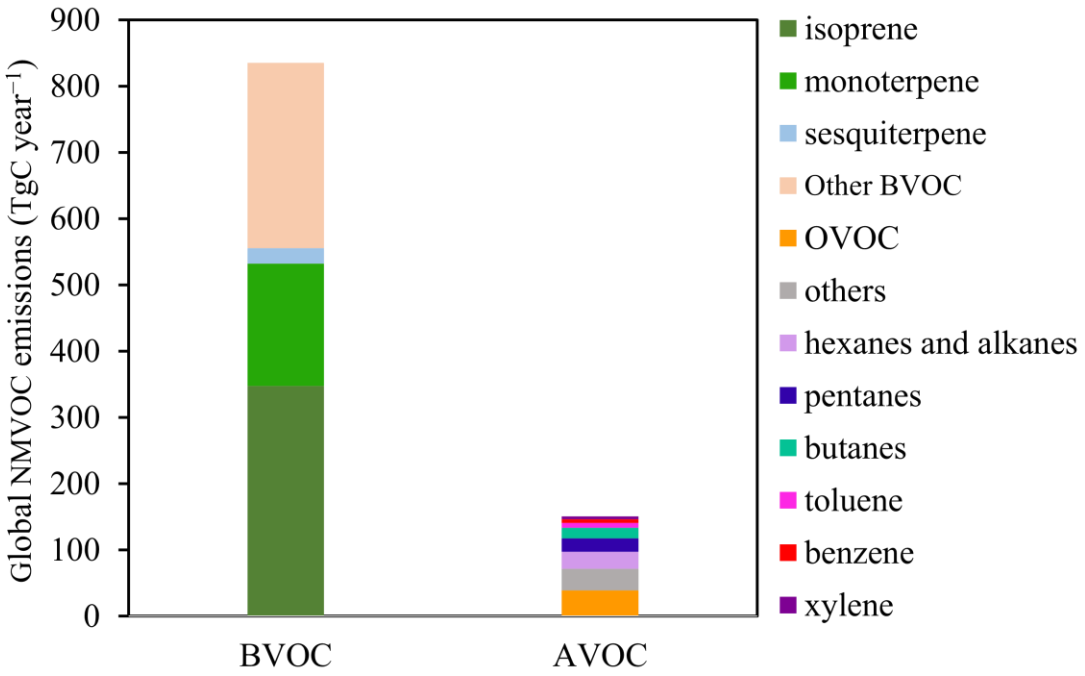

Figure 2. Global non-methane VOC (NMVOC) emissions according to the Global Emissions Initiative (GEIA) (Duan et al., 2023; Wang et al., 2024b).

1.2 Atmospheric aerosol particles

Primary aerosol particles are directly emitted from sources like dust, sea spray, volcanic eruptions, pollen, and soot (Figure 3), while secondary aerosols form through atmospheric reactions of gases such as VOCs (Goldstein and Galbally, 2007). Organic aerosol particles, a major component of secondary aerosols, play a critical role in climate, air quality, and health due to their ability to scatter light, act as cloud condensation nuclei, and carry toxic compounds.

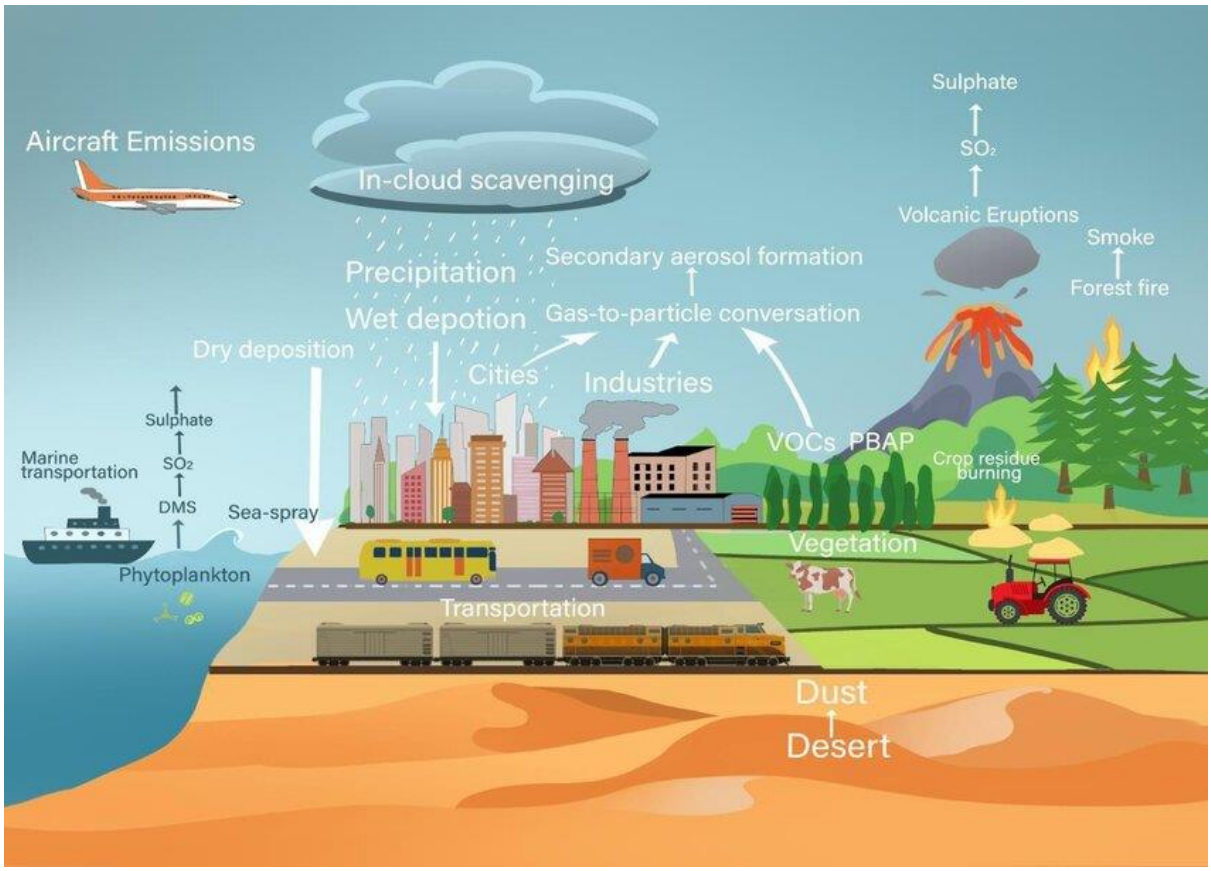

Figure 3. Schematic representation of various sources and sinks of aerosols (Panda et al., 2023).

1.2.1 Primary organic aerosol

POA consists of organic compounds that are either directly emitted as particles or formed through condensation without undergoing chemical reactions. Major sources include **biomass burning**, **fossil fuel combustion**, and **cooking** (De Gouw and Jimenez, 2009; Tang et al., 2018; Liu et al., 2018b). However, in urban areas, traffic emissions dominate, while **waste burning** also contribute significantly (Abbatt and Wang, 2020). Globally, POA contributes around 35 TgC $year^{-1}$, with biomass burning accounting for approximately 70% of this total (Bond et al., 2004; Bhattu, 2017).

For primary **biomass burning organic aerosol** (BBOA), there exist several trace compounds to track and identify it. These include n-alkanes (C_nH_{2n+2}), polycyclic aromatic hydrocarbons (PAHs) such as naphthalene ($C_{10}H_8$), phenanthrene ($C_{14}H_{10}$), and benzo[a]pyrene ($C_{20}H_{12}$), as well as resin acids ($C_{20}H_{30}O_2$) (Simoneit, 2002). Additionally, anhydrous sugars like levoglucosan ($C_6H_{10}O_5$), derived from cellulose pyrolysis, serve as key indicators of biomass combustion (Bhattarai et al., 2019). Methoxyphenols, including guaiacol ($C_7H_8O_2$), syringol ($C_8H_{10}O_3$), and catechol ($C_6H_6O_2$), are characteristic products of lignin decomposition (Wan et al., 2019). High-temperature combustion of lignin releases various methoxyphenol derivatives, such as homovanillyl alcohol ($C_9H_{12}O_3$), vanillin ($C_8H_8O_3$), vanillic acid ($C_8H_8O_4$), syringaldehyde ($C_9H_{10}O_4$), syringic acid ($C_9H_{10}O_5$), p-hydroxybenzaldehyde ($C_7H_6O_2$), and p-hydroxybenzoic acid ($C_7H_6O_3$) (Daniel R Oros and Simoneit, 2001). Furthermore, dehydroabietic acid ($C_{20}H_{28}O_2$) is a major biomarker for the combustion of conifer-derived fuels (Pingqing Fu et al., 2008). Among these, levoglucosan, vanillic acid, syringic acid, p-hydroxybenzoic acid, and dehydroabietic acid are widely recognized as key tracers for BBOA emissions in atmospheric studies (Fu et al., 2011; Fujii et al., 2015; Wan et al., 2017; Wan et al., 2019).

For primary **fossil fuel combustion OA**, key tracers include aromatic VOCs such as toluene (C_7H_8), benzene (C_6H_6), ethylbenzene (C_8H_{10}), and trimethylbenzene (C_9H_{13}) (Liu et al., 2018b), along with polycyclic aromatic hydrocarbons (PAHs) (Liang et al., 2023)like naphthalene ($C_{10}H_8$).

POA from **cooking** emissions typically contain both saturated fatty acids such as myristic acid ($C_{14}H_{28}O_2$), palmitic acid ($C_{16}H_{32}O_2$), and stearic acid ($C_{18}H_{36}O_2$), as well as unsaturated fatty acids including oleic acid ($C_{18}H_{34}O_2$) and linoleic acid ($C_{18}H_{32}O_2$) (Li et al., 2023a).

POA from **waste burning** are characterized by distinct molecular markers: Alkanes (e.g., n-$C_{27}H_{56}$ to n-$C_{33}H_{68}$) and aromatic compounds dominate plastic combustion emissions (Li et al., 2023a), while polycyclic aromatic hydrocarbons (PAHs) such as naphthalene ($C_{10}H_8$), phenanthrene ($C_{14}H_{10}$), and fluoranthene ($C_{16}H_{10}$) (Kanellopoulos et al., 2021)originate from incomplete combustion of synthetic materials. Fatty acids including palmitic acid ($C_{16}H_{32}O_2$) and oleic acid ($C_{18}H_{34}O_2$) indicate co-burning of food waste or cooking-derived residues, whereas bisphenol A ($C_{15}H_{16}O_2$) serves as a tracer for plastic incineration in urban/industrial aerosols.

1.2.2 Secondary organic aerosol (SOA)

SOA forms through a complex oxidation process involving multiple VOCs, producing a wide range of intermediate, semi-volatile, low-volatility, and extremely low-volatility compounds. These products undergo further transformations in the particle phase, including accretion reactions, photolysis, or additional oxidation (Thornton et al., 2020).

Isoprene-derived SOA tracers

Due to the significant emissions of isoprene in many forested regions and its rapid reaction with OH radicals (~1.5h lifetime for [OH] ~1×10^6 cm^{-3}) (Shrivastava et al., 2017), it plays a crucial role in understanding tropospheric atmospheric chemistry and SOA formation. Here, I present the oxidation process leading to SOA formation from isoprene. In gas phase, isoprene reacts with OH radicals to form isoprene hydroxyhydroperoxide (ISOPOOH, $C_5H_{10}O_3$), which subsequently leads to the formation of isoprene epoxydiol (IEPOX, $C_5H_{10}O_3$) as the dominant product (70-80%) at low NO_x concentrations (Berndt et al., 2016). A smaller fraction (~10%) undergoes further oxidation, producing C_5 low-volatility organic compounds (C_5-LVOC, $C_5H_{10,12}O_{5\text{-}6}$). Dihydroxy dihydroperoxides, $(HO)_2$-C_5H_8-$(OOH)_2$ ($C_5H_{12}O_6$), are the main products (Berndt et al., 2016). Additionally, a minor fraction of peroxy radicals (RO_2) contributes to the formation of C_5 hydroxycarbonyl ($C_5H_{10}O_2$), methyl vinyl ketone (MVK C_4H_6O), methacrolein (MACR C_4H_6O), hydroperoxyaldehyde ($C_5H_{10}O_4$), and C_4 hydroxyperoxide ($C_4H_8O_4$) (Wennberg et al., 2018; Mahilang et al., 2021). If a small amount of NO_x is present, RO_2 radicals undergo oxidation, leading to the formation of isoprene nitrate (ISOPN, $C_5H_9NO_{4\text{-}5}$) and dihydroxy dinitrate ($C_5H_{10}N_2O_8$) (Brownwood et al., 2021). At high NO_x concentrations, MVK, MACR, methacryloyl peroxynitrate (MPAN, $C_4H_5NO_5$), peroxy acetyl nitrate (PAN $C_2H_3NO_5$) and isoprene hydroxy nitrate (IHN) $C_5H_9NO_4$ are dominate (Wennberg et al., 2018). In particle phase, IEPOX, C5-alkene triols ($C_5H_{12}O_3$), 2-methyltetrols ($C_5H_{12}O_4$) and hemiacetal dimers ($C_{10}H_{20}O_6$) are the main products in low NOx concentrations (Surratt et al., 2010; Rattanavaraha et al., 2017; Shrivastava et al., 2017). 2-methylglyceric acid (2-MG $C_4H_8O_5$), oligoesters (diesters of 2-MG $(C_4H_8O_5)_2$), hydroxynitrate ($C_5H_7NO_5$), and hydroxynitrate or carboxylated nitrate ($C_5H_9NO_5$) are the main products at high NO_x environments (Surratt et al., 2010; Shrivastava et al., 2017; Schwantes et al., 2019).

Monoterpene-derived SOA tracers

The main RO_2 formed from monoterpenes includes $C_{10}H_{14}O_z$ compounds from ozonolysis and $C_{10}H_{16}O_z$ compounds from hydroxyl-radical reactions. But for β-pinene, C_9 Criegee

intermediates from ozonolysis and $C_8H_{12}O_z$ are the main oxidation products (Zhao et al., 2024). The most abundant monoterpenes, α-pinene and β-pinene, are highly reactive towards ozone (O_3) (Fayad et al., 2021). Pinonaldehyde ($C_{10}H_{16}O$) is a major first-generation oxidation product of α-pinene ozonolysis, and its secondary organic aerosol (SOA) yield from α-pinene oxidation can be as high as 87% (Lee et al., 2006; Gray Be et al., 2017). Following pinonaldehyde, pinonic acid ($C_{10}H_{16}O_3$) and pinic acid ($C_9H_{14}O_4$) have also been identified as tracers of α-pinene oxidation (Upshur et al., 2023). Myrtenal ($C_{10}H_{14}O$), terebic acid ($C_7H_{10}O_4$), terpenylic acid ($C_8H_{12}O_4$) and hydroxy-pinonic acid ($C_{10}H_{16}O_4$) are important further secondary oxidation products (Mutzel et al., 2016). Nopinone ($C_9H_{14}O$), norpinonic acid ($C_9H_{14}O_3$), pinic acid ($C_9H_{14}O_4$), terpenylic acid ($C_8H_{12}O_4$), 3-methyl-1,2,3-butane-tricarboxylic acid (MBTCA $C_8H_{12}O_6$), terebic acid ($C_7H_{10}O_4$) and dicarboxylic acid ($C_7H_{12}O_5$) are the β-pinene derived SOA markers (Mutzel et al., 2016). In the presence of NO_x, the major nitrogen-containing monomers ($C_8H_{11}NO_x$, $C_9H_{13,15}NO_x$, and $C_{10}H_{15,17}NO_x$) serve as tracers for aerosols formed from monoterpene oxidation with NO_x (Zhao et al., 2024).

Sesquiterpene-derived SOA tracers

β-Caryophyllene is the most abundant sesquiterpene in the atmosphere, and its ozonolysis significantly contributes to secondary organic aerosol (SOA) formation (Detlev Helmig et al., 2007; Parshintsev et al., 2008; Upshur et al., 2023). The $C_{14}H_{24}O_{2\text{-}9}$ and $C_{14}H_{22}O_{2\text{-}10}$ homologous series, as well as the $C_{15}H_{24}O_{3\text{-}10}$ and $C_{15}H_{22}O_{4\text{-}10}$ homologous series are the dominant products in β-caryophyllene ozonolysis SOA (Kundu et al., 2017). β-caryophyllon aldehyde ($C_{15}H_{24}O_2$), β-caryophyllonic acid ($C_{15}H_{22}O_4$), β-caryophyllinic acid ($C_{15}H_{24}O_4$) and β-nocaryophyllonic acid ($C_{15}H_{22}O_5$) are important tracers for β-caryophyllene ozonolysis (Kundu et al., 2017; Upshur et al., 2023). And chemical formulas $C_{10}H_{16}O_4$ and $C_{14}H_{22}O_4$ are related to these three tracers. Ambient measurements have also identified $C_{15}H_{22}O$, $C_{15}H_{24}O$, $C_{15}H_{22}O_2$, $C_{15}H_{24}O_2$, and $C_{15}H_{24}O_3$ as typical reaction products from sesquiterpene oxidation (Yee et al., 2018; Li et al., 2021).

Oxygenated carbonaceous compounds derived SOA tracers

Under low NO_x, alcohols ($C_nH_{2n+2}O$), carboxylic acids ($C_nH_{2n}O_2$), ketones ($C_nH_{2n}O$) and carbonyls ($C_nH_{2n}O$) are commonly the first OH radical oxidation products of branched and linear alkanes (Lim and Ziemann, 2009b; Aimanant and Ziemann, 2013). Hydroxycarbonyls ($C_nH_{2n}O_2$), hydroperoxides ($C_nH_{2n+2}O_2$), hydroperoxycarbonyls ($C_nH_{2n}O_4$), hydroxy hydroperoxides ($C_nH_{2n+2}O_3$), peroxycarboxylic acids ($C_nH_{2n}O_4$), peroxyhemiacetals (PHA)

($C_nH_{2n+2}O_4$) and dihydroperoxides ($C_nH_{2n+2}O_4$) are the oxidation products from OH-initiated reactions of n-dodecane (C_{12})/2-methylundecane($C_{12}H_{26}$), hexylcyclohexane and cyclododecane ($C_{12}H_{24}$) (Yee et al., 2013a; Schilling Fahnestock et al., 2015). Under high NOx, 1,4-hydroxycarbonyls ($C_nH_{2n}O_2$), hydroxy-nitrates ($C_nH_{2n+1}NO_3$), dinitrates ($C_nH_{2n}(NO_3)_2$) and alkyl nitrates (R-O-NO_2) are OH oxidation products of alkanes (C_6-C_{15}) (Lim and Ziemann, 2009a; Srivastava et al., 2022). Alcohols, hydroxycarbonyls, hemiacetals ($C_nH_{2n+2}O_2$), nitrate-bearing hemiacetals ($C_nH_{2n+2}O_3N$), and acid anhydrides ($(RCO)_2O$) are the major SOA products from n-alkanes (Li et al., 2017; Docherty et al., 2021).

Aromatic-compounds derived SOA tracers

The major photooxidation products from aromatics (mainly BTX) are glyoxal ($C_2H_2O_2$), methylglyoxal ($C_3H_4O_2$), unsaturated dicarbonyls, furanones ($C_4H_4O_2$), aromatic aldehydes (R-CHO)/acids (R-COOH) and phenols (R-OH). The hydroxycylclohexadienyl radical (like C_6H_7O), an aromatic-OH adduct, is the primary product of the reaction of the aromatic ring with OH (Srivastava et al., 2022).

The major toluene photooxidation SOA products under different NO_x conditions are nitrophenols (like $C_6H_5NO_3$), 2-methyl-4-nitrophenol ($C_7H_7NO_3$), methyl nitrocatechol ($C_7H_7NO_4$), quinones (like $C_6H_4O_2$), aromatic carbonyls (like C_7H_6O), oxoacids (like $C_3H_4O_3$), and unsaturated dicarbonyls (like $C_6H_6O_2$) (Jang and Kamens, 2001; Pereira et al., 2015). Xylene isomers undergo photooxidation to produce unsaturated diketones, aldehydes, and dicarbonyl compounds. Predominant SOA components include dicarbonyls and highly oxidized species (HOS). Notably, 3-methyl-2-oxiranecarbaldehyde ($C_4H_6O_2$) and 3-hexene-2,5-dione($C_6H_8O_2$) are markers for xylene-derived SOA (Forstner et al., 1997; Bethel et al., 2000; Jang and Kamens, 2001; Zhang et al., 2019; Srivastava et al., 2022). The oxidation of TMB under varying NO_x conditions leads to the formation of several key products that serve as markers for SOA formation. Notable compounds include methylglyoxal ($C_3H_4O_2$), O_2-bridged ketones, and isobaric furanone and dicarbonyl ring-opening products with m/z 113. Additionally, 3,5-dimethylbenzaldehyde ($C_9H_{10}O$), nitrogenated compounds, furanones, and dicarbonyls—including low molecular weight organic acids—are observed. Specific products such as 3,5-dimethyl-5(2H)-furanone ($C_6H_8O_2$), 3-methyl-furan-2,5-dione ($C_5H_4O_3$), and 2-methyl-4-oxo-2-pentena ($C_6H_8O_2$), 3-hexene-2,5-dione ($C_6H_8O_2$) and 2,3-butanedione ($C_4H_6O_2$) are also identified (Forstner et al., 1997; Wyche et al., 2009; Birdsall and Elrod, 2011).

Polycyclic aromatic hydrocarbons (PAHs)-derived SOA tracers

PAHs are significant contributors to SOA formation, particularly in urban areas. The oxidation of naphthalene primarily yields acidic compounds and organic peroxides, which are major components of both high- and low-NO_x SOA (Srivastava et al., 2022). During the OH-initiated photooxidation of naphthalene under high-NO_x conditions, the primary gas-phase products are ring-opening compounds, including 2-formylcinnamaldehyde ($C_{10}H_8O_2$), phthaldialdehyde ($C_8H_6O_2$), and phthalic anhydride ($C_8H_4O_3$). Under low-NOx conditions, the oxidation of naphthalene primarily yields ring-retaining compounds such as naphthol ($C_{10}H_8O$), 1,4-naphthoquinone ($C_{10}H_6O_2$), and epoxyquinone. Additionally, 4-nitro-1-naphthol ($C_{10}H_7NO_3$) can serve as an effective ambient organic tracer for naphthalene-derived high-NOx SOA (Kautzman et al., 2010).

In the gas phase, the oxidation products of acenaphthylene include naphthalene-1,8-dicarbaldehyde ($C_{12}H_8O_2$), 1,8-naphthalic anhydride ($C_{12}H_6O_3$), and a 10-carbon ring-opened dialdehyde. Acenaphthenequinone ($C_{16}H_{10}O_2$) was also identified as a product of oxidation with OH and NO_3. Nitroacenaphthene ($C_{16}H_{11}NO_2$), 1,8-naphthalic anhydride ($C_{10}H_6O_3$), 1-acenaphthenone ($C_{16}H_{10}O$) and naphthalene-1,8-dicarbaldehyde ($C_{10}H_6O_2$) were more abundant in the aerosol phase. The major SOA products naphthaldehyde ($C_{11}H_8O$), oxaacenaphthylene-2-one ($C_{16}H_{10}O_2$), and hydroxyl-naphthaldehyde ($C_{11}H_8O_2$) produced by the gas-phase oxidation of naphthalene ($C_{10}H_8$) by hydroxyl (OH) radicals and acenaphthylene ($C_{16}H_{12}$) by ozone (O_3).

Biomass burning intermediates-derived SOA tracers

Researchers at Caltech conducted photooxidation experiments under low-NOx conditions to study the formation of SOA from the oxidation of phenol (C_6H_6O), guaiacol ($C_7H_8O_2$), and syringol ($C_8H_{10}O_3$), which are major components of biomass burning. $C_6H_6O_{2\text{-}5}$ series and ring fragment from oxidation products $C_4H_4O_{3\text{-}4}$ are the main products from phenol-derived SOA (Nakao et al., 2011b; Yee et al., 2013b). Hydroperoxide $C_7H_{10}O_5$, cluster products for the guaiacol OH-adduct $C_7H_8O_{3\text{-}5}$, hydroxy-butenedial ($C_4H_4O_3$), and methoxy-hydroxy-butenedial fragment ($C_5H_6O_{3\text{-}4}$), dihydroxybenzene ($C_6H_6O_2$), $C_6H_6O_5$ and bicyclic hydroperoxide $C_7H_{10}O_7$ are the main oxidation products from guaiacol-derived SOA (Ofner et al., 2011). The primary oxidation products of syringol include the syringol OH-adduct $C_8H_{10}O_{4\text{-}6}$, and its fragments ($C_6H_8O_5$, $C_5H_6O_4$, $C_4H_4O_3$, and $C_4H_6O_4$), and guaiacol + OH ($C_7H_8O_3$) (Yee et al., 2013b). Under high-NO_x conditions, the primary oxidation products of

phenol include dihydroxybenzene ($C_6H_6O_2$), nitrophenol ($C_6H_5NO_3$), ring-opened acids ($C_6H_6O_3$), and the fragment $C_4H_4O_3$. Notably, nitro-products constitute only a small fraction of SOA yield. Most particle-phase products from guaiacol oxidation are nitrogen-containing compounds, such as dihydroxybenzene derivatives with nitro groups ($C_6H_5NO_{4\text{-}6}$). Guaiacol is rapidly converted to nitroguaiacol ($C_7H_7NO_4$). Simultaneously, the formation of dihydroxybenzene and OH adducts still occurs, as observed under low-NO_x conditions. $C_7H_{10}O_6$ and fragment $C_4H_6O_4$ are the dominant syringol oxidation products (Yee et al., 2013b). Substantial progress in measurement techniques, especially online mass spectrometry, has promoted recent studies on the role of VOCs and organic aerosols, as will be shown in the following section.

1.3 Recent advances in VOC and organic aerosol mass spectrometry

Mass spectrometric techniques analyze compounds by detecting the ions they produce, involving three key components: an ionization unit, a mass analyzer, and a detector. While detectors are common across instruments, various ionization and mass filtering techniques exist, each influenced by specific parameters. These techniques and parameters define a mass spectrometer's performance and the range of compounds it can analyze (Noziere et al., 2015).

1.3.1 VOC measurements

GC-MS offers comprehensive VOC analysis with high separation capability but suffers from low time resolution (>1 h) and requires extensive pre-processing, such as preconcentration and interference removal like ozone and water (Noziere et al., 2015). Real-time chemical ionization mass spectrometry (MS) enables fast measurements (0.1-1.0 s resolution), ideal for studying transport processes and detecting highly reactive species (e.g., sesquiterpene). Proton-transfer-reaction (PTR) time-of-flight (TOF) MS, a widely used method, ionizes VOCs via proton transfer from hydronium ions (H_3O^+), offering high sensitivity and time resolution. However, it may suffer from fragmentation and interferences due to dissociative proton or electron transfer reactions. PTR-TOF-MS can detect a wide spectrum of VOC from non-oxidized to medium-oxidized organic molecules. These compounds include BVOCs (isoprene, monoterpene, and sesquiterpene), aromatics (BTEX), oxygenated VOCs (methanol, MVK, MACR, oxidation products of VOC precursors), and biomass burning VOCs (levoglucosan and vanillin acid) (Yuan et al., 2017). In recent years, next-generation PTR instruments, such as the PTR-3 or Fusion PTR-MS (both Ionicon), have adopted softer reagent ions like NH_4^+ to detect highly oxidized organic compounds. As other modern mass spectrometers, the Fusion

PTR-MS system can rapidly switch between H_3O^+ and NH_4^+ modes for enhanced analytical flexibility (Canaval et al., 2019; Reinecke et al., 2023). Another widely used CIMS technique, I^--TOF-CIMS, employs iodide (I^-) as a softer reagent ion to enable real-time detection of highly oxygenated compounds (Lee et al., 2014). However, due to the radioactive sources needed for efficient generation of I^-, its use is subject to stringent regulations, often limiting its deployment in field measurements. In contrast, the reagent ions used in PTR (e.g., H_3O^+) are considered clean and are more suitable for field applications. Additionally, only PTR-MS, utilizing H_3O^+ as the reagent ion, can quantify the signals of uncalibrated organic species with an accuracy of approximately ±30% through a straightforward reaction kinetics approach (Holzinger et al., 2019). I^--CIMS faces challenges in quantification because its sensitivity varies significantly for different compounds (Bi et al., 2021).

1.3.2 Organic aerosol particle measurements

The chemical composition of organic aerosol is highly complex and dynamic, varying with sources, atmospheric processing, and environmental conditions (Fuzzi et al., 2006; Huang et al., 2024). This complexity arises from many organic compounds, spanning a wide range of volatilities, functional groups, and oxidation states (El Haddad et al., 2013; Ylisirniö et al., 2020). To fully characterize OA, advanced analytical techniques are required to resolve its molecular composition, quantify its contributions, and elucidate its formation pathways.

Several state-of-the-art instruments have been employed to probe different aspects of OA. High-Resolution Time-of-Flight Mass Spectrometry (HR-TOF-MS) provides detailed molecular-level characterization of OA, enabling the identification of hundreds of organic species (Decarlo et al., 2006). The high vaporization temperature in AMS leads to extensive fragmentation, limiting the identification of more precise sources and their tracers. A proton-transfer-reaction time-of-flight mass spectrometer (PTR-TOF-MS, Ionicon Analytik GmbH), equipped with a particle inlet (Chemical Analysis of aeRosol ONline, CHARON), was utilized to measure semi-volatile OA in the particle phase. The CHARON inlet was described in detail elsewhere (Eichler et al., 2015b; Muller et al., 2017; Gkatzelis et al., 2018a; Gkatzelis et al., 2018b). The vaporization temperature of CHARON-PTR-MS is relatively low, around 150°C, resulting in less fragmentation compared to AMS. The CHARON-PTR-MS, operating in H_3O^+ mode, allows for sensitive detection of VOC and semi-volatile OA in both gas and particle phases (Eichler et al., 2015a). Additionally, NH_4^+ mode PTR-MS offers complementary insights into more oxygenated organic compounds (Gao et al., 2022b). Adjusting the PTR drift tube's electric field strength minimizes the fragmentation of oxygenated compounds, enhancing

measurement accuracy (Leglise et al., 2019). The Filter Inlet for Gases and AEROsols coupled to an iodide Chemical Ionization Mass Spectrometer (FIGAERO-I-CIMS) further enhances the detection of low-volatility and highly oxygenated organic compounds (Ye et al., 2021), while NO_3^- reagent ions in CIMS provide improved sensitivity for certain organic peroxides and terpenoid oxidation products (Dam et al., 2022; Garmash et al., 2024). Combining different mass spectrometry techniques enables the detection and identification of a wide range of VOC and SOA compounds, providing a kind of molecular fingerprint of their sources.

This work applies advanced techniques in field campaigns to investigate OA composition and dynamics comprehensively. HR-TOF-MS is used to quantify non-refractory $PM_{2.5}$ (NR-$PM_{2.5}$) and detailed molecular speciation, while CHARON-PTR-MS (H_3O^+ mode) is employed to track VOC and SVOC partitioning. These measurements provide a holistic understanding of the studied environment's OA sources, transformations, and impacts.

1.4 Source apportionment using positive matrix factorization (PMF)

Source apportionment is a methodological approach provided to quantitatively attribute measured pollutants to their respective emission sources and/or formation processes (Paatero, 1997). The chemical constituents of OA are typically identified and quantified through the application of PMF to OA mass spectra, which encompass the temporal variations of hundreds or thousands of compounds. These mass spectra are obtained through various types of mass spectrometers (Zhang et al., 2011b; Chen et al., 2022; Song et al., 2024b). PMF is a multivariate receptor model used to decompose complex datasets of pollutant measurements, identifying and quantifying the contributions of various emission sources.

1.4.1 Theoretical basis of PMF

In PMF analysis, temporal measurements of variables, such as m/z intensities from mass spectrometers, can be represented as a data matrix X_{ij}, where columns (j) are variables, and rows (i) are individual time scans. A widely applied approach is the bilinear model, which decomposes X_{ij} into two matrices, G and F, with a residual matrix E, expressed as:

$$X_{ij}=GF+E \tag{1.1}$$

Here, G represents the time series of the p factors (columns), while F captures their corresponding profiles or fingerprints (rows). The residual matrix E accounts for deviations between observed and modeled data. In this framework, factor profiles remain constant over time, and their temporal variability is represented solely by G (Figure 4) (Ulbrich et al., 2009).

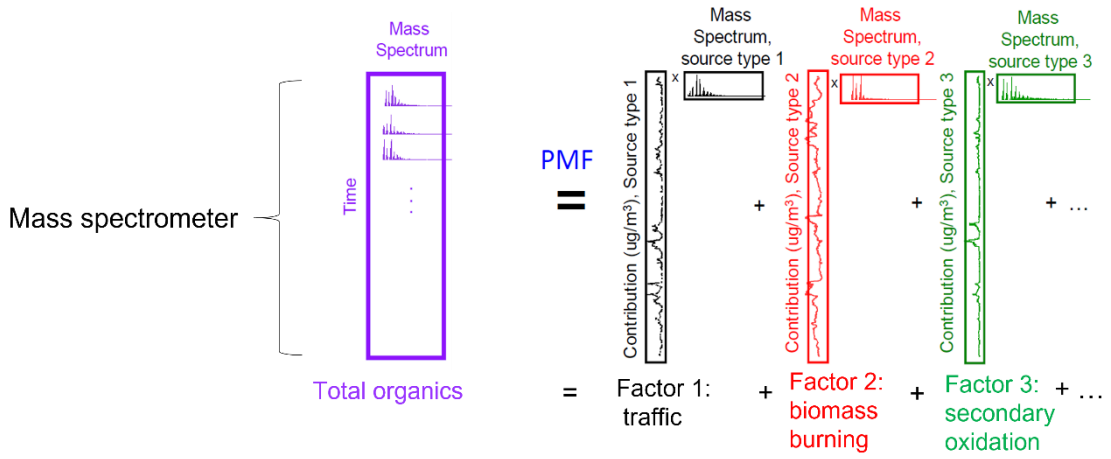

Figure 4. Schematic of the PMF model. The matrix G represents temporal profiles of the factors, while the matrix F contains their corresponding mass spectra, as defined in Equation 1.1 (Ulbrich et al., 2009).

The f_{peak} approach, parameterized by ϕ, is employed to globally regulate matrix rotations in PMF analysis. When ϕ takes positive values, the process involves elementary or successive rotations that amplify the elements in the columns of matrix G (source contributions) while reducing those in the rows of matrix F, maintaining mass balance throughout. In contrast, negative ϕ values reverse this effect, diminishing G's columns and enhancing F's rows. In PMF analysis using f_{peak}, initial and final values, along with the step interval, must be specified. The f_{peak} range should ensure environmentally interpretable solutions with similar mathematical quality (i.e., comparable Q values). The entries in G and F are determined using a least-squares algorithm that minimizes Q, the weighted sum of squared residuals e_{ij} divided by uncertainties σ_{ij} for all data points:

$$Q = \sum_{i=1}^{m} \sum_{j=1}^{n} \left(\frac{e_{ij}}{\sigma_{ij}} \right)^2 \quad (1.2)$$

Here, σ_{ij} typically represents the measurement uncertainty. Data points with e_{ij}/σ_{ij} »1 dominate Q and heavily influence the model. While this emphasizes data with high signal-to-noise ratios, such outliers can also result from local events or instrument noise, which the model should exclude. Monitoring total Q across PMF runs is often not meaningful, as its value depends on the data matrix size and the number of factors. Instead, Q is normalized by the degrees of freedom, yielding Q_{exp}:

$$Q_{exp} = m \cdot n - p \cdot (m+n) \quad (1.3)$$

Here, m represents the number of samples (observations), n represents the number of measured species (variables), and p represents the number of resolved factors. This equation accounts for the total degrees of freedom in the data matrix (m × n) minus the constraints imposed by the

PMF model, which depend on the number of factors (p) and their contributions to both samples and species. In an ideal PMF run, Q/Q_{exp} approaches ~1 if uncertainties account for measurement and modeling errors. However, the modeling of uncertainty is often unknown, especially for ambient data. For the analysis of AMS mass spectra, typical Q/Q_{exp} values range from 1 to 5. Environmental conditions and factor overlap must be considered, as increasing the number of factors often reduces Q/Q_{exp} without significant improvement and may lead to overlapping factors. In such cases, fewer factors should be selected. Only a few studies report Q/Q_{exp} values for the analysis of PTR-MS mass spectra for gases and semi-volatile aerosol particles. But no exact values are provided. Factors should be screened based on their correlation with tracers (e.g., toluene for traffic, levoglucosan, and vanillin acid for biomass burning). Selection of factors should result in high correlations ($R > 0.8$) with tracers for reliable PMF results.

1.4.2 Common PMF software

EPA PMF (US Environmental Protection Agency) represents one of the most extensively applied receptor modeling tools in environmental research, particularly for air and water quality assessments. It supports diverse environmental datasets, including particulate matter, VOCs, and trace metals, without requiring predefined source profiles, making it a purely exploratory approach. A key advantage of EPA PMF is its integrated uncertainty analysis, employing bootstrapping, displacement (DISP), and f_{peak} parameter testing to evaluate solution stability and rotational ambiguity. While widely used in regulatory applications such as the National Air Toxics Trends Stations (NATTS) and Speciation Trends Network (STN), the model has certain limitations. Its inability to incorporate external constraints or prior knowledge restricts its effectiveness in resolving collinear sources (Brown et al., 2015; Frischmon and Hannigan, 2023).

The **PMF Evaluation Tool (PET)** serves as a specialized analytical platform designed primarily for processing AMS/ACSM data, though its adaptable framework permits application to various multivariate datasets. Implemented within Igor Pro's computational environment, this tool offers researchers an interactive interface to conduct complete PMF analyses, encompassing data preparation, uncertainty estimation, iterative model execution, and solution diagnostics. PET distinguishes itself through sophisticated data management capabilities, allowing selective data filtering, customizable convergence parameters, and systematic handling of input/output files. While originally optimized for atmospheric aerosol characterization, particularly in collaboration with the University of Colorado Boulder's

research community, the software's architecture supports extension to other analytical domains requiring multivariate factorization. Its comprehensive documentation and academic origins make PET particularly valuable for detailed source apportionment studies, combining methodological rigor with operational flexibility (Jimenez, 2025).

For more complex source-separation challenges, **SoFi with the Multilinear Engine (ME-2)** offers greater analytical precision by allowing users to impose a priori constraints on factor profiles. This sophisticated tool enables the integration of a priori knowledge through customizable constraints on factor profiles and temporal patterns, significantly enhancing source resolution in complex environmental datasets. Particularly valuable for challenging separation tasks like discriminating between diesel and gasoline emissions or differentiating primary and secondary organic aerosols, SoFi's constrained PMF approach delivers more physically meaningful solutions than unconstrained alternatives. Developed through collaboration between the Paul Scherrer Institute and Datalystica, the software combines ME-2's computational power with an intuitive interface and comprehensive visualization tools. While particularly popular in AMS and VOCs research communities, its adaptable framework supports diverse multivariate applications. The inclusion of robust uncertainty assessment methods, including bootstrap analysis and factor element displacement, further strengthens result reliability. Although the platform's advanced capabilities may present a steeper learning curve for novice users, its capacity to incorporate prior knowledge makes it indispensable for studies requiring high source resolution (Canonaco et al., 2013; Crippa et al., 2014). However, its reliance on scripting and computational intensity may pose challenges for less experienced users.

1.4.3 Applications and limitations

PMF has become a vital tool for identifying and quantifying pollution sources, particularly for aerosols and VOCs in atmospheric studies (Figure 5). By decomposing complex environmental datasets into factor profiles and contributions, PMF helps distinguish emission sources such as vehicular exhaust, industrial activities, biomass burning, and biogenic emissions. Its ability to handle measurement uncertainties and apply non-negative constraints makes it especially valuable for aerosol speciation data (e.g., from AMS or ACSM) and VOC measurements (e.g., PTR-MS or GC-MS) (Liu et al., 2024).

However, PMF has inherent limitations. Collinearity among sources (e.g., diesel and gasoline emissions) can complicate factor separation, requiring advanced implementations like ME-2

with constraints (Zhang et al., 2011a; Drosatou et al., 2019). In VOC studies, reactive losses of species due to oxidation reactions with OH radicals or ozone introduce biases, leading to underestimated contributions from highly reactive sources like biogenic emissions or industrial precursors. Additionally, the method relies heavily on data quality and may struggle with low-concentration species or highly variable sources (Liu et al., 2024). Despite these challenges, PMF remains widely used in air quality research, offering insights for policy-making and pollution mitigation.

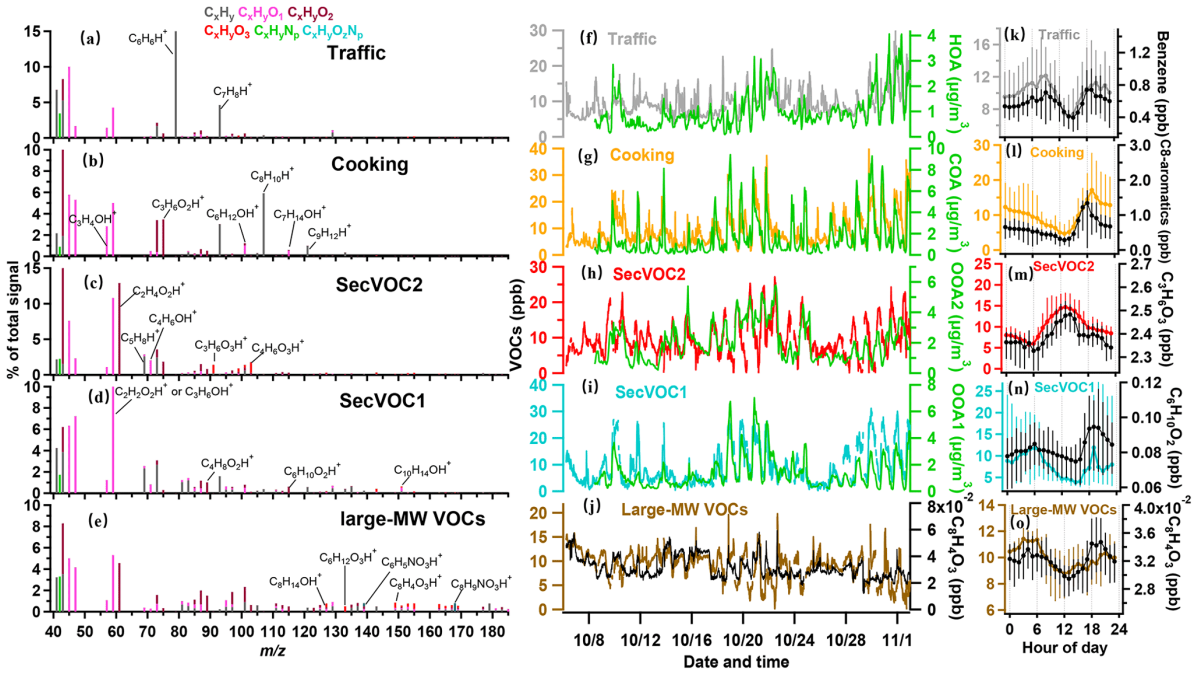

Figure 5. Example of source apportionment by PMF analysis of VOC mass spectra measured by PTR-TOF-MS (Li et al., 2022).

1.5 Research objectives

VOCs and OA play critical roles in atmospheric chemistry, air quality, and climate change. In urban areas, VOCs and OA are predominantly emitted from anthropogenic sources such as traffic, industrial activities, biomass burning, and volatile chemical products (VCPs) (Hafner et al., 2013; Wan et al., 2019; Chen et al., 2022). At the same time, BVOCs from plants and biomass burning VOCs are the primary contributors in forested regions. Key knowledge gaps remain despite significant advancements in source apportionment techniques, real-time monitoring, and modeling (Crippa et al., 2014; Kaltsonoudis et al., 2016; Drosatou et al., 2019; Huang et al., 2024).

While advanced analytical techniques like PTR-MS and AMS have enabled detailed speciation of VOCs and OA in various environments, and PMF analysis has successfully resolved common urban sources like traffic and cooking emissions, significant gaps remain in our

understanding of regional aerosol characteristics. Many urban areas, particularly megacities, and forested regions remain understudied, leaving their aerosol source profiles and influencing factors poorly characterized. The primary sources of VOCs and OA exhibit substantial spatial variability, highly dependent on local emission patterns and environmental conditions (Zhang et al., 2011a; Schäfer et al., 2014; Yuan et al., 2017; Huang et al., 2024). This spatial dependence is particularly evident in ultrafine particle (UFP) dynamics, where concentration, formation, and growth processes vary substantially across regions. While urban UFP shows strong correlations with traffic emissions (Kittelson et al., 2022), the relative contributions of different VOC classes to particle growth remain poorly studied (Thomas et al., 2025). Furthermore, seasonal variations in VOC oxidation pathways and their subsequent impacts on UFP formation are poorly characterized (Li et al., 2023b), creating uncertainties in our understanding of atmospheric processes across different seasons. The atmospheric system exhibits additional complexity through long-range transport mechanisms, which have been shown to contribute significantly to free tropospheric OA (Scholz et al., 2023). However, the relative importance of local emissions versus transported pollutants remains unclear, particularly in remote forested areas. These knowledge gaps extend to our understanding of how different sources (e.g., traffic vs. BVOCs) interact in urban settings, and how meteorological parameters influence VOC emissions and subsequent SOA formation processes. Current limitations in measurement approaches further compound these knowledge gaps. Many existing source apportionment studies rely on offline filter sampling methods that suffer from low time resolution, often missing critical pollution events and transient atmospheric processes (Schnelle-Kreis J. et al., 2001; Timkovsky et al., 2015). This methodological constraint significantly limits our ability to accurately analyze sources and their temporal variations.

This research aims to address these critical gaps by employing state-of-the-art real-time measurement techniques to advance our understanding of VOC and organic particle sources and their ultimate impacts on air quality and climate in urban and forest environments. My primary research objectives are as follows:

(1) Determine composition and identify sources of VOCs and organic aerosol particles in urban and rural/forest areas.
(2) Quantify the contribution of different VOCs to the total VOC budget and their role in forming SOA in urban and rural/forest areas.

(3) Determine the major sources of VOCs and organic particles that contribute to UFP formation and growth in both urban and forested environments, focusing on the role of VOCs and organic aerosols.

(4) Compare the seasonality of sources of OA and VOCs in urban areas and their impact on UFP.

(5) VOCs and aerosol particle sources in a remote rural forested location in the boundary layer and free troposphere, and their potential impact on cloud properties, impact of local, regional sources vs. long-range transport.

2. Methodology

I conducted four field measurement campaigns to achieve the research objectives, three in urban areas and one in a mountainous forested region. These field measurements were designed to identify the primary sources of VOCs and organic particles in both forest and urban environments, as well as to investigate their influence on organic particle formation and growth. For the chemical characterization of VOCs and organic particles, I primarily utilized a CHARON-PTR-MS and an HR-TOF-AMS. Additionally, I employed an Aethalometer (AE33) to measure black carbon concentrations, a Scanning Mobility Particle Sizer (SMPS) and an optical particle counter (OPC) to determine particle size distributions, a Condensation Particle Counter (CPC) to quantify total particle number concentrations, and tracer gas sensors to monitor tracer gases, among other instruments introduced in the following.

2.1 Mass spectrometry

2.1.1 CHARON-PTR-MS

The CHARON-PTR-MS is a state-of-the-art analytical instrument used for the real-time detection and quantification of atmospheric VOCs e.g., aromatics, terpenes, carbonyls, and, alcohols, with a detection limit as low as several parts per trillion by volume (pptv). In this dissertation, I used a PTR-TOF-MS (4000X2, Ionicon Analytik GmbH), equipped with a particle inlet (CHARON), to measure VOCs in the gas phase and semi-volatile aerosols in the particle phase (Muller et al., 2017; Gkatzelis et al., 2018a). This PTR-TOF-MS mainly consists of four parts: ion source, drift tube, transfer system, and detection system (Figure 6). (1) The ion source consists of two chambers. The first chamber (left) contains the hollow cathode discharge, while in the second chamber ion fragments can recombine to form the precursor ions. From this second chamber the reagent ions are extracted into the drift tube and neutral molecules (e.g. H_2O, OH in H_3O^+ mode) are pumped away. Notably, the new FUSION PTR-TOF-MS with a mass resolution of 10000 can switch between different reagent ions (e.g., H_3O^+, O_2^+, NO^+, NH_4^+) in approximately 1 second or less, enabling fast selective reagent ion switching (Reinecke et al., 2023). (2) The sampled air containing VOCs, injected into the drift tube via a venturi-type inlet, undergoes proton or charge transfer with reagent ions (H_3O^+, NO^+ or O_2^+). Reaction pressure in the drift tube is ~2.3 to 3 mbar. In this dissertation, the PTR-MS 4000 was operated at 100°C, 2.7mbar, and 92Td electric field. The Fusion PTR-MS was operated at 120°C, ~2.7mbar, and 120Td electric field. (3) The transfer system consists of a lens-based ion booster and ion guide. The ion booster, an ion funnel positioned at the end of

the drift tube, focuses ions into the exit pinhole toward the transfer lens system. It comprises a series of stacked ring electrodes with progressively decreasing inner diameters (Figure 6b). This design enhances ion transmission through the pinhole, increasing signal intensity in the mass spectrometer. Additionally, the funnel's confining potential minimizes ion losses to the walls, allowing the use of a lower forward drift field in this region. The resulting extended reaction time further improves sensitivity. a hexapole is installed after the ion booster to minimize ion loss and enhance transmission. The hexapole consists of six rods operated with both funnel on and a DC voltage, referred to as the offset, typically set within a range of +/- 1.5 V. This offset voltage ensures smooth ion transfer from the drift tube to the lens system. Excessive DC voltage, however, may increase fragmentation and adversely affect transmission efficiency. (4) The number of ions reaching the detector and the peak resolution highly depend on the voltages applied to the TOF's electric lenses and grids. Periodic adjustment of these voltage presets is necessary to optimize performance. The lens system following the hexapole transfers and focuses ions from the hexapole to the TOF's extraction region. These ions are then accelerated into the cage region and must follow a consistent flight path through the reflectron to reach the detector. The reflectron focuses the ions, ensuring high resolution while maintaining a compact design.

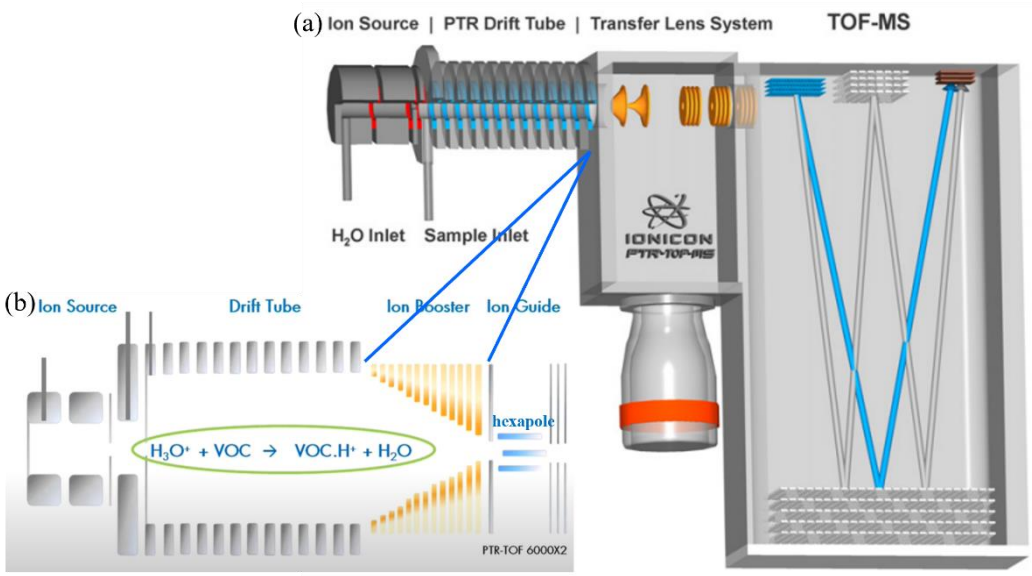

Figure 6. Schematic of the PTR-ToF-MS with ion source, drift tube, transfer system and detection system (ToF-MS) (a) Ionicon recently added an ion booster after the drift tube to focus the ions (https://www.ionicon.com/accessories/details/ion-booster)

PTR-MS operates as a pseudo-absolute method. Under a clear excess of primary ions in the drift-tube reaction chamber, ion-molecule reactions adhere to pseudo-first-order kinetics. For a reaction between analyte A and primary ions H_3O^+, the concentration of A can be determined

using the reaction rate constant (k), reaction time (t), and the measured concentrations of H3O+ and protonated analyte AH^+:

$$H_3O^+ + A \xrightarrow{k} AH^+ + H_2O \tag{2.1}$$

$$[AH^+] \sim [H_3O^+] \cdot k \cdot t \cdot [A] \tag{2.2}$$

The reaction time (t) typically ranges around 100 µs. The reaction rate constant (k) varies depending on the molecule and reaction conditions, but for most relevant VOCs in H_3O^+ mode, deviations are generally within ±30%. For instance, acetone exhibits a reaction rate constant of 3.4×10^{-9} cm^3/s, while benzene has a lower constant of 1.9×10^{-9} cm^3/s.

To calculate volume mixing rations (VMR) from measured data in counts per second (cps), I needed to add several additional parameters like the temperature in the drift tube reaction chamber T_{drift},

Equation (2.3) demonstrates the calculation of volume mixing ratios (VMR) using measured and known quantities from the PTR-MS instrument (De Gouw and Warneke, 2007).

$$VMR_M(ppbv) = \frac{i(MH^+)}{Tr(MH^+)} \cdot \frac{Tr(H_3O^+)}{i(H_3O^+)} \cdot \frac{10^9 \cdot U_{drift} \cdot K_0^{H_3O^+} \cdot V_0 \cdot P_0^2 \cdot T_{drift}^2}{K_M \cdot L^2 \cdot P_{drift}^2 \cdot N_A \cdot T_0^2} \tag{2.3}$$

VMR_M(ppbv) is volume mixing ration of compound M given in ppbv; $i(MH^+)$ is measured ion yield of MH^+ in cps; $Tr(MH^+)$ and $Tr(H_3O^+)$ are transmission correction factors of MH^+ and H_3O^+ obtained from the transmission curve of the instrument, respectively; $i(H_3O^+)$ is measured ion yield of H_3O^+, usually obtained by the isotope corrected ion yield of $H_3{}^{18}O^+$ (m/z=21.022, isotope correction factor 487.6) to avoid detector saturation effects on m/z=19.018; 10^9 is the multiplication factor to arrive at ppbv, U_{drift} is the voltage applied to drift tube given in V; $K_0^{H_3O^+}$ is the reduced ion mobility of H_3O^+ given in $cm^2 \cdot V^{-1} \cdot s^{-1}$, $K_0^{H_3O^+}$=2.81$cm^2 \cdot V^{-1} \cdot s^{-1}$; V_0 is the molar volume given in cm^3, V_m=22414 cm^3; p_0 is the normal pressure given in mbar, p_0=1013 mbar; T_{drift} is the temperature in the drift tube in K; K_M is the reaction rate constant, typically in the range $K_M=(1\text{-}5) \cdot 10^{-9} cm^3 \cdot molecule^{-1} \cdot s^{-1}$; L is the length of the drift tube given in cm, typical L=9.2cm; p_{drift} is the pressure in the drift tube given in mbar; N_A is the Avogadro number, $N_A = 6.022 \cdot 10^{23}$; T_0 is the normal temperature given in K.

Purely calculation-based quantification in PTR-MS has limitations, primarily due to instrument transmission uncertainties (±15%, potentially up to 50%), fragmentation reactions (e.g., alcohols losing H_2O), backward reactions (e.g., formaldehyde), and interference (e.g.,

hydrocarbons). Reaction rate constants are often estimated (±30%). Direct calibration of target compounds is recommended for accuracy. The PTR-MS was calibrated at the start, occasionally during, and at the end of the field campaigns. Prior to July 2023, calibrations were performed using a gas cylinder (Ionicon Analytik GmbH) containing toluene, 1,3,5-trimethylbenzene, m/o/p-xylene, limonene, α-pinene, acetone, benzene, isoprene, and methanol, each at a mixing ratio of ~100 ppb with a 10% accuracy. After that, a new gas cylinder (Ionicon Analytik GmbH) was employed, containing toluene, 1,2,4-trimethylbenzene, o-xylene, α-pinene, 1,2,4-trichlorobenzene, 3-hexanone, acetaldehyde, acetone, acetonitrile, benzene, 1,2-(O-)-dichlorobenzene, isoprene, and methanol, each at ~1 ppm (10% accuracy), as well as decamethylcyclopentasiloxane and hexamethylcyclotrisiloxane, each at ~0.5 ppm (10% accuracy). Figure 7 presents the comprehensive gas calibration data from all the field campaigns. I used two calibrated mass flow controllers (Bronkhorst, Netherlands; 10 L/min and 0.1 L/min, ±5% accuracy) to dilute the gas standard to the desired range (0.01–50 ppb) (Song et al., 2024a). It was observed that sensitivities decrease over time during field measurements due to the gradual contamination of the drift tube and lenses, even after tuning. When tuning fails to restore the target sensitivity, cleaning of these components is required.

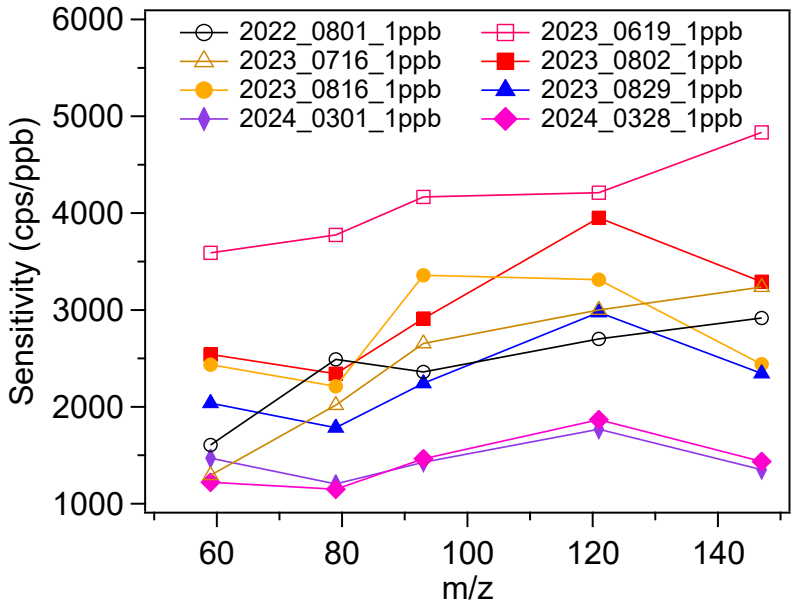

Figure 7. Sensitivities for the PTR-MS calibrated by a reference gas mixture (Ionicon Analytik GmbH) for all field campaigns. The calibrations were conducted before and after the campaigns. The variability is mainly caused by contamination of the instrument inlet throughout the campaign durations.

The CHARON inlet was made to detect the chemical composition of the particle phase. Figure 8a illustrates the schematic of the CHARON inlet. The automated valve, controlled by a sequencer, switches between the HEPA inlet (for particle background measurement) and the particle inlet. Key components of the CHARON inlet include a gas-phase denuder for removing

gaseous organics, an aerodynamic lens system for particle enrichment, and a thermo-desorber set to 150°C to vaporize particles, maintaining an absolute pressure of 7-8 mbar. The PTR-MS was operated at ~60 Td when in CHARON mode. At the start and/or conclusion of the field campaigns, the enrichment factor of the CHARON inlet was evaluated through external calibration using ammonium nitrate particles size-selected by SMPS (NH_4NO_3, ~100-500 nm), which were quantified using a CPC. Figure 8b shows CHARON enrichment factor (EF) in different field campaigns.

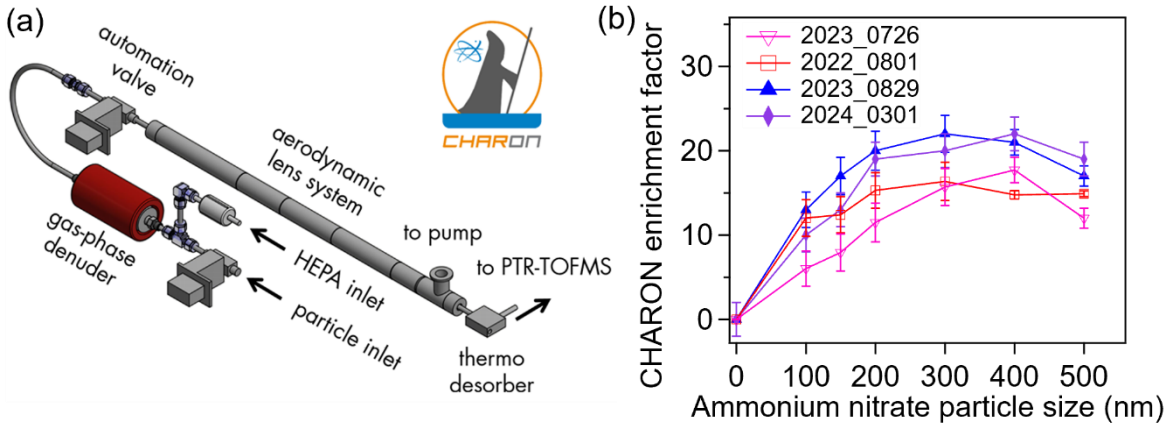

Figure 8. Schematic of the CHARON inlet (https://www.ionicon.com/technologies/details/charon) (a) and the measured enrichment factors (b)

2.1.2 HR-TOF-AMS

A high-resolution time-of-flight Aerosol Mass Spectrometer (HR-TOF-AMS) (Aerodyne Research Inc.), equipped with a $PM_{2.5}$ aerodynamic lens, was used to measure non-refractory $PM_{2.5}$ (NR-$PM_{2.5}$) components, including organic aerosol, nitrate, sulfate, ammonium, and chloride, with a time resolution of 1 minute (Peter F. Decarlo et al., 2006; Canagaratna et al., 2007; Williams et al., 2013). Figure 9 shows the main parts of the HR-TOF-AMS. The instrument comprises four main components: a sampling system, sizing region, vaporization, and ionization systems. Ambient air is drawn through a critical orifice into an aerodynamic lens, focusing particles (0.07-2.5 µm) into a narrow beam while removing most gases via turbo pumps. Particles are accelerated into the sizing region (particle time-of-flight, PTOF) for size determination, then vaporized at 600°C and ionized by electron ionization (70 eV) for analysis by a time-of-flight mass spectrometer. The AMS alternates between V mode (mass concentration, size distribution) and W mode (high-resolution mass spectra, $m/\Delta m > 5000$). In this study, it operated in 1-min intervals for each mode, with V mode data reported and W mode data used for peak fitting. The HR-TOF-AMS was calibrated for ionization efficiency (IE) using ammonium nitrate, which is atomized, dried, and size-selected (typically 300-500

nm) to establish a known mass input. More calibrated details are described in a previous study (Song et al., 2022). I calibrated the AMS for every field campaign on the same days with CHARON-PTR-MS (Figure 8b). The detection efficiency sharply declines for particles below ~60 nm, dropping to <20% for diameters under 30 nm due to incomplete vaporization and ion extraction losses (Guo et al., 2021). To address the issue of particle bounce losses, a chemical-composition-based collection efficiency (CE) of approximately 0.5 was applied to calculate the particle mass concentrations (Docherty et al., 2011; Middlebrook et al., 2012). For the elemental analysis of organic aerosol (OA), including the hydrogen-to-carbon ratio (H: C) and the oxygen-to-carbon ratio (O: C), I utilized the improved ambient method (Allison C. Aiken et al., 2008; Canagaratna et al., 2015). AMS datasets combined with PMF can quantitatively identify major primary organic aerosol (POA) sources, including traffic-related hydrocarbon-like organic aerosol (HOA) and biomass burning organic aerosol (BBOA)(Chakraborty et al., 2017; Lalchandani et al., 2021).

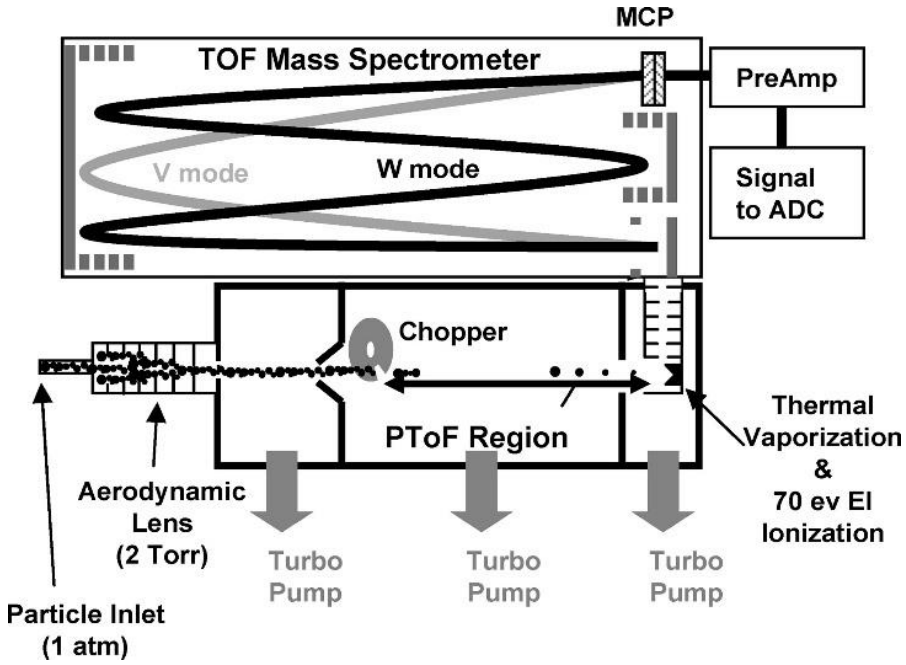

Figure 9. A schematic of the HR-ToF-AMS (Decarlo et al., 2006)

2.2 Data analysis methods

2.2.1 MS analysis software

The CHARON-PTR-MS data were analyzed by the software PTR Viewer 3.3.12 (updated version 3.4.4, Ionicon Analytik GmbH) and the Ionicon Data Analyzer (IDA 2.2.0, Ionicon Analytik GmbH) especially for larger sets of data. In the PTR Viewer, chemical formulas for ion masses were assigned using a software-generated peak list, supplemented by PTR-MS

literature data (Pagonis et al., 2019; Yáñez-Serrano et al., 2021). A high-resolution peak fitting algorithm was manually adjusted, and PTR Viewer calculated ion counts, performing baseline correction and mass discrimination correction. Uncalibrated compound concentrations were determined using transmission curve coefficients and estimated rate constants. The transmission curve, calculated in PTR Viewer, was applied in IDA for quantification. I primarily utilized IDA for data analysis due to its enhanced analytical capabilities compared to PTR Viewer. IDA enables comprehensive analysis of PTR-MS data with the following features: (i) Presets select intensity and m/z ranges; (ii) Timing tool defines instrument stability periods and filters time-series segments; (iii) Mass Calibration Tool selects calibration peaks and visualizes mass accuracy metrics; (iv) Peakshape automatically calculates peak shapes from recorded spectra; (v) Peak Detection Tool identifies isobaric ion signals and assigns chemical compositions; (vi) Time Series Tool initializes calculations for time- and mass-resolved results; (vii) Transmission Tool visualizes transmission data and primary ion information; (viii) Sensitivity tool assigns reaction rate coefficients (k-rates) to detected m/z or compositions, proportional to instrument sensitivity; (ix) Concentration Tool applies transmission, primary ion, and reaction rate data to quantify datasets within selected smoothing windows (Müller et al., 2011; Müller et al., 2013; Müller et al., 2017; Sekimoto et al., 2017).

Data from the AMS were processed and analyzed using the SQUIRREL 1.65G and PIKA 1.25G software packages. For the HR-TOF-AMS data analysis, I adhered to the standardized procedures outlined by the Jimenez Research Group (University of Colorado Boulder. Retrieved [14th May, 2025], http://cires1.colorado.edu/jimenez-group/wiki/index.php/ToF-AMS_Analysis_Software). The workflow included the following steps: loading raw data, performing mass calibration, conducting baseline calibration, and applying parameter corrections (e.g., air beam, ionization efficiency, and collection efficiency). Unit resolution data for non-refractory compounds were processed, followed by high-resolution fitting in PIKA to refine peak width and peak shape. Peak identification was then performed, and high-resolution graphs were generated.

2.2.2 Positive matrix factorization software for source analysis (PMF)

The PMF receptor model is a bilinear algorithm that separates air pollutant time series into sources characterized by factor profiles, time series, and residuals (Paatero and Tapper, 1994; Paatero, 1999). It is widely used to identify particle and VOC sources (Kim et al., 2004; Reyes-Villegas et al., 2016; Huang et al., 2018b; Gkatzelis et al., 2021). To investigate the sources of VOC, SVOA, and OA, I conducted PMF analysis on VOC mass spectra from PTR-MS, semi-

volatile aerosol particle mass spectra measured by CHARON-PTR-MS, and mass spectra measured by HR-TOF-AMS for non-refractory $PM_{2.5}$ particles, respectively.

The Source Finder (SoFi Pro 9.0, Datalystica Ltd., Villigen, Switzerland) offers a constrained PMF approach and can integrate data from diverse mass spectrometry instruments. This function elevates its analytical precision beyond single-instrument workflows. While SoFi itself does not directly merge raw data streams from separate instruments (e.g., HR-TOF-AMS, GC-MS, or CHARON-PTR-MS), its ME-2-driven framework enables cross-validation and harmonized interpretation of multi-instrument datasets. For instance, SoFi can ingest factor profiles derived from HR-TOF-AMS organic aerosol data and align them with PTR-MS-resolved VOC tracers, creating a unified source apportionment model. This interoperability is critical for resolving complex emission scenarios, such as distinguishing biomass burning markers (e.g., levoglucosan from AMS) from overlapping industrial VOCs (e.g., benzene derivatives detected via PTR-MS). By leveraging a priori constraints in ME-2, users can anchor ambiguous factors to instrument-specific tracers, reducing rotational ambiguity and enhancing physical interpretability (Canonaco et al., 2013; Timkovsky et al., 2015; Tong et al., 2022). In my own research, I attempted to combine AMS and CHARON-PTR-MS data for PMF analysis to investigate SOA sources. However, I have not yet fully mastered the technical nuances of this integration, particularly in optimizing error estimations and resolving factor rotational ambiguities. After completing my thesis, I plan to further explore SoFi's capabilities to refine this approach, as it holds great promise for disentangling complex emission sources.

Beyond instrument integration, SoFi's second standout feature is its seamless incorporation of meteorological data (e.g., wind speed/direction, temperature) to contextualize source apportionment results. The software's built-in tools can generate polar plots (wind roses) and bivariate polar concentration plots, which visually link source contributions to atmospheric transport patterns (Tong et al., 2018). For instance, a high PMF factor loading for industrial tracers (e.g., heavy metals, sulfate) combined with wind plots revealing dominant upwind directions can pinpoint potential pollutant origins.

In this study, SVOA ions (mainly C_xH_y, $C_xH_yO_z^+$, and $C_xH_yO_zN_n^+$) from gas and particle were used for PMF analysis, employing VOC-PMF inputs from a previous study (Song et al., 2024b) and SVOA-PMF inputs directly from High-Efficiency Particulate Air (HEPA) data and Direct (Dir) sampling data. The HEPA filter measurements provide background or particle-free reference data, enabling researchers to differentiate between gas-phase and particle-phase components through comparative analysis of filtered and unfiltered measurements. In contrast,

Dir sampling collects unfiltered air samples that contain both gas-phase and particle-phase SVOA ions. Low-molecular-weight VOC (m/z $\leqslant$ 60) and less abundant VOC with $\geqslant$20% missing data were excluded from the PMF input. PMF analyses for VOC and SVOA were conducted using Source Finder (SoFi Pro 9.0, Datalystica Ltd., Villigen, Switzerland). The sources of OA (m/z 12–120) were resolved through an unconstrained PMF analysis using the PMF Evaluation Tool (v3.08C) in the IGOR Pro software (v8.04, Wavemetrics, Portland, OR).

2.3 Auxiliary instruments

Throughout my PhD research, a suite of auxiliary instruments was employed to complement gas, particle, and meteorological measurements, as briefly outlined below.

Gas monitors: Trace gases were measured using FEP sampling tubes connected to gas monitors: nitrogen dioxide (NO_2, AS32M, Environment SA), ozone (O_3, O341M, Environment SA), and sulfur dioxide (SO_2, AF22M, Environment SA). NH_3 was measured using cavity ring-down spectroscopy (G2103, Picarro, USA). Dr. Harald Saathoff operated the instruments and provided time-resolved concentration data.

Meteorological data: Meteorological data, including atmospheric pressure, radiation, wind direction, wind speed, air temperature, relative humidity, and precipitation, were primarily obtained from a compact sensor (WS700, Lufft). Hourly boundary layer height (BLH) data for the measurement region (0.25°×0.25° resolution) were retrieved from the ERA5 reanalysis by the European Centre for Medium-Range Weather Forecasts to assess their influence on ambient air pollutant variations. Operations and data analysis were primarily conducted by Dr. Harald Saathoff and myself.

Optical particle counter (OPC): The Fidas200 (Palas, Germany), an optical particle counter (OPC), was utilized to measure aerosol particles in the size range of 0.18–18 μm. This instrument employs Lorenz-Mie scattered light analysis to determine particle size and calculate mass concentrations (e.g., PM_1, $PM_{2.5}$, PM_4, and PM_{10}) based on the measured size distribution. Operating at a flow rate of 5 L min^{-1} with a 1-second time resolution, the Fidas200 provided continuous, high-temporal-resolution data. The operations and data analysis were jointly conducted by Dr. Harald Saathoff and myself, yielding e.g. time-resolved mass concentration profiles for $PM_{2.5}$ and PM_{10}.

Condensation particle counter (CPC): During my research, particle number concentrations were measured using different CPCs (CPC3022A, CPC3788, CPC3756, and CPC3776, TSI

Inc., USA). The CPC3788 uses water as the working fluid, while the other models (CPC3022A, CPC3756, and CPC3776) utilize butanol. These instruments draw aerosol samples through a heated saturator, where the working fluid (water or butanol) vaporizes and diffuses into the aerosol stream. The vapor condenses onto particles, causing them to grow into larger droplets, which are then detected optically. The CPC3022A detects particles >7 nm, while the CPC3788, CPC3756, and CPC3776 detect particles >2.5 nm. During the Karlsruhe campaign (July 2022), the CPC3788 and CPC3776 were deployed. In the SwabianMOSES campaign (June 2023), CPC3756 and CPC3022 were used, while the Munich campaigns (August 2023 and March 2024) utilized CPC3756 and CPC3776, and CPC3022 and CPC3776, respectively. All CPC operated with a time resolution of 1 second. The operations and data analysis were primarily conducted by Dr. Harald Saathoff and me.

Scanning Mobility Particle Sizer (SMPS): During my experiments, particle size distributions were measured using various SMPS systems. In the Karlsruhe campaign (July 2022), a Nanoscan 3910 (TSI Inc.) was employed to measure particles in the range of 10-410 nm with a time resolution of 1 minute. For the SwabianMOSES campaign (June 2023), a Universal Scanning Mobility Particle Sizer (U-SMPS 2100/2200, PALAS) was used. In the Munich campaign (August 2023), a traditional SMPS system consisting of a Differential Mobility Analyzer (DMA 3081, TSI Inc.) and a Condensation Particle Counter (CPC3022, TSI Inc.) measured particles in the range of 13.6-763.5 nm with a time resolution of 7 minutes. Similarly, in the Munich campaign (March 2024), the Nanoscan 3910 was again utilized for measurements in the 10-410 nm range at a 1-minute resolution.

The SMPS systems operate by charging particles using a bipolar aerosol charger, classifying them based on electrical mobility in a DMA, and quantifying their concentration with a CPC. Operations and data analysis were primarily conducted by Dr. Harald Saathoff and myself.

Aethalometers: Black carbon (BC) concentrations were measured using the AE33 aethalometer (Magee Scientific, USA), which quantifies aerosol light absorption at seven wavelengths (370, 470, 520, 590, 660, 880, and 950 nm). The instrument operates at a flow rate of 5 L min^{-1} with a time resolution of 1 minute. BC mass is derived from light absorption at 880 nm, where the contribution from other aerosol components (e.g., organic aerosols or minerals) is minimal, using a mass absorption cross-section of 7.77 m^2 g^{-1}. The AE33 employs a dual-spot measurement technique, with two sampling spots at different flow rates and a reference spot to correct for filter loading effects. Additionally, scattering effects within the filter are corrected using a default scattering correction factor of 1.57 (Drinovec et al., 2015).

The absorption Ångström exponent (AAE), calculated from absorption at 470 nm and 950 nm, distinguishes between BC from fossil fuel combustion (BC_{ff}, AAE = 0.95) and biomass burning (BC_{bb}, AAE = 1.60) (Saarikoski et al., 2021). Operations and data analysis were primarily conducted by Dr. Harald Saathoff and myself.

Air mass back trajectory analysis and wind polar plot: To investigate the impact of air mass origins on atmospheric pollutants, 72-hour back trajectories at an altitude of 500m were computed hourly using MeteoInfoMap (MeteoInfo v1.8, an open-source software tool for meteorological data visualization and analysis, Beijing, China) (Wang, 2019). Finally, all trajectories were grouped into different clusters.

Measurement container and inlets used: The experimental setup utilized specialized measurement containers housing all instrumentation. Prior to 2024, I employed a 16 m^2 container (461 cm × 340 cm × 250 cm), which was subsequently replaced with a larger 20 m^2 container (600 cm × 330 cm × 244 cm) for post-2024 experiments. Both containment systems were equipped with multiple sampling inlets: a $PM_{2.5}$ inlet port (16.7 standard liters per minute) serving various mass spectrometers, a total suspended particulate (TSP) inlet port for instruments including the Fidas, SMPS, and CPC for comprehensive particle measurements, along with a fluorinated ethylene propylene (FEP) tube port for gas sampling. Additionally, a WS700 inlet was incorporated for meteorological parameter monitoring. This integrated inlet configuration enabled simultaneous characterization of both particulate and gaseous components under controlled conditions.

2.4 AIDA simulation chamber campaigns

The AIDA (Aerosol Interaction and Dynamics in the Atmosphere) simulation chamber, located at the Institute of Meteorology and Climate Research (IMK) of the Karlsruhe Institute of Technology (KIT), is designed to study aerosol and cloud formation processes under atmospheric conditions (Figure 10). The chamber comprises an aluminum cylinder with a volume of 84.5 m^3, capable of operating across a wide range of temperatures (183-333 K), pressures (1-1000 hPa), and relative humidity (RH, 0-200%). It also features adjustable warming and cooling rates, along with an LED-based light source to simulate solar radiation for investigating aerosol photochemistry. A detailed description of the AIDA chamber, its operational modes, and associated measurement techniques has been previously published (Saathoff et al., 2009; Vallon et al., 2022).

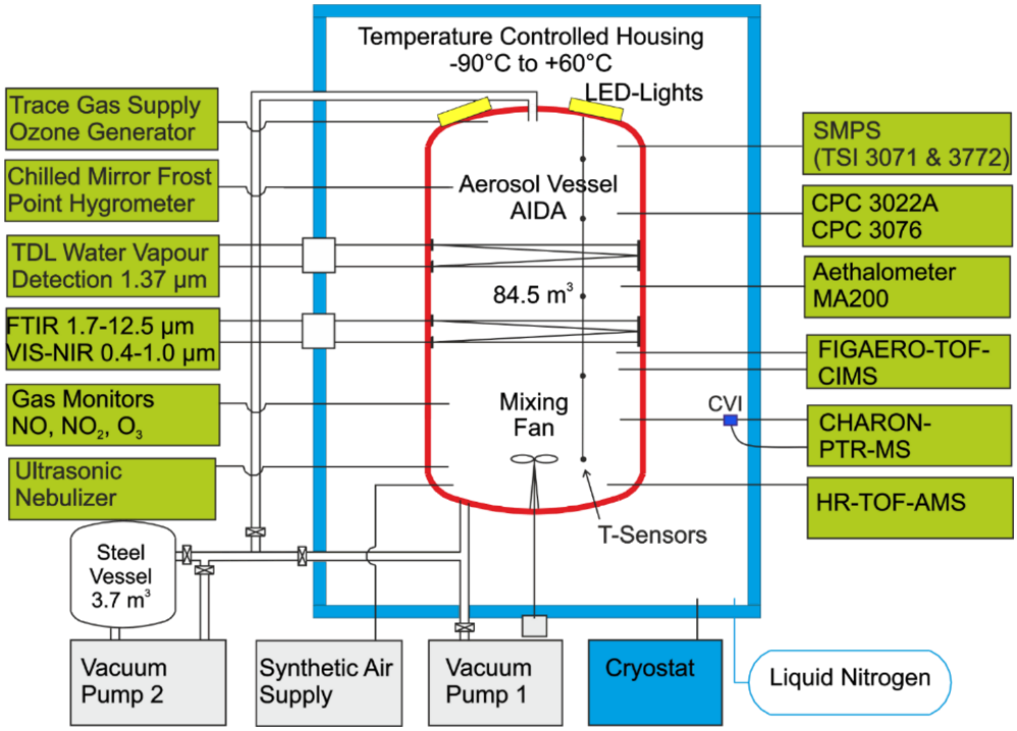

Figure 10. Schematic of the AIDA aerosol and cloud chamber with typical instrumentation (Gao et al., 2022a)

During my PhD study, I participated in 10 chamber campaigns (SOA21b, SOA22a, SOA22b, SOA23a, SOA24a, INAMA01, ARCTEx, CAINA01, CAINA02, and WSPA02), as summarized in Table 1. The SOA21b campaign focused on the formation of secondary organic aerosols (SOA) from the OH oxidation of indole. In SOA22a, the ozone oxidation process of β-pinene was investigated. The SOA22b, SOA23a, and SOA24a campaigns explored SOA formation from the ozone and OH oxidation of biogenic volatile organic compound (BVOC) mixtures. During these SOA campaigns, I conducted VOC concentration measurements.

The INAMA01 campaign studied the ice nucleation properties of ammonium sulfate mixed with SOA. In ARCTEx, the aging of black carbon (BC) under quasi-realistic conditions was examined, where I primarily operated the Aerodyne Mass Spectrometer (AMS) and provided AMS mass concentration data. The CAINA01 and CAINA02 campaigns investigated aerosol-cloud interactions under high reactive nitrogen concentrations, during which I operated both the AMS and CHARON-PTR-MS instruments. Finally, the WSPA02 campaign assessed the effects of photochemical aging on the optical and chemical properties of water-soluble brown carbon (BrC) under mixed-phase and cirrus cloud conditions. In this campaign, my colleague Xuefeng and I operated the AMS and analyzed the AMS mass concentration data.

This diverse range of campaigns allowed me to gain extensive experience in chamber experiments, instrument operation, and data analysis, contributing to a deeper understanding of aerosol formation, aging, and cloud interactions.

Table 1 Overview of AIDA chamber campaigns: Research topics and my Contributions

Name	Date	Research topic	Main contributions	Publications
SOA21b	Nov. 2021	Indole SOA chemistry	Operate PTR and data analysis	Co-authored paper (Jiang et al., 2024)
SOA22a	Mar. 2022	β-pinene SOA chemistry	Operate PTR and data analysis	Co-authored paper (Gong et al., 2024)
ARCTEx	Oct. 2022	Impact of aging on BC properties	Operate AMS and data analysis	Co-authored paper under review
SOA22b	Nov. 2022	BVOC mixture SOA chemistry	Operate PTR and AMS, data analysis	Analysis ongoing
CAINA01	Jan. 2023	aerosol-cloud interactions under high nitrogen concentrations	Operate PTR and AMS	Analysis ongoing
SOA23a	Mar. 2023	BVOC mixture SOA chemistry	Operate PTR and AMS, data analysis	Analysis ongoing
CAINA02	Sep. 2023	aerosol-cloud interactions under high nitrogen concentrations	Operate PTR and AMS	Analysis ongoing
WSPA02	Oct. 2023	photochemical aging on the optical and chemical properties of brown carbon (BrC)	Operate PTR and AMS, data analysis	Analysis ongoing
SOA24a	Feb. 2024	BVOC mixture SOA chemistry	Operate PTR and AMS	Analysis ongoing
INAMA01	Apr. 2024	Ice nucleation of ammonium sulfate mixed with SOA	Operate AMS and data analysis	Analysis ongoing

2.5 Field campaigns at urban and forest sites

During my PhD study, I participated in four field campaigns to investigate the sources and characteristics of aerosols and trace gases in diverse environments, including urban, urban fringe, and forest areas (Figure 11). The four campaigns include: one in the urban fringe area of Karlsruhe in summer, one on top of the Feldberg (1500 masl.) in the Black Forest also in summer, and two at the same urban curbside in downtown of Munich during summer and winter, respectively. Detailed information about each campaign, including research topics and my contributions, are summarized in Table 2. The main findings from these campaigns are presented in Chapter 3. Pictures of the locations and the mass spectrometers used in these

studies, including the AMS, CHARON-PTR-MS, and FUSION-PTR are shown in Figure 11, while the primary instruments available in each campaign are listed in Table 3.

Campaign in Karlsruhe in July 2022. I conducted a field campaign from 17th July to 3rd August 2022 on top of Mulldeponie West, located in the urban fringe of Karlsruhe (49.11°N, 8.20°E) in southwest Germany. Karlsruhe, a city of approximately 304,000 inhabitants, is

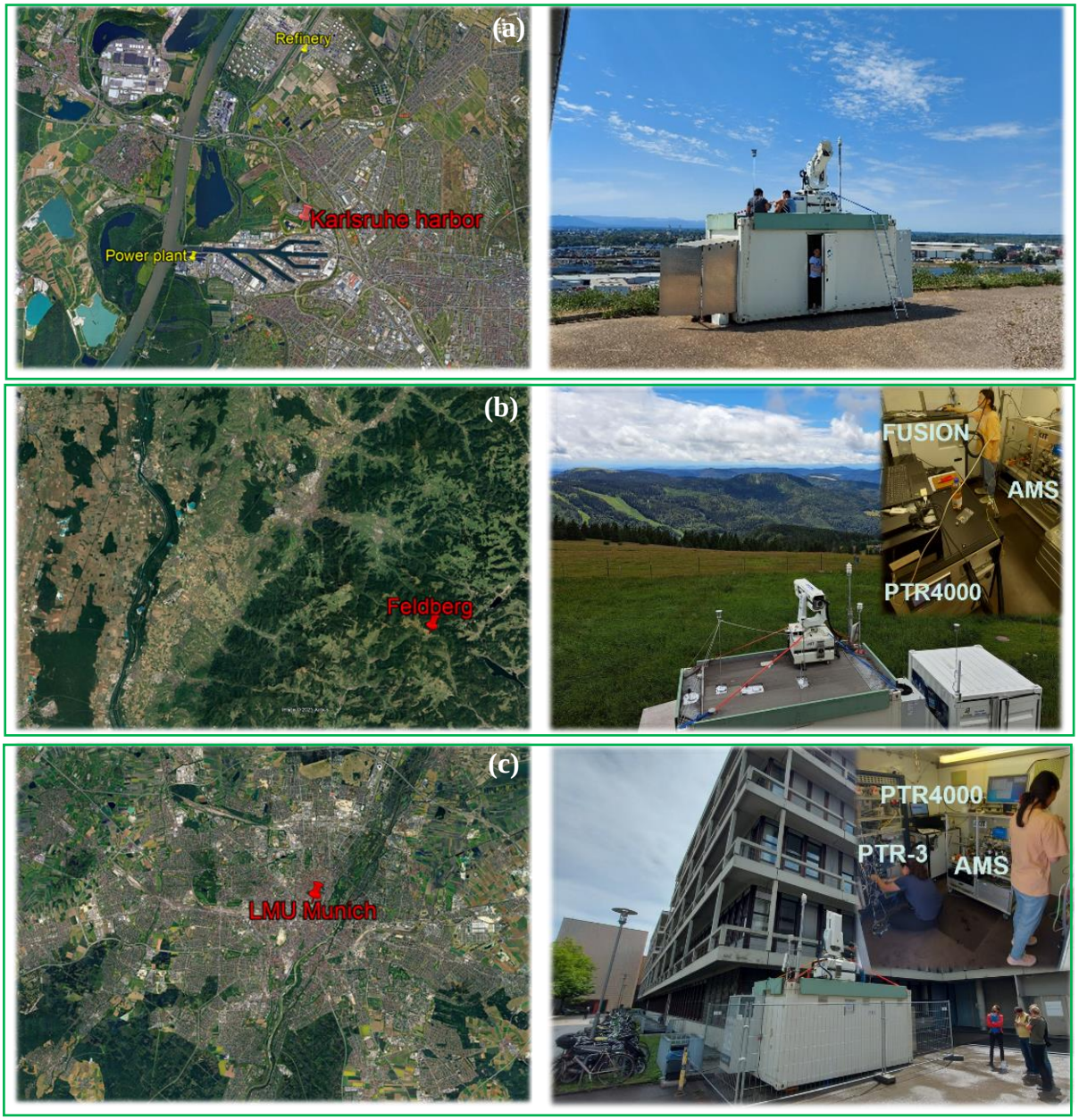

Figure 11. Maps of field measurement sites for (a) an old landfill hill at the Karlsruhe harbor (49.11°N, 8.20°E) (b) the Feldberg (1500 m a.s.l.) (47.86°N, 8.09°E) in the black forest area, and (c) in the street canyon in downtown of Munich (Ludwig-Maximilians-Universität München (LMU), 11°34'E, 48°8'N) during summer and winter. The mass spectrometers inside the container: PTR-MS 4000, FUSION-PTR, AMS, and PTR-3 are marked.

located in the Upper Rhine Valley and is considered a moderately low-polluted urban area. The predominant wind direction in summer was southwest, influenced by the channeling effect of

the Rhine valley. Measurements were performed in a container atop a landfill hill (approximately 60m above city level, [May 15th, 2025], https://de.wikipedia.org/wiki/Windm%C3%BChlenberg_ (Karlsruhe)). This site is located on the western edge of Karlsruhe, with potential pollutant sources from urban and agricultural areas to the north, including a refinery located about 2.3 km away. To the south and east, pollutants originate from urban areas, including a coal-fired power plant situated 1.5 km to the southwest and the various industrial activities in the harbor area directly south of the measurement site. To the west, cleaner air masses from forests, lakes, and agricultural fields (approximately 0.5 km away) influence the site. Therefore, the site is affected by urban, biogenic, industrial, and regional transport sources and meteorological conditions such as high temperatures (heatwave) and rainfall. My research objectives for this campaign were: To investigate the sources and characteristics of organic aerosols (OA) at this site.

- To investigate the sources and characteristics of organic aerosols (OA) at this site.
- To identify the main VOCs and SVOA sources
- To quantify the contribution and influence of biogenic secondary organic aerosols (SOA) to the total OA, especially during a typical heatwave period.
- To characterize the aerosol flow into the city for southwesterly winds

Campaign on top of the Feldberg in July 2023. From 17th June to the 26th of July 2023, I participated in a field campaign as part of the MOSES (Modular Observation Solutions for Earth Systems) project. The campaign was conducted on Mt. Feldberg in the Black Forest region of Germany (47.86°N, 8.09°E), with an elevation of approximately 1,493 meters. The sampling site was located at the top of the mountain, surrounded by forests dominated by Picea abies, Picea spp., and Fagus sylvatica, which are significant emitters of monoterpenes and sesquiterpenes.

During the campaign, which coincided with the summer high-temperature period, I expected to observe increased BVOC concentrations due to elevated temperatures. During the daytime, I anticipated detecting regional sources, while at night, when the boundary layer height decreased, I expected to observe free tropospheric components.

I initially used the FUSION-PTR-MS in this campaign to detect VOCs and more oxidized VOCs at the site until June 26, 2023. After that, I used the CHARON-PTR-MS and AMS to measure VOCs in gas and particle phases, aiming to study their sources. My research objectives were:

- To investigate the sources and characteristics of organic aerosols (OA) in the Black Forest area.
- To identify the main VOC and SVOC sources.
- To analyze BVOC concentration changes with temperature and their impact on new particle formation and particle growth.
- To quantify the contribution and influence of biogenic SOA to the total OA during the campaign.
- To compare the aerosol chemical composition with ice nucleating particle concentrations and results from ICON-ART model calculations.

Field campaign in Munich 2023/24. Field observations were conducted in Munich during two seasons: August 3rd to August 29th, 2023 (summer) and March 1st to April 15th, 2024 (winter and spring). Munich, the capital of Bavaria, Germany, is a major cultural and economic center with a population of 1.5 million as of 2023, making it the third-largest city in Germany. It has a population density of 4,700 people per square kilometer (München, 2023). The sampling site (11°34'E, 48°8'N) was located on a parking lot adjacent to a 30-meter-tall building of the Ludwig-Maximilians-University (LMU) in a street canyon along Theresienstrasse 41. The elevation at street level is approximately 520 meters above sea level (m.a.s.l.). The surrounding area features restaurants, apartment buildings, museums, university workshops, laboratories, and significant car traffic. Consequently, the site is influenced by emissions from cooking, heating, and traffic.

I utilized the CHARON-PTR-MS and AMS to measure VOCs in both gas and particle phases, aiming to study their sources. My research objectives were:

- Identify the primary sources of VOCs, semi-volatile organic aerosols (SVOA), and total organic aerosols (OA).
- Elucidate the contribution of different sources to major VOCs, SVOA, and OA.
- To analyze BVOC concentration and their impact on new particle formation and particle growth.
- To provide data to validate the high-resolution model PALM-4U and a network of low-cost sensors distributed by the Technical University of Munich (TUM).

Table 2 Field campaigns with the research topics, my contributions, and tentative publications

Site	Time	Research topic	Main contribution	Publication
Karlsruhe	July 2022	Characteristics of VOCs and particles at Karlsruhe harbor	Operation of CHARON-PTR-MS and AMS	Analysis ongoing, First-author paper planned
Feldberg	June-July 2023	Characteristics of VOCs and aerosol particles at highest mountain of the black forest	Operation of Fusion-PTR-MS, CHARON-PTR-MS and AMS	Co-author (Handwerker J. et al., 2025) (minor revision) First-author paper (in preparation)
Munich	August 2023 March 2024	Seasonal characteristics of VOCs and particles in downtown of Munich	Operation of CHARON-PTR-MS and AMS	First-author paper (in preparation)

Table 3 Main instruments used in the different field campaigns

Parameter	Instrument (Manufactorer)	Karlsruhe	Feldberg	Munich23	Munich24
VOCs/semi-volatile particles	CHARON-PTR-MS (IONICON Analytik GmbH)	×	×	×	×
Particle mass composition (0.07-2.5 μm)	HR-ToF-AMS (Aerodyne Research)	×	×	×	×
VOCs and more oxygenated organic molecules	FUSION-PTR-MS (IONICON Analytik GmbH)	×	×	×	×
PM_1, $PM_{2.5}$ and PM_{10} mass	FIDAS200 (Palas GmbH)	×	×	×	×
Black Carbon	AE33 (Magee Scientific)	×	×	×	×
Particle number concentration (>2.5 nm)	CPC3022A (TSI Inc.)		×		×
Particle number concentration (>7 nm)	CPC3750 (TSI Inc.)	×			
Particle number concentration (>7 nm)	CPC3756 (TSI Inc.)		×	×	
Particle number concentration (>7 nm)	CPC3776 (TSI Inc.)	×		×	×
Particle size distribution (10-410 nm)	Nanoscan 3910 (TSI Inc.)	×			×
Particle size distribution (10-800 nm)	U-SMPS 2100/2200 (PALAS GmbH)		×		
Particle size distribution (13.6-763.5 nm)	SMPS (DMA 3081, TSI Inc.)			×	
Meteorological parameters	WS700 (Lufft GmbH)	×	×	×	×
NO_2	AS32M (Environment SA.)	×	×	×	×
O_3	O341M (Environment SA.)	x	x	x	x
NH_3	G2103 (Picarro)			×	×

3. Results and discussion

Understanding the sources and transformations of BVOCs and their role in SOA formation is central to this study. This chapter presents the results of my field campaigns conducted in four distinct environments: the top mountain of Feldberg in the Black Forest in summer, a small hill at Karlsruhe harbor in summer, and an urban street canyon in Munich during both summer and winter. These campaigns were designed to address the research questions outlined in the introduction, focusing on the sources, characteristics, and seasonal variability of VOCs and OA in different atmospheric settings.

The results are organized to reflect the differences from less anthropogenically influenced regions to highly urbanized areas. In Section 3.1, I discuss the findings from the Feldberg campaign, which represents a biogenic-dominated environment in the Black Forest. This site provides insights into the role of BVOCs and their contribution to SOA formation with minimal anthropogenic interference, as well as information on aged aerosol in the free troposphere. In Section 3.2, I focus on the measurements at the Karlsruhe harbor, which represents an urban and industrial-influenced environment, where biogenic and anthropogenic precursors contribute to aerosol formation. Finally, in Section 3.3, I examine the seasonal variability of VOCs and OA in Munich, comparing summer and winter measurements to elucidate the impact of anthropogenic activities, meteorological conditions, and source contributions in a densely populated urban environment.

Through this structured discussion, I aim to comprehensively understand the sources, transformations, and impacts of VOCs and OA across diverse environments, addressing the key research questions posed in this study.

3.1 Sources of VOC and aerosol particles on top of Mt. Feldberg

In forested regions, BVOCs emitted by vegetation are a dominant source of reactive organic gases, which can undergo oxidation to form SOA. Mountainous sites, such as those in the Black Forest, provide unique conditions for studying aerosol processes due to their elevation, reduced anthropogenic influence, and exposure to both boundary layer and free tropospheric air masses. Understanding the sources of VOCs and organic aerosol particles in such environments is critical for assessing their role in aerosol growth and affecting cloud condensation nuclei (Scholz et al., 2023; Du et al., 2025). The Black Forest, a mountainous region in southwestern Germany, provides an ideal natural laboratory to study these interactions due to its rich vegetation and elevated terrain (~1500 m a.s.l.). Furthermore, the location was chosen as a

potential trigger area for strong convection, e.g., thunderstorms downwind, and therefore part of the Swabian MOSES campaign 2023 ((Handwerker J. et al., 2025)) on severe weather events.

I aim to quantify the contributions of anthropogenic and biogenic sources to VOC and OA concentrations, with particular emphasis on the role of BVOCs in particle growth. Ultrafine particles (UFPs), formed through nucleation and growth processes, are strongly influenced by BVOC oxidation products, which can also enhance the formation of cloud condensation nuclei (CCN). Understanding these mechanisms is crucial for improving air quality models and assessing the climate impacts of aerosols.

The air mass cluster analysis of back trajectories at 500m and 1500m above sea level helps understand the vertical distribution of VOCs and OA in the atmosphere. At 500m, the air masses are typically within the planetary boundary layer (PBL), where anthropogenic activities (e.g., traffic, industrial emissions) have a more pronounced impact on VOC and OA concentrations. In contrast, at 1500m, the air masses are often situated in the free troposphere, less influenced by local anthropogenic sources and more representative of regional or long-range transported air, including aged emissions. Figure 12a presents the air mass cluster analysis at 500m and 1500m, revealing four distinct clusters at each altitude. At 1500 m the 72 hours back trajectories origin at the Belgium cost (Cluster(a), 19%), Atlantic Ocean (Cluster(b), 56%), Balearic Sea (Cluster(c), 16%), and the wider Atlantic Ocean (Cluster(d) 8%). At 500 m, the 72-hour back trajectories originate at the German-French-Swiss border (Cluster1, 33%), Atlantic Ocean (Cluster2, 36%), Balearic Sea (Cluster3, 8%), and North Sea (Cluster4, 24%).

Figure 12b presents the wind rose at the container roof (3.5m a.g.l; ~1500 m a.s.l.), demonstrating prevailing winds originating predominantly from western directions (west, southwest, and northwest), with minimal easterly contributions. The alignment of wind directions with the air mass trajectories reinforces the transport pathways. Moderate to strong winds (indicated by green, yellow, and blue shades) are prevalent, suggesting efficient air masses and pollutants transport over long distances. This pattern strongly suggests maritime sources (Atlantic Ocean) dominate, contributing significantly to the total 1500m air mass transport. Their prevalence suggests a strong influence of clean, marine air on the study region, which may lead to lower concentrations of pollutants during periods dominated by these areas. Continental European sources, originating from industrialized or urbanized regions, also play a notable role, as indicated by the low altitude back trajectories. Their presence is often associated with higher concentrations of anthropogenic pollutants, such as sulfate, nitrate, and black carbon.

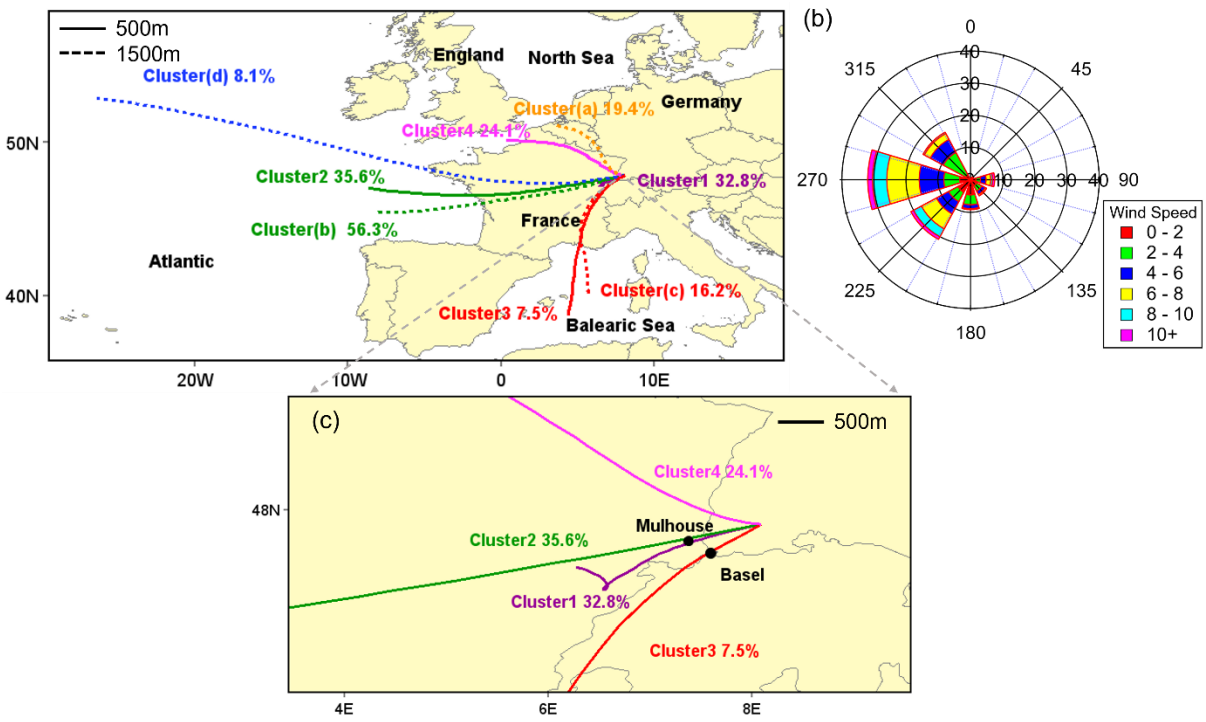

Figure 12. (a) The air mass cluster analysis of 72 h back trajectories at 500m and 1500m (a.s.l), Solid lines represent clusters at 500m, while dashed lines denote air masses at 1500m; and (b) wind rose measured at container roof (c) zoom into cluster1(purple), cluster2 (green), cluster3(red), and cluster4 (pink) for500m.

Figure 13 presents a comprehensive time series analysis of meteorological and chemical parameters, illustrating the dynamic interplay between air mass origins, weather conditions, and aerosol composition. The top panels (a) and (b) depict the temporal variability of air mass cluster assignments at 1500 m and 500 m, respectively, showing alternating dominance of marine (e.g., Atlantic Ocean and North Sea) and continental air masses, with their influence varying over time. Panel (c) highlights fluctuations in relative humidity (RH) and precipitation, where periods of high RH often coincide with rainfall events. Precipitation typically leads to wet scavenging of aerosols. Diurnal temperature and solar radiation cycles are shown in panel (d), with daytime peaks driving photochemical processes and nighttime cooling promoting condensation processes. Panel (e) reveals the mass concentrations of key aerosol species, with organic aerosols dominating, followed by sulfate, nitrate, ammonium, chloride, and black carbon, while $PM_{2.5}$ concentrations exhibit variability linked to air mass changes. Finally, panel (f) displays the particle size distribution and BLH, showing particle growth events and higher BLH during the day, which enhances vertical mixing and influences aerosol dynamics.

The variation in air mass clusters, as depicted in Figure 13, significantly influences aerosol composition, meteorological conditions, and atmospheric dynamics. Shifts between marine and continental air masses drive changes in $PM_{2.5}$ concentrations and aerosol species, with continental sources enhancing sulfate, nitrate, and black carbon levels. Marine air masses are

associated with higher relative humidity and precipitation, promoting aerosol scavenging, while continental air masses often coincide with drier conditions and pollutant accumulation.

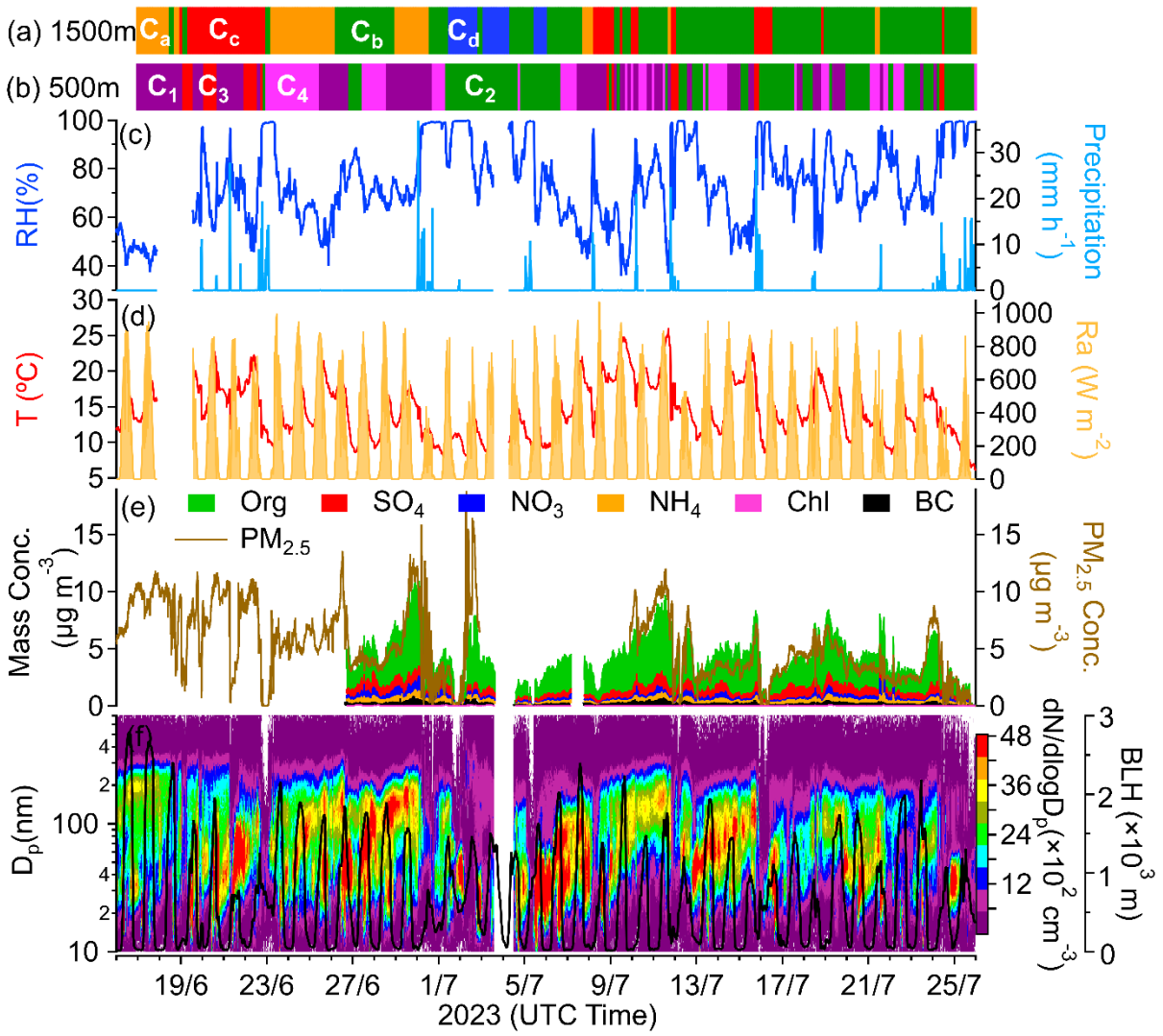

Figure 13. Time series of air mass clusters, meteorological parameters, and aerosol properties: (a) Air mass cluster assignments at 1500 m, (b) Air mass cluster assignments at 500 m, (c) Relative humidity and precipitation, (d) Temperature and solar radiation, (e) Aerosol species (organic, sulfate, nitrate, ammonium, chloride, and black carbon) and $PM_{2.5}$ concentrations, (f) Particle size distribution and boundary layer height.

3.1.1 Sources of organic aerosol particles

To investigate potential differences between boundary layer (BL) and free tropospheric (FT) aerosols, I initially planned stratified PMF analyses of AMS data based on boundary layer height (BLH): one subset for BLH >1500 m a.s.l. (representing mixed local/regional air masses with potential biogenic influence) and another for BLH ⩽1500 m a.s.l. (sampling FT air dominated by long-range transport). However, BLH exceeded the site elevation (>1500 m a.s.l.) only sporadically (3-4 hours on a few days) during the month-long campaign. As these

instances constituted negligible influence on the overall dataset, a single PMF analysis was performed using the entire measurement period to ensure robust source characterization.

Figure 14 presents four identified factors: aged biomass burning OA (Aged BBOA), regional background OA, semi-volatile oxygenated OA (SV-OOA), and low-volatile oxygenated OA (LV-OOA), along with their diurnal patterns. These factors were resolved based on their O: C and H: C ratios and correlations with tracer gases and particulate compounds measured by CHARON-PTR-MS and AMS. Figure S1 shows the mass profiles of the AMS-PMF factors, and Table S1 summarizes the key tracers correlated with each factor. The aged BBOA factor, with an O: C ratio of 0.66, shows strong correlations with biomass burning tracers such as syringalkohol, vanillin, and vanillic acid (Table S1), consistent with aged biomass burning influence. The Regionally background OA factor exhibits strong correlations with formaldehyde (R = 0.76) and tracers indicative of SOA formation, including organonitrates (C_4H_6NO), organosulfates ($C_5H_{10}SO_3$), aromatic oxidation products ($C_7H_6O_5$), and biomass burning markers (C_5H_6O). This factor's lack of diurnal variation suggests it is influenced by well-mixed, transported air masses rather than local sources. The SV-OOA factor, with an O: C ratio of 0.59 and H: C of 1.74, is moderately oxidized and strongly associated with nitrate (R = 0.82). Its midday peak in the diurnal profile indicates formation via photochemical aging. Finally, the LV-OOA factor, the most oxidized component (O: C=1.16), shows a pronounced afternoon peak, typical of aged SOA. Its correlation with benzonitrile (C_7H_5N, R = 0.70) suggests also significant influence from aged biomass burning aerosols.

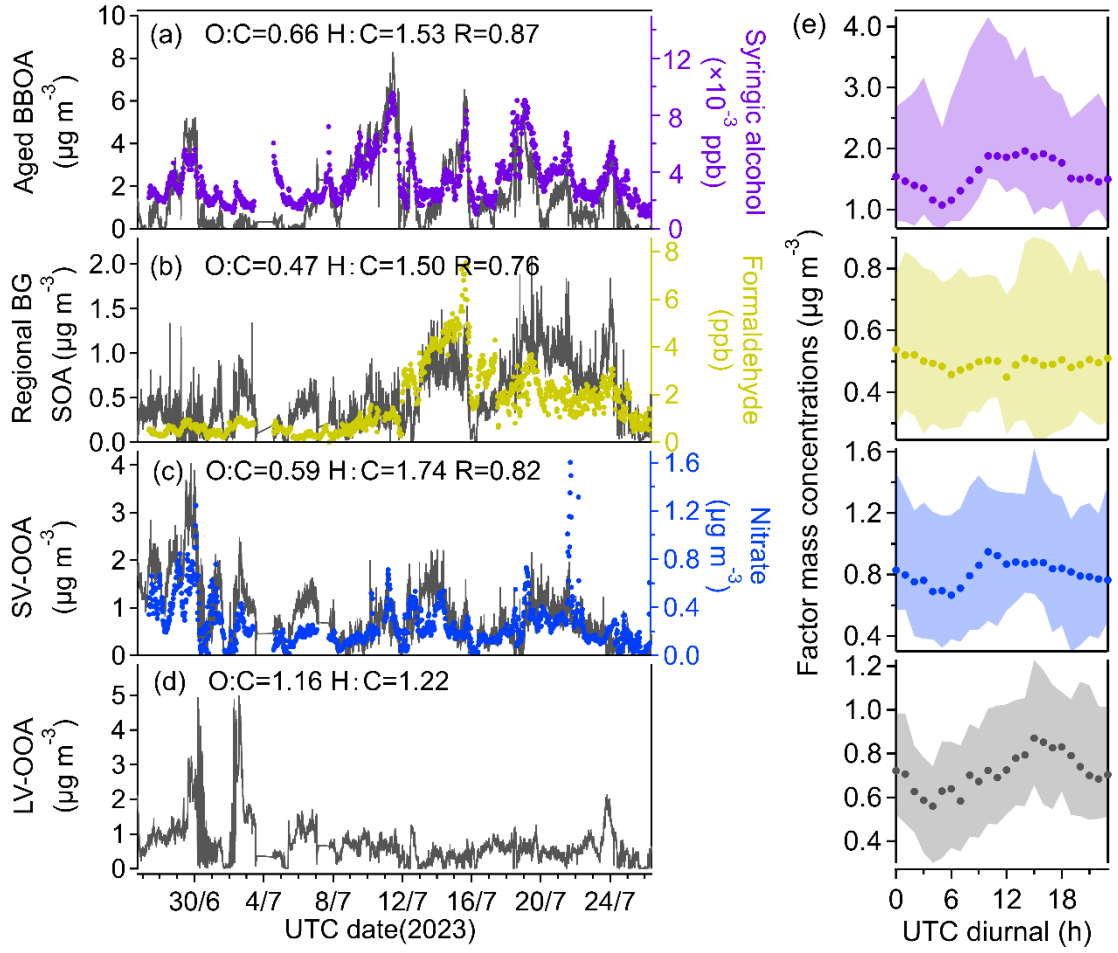

Figure 14. Time series (left) and diurnal variations (right) of PMF-resolved organic aerosol factors. (a) Aged BBOA (O: C = 0.66, H: C = 1.53) is strongly correlated with syringic alcohol (R = 0.87). (b) Regional background factor (O: C = 0.47, H: C = 1.50), strongly correlated with formaldehyde (R = 0.76), indicating a secondary source. (c) SV-OOA (O: C = 0.59, H: C = 1.74), moderately oxidized, correlated with nitrate (R = 0.82). (d) LV-OOA (O: C = 1.16, H: C = 1.22), representing the most aged/oxidized organic aerosol. (e) Diurnal profiles of each factor mass concentration; the shaded area between the 25th percentile (P25) and 75th percentile (P75) shows the interquartile range (IQR) — the middle 50% of the data — reflecting the variability in factor concentrations throughout the day.

3.1.2 Sources of semi-volatile organic aerosol particles

The application of PMF to CHARON-PTR-MS data enables a more refined classification of SVOA, allowing for the observation of detailed molecular compounds within aerosol particles. Figure 13 presents the mass spectral characteristics (a) and diurnal trends of three SVOA factors resolved by this PMF analysis (b). Additionally, Figure S2 shows the time series of these factors correlated with corresponding tracer compounds.

Panel (a) of Figure 15 displays the unit-mass-resolved spectra for the three SVOA factors: background BBOA (Biomass Burning Organic Aerosol), photochemical SOA, and aged BBOA. These spectra reveal distinct differences in molecular composition and oxidation states. Both background BBOA and photochemical SOA exhibit similar O:C ratios (~0.58) and H:C

ratios (~1.56-1.57), indicating a moderate degree of oxidation. The Background BBOA factor shows relatively constant and low concentrations throughout the day, suggesting a persistent, aged source with limited temporal variability. Notably, the compounds associated with this factor exhibit stronger correlations with BBOA tracers (Table S2), indicating that this factor is influenced by aged biomass burning emissions.

In contrast, the Photochemical SOA factor displays a pronounced daytime peak, consistent with its formation through photochemical oxidation of VOC precursors under sunlight. This factor is strongly associated with photochemical oxidation products such as heptadienedione $C_7H_{11}O_2^+$, furaneol $C_6H_9O_3^+$, guaiacol $C_7H_9O_2^+$, dimethylphenol $C_8H_{11}O_2^+$, methyl vinyl ketone $C_4H_7O_1^+$, unsaturated aldehydes $C_6H_9O_1^+$, $C_6H_7O_3^+$, catechol $C_6H_7O_2^+$, $C_7H_{11}O_1^+$, $C_7H_{11}O_3^+$, and acrylic acid $C_4H_7O_3^+$ (Table S2) (Forstner et al., 1997; Bethel et al., 2000; Jang and Kamens, 2001; Wyche et al., 2009; Birdsall and Elrod, 2011; Pereira et al., 2015; Zhang et al., 2019; Srivastava et al., 2022).

The Aged BBOA factor is characterized by a higher O:C ratio (0.67) and a slightly lower H:C ratio (1.50), reflecting advanced atmospheric oxidation and aging processes. This factor is dominated by highly oxygenated compounds, including $C_8H_{13}O_5^+$, vanillic acid $C_8H_{11}O_4^+$, syringic acid oxidation products $C_8H_{11}O_5^+$, vanillin $C_8H_9O_3^+$, galactaric acid $C_6H_9O_5^+$, protocatechuic acid $C_7H_9O_4^+$, $C_7H_9O_5^+$, $C_9H_{13}O_4^+$, and $C_8H_{11}O_3^+$ (Table S2) SOA (Ofner et al., 2011; Yee et al., 2013b), which are consistent with the secondary processing of biomass burning emissions. The diurnal profile of Aged BBOA shows a broad nighttime enhancement, likely driven by boundary layer dynamics and the nighttime accumulation or condensation of oxidized compounds. This pattern agrees with the aged and secondary nature of this factor.

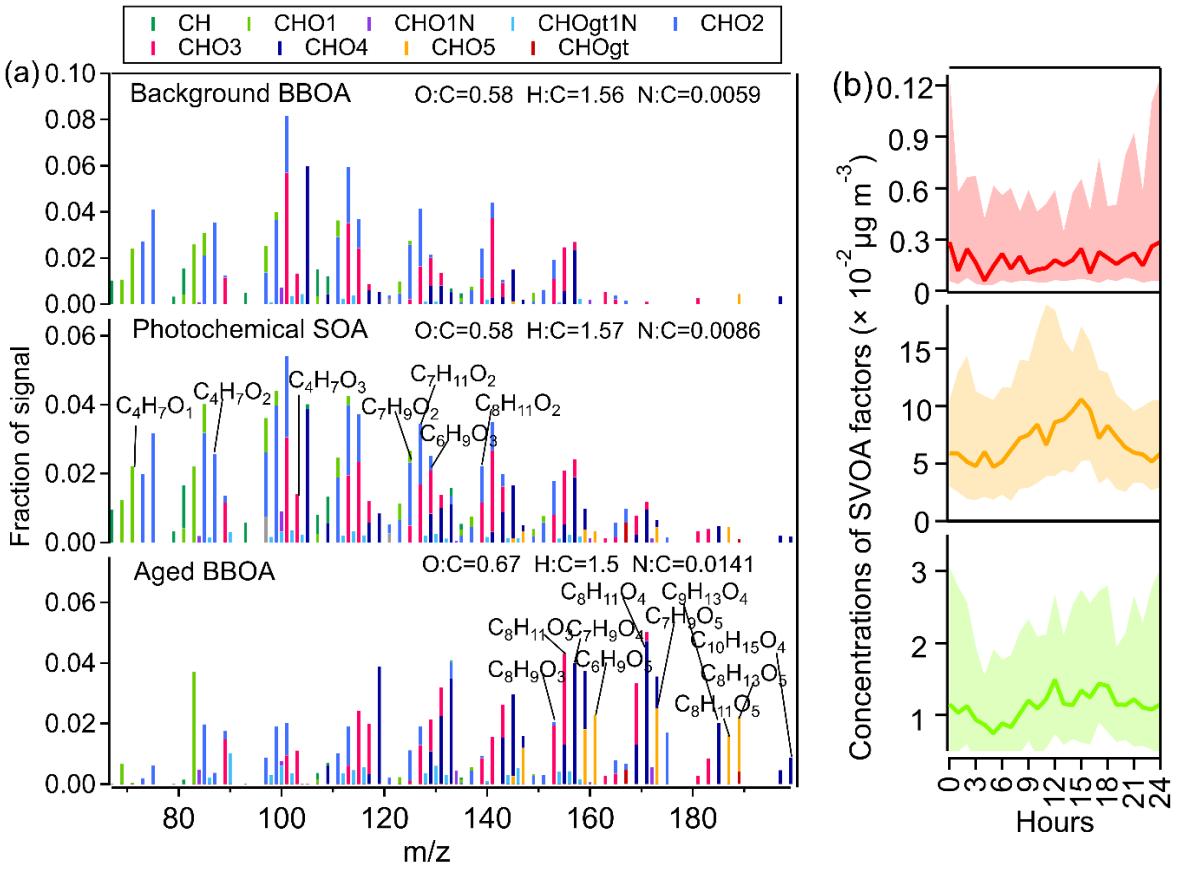

Figure 15. (a) CHARON-PTR-MS high-resolution mass spectra of three PMF-resolved SVOA factors: Background BBOA, Photochemical SOA, and Aged BBOA. (b) Diurnal variation of the corresponding factor concentrations; the shaded area between the P25 and P75 shows the IQR— the middle 50% of the data — reflecting the variability in factor concentrations throughout the day.

3.1.3 Sources of VOC

Four distinct VOC factors were resolved by PMF analysis (Figure 16). Oxidized Biogenic VOCs (BVOCs) were dominated by less oxidized biogenic compounds, including isoprene oxidation products (e.g., $C_5H_9O_1^+$, $C_5H_{11}O_1^+$, $C_5H_9O_2^+$) and terpene oxidation products (e.g., $C_7H_{11}O_1^+$, $C_6H_9O_2^+$, $C_8H_{13}O_1^+$) (Li et al., 2020a; Li et al., 2021). Additionally, ions such as $C_6H_{11}O_2^+$, $C_6H_{13}O_1^+$, and $C_6H_9O_1^+$ were present, which are likely emitted from vegetation under mechanical stress or herbivory, such as when plants are damaged by insects or bees (Jakobsen and Christensen, 2002; Verbruggen and Hermans, 2008; Penuelas et al., 2005; Hamilton et al., 2009; Hafner et al., 2013; Vita et al., 2015; Taiti et al., 2018). These marker ions exhibited high correlations with the oxidized biogenic VOC factor (Figure S3 and Table S3). The diurnal pattern of this factor peaked during daytime and decreased at night, consistent with the influence of the daytime boundary layer development, which enhances the vertical mixing and brings more biogenic VOCs from vegetated areas into the measurement site.

The Long-range transported aged VOCs factor was characterized by organosulfur compounds such as $C_3H_9S_1O_3^+$ (a methanesulfonic acid derivative), $C_4H_9S_1O_4^+$ (alkylsulfonic acid or a sulfate-organic species), and $C_3H_9S_1O_4^+$ (another methanesulfonic acid-related species) (Froyd et al., 2010). These ions showed strong correlations with this factor (R ~ 0.80; Figure S3 and Table S3). Moreover, this factor exhibited the highest S:C ratio (0.013), indicating a significant contribution from organosulfate compounds, which are often formed through long-range atmospheric aging and secondary processes (Huang et al., 2018a). The diurnal profile showed higher concentrations at night, with a small peak around UTC 4:00 and a maximum shortly after sunrise, consistent with a transported, aged secondary VOC source.

The aged biomass burning VOCs factor showed strong correlations with several well-known tracers of biomass burning emissions, including $C_7H_9O_3^+$ (methoxyphenols, R=0.87), $C_8H_{11}O_3^+$ (methoxy-substituted aromatics, R=0.85), $C_7H_9O_2^+$ (cresol or guaiacol, R=0.85), $C_{10}H_{13}O_2^+$ (guaiacol derivatives, R=0.84), and $C_8H_{11}O_4^+$ (methoxy-phenolic acids, R=0.81) (Ofner et al., 2011; Yee et al., 2013b). These species are commonly associated with aged biomass burning emissions. The diurnal variation showed a minimum during daytime and higher concentrations at night, suggesting influence from long transport of aged biomass burning plumes in the free troposphere.

The regional anthropogenic VOCs factor exhibited strong correlations with $C_3H_9O_2^+$ (hydroxypropyl fragment, R=0.94), $C_2H_7O_3^+$ (ethylene glycol monoformate ion, R=0.93), and $C_2H_7O_2^+$ (ethoxy fragment from ethanol derivatives, R=0.93) (De Gouw et al., 2005; Warneke et al., 2007; Mcdonald et al., 2018). These compounds are indicative of oxygenated VOCs (OVOCs) commonly found in industrial solvents, cleaning agents, or personal care product emissions. Given the strong presence of these solvent-like fragments and the highest O:C ratio (0.52) among all factors, this factor is interpreted as aged anthropogenic VOCs transported from urban or sub-urban areas. The diurnal profile showed higher levels during daytime, which could reflect the upslope transport of anthropogenic emissions from nearby human activities such as hotels, restaurants, or traffic emissions in the valley.

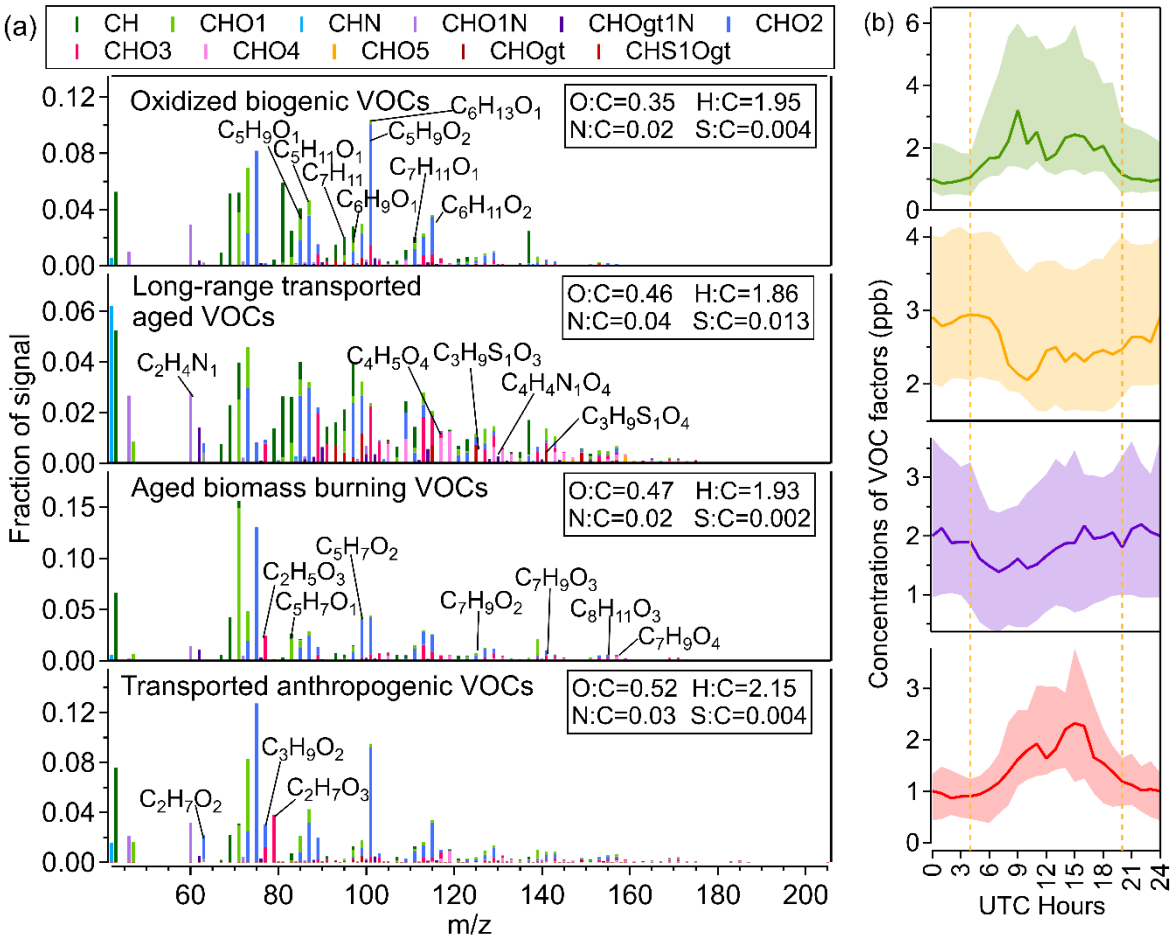

Figure 16. (a) Mass spectra of four PMF-resolved VOC factors with selected marker compounds and elemental ratios. (b) Diurnal variation of the corresponding factor concentrations showing distinct source-related temporal patterns; the shaded area between the P25 and P75 shows the IQR— the middle 50% of the data — reflecting the variability in factor concentrations throughout the day.

3.1.4 Composition and main sources of the organic aerosol in gas and particle phase

The organic aerosol composition is dominated by aged BBOA (35±24%), indicating a strong influence of aged biomass combustion emissions. SOA components, including SV-OOA (24±14%) and LV-OOA (23±14%), contribute significantly, highlighting the role of atmospheric oxidation of VOC in organic aerosol formation. Regional background OA (18±11%) suggests that transported emissions also contribute to OA loading (Figure15). Since the CHARON-PTR-MS primarily measures semi-volatile compounds, its sensitivity to primary organic aerosol is therefore somewhat lower. The semi-volatile organic aerosol (SVOA) particle composition is dominated by photochemically formed SOA (79±18%), highlighting the strong influence of secondary formation processes in this fraction. Aged BBOA accounts for 16±11%, indicating a contribution from transported or processed biomass burning emissions. A small fraction (5±8%) is attributed to background organic aerosol mixed with

BBOA, suggesting minor residual influences from primary sources. This distribution emphasizes the dominance of photochemical aging over direct emissions in shaping the semi-volatile organic aerosol composition. Long-range transport and aged VOCs (35±15%) and aged biomass burning VOCs (21±12%) indicate significant contributions from aged emissions undergoing atmospheric processing. Oxidized biogenic VOCs (25±16%) reflect oxidation of locally or regionally emitted BVOCs. Transported anthropogenic VOCs (20±15%) highlight the role of human-related emissions reaching the site, emphasizing the mixed influence of biogenic and anthropogenic sources.

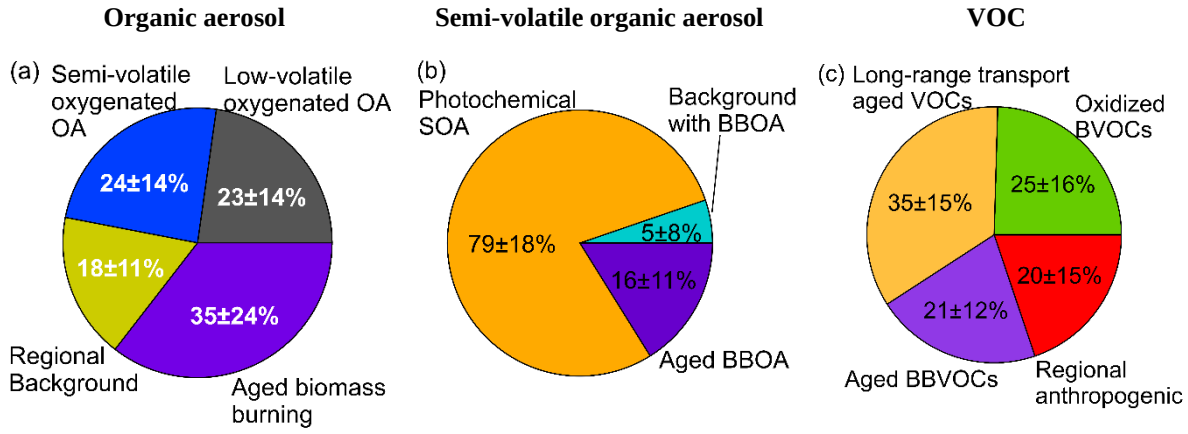

Figure 17. Fractions of organic aerosol particle factors (a), Semi-volatile organic aerosol particle (SVOA) factors (b), and VOC factors (c) at the top of the Feldberg (~1500 m asl.).

3.1.5 Canadian wildfire event

Canada's 2023 wildfire season was the most destructive ever recorded (Canada, 2024). It affected not only north America but large parts of the northern hemisphere by long range transport (Wang et al., 2024c). Figure 18 (a) and (b) illustrate the air mass cluster assignments derived from back trajectory analysis at 1500 m and 500 m above sea level. From June 29th to 30th, the air masses were predominantly classified as Cluster 1 (1500 m), which is associated with long-range transport from the northwest and northern Europe, as shown in Figure 12. This period coincides with the expected arrival of aged plumes from the Canadian wildfires in Central Europe (Chappell, 2023).

During this period (highlighted by the dashed vertical black lines in Figure 18), a sharp and rapid increase in aged biomass burning VOCs was observed, reaching a distinct peak before declining. This strongly suggests the influence of aged wildfire emissions, which had undergone significant atmospheric processing during their long-range transport. Please note, that also the night before some influence of the wildfire plume was observed in free tropospheric air masses reaching the top of the Feldberg.

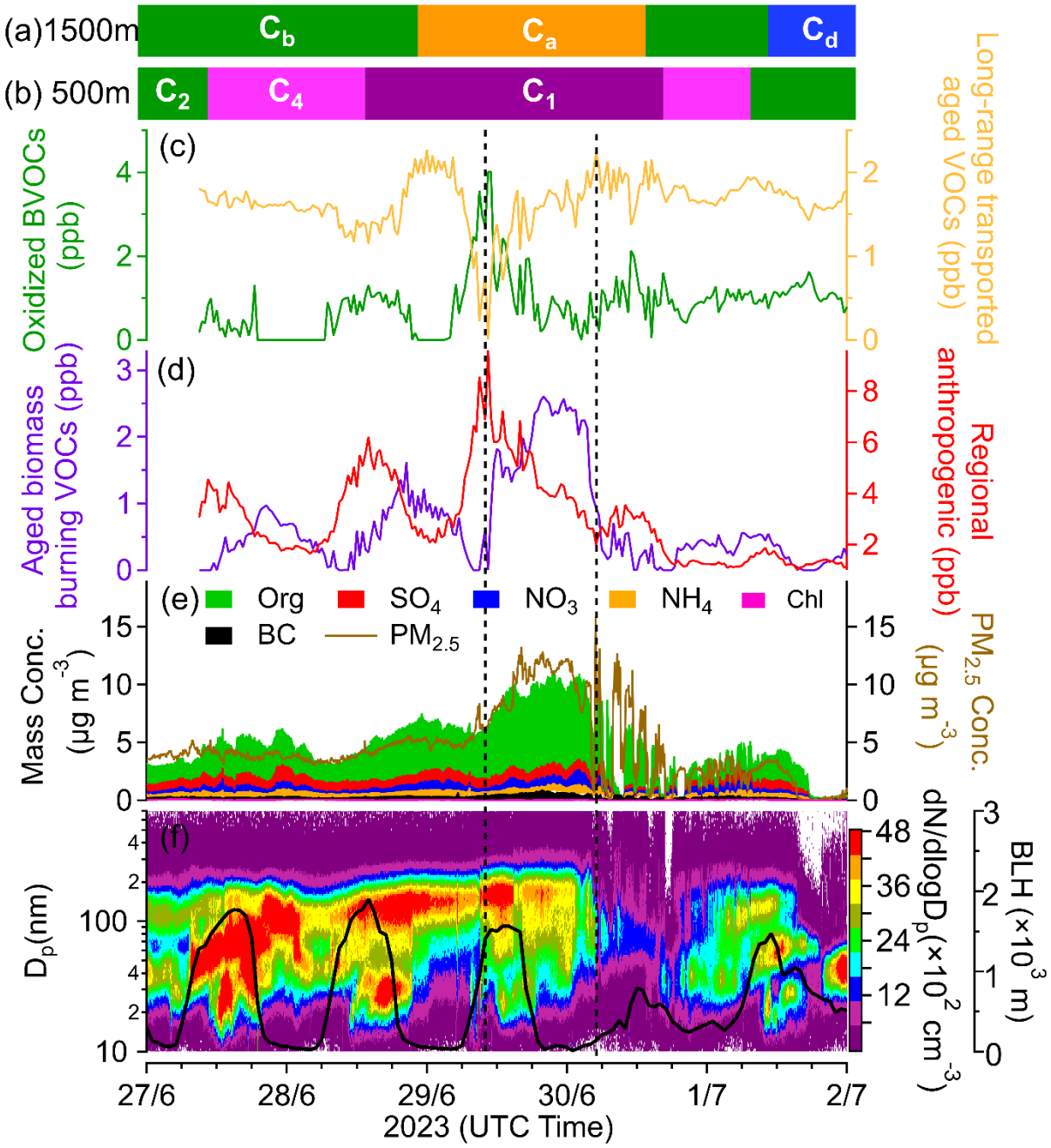

Figure 18. Time series of air mass clusters (a,b), VOC factor concentrations (c,d), aerosol composition (e), particle size distribution (f), and boundary layer height (f). The vertical dashed lines mark the period influenced strongest by Canadian wildfire plumes, showing sharp increases in aged biomass burning VOCs and OA, along with shifts in air mass trajectories.

Interestingly, oxidized BVOCs and transported anthropogenic VOCs reached their maximum concentrations before the sharp increase in aged biomass burning VOCs. Simultaneously, the BLH peaked, indicating that the increase in oxidized BVOCs and anthropogenic VOCs was likely driven by boundary layer air masses reaching the summit rather than direct transport. In contrast, the concentration of long-range transported aged VOCs decreased significantly during this period of high BLH, suggesting that this factor was related to free tropospheric air masses.

However, once the Canadian wildfire plume arrived, the long-range transported aged VOCs also showed a rapid increase, although the rise was more gradual compared to the steep increase observed in aged biomass burning VOCs.

The OA concentration measured by AMS exhibited a trend very similar to that of the aged biomass burning VOCs, further supporting the interpretation that OA during this period was strongly influenced and likely dominated by wildfire-derived aged biomass burning emissions. In addition, particle size distributions reveal that the particles transported during this period were predominantly in the accumulation mode size range (Dp ~100-300 nm), consistent with aged, long-range transported particles rather than fresh local emissions which typically include also smaller particles.

These observations provide robust evidence that the Canadian wildfire event significantly influenced the aerosol and VOC composition at the measurement site, with aged biomass burning emissions playing a dominant role in increasing both organic aerosol and accumulation mode particle concentrations.

Aged BBOA from CHARON-PTR-MS and black carbon (Figure 19d) showed a notable increase at the same time, indicating the long-range transport of biomass burning aerosols from wildfire emissions. In contrast, background BBOA and photochemical SOA (Figure 19c) remained relatively stable, suggesting that local emissions played a minor role during this period. The increase in LV-OOA and SV-OOA (Figure 19e) and aged BBOA (Figure 19f) from AMS implies enhanced SOA formation, likely driven by the oxidation of fire-related VOCs.

However, regional background OA (Figure 19f) showed a decreasing trend rather than an increase. This suggests that the transported Canadian wildfire plume may have diluted or suppressed the formation of regionally aged SOA, altering the composition of transported aerosols. Following this period, rainfall occurred, leading to a noticeable increase in SV-OOA and regional background SOA, which closely followed the trend of BLH. In contrast, other factors remained relatively stable, indicating that in the post-rainfall relatively clean air masses, these two factors were strongly influenced by boundary layer dynamics, as pollutants from nearby sources were reaching the measurement site. Meanwhile, long-range transported organic aerosol was efficiently removed by wet scavenging, leaving behind a cleaner atmospheric background also in the free troposphere (Andronache et al., 2006; Niu et al., 2023).

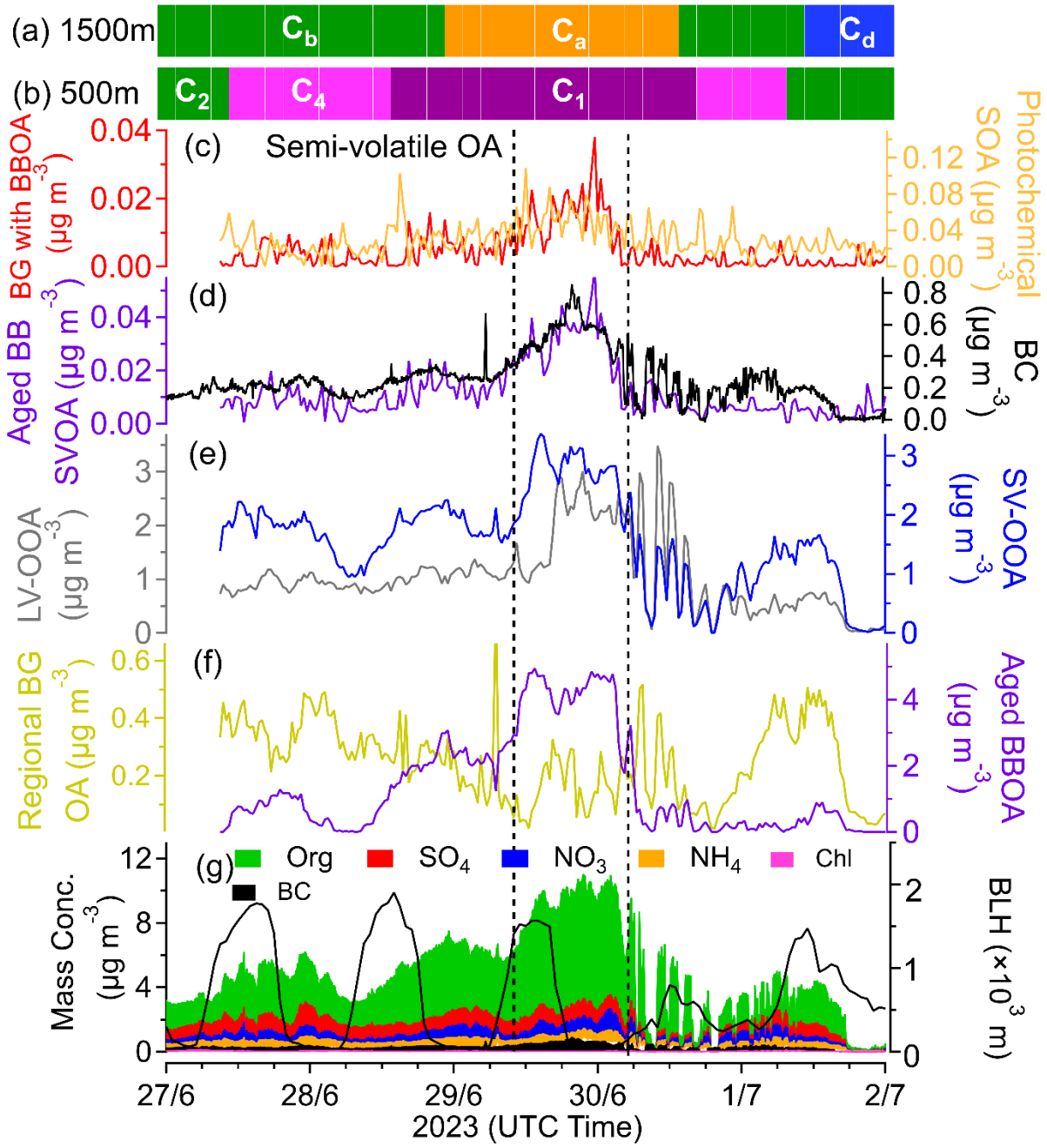

Figure 19. Time series of (a, b) air mass clusters at 1500 m and 500 m, (c) background BBOA and photochemical SOA, (d) aged BB SVOA (CHARON-PTR-MS) and black carbon (BC), (e) LV-OOA and SV-OOA, (f) regional background SOA and aged BBOA (AMS), and (g) mass concentrations of major aerosol components and BLH.

Figure 20a shows that the ultrafine particle ratio remained relatively low during the wildfire event, dropping below 60%, whereas it was above 60% for most other periods. This indicates that the biomass burning plume introduced a significant number of larger particles, reducing the fraction of ultrafine particles. After the wildfire influence ceased, the ultrafine particle ratio increased sharply, even reaching 100%, suggesting that cleaner air masses facilitated e.g. new particle formation. Figure 18b reveals a large difference between total particle number (black) and the 7-100 nm fraction (blue) during the wildfire event. This suggests that a significant

fraction of the transported particles was larger than 100 nm. After the wildfire period, the gap between total particles and the 7-100 nm fraction became much smaller, again indicating a shift toward smaller particle sizes.

Figure 20c further breaks down the size distribution. The concentrations of 20-50 nm (purple) and 50-100 nm (magenta) particles were nearly identical throughout the entire period, suggesting similar sources or atmospheric processing. In contrast, the 7-20 nm (red) particle number was particularly low during the wildfire period, reinforcing the idea that new particle formation was suppressed in the presence of biomass burning aerosols. Figure 20d shows that INP concentrations were relatively high during the wildfire period compared to the following days. This suggests that large biomass burning particles enhanced ice nucleation particle number, possibly by providing additional surfaces or INP-active components. After the wildfire plume disappeared, INP concentrations decreased as well, aligning with the transition to cleaner air dominated by smaller less ice active particles.

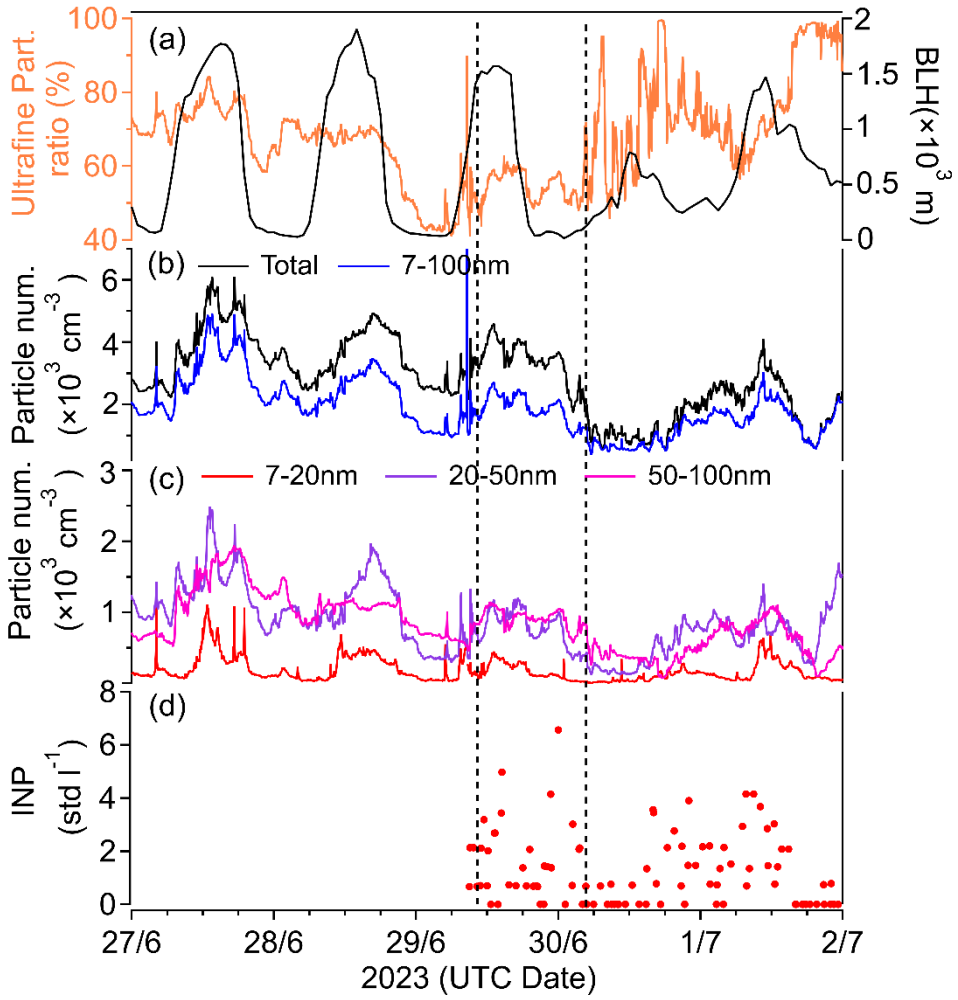

Figure 20. Temporal variations of (a) ultrafine particle ratio and BLH, (b) total and 7–100 nm particle number, (c) size-resolved particle number (7-20 nm, 20-50 nm, 50-100 nm), and (d) ice nucleation particle number during a Canadian smoke event.

3.1.6 Strong pollution event

A second period with elevated pollution levels and associated particle growth events spanned from July 5th to July 14th. Figure 21a and b show that during this period, the air mass at 1500 m predominantly originated from the Atlantic Ocean (C_b air mass cluster), while at 500 m, air masses were mainly from C_1 (German-French border) and C_4 (North Sea, passing over France). These air masses brought significant pollution between July 9th and 12th, with concentrations peaking on July 11th.

During the particle growth events on July 5th and 6th, no significant changes were observed in VOC concentrations on July 5th. However, on July 6th, oxidized BVOCs, aged biomass burning VOCs, and regional anthropogenic VOCs showed a significant increase. Overall, oxidized BVOCs and regional anthropogenic VOCs exhibited peak concentrations simultaneously, while long-range transported aged VOCs displayed an inverse trend, reaching their lowest values during the same period. This suggests that these VOCs were influenced by BLH variations-when BLH increased, oxidized BVOCs and regional anthropogenic VOCs reached their peak values, whereas long-range transport aged VOCs decreased. In contrast, aged biomass burning VOCs were affected by long-range transport and BLH, as their variations showed similarities with multiple VOC factors. Between July 9th and 11th, organic aerosol (OA) concentrations experienced a significant increase. Among the VOC factors, aged biomass burning VOCs exhibited a trend most closely aligned with OA concentrations, indicating a more substantial influence from biomass burning emissions. The particle size distribution suggests minimal new particle formation or particle growth events, implying that the observed variations were primarily driven by changes in the 40-200 nm particle fraction.

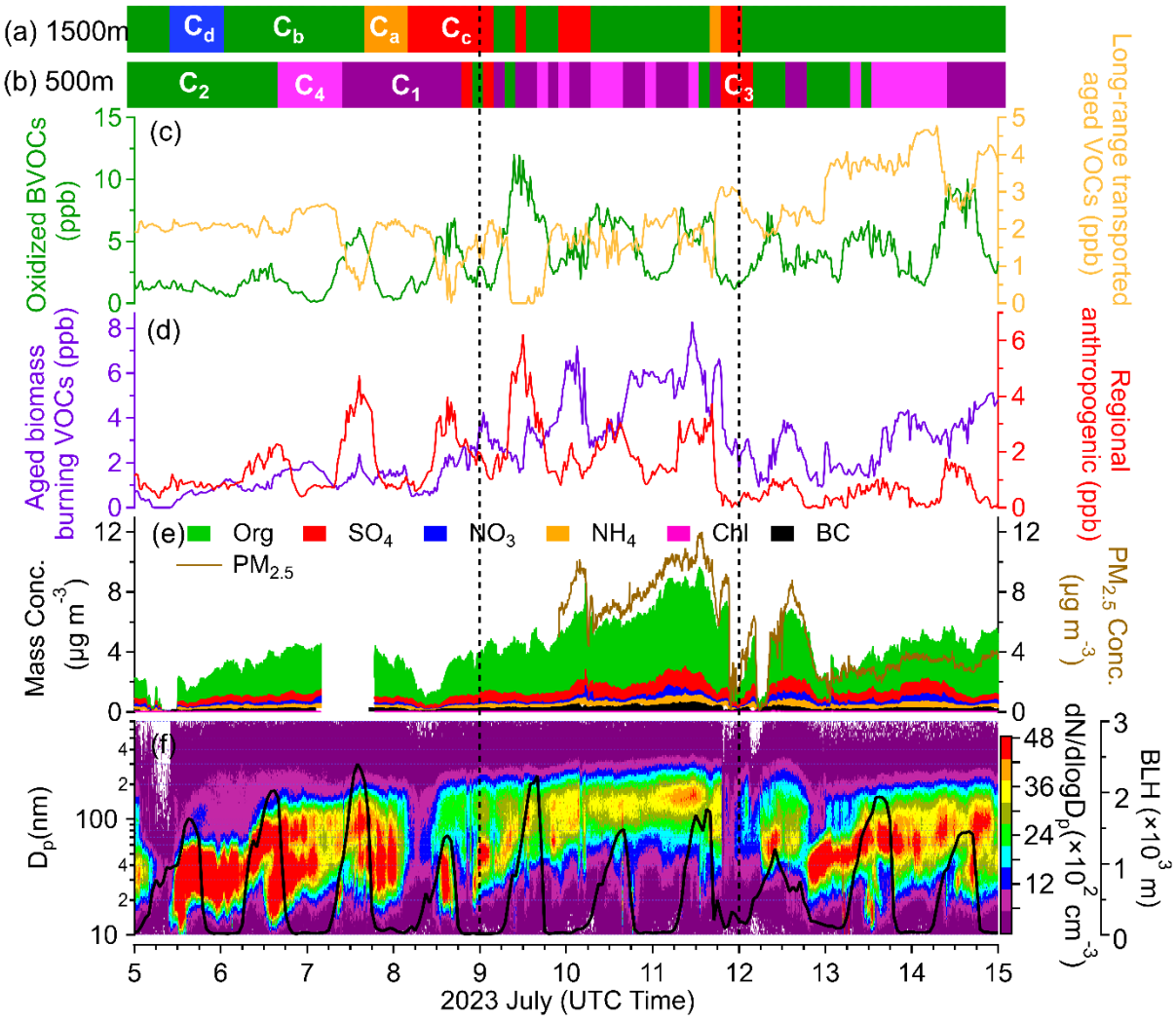

Figure 21. Time series of air mass clusters at 1500 m and 500 m, respectively (a) and (b), oxidized BVOCs and long-range transported aged VOCs (c), aged biomass burning VOCs and transported anthropogenic VOCs (d), aerosol chemical composition (e), and particle size distribution with the BLH (f) from July 5 to July 14.2023. The dashed lines mark increased aerosol concentrations during the pollution period.

From July 6th onward, Aged BBOA detected by CHARON-PTR-MS (Figure 22b) and AMS (22d) increased, peaking between July 9th and 11th, before declining. This trend was influenced by both transport and BLH, suggesting the advection of aged BBOA. The persistent relatively high temperatures (Figure 13) favored pollutant accumulation during this period. Afterwards, rainfall led to wet scavenging and cleaner air with less aged BBOA. Background BBOA also increased with aged BBOA, especially from July 9th to 11th. Between July 6th and 11th, photochemical SOA (Figure 22a) gradually increased. The rise in aged BBOA, combined with high temperatures, likely enhanced photochemical SOA formation. SV-OOA (Figure 22c) was influenced by both LV-OOA (Figure 22c) and regional background SOA (Figure 22d). When regional background OA and LV-OOA were dominant, SV-OOA followed a similar temporal trend. However, when aged BBOA was the primary contributor, SV-OOA variations aligned more closely with aged BBOA. This suggests that SV-OOA results from the photochemical

oxidation of other organic aerosol sources and is strongly influenced by surrounding pollutants. During periods of cleaner air (e.g., July 5th-7th and July 12th-14th), transported sources became more pronounced, highlighting the role of long-range transport and regional background under low local pollution conditions.

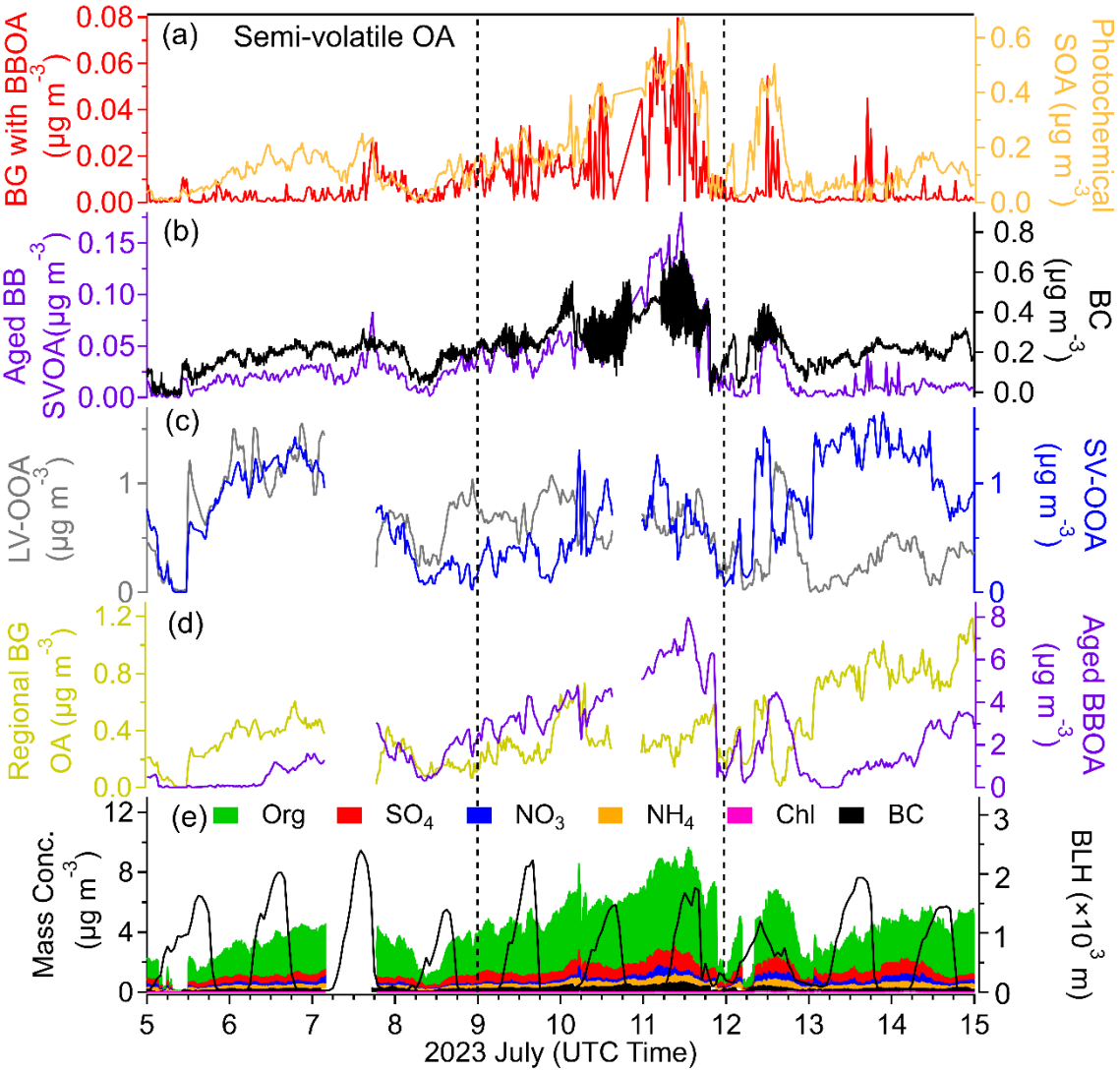

Figure 22. Temporal variations of different organic aerosol factors from July 5 to July 15, 2023. Panels show (a) background BBOA and photochemical SOA, (b) aged BBOA from Charon-PTR-MS PMF analysis and black carbon (BC), (c) LV-OOA and SV-OOA, (d) regional transported SOA and aged BBOA from AMS PMF analysis, and (e) PM2.5 aerosol mass composition as well as BLH.

From the ultrafine particle number concentrations on July 5th and 6th, I observed peaks in the 7-20 nm and 20-50 nm size range particle number concentrations (Figure 23c), indicating new particle formation events. However, as aged BBOA steadily increases from July 7th to July 11th, the ultrafine particle number ratio decreases from 100% to 40% (Figure 23a). On July 5th, the 7-100 nm particle number was almost identical to the total particle number (Figure 23b). Over the following days, the gap between them widened, reaching its maximum on July 11. This

trend is consistent with the ice-nucleating particle (INP) number (Figure 23d), suggesting that as fine particles (100-600 nm) become more abundant, INP formation is enhanced.

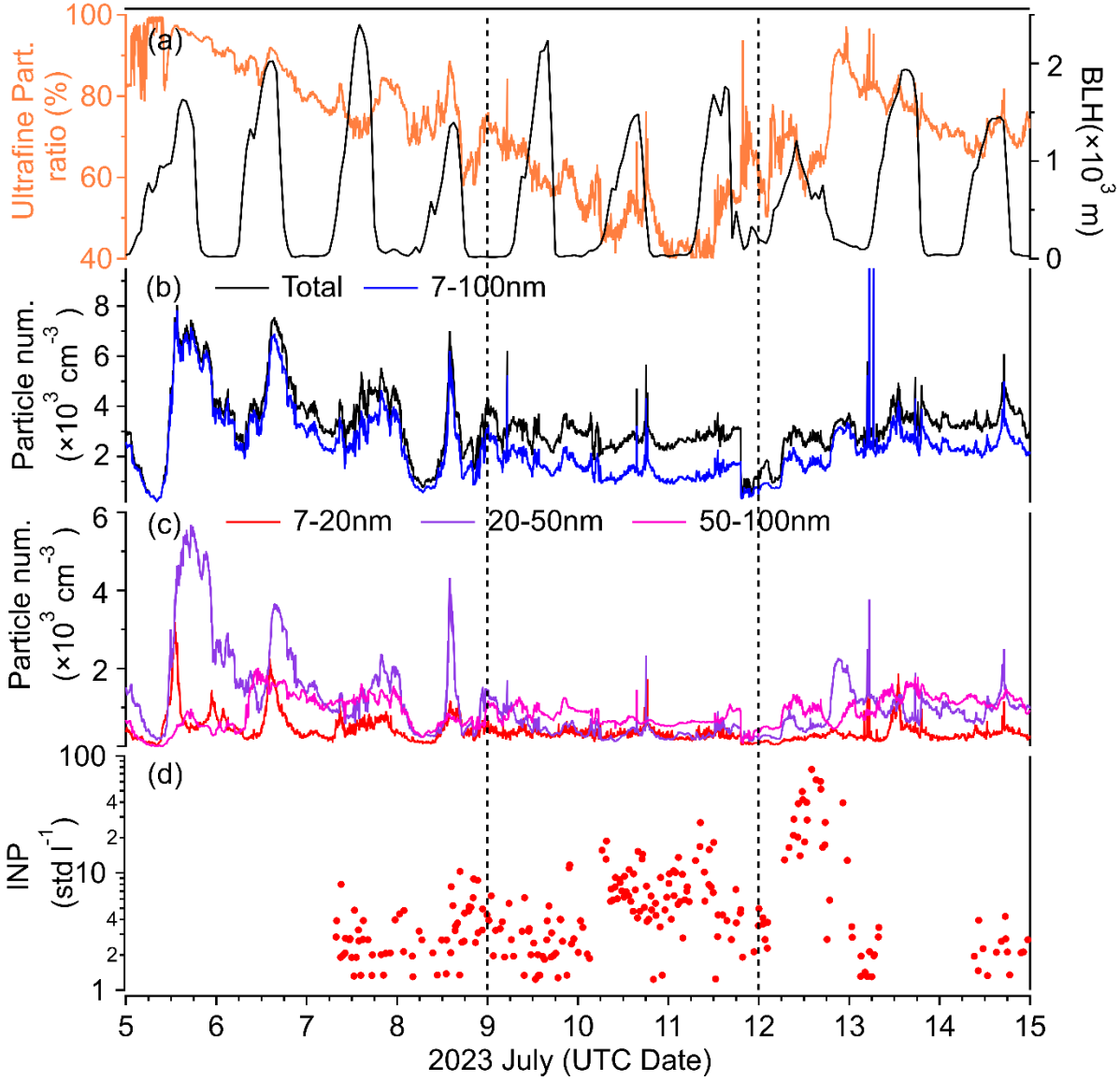

Figure 23. Temporal variations of (a) ultrafine particle ratio and BLH, (b) total and 7-100 nm particle number, (c) size-resolved particle number (7-20 nm, 20-50 nm, 50-100 nm), and (d) INP during high pollution period

3.1.7 Summary

In this top of forest mountain measurement site, air mass analysis shows marine sources dominate at 1500m (56.3% Atlantic Sea), reducing pollutants, while 500m reflects more anthropogenic influence (32.8% local area surround villages). Prevailing westerly winds enhance long-range transport. Air mass shifts (marine/continental) drive aerosol changes: marine brings rain/scavenging, continental increases pollutants. Temperature, RH, and BLH diurnal cycles affect aerosol dynamics and composition. The AMS PMF analysis resolved four OA factors: Aged BBOA, Regional background OA, SV-OOA, and LV-OOA. Separately,

CHARON-PTR-MS identified three semi-volatile OA components: Background with BBOA, photochemical SOA, and aged BBOA. Surprisingly, no biogenic semi-volatile organic aerosols (SVOA) or organic aerosols (OA) were detected, as the extremely low NOx levels suppressed oxidation processes (Dewald et al., 2022). PTR-MS analysis distinguished four VOC sources: oxidized BVOCs, long-range transported aged VOCs, aged biomass burning VOCs, and transported anthropogenic VOCs (Figure 17). Photochemical SOA dominates the SVOA fraction, while aged biomass burning and transport emissions influence both OA and VOC. Mixed biogenic and anthropogenic sources highlight the role of long-range transport and boundary layer dynamics in atmospheric processing at the measurement site.

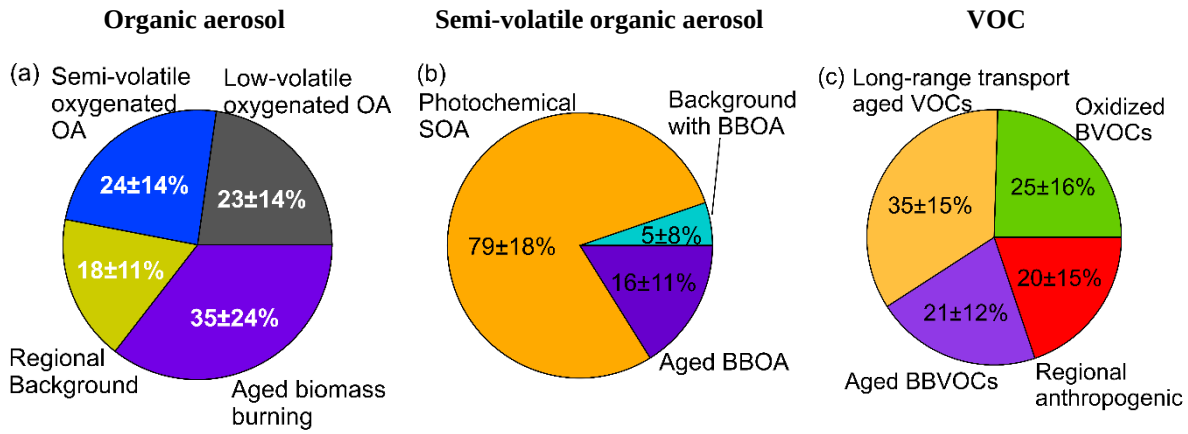

Figure 17. Fractions of organic aerosol particle factors (a), Semi-volatile organic aerosol particle (SVOA) factors (b), and VOC factors (c) at Feldberg mountaintop

Two periods with characteristic pollution were identified: (1) Canadian wildfire episode marked by long-transport biomass burning aerosols that substantially increased organic aerosol concentrations, fine particle counts, and ice-nucleating particle number; (2) Regional pollution episode where aged BBOA levels were similarly elevated but driven by combined transported and boundary layer effects, including potential upslope transport of aged BBOA from lower elevations. During cleaner conditions, regional background OA showed significant increases while aged BBOA concentrations dropped substantially, leading to higher fractions of ultrafine particles.

3.2 Sources of VOC and aerosol particles at Karlsruhe harbor in Summer

Conducting the field campaign on top of the old landfill (Mülldeponie, 60 m above the city level) west at the Rhine harbor of Karlsruhe is significant due to its unique location, which integrates influences from urban, industrial, and natural sources. For the predominant southwesterly winds at Karlsruhe, the site is located upwind and allows to detect the inflow of regional into the city (see Figure 9a). Situated near urban areas, agricultural fields, a refinery, a coal-fired power plant, and cleaner environments like forests and lakes, this site offers a comprehensive setting to study the interplay of diverse aerosol sources. The experiment aims to investigate the characteristics and sources of organic aerosols (OA), particularly the contributions of biogenic secondary organic aerosols (SOA) and anthropogenic emissions, under varying meteorological conditions during a summer period with a typical heatwave. Understanding these dynamics is crucial for assessing the impact of mixed pollution sources on air quality in urban areas, providing insights for regional air quality management and pollution control strategies.

The primary objectives of this campaign were to (1) investigate the sources and characteristics of OA, (2) identify the main VOCs and SVOA sources, and (3) quantify the contribution of biogenic SOA to the total OA. Additionally, this study aims to compare the aerosol sources and composition with previous measurements conducted in Karlsruhe's city center, highlighting differences in particle origins and contributions from urban versus peripheral environments.

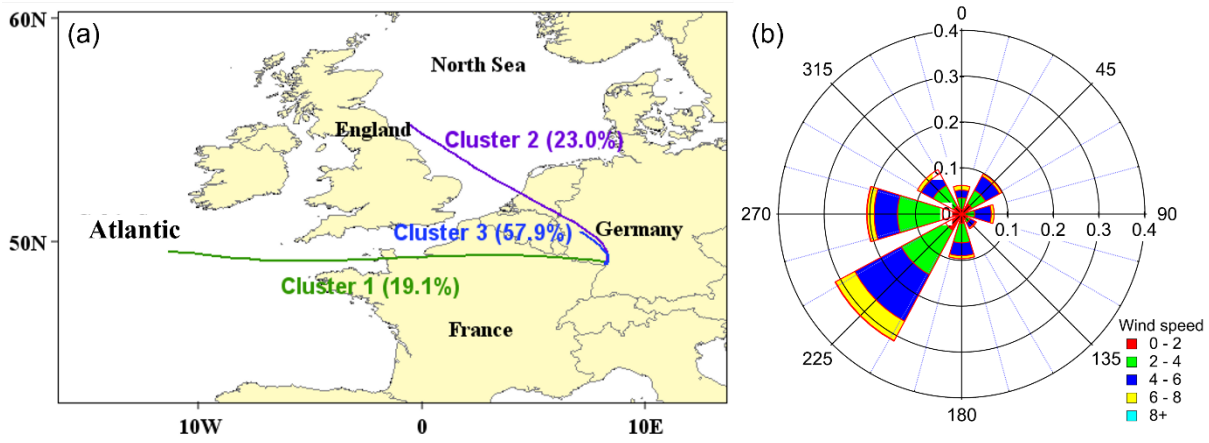

Figure 24. 72h back trajectory air mass cluster analysis for 500 m and wind rose diagram illustrating air mass origins and wind patterns at the Karlsruhe harbor in southwest Germany.

The analysis of the trajectory cluster map and wind rose diagram reveals critical insights into the air mass origins and wind patterns at the study location in Germany. The trajectory cluster

analysis identifies three primary air mass pathways (Figure 24a): Cluster 1 (19.1%), originating from the Atlantic Ocean and moving eastward through France; Cluster 2 (23.0%), originating from the North Sea and passing over England; and Cluster 3 (57.9%), representing regional air masses from western Germany and nearby areas. Notably, the dominant air mass (Cluster 3) originates from the west, indicating a strong influence of Atlantic and continental European flows rather than long-range transport from the UK. This suggests that the air masses arriving at the study site are predominantly influenced by regional transport, which is likely to carry pollutants due to their passage over industrialized and urbanized regions in Europe, such as France, Belgium, and Germany.

The wind rose diagram further supports this conclusion, showing that the dominant wind directions are from the southwest and west (Figure 22b), with mainly moderate wind speeds. These wind patterns align with the trajectory clusters, particularly Cluster 3, and suggest that stronger westerly and southwesterly winds may enhance the transport of pollutants over long distances. Given the industrial and urban emission sources along these transport pathways, the air masses are expected to carry regional pollution rather than clean marine air. In summary, the combined analysis indicates that the study location is primarily influenced by westerly air masses originating from continental Europe, which are likely to transport pollutants from industrialized regions, with wind patterns further facilitating the dispersion and transport of these pollutants. This highlights the importance of regional emission sources in shaping air quality at the site.

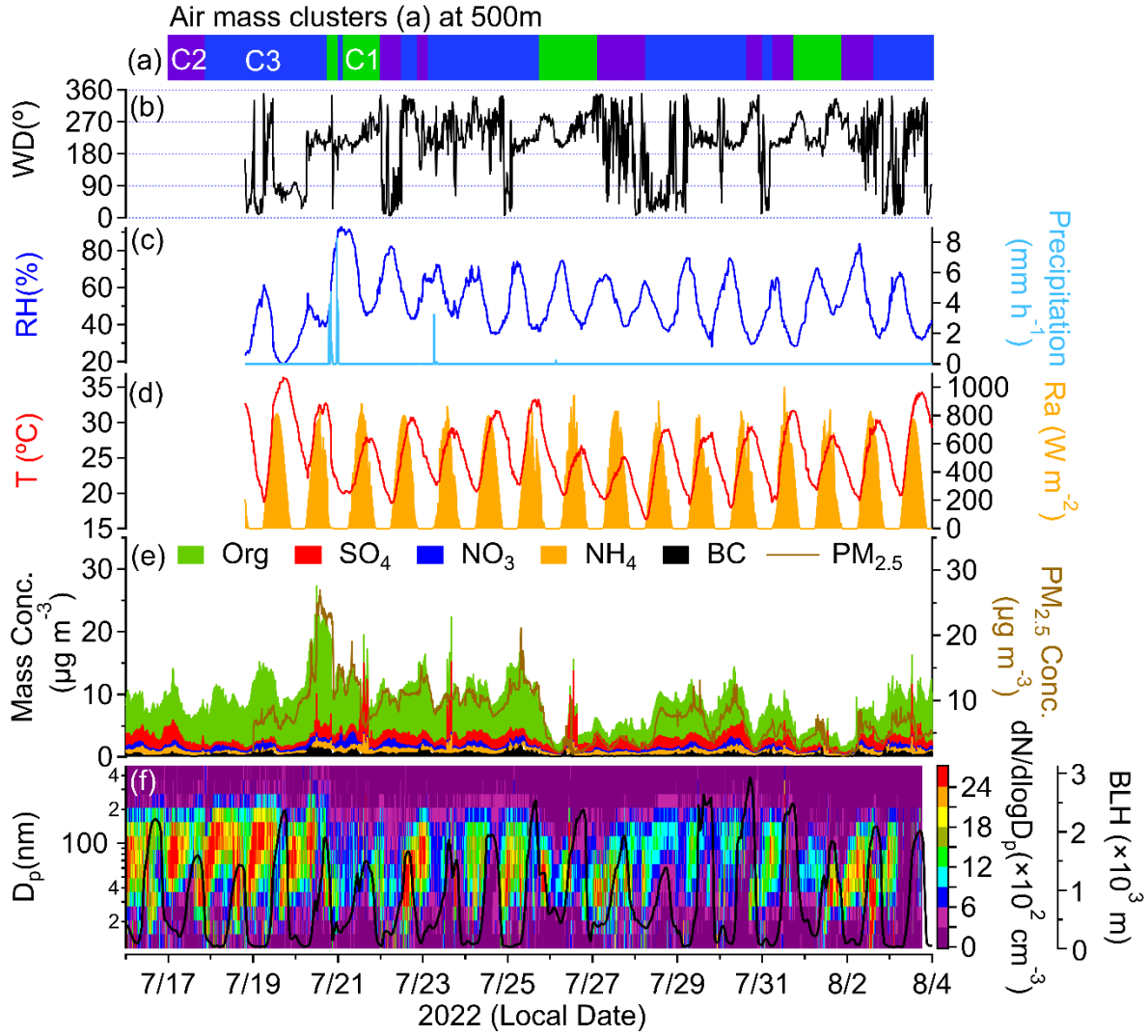

Figure 25. Time series of air mass clusters, meteorological parameters, and aerosol properties: (a) Air mass cluster assignments at 500 m, (b) Wind direction, (c) Relative humidity and precipitation, (d) Temperature and solar radiation, (e) Aerosol species (organic, sulfate, nitrate, ammonium and black carbon) and PM2.5 concentrations, (f) Particle size distribution and boundary layer height.

Figure 25 provides a detailed analysis of meteorological and aerosol parameters influencing particle growth. Different air mass clusters at 500m origins are color-coded (Fig. 25a). Relative humidity (RH, Fig. 25c) shows moderate to lower values, while only a few precipitation events reduce particle concentrations through wet scavenging. Temperature and solar radiation (Fig. 25d) exhibit strong diurnal cycles, with daytime peaks coinciding with particle growth events, driven by enhanced photochemical reactions. Aerosol composition (Fig. 25e) reveals that the dominating organic aerosols and sulfate are key contributors to particle growth, with nitrate playing a lesser role. The distinct spikes in sulfate and organic concentrations caused be local emission from the power plant. The particle size distribution (Fig. 25f) indicates periodic bursts of ultrafine particles, particularly during daytime, suggesting new particle formation (NPF) and

growth events. Most particle growth events appear during periods when Cluster 3 is dominant. This air mass likely brings precursors for new particle formation from continental sources.

3.2.1 Sources of organic aerosol particles

Through PMF analysis of AMS data, I identified six distinct OA factors: Diesel combustion OA (DCOA), Landfill gas combustion OA (LGCOA), Biogenic OA (BOA), More oxygenated OA (MOOA), Low-volatility oxygenated OA (LV-OOA), and Industrial food process OA (IFPOA). The sources of these factors were determined based on their correlations with relevant markers (Figure 26, Table S4), diurnal patterns, key elemental ratios, and mass spectra (Figure S4).

The diesel combustion OA factor exhibited characteristic fresh primary emission signatures, with an O: C ratio of 0.18 and H: C ratio of 1.89, consistent with minimally oxidized diesel exhaust. Its diurnal profile displayed a pronounced peak at 08:00 local time, strongly aligned with routine port operations such as ship unloading/loading activities and diesel truck fleet movements during early morning logistics. Chemically, this factor demonstrated moderate correlations (R=0.55) with established diesel tracers, including $C_{12}H_{17}^+$ (alkylbenzenes, indicative of unburned fuel components) (Corma et al., 2001), NO_2 (a key combustion byproduct, R=0.55), and black carbon (R=0.53) further corroborating its origin from diesel-powered port activities. The combined temporal and compositional evidence robustly identifies this source as port-related diesel emissions rather than regional traffic or industrial combustion, given the precise synchronization with port operational schedules and absence of higher oxidation markers typical of aged transport plumes.

The observed organic aerosol factor, identified as Landfill gas combustion OA (LFGOA), exhibits distinct chemical and temporal signatures indicative of mixed combustion and oxidation processes. With an O:C ratio of 0.41 and H:C ratio of 1.49, this factor reflects moderately oxidized organic compounds, consistent with the combustion of landfill-derived VOCs in nearby thermal power plants, followed by atmospheric aging. The diurnal peak at 8-10 AM aligns with operational patterns typical of landfill sites, including intensified waste transportation, mechanical operations (e.g., diesel exhaust from machinery. Key molecular tracers further support this interpretation: high correlations with acenaphthylene ($C_{11}H_9^+$, R=0.80) (Mentes et al., 2022) and formamide ($C_1H_4N_1O_1^+$, R=0.74) (Shi et al., 2024) point to combustion-derived emissions, while fatty acids such as decanoic acid ($C_{10}H_{21}O_2^+$, R=0.78) and palmitoleic acid ($C_{16}H_{31}O_2^+$, R=0.74) likely originate from the combustion of lipid-rich

waste (e.g., food residues or packaging materials) (Crossman et al., 2004; Atanassova et al., 2019). The coexistence of nitrogen- and sulfur-containing compounds suggests additional contributions from waste degradation byproducts. Together, these observations underscore LFGOA as a hybrid source influenced by both anthropogenic landfill activities and subsequent photochemical processing.

BOA factor exhibited characteristic elemental ratios (O:C = 0.39, H:C = 1.59), consistent with moderately oxidized biogenic compounds. This factor showed strong correlations (R = 0.90) with carvone ($C_{10}H_{15}O_1^+$) and pinonaldehyde ($C_{10}H_{17}O_1^+$, R = 0.84), both of which are known oxidation products of monoterpenes and serve as reliable BOA tracers. Additionally, the monoterpene fragment $C_6H_9^+$ demonstrated significant correlation (R=0.85), further supporting the biogenic origin. The observed diurnal pattern (Figure 26b), featuring early morning peaks, is consistent with typical BOA behavior. Although, monoterpene emissions are enhanced during warmer daytime conditions, the nucleation and growth of the BOA seems to be limited to the cooler morning hours at this location.

The MOOA factor exhibited highly oxidized characteristics, with an O:C ratio of 0.90 and H:C ratio of 1.32, which falls within the typical range for MOOA. The observed diurnal profile, showing afternoon peaks, confirms its photochemical chemical process. This factor demonstrated strong correlations with highly oxidized compounds measured by CHARON-PTR-MS, including: multi-oxidized guaiacol derivatives ($C_7H_9O_5^+$, R = 0.90), syringol dicarboxylic acid derivatives ($C_8H_{11}O_5^+$, R = 0.88), and other oxygenated species ($C_6H_7O_4^+$, R = 0.87; $C_6H_9O_5^+$, R = 0.86) (Ofner et al., 2011; Yee et al., 2013b) that represent levoglucosan oxidation products. These molecular markers collectively indicate significant contributions from plant emissions and aged biomass burning organic aerosol (BBOA), a conclusion further supported by the temporal coincidence with transported plumes from a forest fire event on 19th July in France. This factor also has a strong correlation (R=0.8) with Industrial phyto SVOA from CHARON-PTR-MS supporting that it was from plant emission.

The low-volatile oxygenated organic aerosol (LV-OOA) , characterized by an O:C ratio of 0.69 (Crippa et al., 2013) and H:C ratio of 1.37, exhibits moderate oxidation levels consistent with processed combustion-derived aerosols. Notably, this factor displays the highest sulfur-to-carbon ratio (S:C=0.001) among all identified factors, strongly suggesting sulfur-rich emissions as its predominant source. It has a correlation with sulfate (R=0.57) and ammonium (R=0.51). The factor's persistent mass concentrations throughout the measurement period indicate a continuous emission source rather than episodic contributions. The combination of

its exceptional sulfur content, stable temporal pattern, and moderate oxidation state suggests origins from regionally mixed, aged secondary OA derived from multiple sustained sources. The uniquely high S:C ratio serves as a definitive marker for industrial influences in this urban-industrial environment, distinguishing it from other OA types.

This Industrial food process OA factor exhibits moderate oxidation (O:C=0.38, H:C=1.54) and contains the highest nitrogen content (N:C=0.01) among all resolved factors, indicating significant contributions from nitrogen-rich organic compounds associated with industrial food processing activities. The diurnal pattern, showing elevated concentrations during daytime working hours (06:00-20:00) and lower levels on weekends, further supports an industrial origin, as it aligns with typical operational schedules of industrial facilities. The factor shows strong correlations with both gas-phase and particle-phase species, including methylmalonic acid/maleic acid ($C_6H_7O_4^+$, R=0.83) (Dash et al., 2024), 3-(methylthio)propionic acid ($C_5H_9SO_2^+$, R=0.75) (George et al., 2025), caprolactam ($C_6H_{10}NO^+$, R=0.73) (Zhu et al., 2021), and pyroglutamic acid ($C_5H_5NO_2^+$, R=0.64) (Aiello et al., 2022) in the gas phase, as well as fatty acid esters ($C_9H_{15}O_2^+$, R=0.77) (Wang et al., 2021b) and benzothiophene derivatives ($C_9H_{11}SO^+$, R=0.74) in the particle phase. The presence of azelaic acid fragment ($C_9H_{14}O_3^+$, R=0.64) (Todea et al., 2021), a known marker for fatty acid oxidation commonly emitted during food processing, along with these nitrogen- and sulfur-containing compounds, further supports the industrial food processing origin of this factor. The combined evidence from both gas and particle phase compounds point to emissions resulting from various food production processes including lipid oxidation, protein thermal degradation, and high-temperature cooking operations.

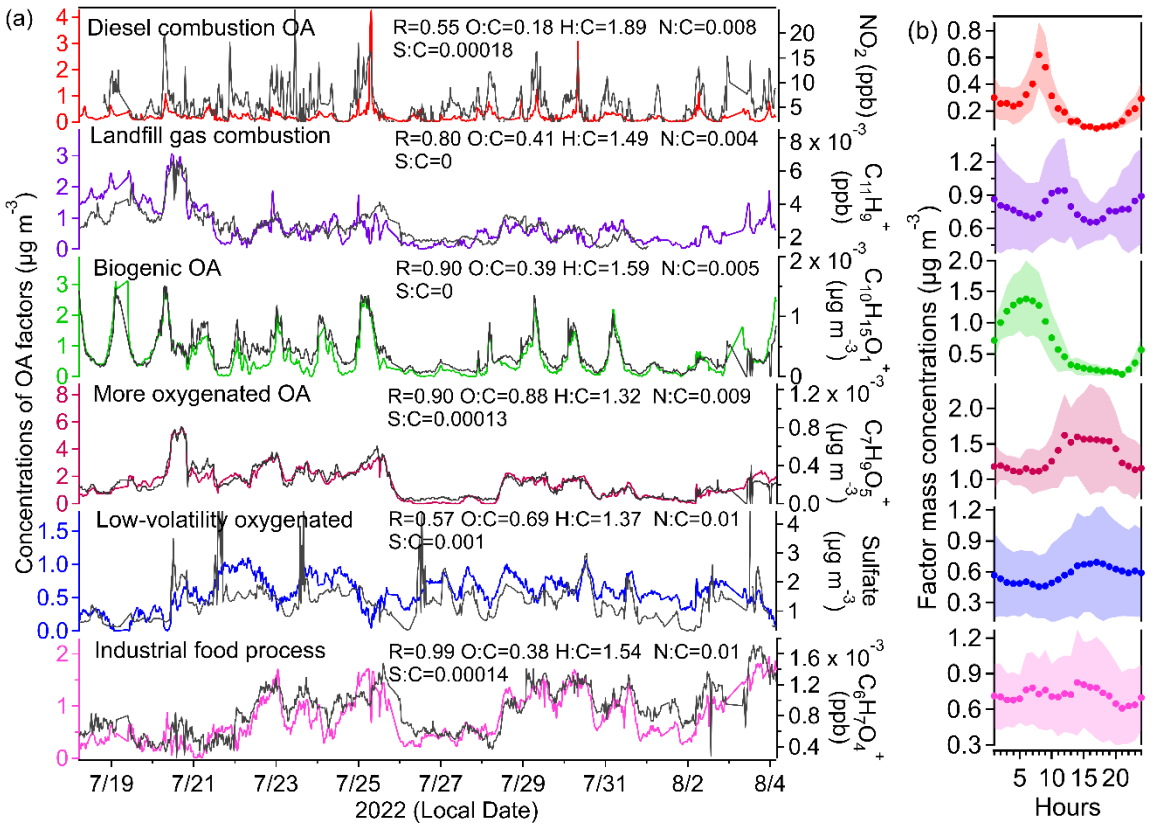

Figure 26. presents time series and diurnal patterns of organic aerosol (OA) factors derived from positive matrix factorization (PMF). Panel (a) displays the time series of six OA factors, including Diesel combustion OA, Landfill gas combustion, biogenic OA, More oxygenated OA, Low-volatility oxygenated OA, and Industrial food process OA. Each factor is color-coded, and key elemental ratios (O:C, H:C, N:C, and S:C) are provided. The black lines indicate total OA concentrations. Panel (b) shows the average diurnal profiles of these factors, highlighting their characteristic temporal variations; the shaded area between the P25 and P75 shows the IQR—the middle 50% of the data — reflecting the variability in factor concentrations throughout the day.

3.2.2 Sources of semi-volatile organic aerosol particles

The semi-volatile organic aerosol (SVOA) could be distinguished into four distinct factors based on mass spectral characteristics, including highly correlated specific compounds, tracer markers, and diurnal variation patterns (Figure 27, S5, and Table S5). These factors were identified as (1) industrial & fossil fuel combustion, (2) biomass burning, (3) biogenic emissions, and (4) industrial phyto-emissions. Each factor was validated through its unique chemical profile and temporal behavior.

The first factor was identified as More oxygenated SVOA, distinguished by possessing the highest elemental ratios of N: C (1.57) and S: C (0.019) among all factors, coupled with an elevated O: C ratio (0.532). These distinct compositional characteristics reflect the dominance of nitrogen- and sulfur-containing compounds commonly associated with industrial emissions. The diurnal profile of this factor, exhibiting a gradual increase from 06:00, peaking at 12:00,

and subsequently declining until 22:00, suggests dual influences from both solar radiation patterns and daytime industrial activity cycles. This factor exhibited moderate correlations with particulate-phase compounds such as Nitrobenzene ($C_6H_6N_1O_3^+$, R = 0.67) and Undecanal ($C_{11}H_{19}O_1^+$, R = 0.65).

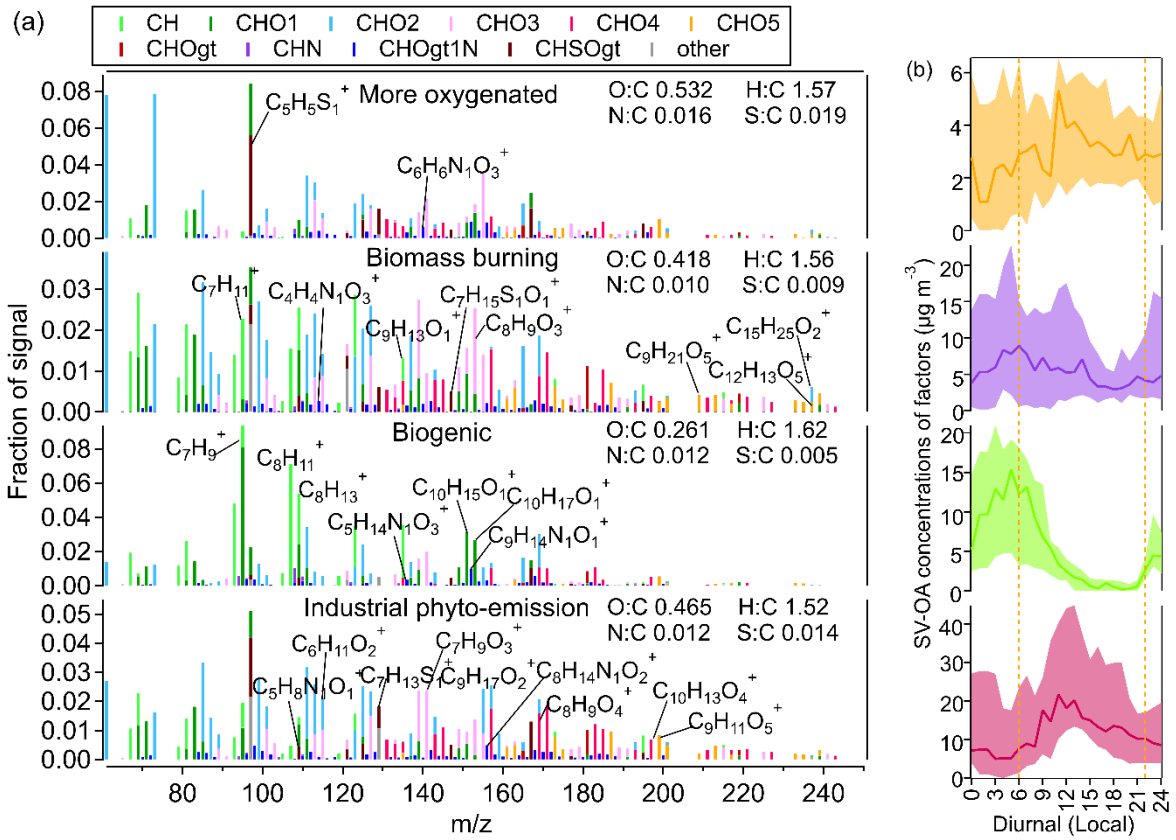

Figure 27. Source apportionment of SVOA components based on molecular composition and diurnal variation. (a) Normalized mass spectra of four identified SVOA factors: More oxygenated, Biomass burning, Biogenic emissions, and industrial phyto-emisson SVOA. Colors represent different molecular classes (e.g., CH, CHO_1, CHO_2, CHON, etc.). The O:C, H:C, N:C, and S:C atomic ratios of each factor are provided. (b) Diurnal profiles of factor concentrations (μg m^{-3}), indicating distinct temporal behaviors; the shaded area between the P25 and P75 shows the IQR—the middle 50% of the data—reflecting the variability in factor concentrations throughout the day.

The second factor was identified as Biomass burning SVOA, with its identification strongly supported by two key lines of evidence. First, a pronounced concentration peak was observed around July 20th, temporally coinciding with the transport of aerosol plumes from large-scale forest fires in France. Second, this factor exhibited a distinct diurnal pattern characterized by increasing concentrations from 22:00 to 06:00 followed by a gradual decrease to minimum levels at 15:00 (coinciding with peak solar radiation), suggesting significant influence from boundary layer height dynamics on the vertical transport and dilution of biomass burning emissions. The chemical composition of this factor was remarkably consistent with biomass burning signatures, showing particularly strong correlations (R > 0.80) with several known

biomass burning tracers. These included vanillin ($C_8H_9O_3^+$, R=0.80), a well-established marker for wood combustion, along with other oxygenated aromatic compounds such as 4-hydroxy-3-methoxybenzoic acid ($C_{12}H_{13}O_5^+$, R=0.87) (Liu et al., 2022) and methyl-1,4-benzoquinone ($C_8H_7O_3^+$, R=0.85) (Gerritz et al., 2023). The presence of these compounds reflects the pyrolysis of lignin, a major component of plant biomass. Additionally, the factor correlated strongly with sesquiterpenoid oxidation products like β-caryophyllene oxide ($C_{15}H_{25}O_2^+$, R=0.84), indicative of smoldering combustion of vegetation. This factor shows a good correlation (R=0.66) with landfill gas combustion OA, suggesting that it is significantly influenced by this OA or often shares a similar profile.

The third factor was clearly identified as Biogenic SVOA, primarily characterized by strong correlations with established monoterpene oxidation products. This factor showed particularly high associations with carvacrol ($C_{10}H_{15}O_1^+$, R=0.91) and pinonaldehyde ($C_{10}H_{17}O_1^+$, R=0.83), both well-known markers of monoterpene oxidation processes. It also correlates strongly (R=0.85) with biogenic OA in AMS, further indicating biogenic sources. The factor exhibited a pronounced diurnal cycle with concentrations peaking at 05:00 (early morning), which closely aligns with typical nighttime biogenic emission patterns and oxidation chemistry, especially for monoterpenes. This strongly suggests that monoterpene-derived secondary organic aerosols make significant contributions to the observed biogenic organic aerosol loading in the region.

The fourth factor was classified as Industrial phyto-emission SVOA based on its distinct chemical and temporal characteristics. This factor exhibited intermediate N:C (0.012) and S:C (0.014) ratios (second highest among all factors), along with a pronounced daytime concentration peak that correlated well with industrial working hours, suggesting anthropogenic emission sources. The chemical profile revealed strong associations (R = 0.78-0.87) (Table S5) with numerous plant-derived compounds, but their specific molecular signatures and temporal patterns indicate they are more likely industrial byproducts rather than natural biogenic emissions. The observed compounds can be categorized into three main groups explaining their industrial phytogenic origin: (1) plant hormone analogs and agricultural chemicals (methyl 2-aminobenzoate $C_8H_{14}N_1O_2^+$, sorbic acid $C_6H_{11}O_2^+$, ionones $C_9H_{15}O_2^+$) , commonly used in industrial-scale farming operations (Cáceres et al., 2016; Cao et al., 2024; Islam et al., 2024); (2) Phenolic compounds (protocatechuic acid $C_7H_9O_3^+$, vanillic acid $C_8H_9O_4^+$, ferulic acid $C_9H_{11}O_4^+$, coniferyl alcohol $C_{10}H_{13}O_4^+$) that may originate from wood processing industries or lignin decomposition in paper/pulp manufacturing; and (3) organic

acids (nonanoic acid $C_9H_{17}O_2^+$, pyroglutamic acid $C_5H_8N_1O_1^+$, gallic acid $C_9H_{11}O_5^+$) potentially released from food processing or bio-based chemical production (European Food Safety et al., 2021; Saeed et al., 2021; Aiello et al., 2023). This factor exhibits a strong correlation with more oxygenated OA (R=0.80), indicating that it significantly influences more oxygenated OA and constitutes a major component of it. Please note, that the paper factory at the Karlsruhe harbor is producing up to 500.000 tons of paper per year.

3.2.3 Sources of VOC

The VOCs were grouped into five distinct factors through PMF analysis based on mass spectral characteristics, including highly correlated specific compounds, markers, and diurnal variation patterns (Figure 28, S6, and Table S6). These factors were identified as (1) biofuel combustion, (2) industrial solvent use, (3) biogenic emissions, (4) French wildfire influence, and (5) industrial food processing emissions. Each factor was validated through its unique chemical profile and temporal behavior.

The Industrial Phyto-emission VOC factor exhibits significantly elevated N:C (0.045) and S:C (0.017) ratios compared to other sources. It also shows a strong correlation with Industrial Phyto-emission SVOA (R=0.87) and a moderate correlation with more oxygenated OA (R=0.54), confirming its origin from Industrial Phyto-emission VOC. Its diurnal profile featured persistent morning emissions (06:00-12:00) attributable to working hours, followed by afternoon depletion due to boundary layer expansion and photochemical degradation (minimum at 15:00). The factor's identity was confirmed through strong correlations (R > 0.85) with canonical lignocellulosic compounds including levulinic acid ($C_5H_9O_3^+$) (Victor et al., 2022), nitrophenols ($C_7H_6NO_3^+$) (Zhang et al., 2023), and nitroaromatic compounds ($C_7H_6NO_4^+$) (Zhang et al., 2023).

The industrial solvent VOC factor was identified by its dominant ethanol signal ($C_2H_7O_1^+$, R=0.99) and associations with nitrobenzene ($C_6H_8NO_3^+$) and fatty acid derivatives ($C_{16}H_{33}O_2^+$, $C_{12}H_{27}O_3^+$). The characteristic single-peak diurnal profile, exhibiting a gradual increase from 22:00 to reach maximum concentrations at 08:00 before declining, strongly suggests emissions dominated by industrial fugitive sources rather than direct production activities. This nocturnal accumulation pattern likely results from the combination of solvent evaporation from storage tanks or waste repositories under stable nighttime atmospheric conditions and enhanced vertical mixing during daytime that promotes dispersion, with the ethanol dominance and co-

occurring hydroxy fatty acids particularly indicative of paint/ink manufacturing or landfill-related solvent emissions (Li et al., 2015; Stockwell et al., 2021).

The biogenic VOC factor was clearly identified by its characteristically low O:C ratio (0.111) and strong correlations with established biogenic markers, including oxygenated monoterpenes ($C_{10}H_{15}O^+$, R=0.90; $C_{10}H_{17}O^+$, R=0.84) and monoterpene fragments ($C_6H_9^+$, R=0.85). Additionally, this factor shows strong correlations with both biogenic SVOA (R=0.72) and biogenic OA (R=0.71), further supporting its connection to biogenic sources. The distinctive early morning peak in its diurnal profile represents a classic biogenic emission pattern, driven primarily by temperature-induced stomatal opening at dawn that enhances plant volatile release, combined with the accumulation of emissions under stable nocturnal boundary layer conditions.

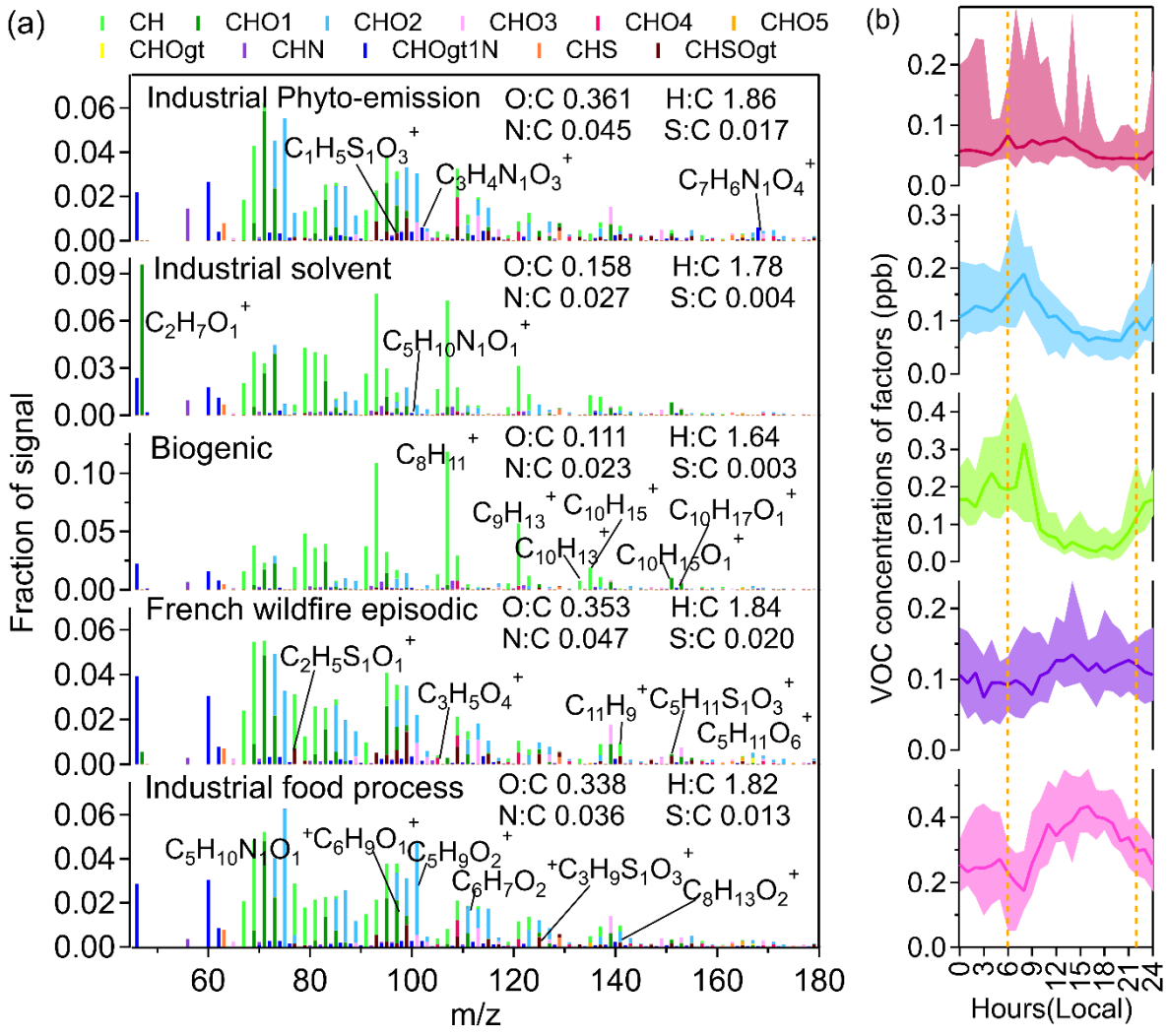

Figure 28. Source apportionment of VOC components based on molecular composition and diurnal variation. (a) Normalized mass spectra of five VOC factors identified: Industrial Phyto-emission, Industrial solvent, Biogenic emissions, French wildfire episodic, and Industrial food process. Colors represent different molecular classes (e.g., CH, CHO_1, CHO_2, CHON, etc.). The O:C, H:C, N:C, and S:C atomic ratios of each factor are provided. (b) Diurnal profiles of factor concentrations (ppb), showing distinct temporal patterns; the shaded area between the P25 and P75 shows the IQR, reflecting the variability in factor concentrations.

The French wildfire episodic VOC factor exhibited dramatically elevated concentrations specifically on 20th-21st July, perfectly coinciding with documented wildfire events in France and corresponding atmospheric transport patterns, before rapidly diminishing to background levels - clear evidence of a transient pollution episode. The factor exhibited the most oxidized signature among all sources (O: C=0.353), along with remarkably elevated N: C (0.047) and S:C (0.02) ratios. These chemical fingerprints indicate: (1) extensive atmospheric aging and oxidation during transport (elevated O:C) and (2) significant incorporation of NOx into organic compounds through nighttime nitrate radical chemistry (high N:C). This factor demonstrates moderate correlations with biomass burning SVOA (R=0.65) and landfill gas combustion OA (R=0.63), suggesting its primary origin from biomass combustion sources.

The industrial food processing VOC factor was identified through its characteristic chemical profile containing multiple compounds associated with food production and additives. This factor exhibited strong correlations with: octenone/octenoic acid ($C_8H_{13}O_2^+$, R=0.92) (Nimbkar et al., 2022), methylfuranone ($C_6H_7O_2^+$, R=0.89) (Nareman Adeem Shnaa Aljazy and Abdulstar, 2023; Darsih et al., 2024), cyclohexenone ($C_6H_9O^+$, R=0.87), hexenoic acid ($C_6H_{11}O_2^+$, R=0.86) (Milani and Dehghan, 2024), and other food-related markers including fatty acid derivatives and malic acid fragments. Additionally, it shows a correlation with industrial food process OA (R=0.41), suggesting some influence from food processing sources. The moderate correlation coefficients likely reflect variability in gas-particle partitioning and differential atmospheric lifetimes between the emissions and observed OA components. The distinct daytime concentration peak, synchronized with industrial working hours, strongly suggests emissions from food manufacturing processes rather than household cooking activities.

3.2.4 Example of a polluted episode

During the measurement period from 18th to 26th July, a pronounced high-pollution event was observed (Figure 29). The period exhibited significant variability in air quality, with particularly clean conditions associated with air masses (C1) of marine origin. On 21st July, these cleaner air masses effectively diluted the highly polluted organic aerosol concentrations that peaked on 20th July, while 26th July represented the cleanest day of the campaign with the lowest organic aerosol concentrations (Figure 30e).

The analysis revealed distinct patterns in VOC sources: Biomass burning VOCs showed a marked increase during the transport of air masses influenced by French forest fires, followed

by a rapid decline to near-background levels. In contrast, Industrial Phyto-emission VOCs demonstrated more stable emissions throughout the measurement period, becoming dominant after the biomass burning episode. The subsequent increase in Phyto-emission VOC concentrations likely reflects the influence of local industrial activities in the region. The paper factory Maxau is located north west of the measurement site. Consequently, these wind directions coincide with higher values of this factor.

Both industrial solvent VOCs and biogenic VOCs exhibited similar diurnal patterns, with concentrations increasing during nighttime hours. This synchronous behavior can be attributed to the BLH evolution. For industrial solvent VOCs, this pattern may be further amplified by reduced dispersion conditions at night combined with continued industrial emissions. In contrast, industrial food processing VOCs showed distinct daytime peaks, consistent with operational hours of these facilities.

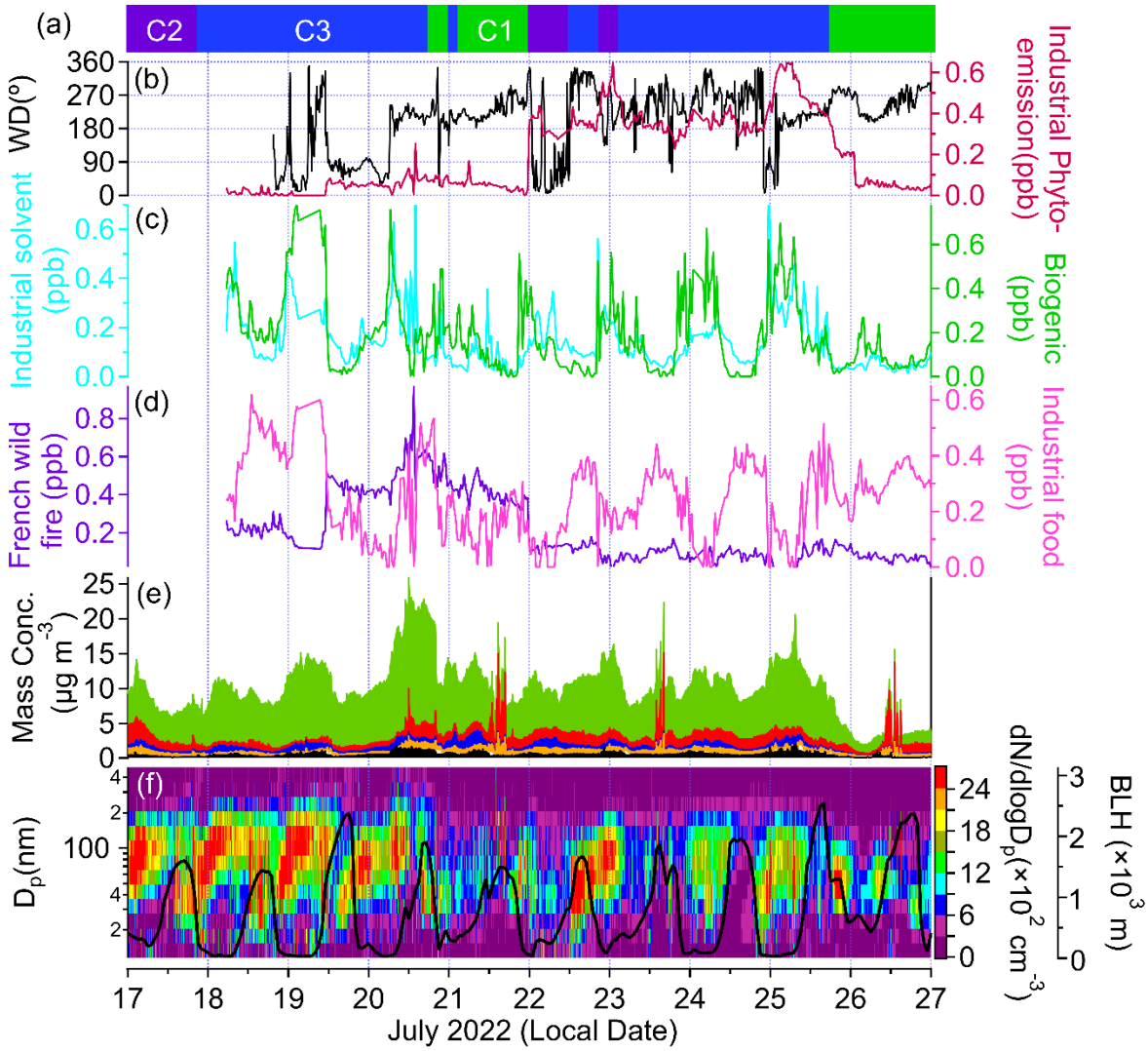

Figure 29. Time series of meteorological conditions, VOC sources, and aerosol properties at Karlsruhe in July 2022. (a) Air mass classification based on back trajectories: C1 (green, oceanic), C2 (purple, from the North Sea), and C3 (blue, regional continental air). (b) Wind direction and Industrial Phyto-emission VOC. (c) Industrial solvent VOC and Biogenic VOC. (d) Biomass burning VOC and Industrial food process VOC. (e) Mass concentration of submicron aerosol species (μg/m³). (f) Particle size distribution and planetary boundary layer height.

The temporal variation of SVOA (Figure 30) reveals that the C1 air mass, associated with cleaner marine air masses, led to a reduction in the concentrations of all SVOA components except the more oxygenated fraction. It seems that More oxygenated SVOA is more related to long range transport. Analysis of the SVOA time series indicates that the total organic aerosol concentrations were primarily driven by two major sources: Biogenic SVOA, which dominated nighttime chemistry, and Industrial Phyto-emission SVOA, which influenced daytime photochemical pollution. Notably, the influence of Biomass Burning SVOA was transient, with concentrations dropping to nearly negligible levels following the passage of the forest fire plume.

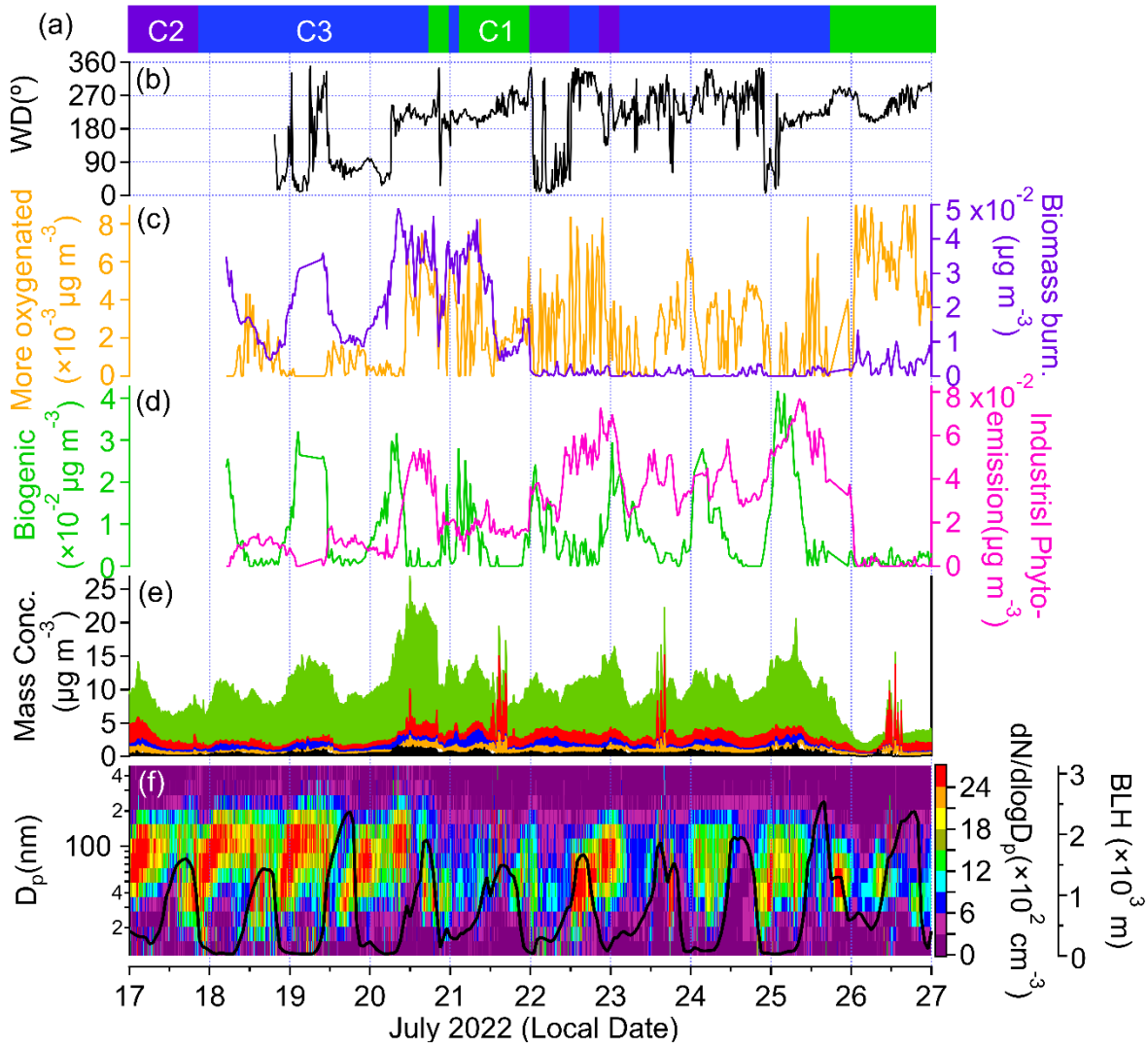

Figure 30. Time series of meteorological conditions, SVOA sources, and aerosol properties at Karlsruhe in July 2022. (a) Air mass classification based on back trajectories. (b) Wind direction (c) More oxygenated SVOA and Biomass burning SVOA. (d) Biogenic SVOA and Industrial Phyto-emission SVOA. (e) Mass concentration of submicron aerosol species (µg/m³). (f) Particle size distribution and planetary boundary layer height.

Figure 31 demonstrates that OA sources were more strongly influenced by air mass origin than by wind direction, which remained relatively consistent throughout the measurement period, predominantly from 180-270° with occasional contributions from 0-90°. Despite this variability, the particle sources associated with these two wind sectors showed only small differences in composition. Diesel combustion OA and Landfill gas combustion OA exhibited nearly identical temporal patterns during the high-pollution episode, suggesting a coupled emission mechanism-likely from diesel trucks transporting waste, which simultaneously contributed to diesel-related emissions while waste handling processes released landfill-derived organics. Biogenic OA displayed a pronounced influence from nighttime chemistry, whereas the other three OA components showed no clear diurnal trends. Notably, LV-OOA peaked during the arrival of the C1 air mass, indicating a stronger dependence on regional

transport compared to other OA components. This observation suggests that LV-OOA was predominantly influenced by aged secondary organic aerosols advected from distant sources rather than local production.

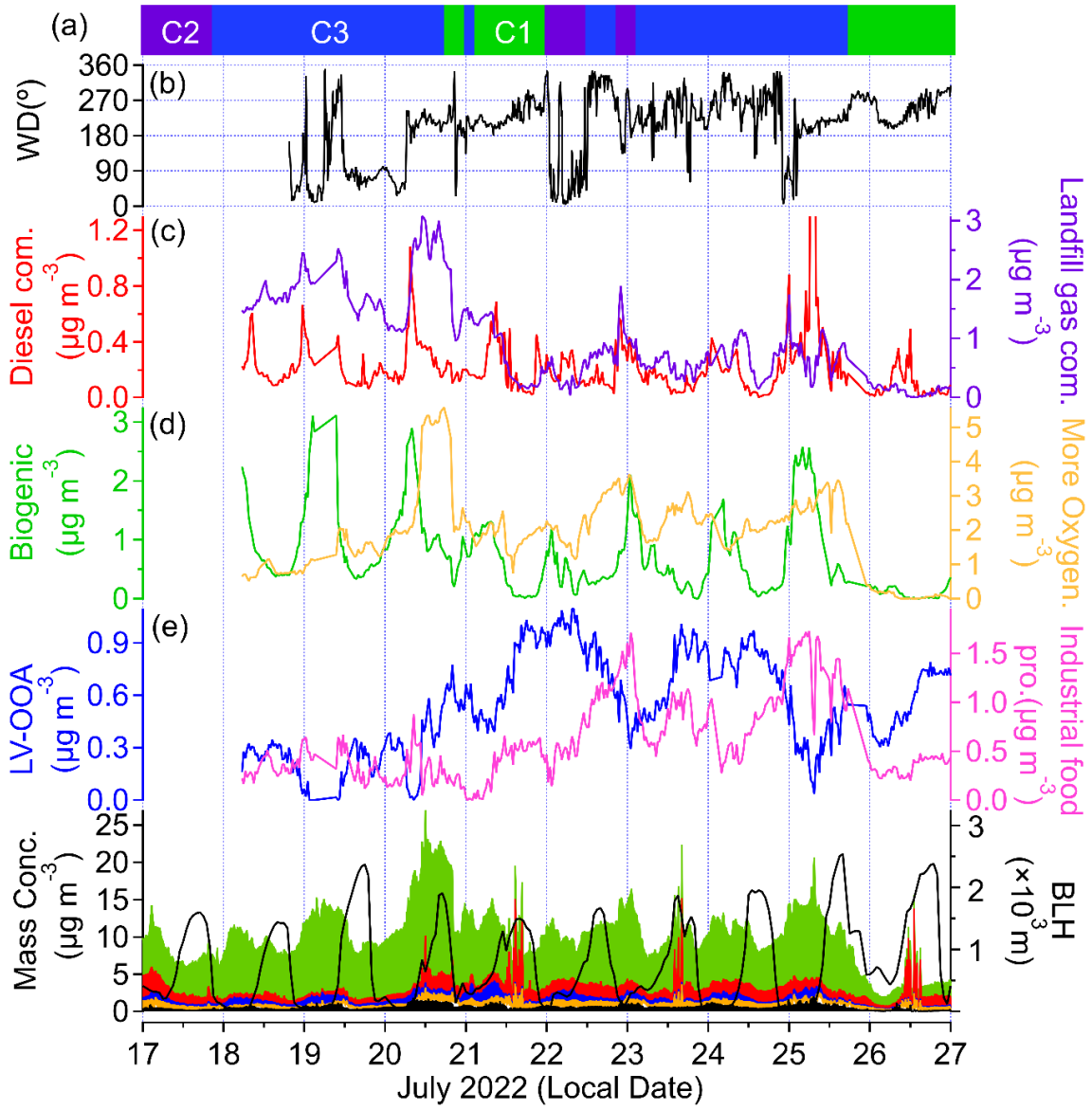

Figure 31. Time series of meteorological conditions, OA sources, and aerosol properties at Karlsruhe in July 2022. (a) Air mass classification based on back trajectories. (b) Wind direction (c) Diesel combustion OA and Landfill gas combustion OA. (d) Biogenic OA and More oxygenated OA. (e) Low-volatile oxygenated OA and Industrial food process OA. (f)Mass concentration of submicron aerosol species (μg/m³) and planetary boundary layer height.

Figure 32 and Table S7 show a comprehensive correlation analysis between OA, SVOA, and VOC factors with particle number concentrations across three size bins (11-20 nm, 20-50 nm, and 50-90 nm), and the ultrafine particle ratio revealed several key patterns. While all factors demonstrated weak negative correlations with the ultrafine particles, only biogenic OA, industrial solvent VOC, and landfill gas combustion OA displayed small but significant positive (0.44-0.49) correlations with 50-90 nm particles, with no significant correlations observed for other size ranges. These weak correlations across multiple size fractions strongly

suggest highly mixed source contributions at this sampling site, where primary emission signatures have likely been substantially modified through atmospheric aging and processing. Additionally, black carbon also has weak correlations with ultrafine particle concentrations. The predominant negative trend with ultrafine particle ratio may further indicate that secondary formation processes rather than primary emissions dominate nanoparticle production in this environment.

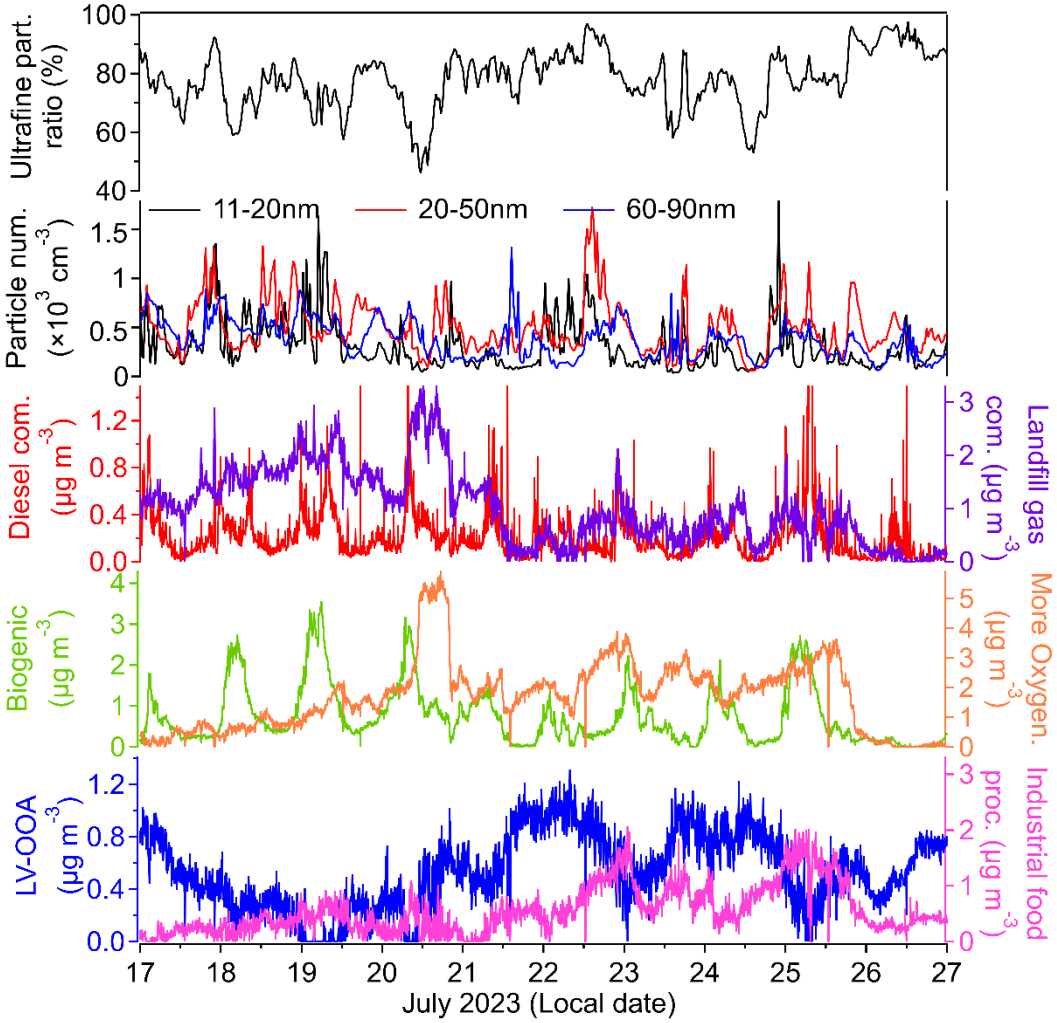

Figure 32. Time series of ultrafine particle ratio, particle number concentrations (11-20 nm, 20-50 nm, 60-90 nm), and diesel combustion, landfill gas, biogenic emissions, more-oxygenated, and industrial food processing OA.

3.2.5 Summary of VOC and aerosol particles at Karlsruhe harbor in Summer

The study identified three primary air mass pathways influencing the location at the Karlsruhe harbor, with 57.9% originating regionally from western Germany. Prevailing westerly/southwesterly winds transported industrial pollutants, driving local air quality, while particle growth events were. Figure 33 presents the fractional contributions of various sources to OA, SVOA, and VOC concentrations. The analysis reveals industrial food processing as the dominant source, contributing 41±23% to VOC and 20±9% to OA. Industrial phyto-emissions

also showed substantial contributions, accounting for 13±14% of VOC and 44±27% of SVOA. The OA fraction was notably characterized by more oxygenated OA (30±15%), which exhibited strong influence from Industrial phyto-emissions SVOA. The measurement period coincided with French wildfire events, which elevated biomass burning contributions to 17±15% in VOC and 26±21% in SVOA. These wildfire emissions showed partial spectral overlap with landfill gas combustion profiles, suggesting biomass burning and landfill gas combustion sources mixing. Biogenic sources demonstrated consistent but relatively small contributions across all phases (VOC: 16±12%; SVOA: 15±14%; OA: 12±9%), reflection the strong role of industrial emissions at the Karlsruhe harbor.

Biogenic, landfill gas combustion OA, black carbon, and industrial solvent VOC exhibited relatively weak correlations with 50-90 nm particles (Liu et al., 2025). The overall weak correlations with UFP suggest highly mixed sources and substantial atmospheric aging.

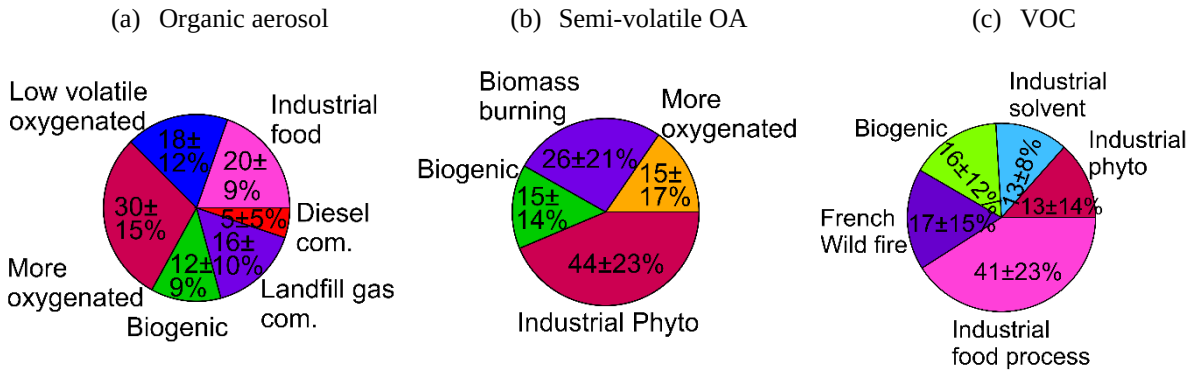

Figure 33. Average fractional contributions (± standard deviation) of (a) OA, (b) SVOA, and (c) VOC sources.

3.3 Sources of VOC and aerosol particles in downtown Munich in Summer and Winter

Conducting this comprehensive field campaign at Theresienstrasse 41 in downtown Munich is scientifically significant due to its location in a dense urban street canyon, representing typical urban air pollution challenges in a major European metropolis. As Germany's third-largest city (population: 1.5 million; density: 4,700/km²), Munich's air quality is influenced by complex emission sources including traffic, residential heating, and regional transport, yet molecular-level characterization of OA and VOCs across seasons remains limited. Previous studies in Munich have identified traffic emissions, biomass burning, and cooking as key aerosol sources (Qadir et al., 2013; Schnell, 2014) but lacked comprehensive seasonal analysis using advanced online instrumentation.

The primary objectives of this study were to: (1) determine the molecular composition and seasonal variability of VOCs and OA at high temporal resolution, (2) identify and quantify contributions from key sources (e.g., traffic, cooking, biomass burning) to VOCs, SVOA, and total OA using complementary PTR-ToF-MS and HR-ToF-AMS measurements, and (3) establish source-receptor relationships through combined PMF analysis of SVOA and OA datasets. This approach provides unprecedented chemical resolution for urban aerosol characterization, addressing critical knowledge gaps in Munich's air pollution dynamics and supporting targeted mitigation strategies.

Field observations were conducted from August 3rd to August 29th, 2023, in summer and from March 1st to April 10th, 2024, in winter. The sampling site (11°34'E, 48°8'N) was located on a parking lot next to a 30 m tall building of the Ludwigs-Maximilians-University (LMU) of Munich in a street canyon of Theresienstrasse 41 (Figure 34). The street has several restaurants, apartment houses, museums, university workshops and laboratories, and substantial car traffic. Consequently, the sampling site is affected by emissions from cooking, heating, and traffic. The wind direction at the container site predominantly originates from the south and southeast due to channeling in the street canyon. At the rooftop of the 30-meter LMU building, it mainly came from the west and east. Wind speed and direction exhibit only little differences between summer and winter measurements (Figure 34).

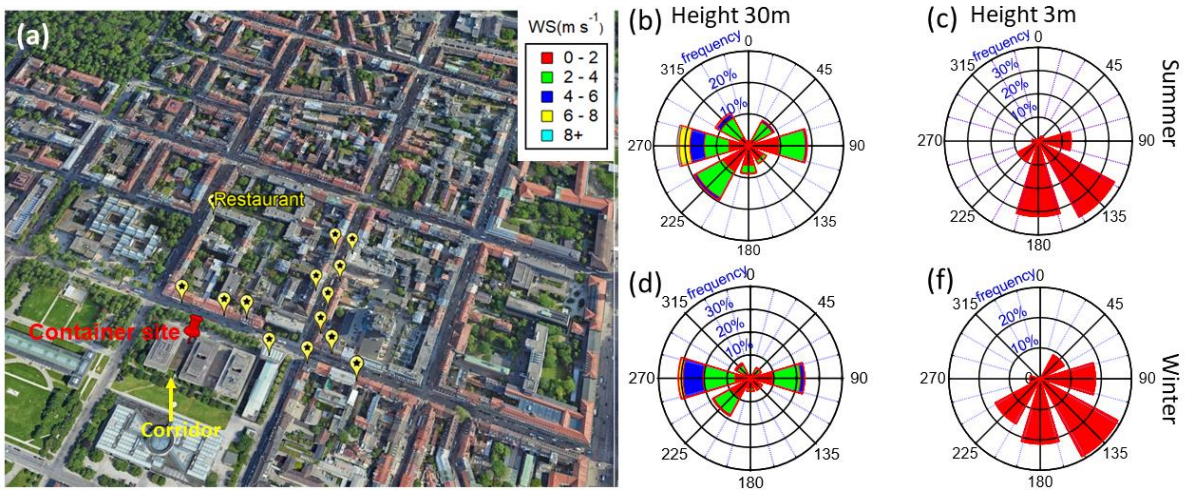

Figure 34. (a) Map of the measurement location (red pin, LMU) and surrounding restaurants (yellow markers). (b) and (d) illustrate wind direction and wind speed measured by the Institute of Meteorology of LMU at the rooftop (30 meters above ground level) of the Environmental Department building adjacent to the measurement container in summer and winter, respectively. (c) and (f) show wind direction and wind speed measured at 3 meters above the street level on the measurement container in summer and winter, respectively.

3.3.1 Overview of meteorological and particle observations

The summer period was characterized by frequent sunny weather with moderate to high temperatures and significant precipitation events mainly at the beginning and end of the summer campaign. The winter/spring period shows typical winter conditions until March 8th and more spring-like warmer conditions thereafter.

Figure 35a and b show wind speed and direction at 3m and 30m above ground in summer and winter. In different seasons, wind speed at different heights shows similar time series. The average wind speed is 0.7±0.4 m s^{-1} at 3m and 2.6 ± 1.4 m s^{-1} at 30m in summer and winter/spring. Figure 35c and d present the time series of meteorological parameters during the summer and winter campaigns. The average ambient temperature in summer was 21.9 ± 5.8 °C, significantly higher than the winter/spring average of 8.4 ± 3.0 °C / 10.2 ± 3.8 °C. Solar radiation levels were also notably higher in summer compared to winter. Relative humidity and precipitation showed seasonal variation, with values of 66.5 ± 17.3% and 7.23mm day^{-1} in summer, compared to 73.4 ± 16.2 % / 67.3 ± 14.3 % and 9.75mm day^{-1} / 24.00mm day^{-1} in winter/spring, respectively. This indicates that there was more precipitation in spring. Trace gases exhibited seasonal differences: NO_2 averaged 10.2 ± 7.7 µg m^{-3} in summer and 26.1 ± 9.9 / 28.4 ± 10.8 µg m^{-3} in winter/spring, likely influenced by higher emissions and less dilution in winter. Similarly, NH_3 mixing ratios were lower in summer (1.3 ± 0.1 µg m^{-3}) compared to winter (5.4 ± 1.5 µg m^{-3}) and spring (4.0 ± 1.8 µg m^{-3}). O_3 levels also varied seasonally, with surprisingly lower summer concentrations (67.1 ± 26.6 µg m^{-3}) than in winter (90.5 ± 56.9 µg

m^{-3}) and spring (120.0 ± 46.6 μg m^{-3}). Summer's low NO_2 limits O_3 despite high sunlight, while winter/spring's high NO_2 sustains O_3. The region is NO_x-limited, making NO_x control key for ozone reduction. As expected, the average boundary layer height (BLH) was lowest in winter (339 ± 298 m), compared to summer (510 ± 477 m) and spring (516 ± 453 m) with similar and significantly higher values, further influencing pollutant dispersion and accumulation.

Comparison of size distribution measurements over the entire summer and winter periods reveals a higher frequency of particle formation events and significantly higher particle concentrations during summer (Figures 35e and f). The average total particle number concentration was highest in summer at 9988 ± 5118 cm^{-3}, with sub-100 nm particles accounting for 8175 ± 4623 cm^{-3} and representing 80.6 ± 8.2% of the total. In comparison, winter showed lower concentrations with a total of 8879 ± 3515 cm^{-3}, of which sub-100 nm particles constituted 5459 ± 2524 cm^{-3} (63.9 ± 45.2%). Similarly, spring exhibited intermediate levels with an average total particle count of 7047 ± 3941 cm^{-3}, including 5946 ± 3847 cm^{-3} of sub-100 nm particles (89.7 ± 27.8%). This indicates higher ultrafine particle concentrations in summer and spring compared to winter. $PM_{2.5}$ concentrations exhibited distinct seasonal variations, with the lowest levels observed in spring (4.2 ± 3.1 μg m^{-3}) and summer (6.7 ± 3.7 μg m^{-3}), while winter showed significantly higher concentrations (13.0 ± 7.4 μg m^{-3}). In contrast, PM_{10} displayed a different seasonal pattern, with summer concentrations (14.0 ± 9.6 μg m^{-3}) slightly lower than winter levels (15.4 ± 8.4 μg m^{-3}), followed by substantially reduced spring concentrations (6.5 ± 4.3 μg m^{-3}). This is reflecting the larger total precipitation and potential wet scavenging in spring.

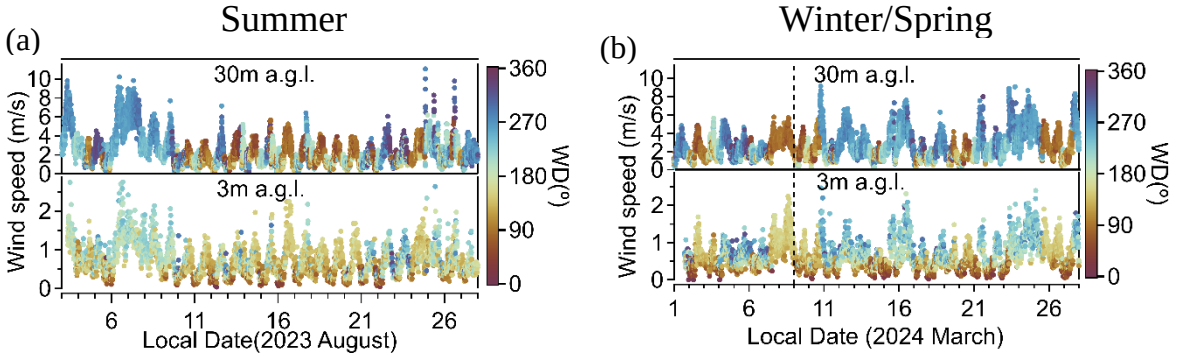

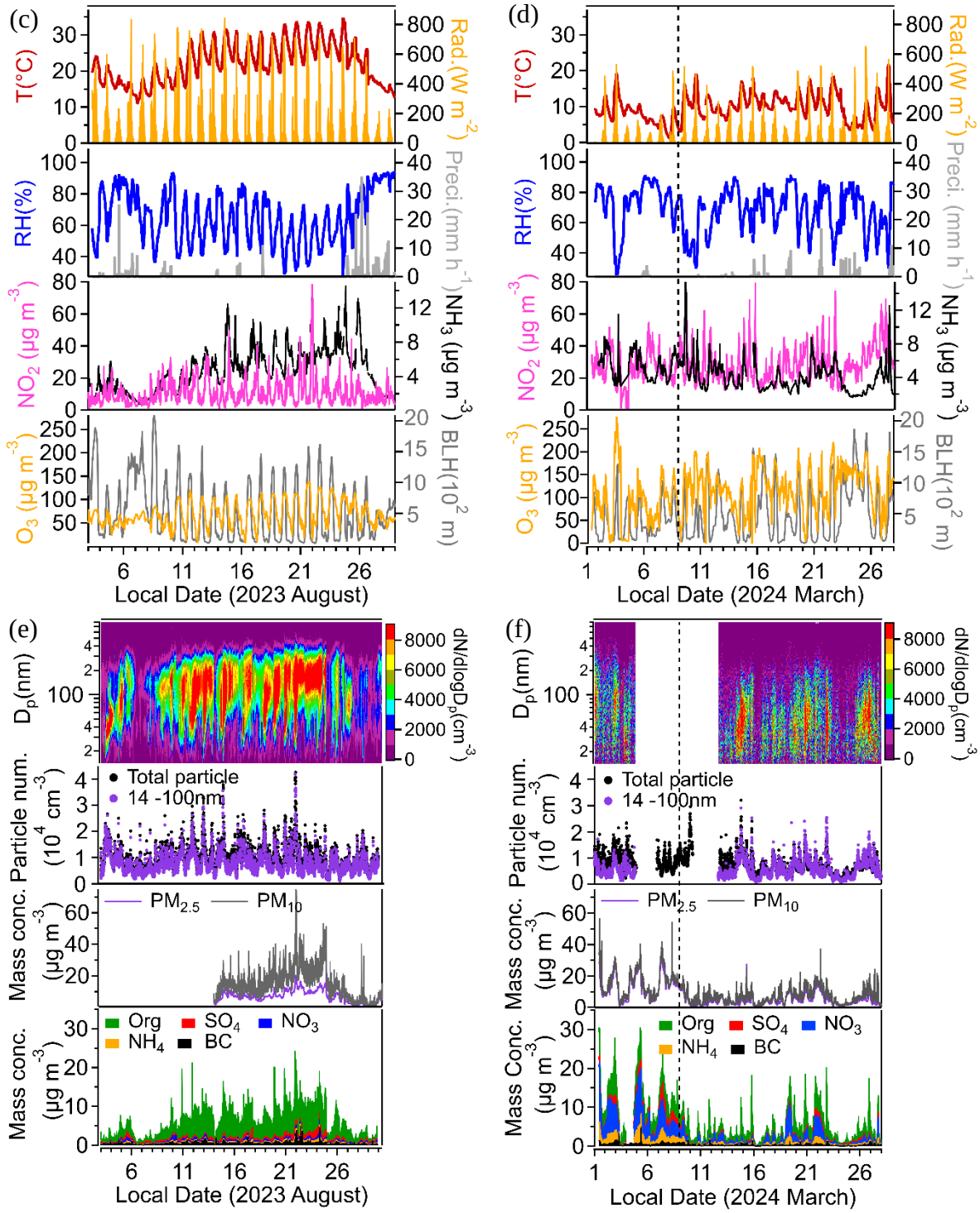

Figure 35. Time series of wind speed & direction 3m (above ground level) and 30 m(above ground level) in summer (a) and winter (b); temperature (T); global radiation (Ra); relative humidity (RH); precipitation; NO_2; NH_3; O_3 and boundary layer height (BLH*) in summer (c) and winter (d); Particle number size distributions; particle number of total and below 100nm ultrafine particles; $PM_{2.5}$ and PM_{10} mass concentrations; Organic aerosol (OA), sulfate, nitrate, and ammonium; Black Carbon (BC) in summer (e) and (f) in winter; #All data plotted except the wind data were measured at the container roof. *Please note that the BLH data refer to ERA5 reanalysis data (Guo et al., 2024).

Aerosol particle mass composition varies by season. Organic aerosol particles dominate in summer, averaging 4.3 ± 2.9 μg m^{-3}, higher than 3.4 ± 1.7 μg m^{-3} in winter and 1.8 ± 1.8 μg m^{-}

^{3} in spring. Nitrate is the main component in winter, with 4.5 ± 3.2 µg m^{-3}, compared to 1.0 ± 1.3 µg m^{-3} in spring and 0.3 ± 0.2 µg m^{-3} in summer. Ammonium also peaks in winter at 1.8 ± 1.1 µg m^{-3}, compared to 0.4 ± 0.4 µg m^{-3} in spring and 0.3 ± 0.2 µg m^{-3} in summer. Black carbon (eBC) average mass concentrations were 0.47 ± 0.35 µg m^{-3} in summer, 0.64 ± 0.35 µg m^{-3} in winter, and 0.31 ± 0.22 µg m^{-3} in spring. The average fractions are shown as pie charts (Figures 36).

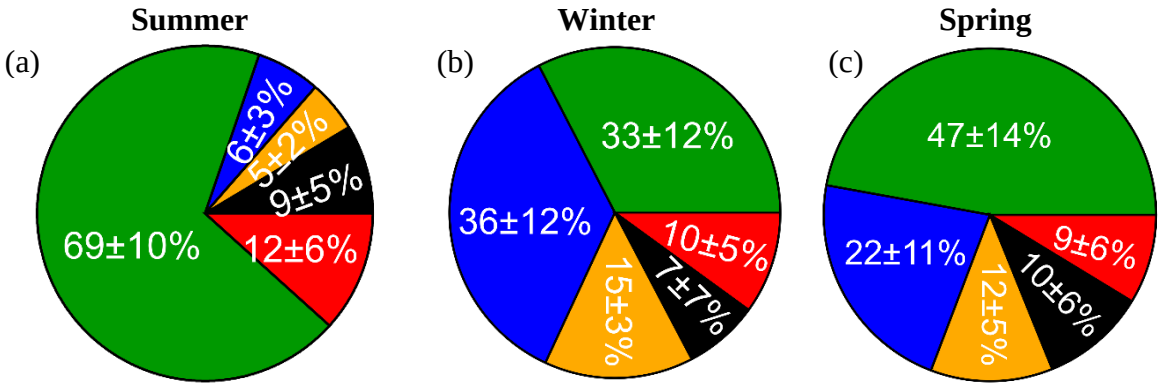

Figure 36. Fractions of OA (green), sulfate (red), nitrate (blue), ammonium (yellow) and BC (black) in summer 2023 (a), (b) in winter (until March 8th) and (c) in spring 2024 in downtown Munich.

3.3.2 Sources of organic aerosol (OA) particles

This study thoroughly examined factor profiles, diurnal patterns, and correlations with tracers (Figure 37, S7) in summer and in winter (Figure 38, S8). Five OA factors were identified from PMF analysis of the AMS mass spectra as the optimal interpretable solutions for summer and winter, respectively. The average organic aerosol concentration was 4.3 ± 2.9 µg m^{-3} in summer, 3.4 ± 1.7 µg m^{-3} in winter, and 1.8 ± 1.8 µg m^{-3} in spring.

In summer, the first factor was identified as cooking organic aerosol (COA), based on its high H: C ratio (1.82), low O: C ratio (0.19) (Figure S7a), higher contributions at m/z 55 ($C_3H_3O^+$) and m/z 57 ($C_3H_5O^+$), and the mass spectrum dominated by hydrocarbon ions. These characteristics are consistent with reported COA in urban areas (Mohr et al., 2012; Elser et al., 2016; Äijälä et al., 2017; Liu et al., 2018a). Additionally, fatty acid ($C_{16}H_{35}O_3^+$) detected by CHARON-PTR-MS showed a moderate correlation (R = 0.54) with the COA time series (Figure 35a). The second factor is characterized by a mass spectrum also dominated by hydrocarbon ions, a similar O: C ratio, and a high O: C ratio, but with higher contributions at m/z 55 ($C_4H_7^+$) and m/z 57 ($C_4H_9^+$) (Elser et al., 2016). These features are consistent with the characteristics of hydrocarbon-like organic aerosol (HOA), which is related to traffic emissions. Additionally, HOA shows a good correlation (R=0.66) with the BC time series. The third factor is assigned to Biogenic organic aerosol (BOA), based on its H: C ratio of 1.63 and O: C of 0.44.

The O/C ratio falls within the range typically associated with semi-volatile oxidized organic aerosol (SVOOA), which is approximately 0.35±0.14 (Setyan et al., 2012). And it has a good correlation of 0.86 with monoterpene oxidation products (e.g. Pinoaldehyde) measured by CHARON-PTR-MS. BOA's diurnal pattern (Figure 37b) shows an increase starting at 8 pm, reaching its peak at 7 am. This trend aligns with the nighttime oxidation process of monoterpenes, supporting its identification as BOA. The fourth factor was identified as aged biomass burning organic aerosol (BBOA) because its O/C ratio of 0.597 is slightly higher than that of fresh BBOA (0.15-0.5) and falls within the range of aged BBOA (0.5-0.87) (Ortega et al., 2013). Its diurnal profile shows a small peak at 3 pm and a higher peak at 10 pm. BBOA shows a strong correlation (R=0.93) with the BBOA tracer levoglucosan detected by CHARON-PTR-MS. Therefore, the fourth factor is identified as aged BBOA. The fifth factor has the lowest H: C ratio (1.43) and the highest O:C ratio 0.75, which falls within the range of low-volatile oxygenated organic aerosol (LVOOA) (0.6-1.0) (J. L. Jimenez et al., 2009). LVOOA is dominated by CO^+ and CO_2^+ in the AMS mass spectra and shows a strong correlation (R=0.70) with O_3, indicating that it is associated with photochemical oxidation processes (Kumar et al., 2016). Its diurnal pattern shows a daytime peak. These characteristics align well with the typical properties of LVOOA, leading to its identification as LVOOA.

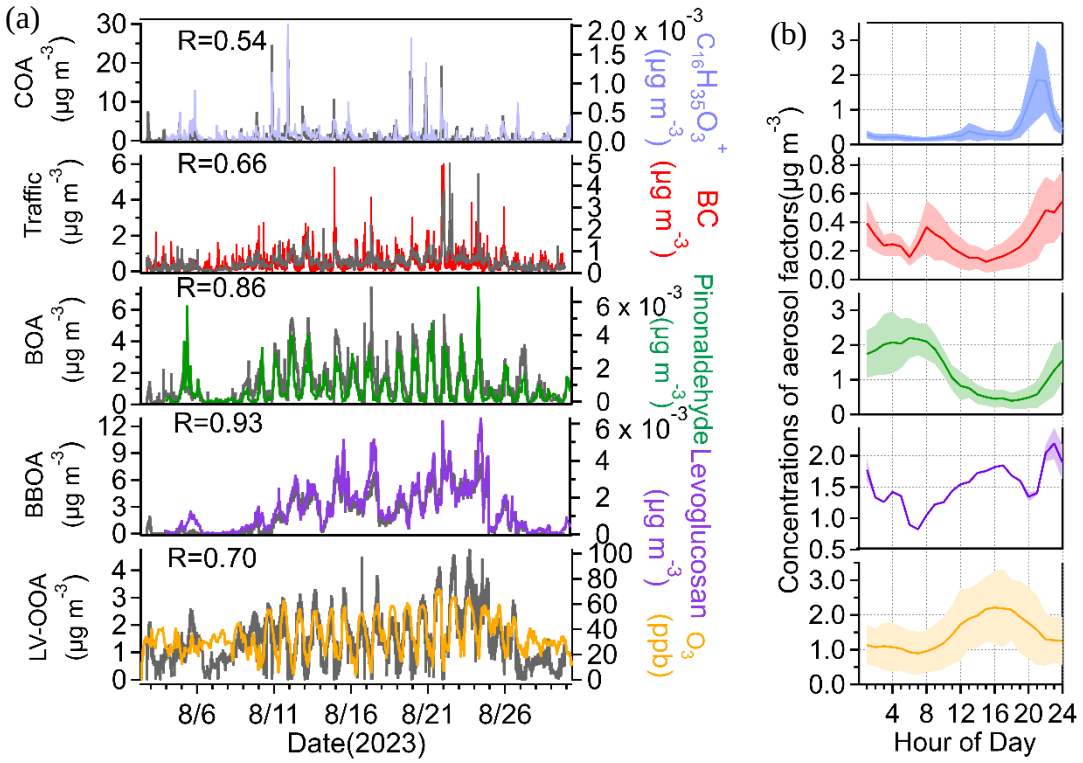

Figure 37. Source apportionment of OA in summer measured by the AMS. (a) Time series of OA factors – cooking OA(COA), hydrocarbon-like OA (HOA), biogenic secondary OA(BOA), aged biomass burning OA (BBOA), and low-volatility oxygenated OA (LV-OOA) and external tracer species (fatty acid, pinon aldehyde and levoglucosan, BC, and O_3. (b) Median diurnal variations in OA factors.

In winter, I identified all the factors using the same method as in summer. The difference is that the traffic diurnal cycle (Figure 38) exhibits distinct peaks during the morning and evening rush hours. Fresh BBOA shows an evening peak, indicating evening residual heating activities. Aged BBOA is characterized by its correlation with $C_6H_7O_5^+$, which I identified as an oxidation product of BBOA in the CHARON-PTR-MS section. Its diurnal pattern is very flat, suggesting it may be associated with regional background levels or long-range transport. For LVOOA, NH_4^+ is used as an indicator, as it correlates strongly with inorganic aerosol during autumn and winter (Freney et al., 2011).

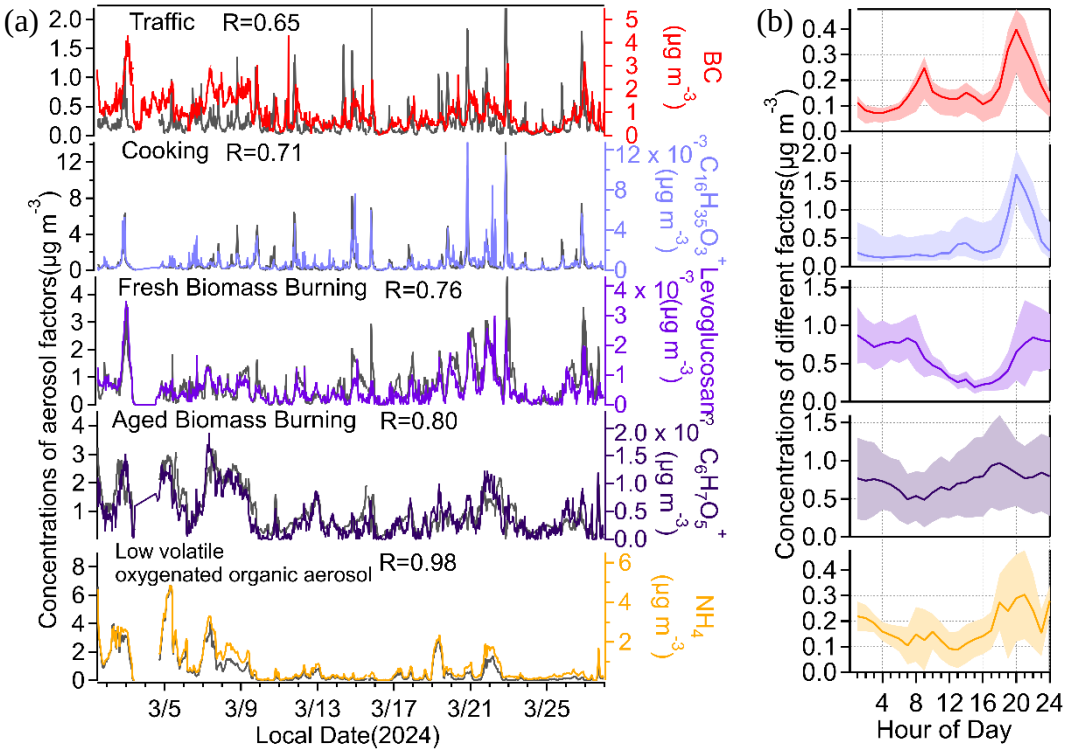

Figure 38. Source apportionment of OA in winter/spring measured by the AMS. (a) Time series of OA factors -traffic OA, cooking OA(COA), fresh biomass burning aerosol (BBOA), aged biomass burning aerosol (BBOA), and low-volatile oxygenated OA (LV-OOA) and external tracer species (BC, fatty acid $C_{16}H_{35}O_3^+$, Levoglucosan, $C_6H_7O_5^+$, and ammonium aerosol NH_4^+). (b) Median diurnal variations in OA factors.

In summer, OA contributions are as follows: traffic 8±8%, cooking 11±13%, BOA 22±14%, aged BBOA 25±21%, and LVOOA 33±20%. In winter, the contributions are: traffic 5±4%, cooking 12±12%, fresh BBOA 13±9%, aged BBOA 36±12%, and LVOOA 33±17%. In spring, the contributions are: traffic 9±7%, cooking 19±16%, fresh BBOA 27±17%, aged BBOA 37±19%, and LVOOA 9±10% (Figure 39).

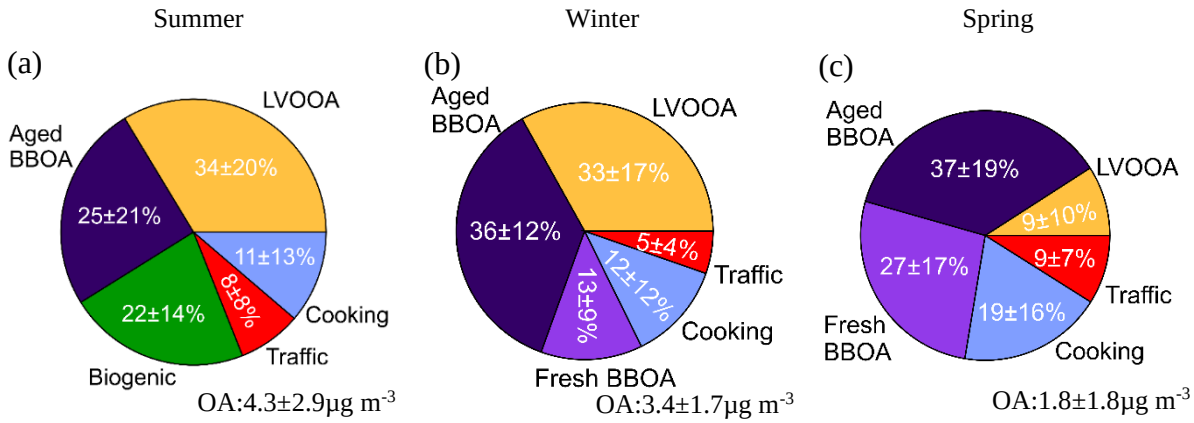

Figure 39. The relative mass contribution of every organic aerosol (OA) factor to total OA concentrations in (a) summer (traffic, cooking, aged biomass burning, biogenic and low-volatile oxygenated OA),(b) winter, and (c) spring (traffic, cooking, Fresh biomass burning, aged biomass burning and low-volatile oxygenated OA).

3.2.3 Sources of semi-volatile organic aerosol particles

This study excluded abundant ions that could skew results and very low ion signals with minimal impact. The average semi-volatile organic aerosol concentration was 0.3±0.2 μg m^{-3} in summer, 0.14 ± 0.08 μg m^{-3} in winter, and 0.07 ± 0.07 μg m^{-3} in spring. Through a comprehensive analysis of factor profiles, diurnal variations, and tracer correlations in summer (Figure 40, S9 and Table S8) and in winter (Figures 41, S10 and Table S9). Five SVOA factors were identified as the most interpretable solution for both summer and winter campaigns.

In summer, the first factor showed distinct signals from primary oxidation products of terpenes, including oxidized molecules of monoterpenes $C_{10}H_{15}O_1^+$ (R=0.93) and $C_{10}H_{17}O_1^+$ (R=0.89) (Li et al., 2020a). While the expected monoterpene oxidation products are typically $C_9H_{15}O_{1\text{-}5}^+$, I found that $C_9H_{13}O_1^+$ and $C_9H_{13}O_2^+$ also correlated well with this factor, with correlation coefficients R=0.91 and R=0.85, respectively. This suggests that the $C_9H_{15}O_{1\text{-}2}^+$ compounds may lose hydrogen, forming $C_9H_{13}O_1^+$ and $C_9H_{13}O_2^+$ (Gkatzelis et al., 2018b). Additionally, nitrogen-containing species like $C_9H_{13}N_1O_1$, $C_9H_{12}N_1O_2$, and $C_9H_{13}N_1O_5$ displayed strong signals and significant correlation with this factor, which may indicate they are fragments of monoterpene-derived organic nitrates, such as $C_9H_{15}N_1O_{5\text{-}7}$ (Massoli et al., 2018). The diurnal cycle shows a nighttime peak (Figure 40b). Therefore, I have attributed to terpene oxidation OA also based on the presence of a monoterpene oxidation tracer and the observed diurnal pattern.

The second factor includes clear markers of isoprene oxidation products, specifically $C_5H_8O_n$ species (Li et al., 2020a), with $C_5H_9O_6^+$ (R=0.83) and $C_5H_9O_3^+$ (R=0.82) showing strong correlations (Riva et al., 2016). Additionally, the ion with the highest fraction, $C_3H_5O_4^+$

(R=0.85), likely originates from the oxidation of ISOPOOH (Rios, 2018). However, benzoic acid $C_7H_7O_2^+$ (R=0.95), showing a strong signal, and phthalic anhydride $C_8H_5O_3^+$ (R=0.83) are both known emissions from biomass burning aerosols (Bruns et al., 2017; Koss et al., 2018). $C_6H_8O_5$ (R=0.84) (Molteni et al., 2018) is an oxidation product of benzene, while $C_7H_{10}O_6$ (R=0.84) as reported by Nakao et al. (Nakao et al., 2011a), is an oxidation of o-cresol, an emission from oxygenated aromatic BBOA. Therefore, I define this factor as mixed oxidized isoprene OA and BBOA.

The third factor was identified as BBOA due to its strong correlation (R=0.88) with vanillic acid $C_8H_8O_4$ (Fleming et al., 2020) and its prominent fragment ($C_8H_6O_4$) with even higher correlation (R=0.96), which constitutes a significant portion of this factor. Additionally, another BBOA tracer, syringic acid ($C_9H_{10}O_5$) (Wan et al., 2019), and its fragment ($C_9H_6O_3$, R=0.95), likely formed by the loss of two H_2O molecules, or as a direct BBOA emission (Fleming et al., 2020), further support this identification. Other ions, such as $C_6H_6O_5$ and $C_7H_8O_5$, are oxidation products of guaiacol (Yee et al., 2013b). The diurnal cycle of this factor, peaking during the daytime, suggests that agricultural activities or barbecue events may be contributing sources during the summer.

The fourth factor shows no correlation with other compounds and exhibits a distinct nighttime peak (Figure 40b). However, it correlates strongly with nitrate detected by AMS (R = 0.71). This suggests that the factor represents regional background, with its nighttime increase likely influenced by local accumulation effects and boundary layer dynamics.

The fifth factor was identified as more oxidized monoterpene OA, comprising highly oxidized monoterpene products such as $C_{10}H_{15}O_{3\text{-}5}^+$ (R=0.86, 0.85, 0.84), diacetin $C_7H_{13}O_5^+$ (R=0.79), oxidized molecules of monoterpenes $C_8H_{13}O_2^+$ (R=0.81), $C_8H_{13}O_4^+$ (R=0.80), and its fragment ($C_8H_{11}O_3^+$, R=0.83). Compounds like $C_9H_{13}O_{3\text{-}4}^+$ (R=0.81, 0.78) likely arise from fragments of the $C_9H_{14}O_n$ series, representing more oxidized monoterpene products that have lost hydrogen. Compared to the diurnal pattern of less oxidized terpene products, this factor's peak displays a delay, suggesting that primary oxidation products form initially and then undergo further oxidation, resulting in more oxidized BOA.

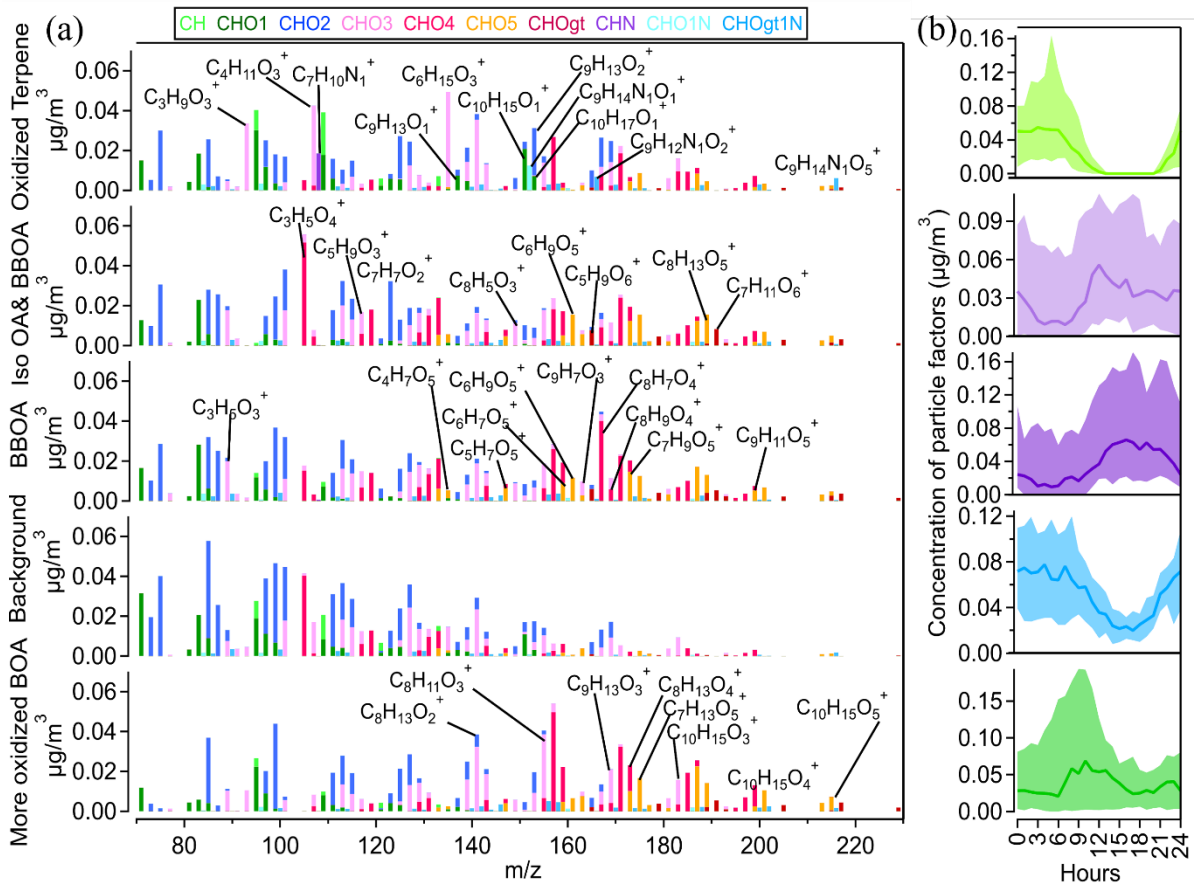

Figure 40. (a) Normalized SVOA factor spectra from PMF analysis and characteristic mass /z peaks in summer; (b) Median diurnal variations in SVOA factors during summer time

For the winter, the first factor is identified as night-time aged BBOA due to the presence of distinct BBOA tracers, $C_6H_6N_1O_4^+$ and $C_7H_8N_1O_4^+$ (Figure 41a), which do not appear in the mass spectra of other factors. Nitrocatechols ($C_6H_5N_1O_4$) originates from anthropogenic activities, including biomass burning and vehicle emissions. Meanwhile, methyl-nitrocatechos ($C_7H_7N_1O_4$) are specific markers for BBOA, as they are formed from m-cresol released during biomass combustion and diesel exhaust (Kourtchev et al., 2016). These tracers also exhibit the same strong correlation of 0.97 with this factor (Table S9). Syringic acid ($C_9H_{10}O_5$) also correlates well (R=0.70) with this factor. Its daily cycle did not show peaks during morning or evening rush hours; instead, a peak was observed around 8 p.m., suggesting it aligns more with biomass burning in the evening. This factor showed a strong correlation with highly oxidized nitrogen-containing compounds and secondary organic aerosols (syringic acid). This factor is more related to highly oxidized nitrogen-containing secondary organic aerosols, indicating that nitrogen-containing compounds are produced by BBOA. Therefore, I identified it as night-time aged BBOA.

The second factor was characterized by a high fraction of oleic acid $C_{18}H_{35}O_2^+$ (R=0.90), $C_{16}H_{35}O_3^+$ ($C_{16}H_{33}O_2(H_2O)^+$) (R=0.88), $C_{16}H_{33}O_2^+$ corresponding to palmitic acid (R=0.54), and $C_{16}H_{31}O_1^+$ is the fragment of $C_{16}H_{33}O_2^+$ (R=0.54). $C_{18}H_{34}O_2$ is identified as the cooking tracer oleic acid, while $C_{16}H_{33}O_2^+$ serves as another cooking aerosol tracer, corresponding to palmitic acid (Reyes-Villegas et al., 2018; Wang et al., 2020; Huang et al., 2021). $C_{16}H_{31}O_1^+$ is thought to originate from $C_{16}H_{33}O_2^+$ due to fragmentation involving the loss of one H_2O molecule. These findings strongly suggest that this factor represents cooking aerosol.

The third factor was identified as aged combustion. In this factor, the aromatic hydrocarbon $C_7H_9^+$ accounts for a relatively higher fraction and exhibits a strong correlation (R = 0.79). Although $C_8H_{13}^+$ does not contribute as significant as $C_7H_9^+$, it also shows the same strong correlation. These compounds are attributed to combustion sources (Wang et al., 2022). The ion $C_7H_{10}N_1^+$, potentially a fragment of acridine ($C_7H_{12}N_1^+$) originating from coal combustion (Wang et al., 2021a), exhibits a distinct signal and the highest correlation (R = 0.94). Similarly, $C_6H_{15}O_3^+$ (R = 0.93) corresponds to 2-methoxyethyl ether (MXEE), a product of fuel combustion. Monoterpene oxidation products, such as $C_{10}H_{17}O_1^+$ (R = 0.86) and $C_9H_{13}O_1^+$ (R=0.82), are also observed. This is likely because monoterpenes, serving as biofuel components in engines and boilers, form oxidized monoterpene products when combusted and oxidized (Philippe Dagaut et al., 2024). Additionally, benzocaine $C_9H_{12}N_1O_2^+$ exhibits strong correlation (R = 0.80) with this factor and is likely a product of oxidized combustion processes.

The fourth factor has C_6 carboxylic acids ($C_6H_7O_5^+$) which is the phenol oxidation products with OH radicals in the low-NOx system, and $C_7H_9O_5^+$ denoted as the third-generation guaiacol with OH adduct. Propanedioic acid $C_3H_5O_4^+$, pentanedione $C_4H_5O_3^+$, and 2-oxopentanedioic acid $C_5H_7O_4^+$ are fragments derived from the OH oxidation products of biomass burning VOC (BBVOC) such as guaiacol and syringol (Yee et al., 2013b). Additionally, $C_6H_6O_2$ is an OH radical oxidation product from phenol. A higher fraction of 2,5-di-(hydroxymethyl)furan $C_6H_9O_3^+$ was observed, which may result from $C_6H_7O_2^+$ binding with a water molecule. These photochemical products, formed from BBVOC oxidation by OH radicals, confirm that this factor represents aged BBOA. All the aforementioned ions exhibit a strong correlation of approximately 0.85 with this factor, as shown in Table S9. Furthermore, its diurnal pattern, with a peak at 15:00 during the day, leads to its identification as day-time aged BBOA.

The fifth factor shows a very strong correlation with stearic acid $C_{18}H_{37}O_2^+$ (R = 0.95), $C_{16}H_{33}O_2(H_2O)^+$ (R = 0.91), $C_{18}H_{15}O_1^+$ (R = 0.90), $C_{19}H_{15}O_1^+$ (R = 0.88), and oleic acid $C_{18}H_{35}O_2^+$ (R = 0.88). However, these compounds do not account for significant fractions in

this factor's mass spectrum as they do in factor 2's mass spectrum. Notably, trimethoxy methane $C_4H_{11}O_3^+$ is a key ion in this factor but contributes minimally to others and shows no correlation with the factor (R = 0.02). While the composition includes unrelated compounds, its strong correlation with sulfate detected by AMS (R=0.74) suggests a regional background origin, with the nighttime peak indicating local accumulation effects related to boundary layer dynamics.

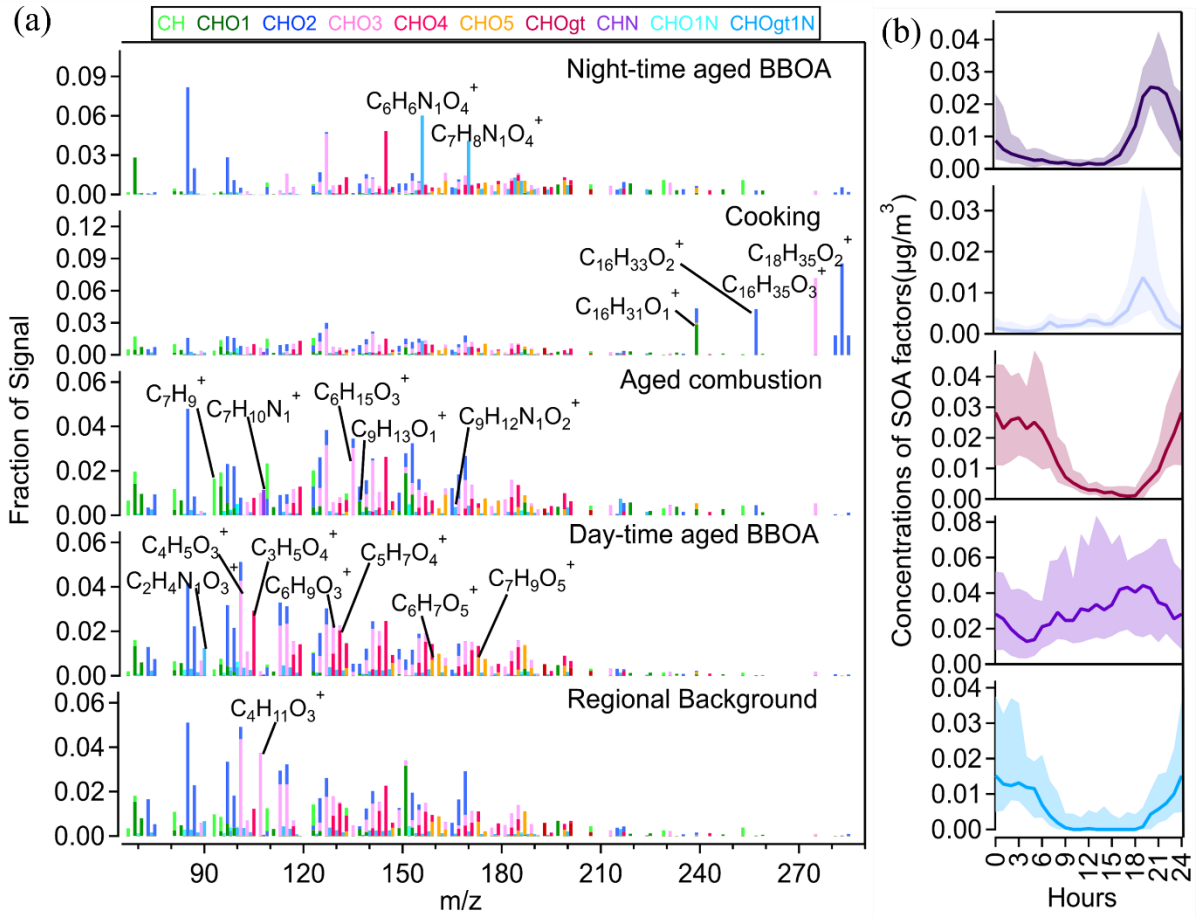

Figure 41. (a) Normalized SVOA factor spectra from PMF analysis and characteristic mass /z peaks in winter; (b) Median diurnal variations in SVOA factors during winter time

During summer, the composition of SVOA includes 11±15% weakly oxidized monoterpene OA, 16 ± 15% oxidized isoprene & BBOA (mixture of oxidized isoprene OA and BBOA), 25 ± 21% BBOA, 30 ± 22% attributed to regional background sources, and 18 ± 16% to highly oxidized monoterpene OA (Figure 42). In winter, nighttime aged BBOA accounts for 10 ± 9%, cooking OA contributes 4 ± 5%, aged combustion OA makes up 9 ± 10%, daytime aged BBOA constitutes the largest fraction at 55 ± 21%, and regional background sources contribute 23 ± 17%. In spring, nighttime aged BBOA accounts for 12 ± 12%, cooking OA contributes 11 ± 12%, aged combustion OA makes up 24 ± 18%, daytime aged BBOA constitutes the largest fraction at 46 ± 25%, and regional background sources contribute 7 ± 9%.

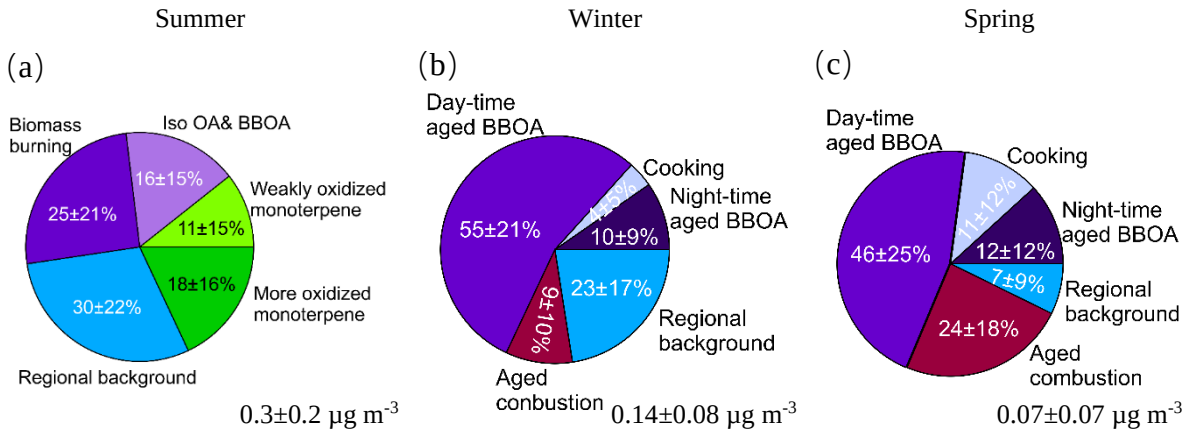

Figure 42. The relative contribution of each semi volatile organic aerosol (SVOA) factor to total SVOA concentrations in (a)summer (isoprene mixed with biomass burning, biomass burning, weakly oxidized monoterpene and more oxidized monoterpene OA), (b) winter and (c) spring (cooking, day-time aged biomass burning, night-time aged biomass burning, aged combustion and regional background OA).

3.3.4 Sources of VOC

The average VOC mixing ratio is 3.4±1.0 ppb in summer, 2.1±0.7 ppb in winter, and 3.4 ±1.7 ppb in spring. This study thoroughly examined factor profiles, diurnal patterns, and correlations with tracers (Figure 43, S11, and Table S10) in summer and in winter (Figures 44, S12, and Table S11). Five factors were identified based on measured VOC as the optimal interpretable solutions for summer and winter, respectively.

In summer, the first factor was characterized by high contributions and strong correlations with aromatic hydrocarbon ions, such as $C_7H_9^+$ (m/z 93.07), $C_8H_{11}^+$ (m/z 107.086), and $C_9H_{13}^+$ (m/z 121.102). These compounds correspond to toluene, xylenes, and C_9-aromatics, commonly used as vehicular emission markers (Squires et al., 2020; Jain et al., 2022). I assigned it to traffic VOC. These ions show a correlation coefficient (R) of approximately 0.9 with traffic emissions (Table S10). According to the diurnal profiles of traffic (Figure 41) in summer, it shows distinct peaks during morning and evening rush hours.

The second factor was classified as weakly oxidized BVOC. It was identified by oxidation products of monoterpenes, specifically $C_9H_{15}O_1^+$ myrcenol (m/z 139.112), $C_{10}H_{13}O_1^+$ carvone (m/z 149.097), weakly-oxidized molecules of monoterpenes $C_{10}H_{15}O_1^+$ (m/z 151.112), $C_{10}H_{17}O_1^+$ (m/z 153.128) and $C_{10}H_{15}O_2^+$ (m/z 167.107) (Li et al., 2020a). These ions show strong correlations with the Oxidized BVOC factor, with R values of 0.93, 0.93, 0.93, 0.91, and 0.87, respectively. Oxidized BVOC have a nighttime peak in the diurnal profile and drop to nearly zero by noon, likely due to enhanced dilution and quicker oxidation to higher oxidation states not detectable by PTR-MS.

The third factor was identified as BVOC due to the predominance of $C_{10}H_{17}^+$ monoterpene (m/z 137.133) and its fragmentation $C_6H_9^+$ (m/z 81.07) ions in this VOC factor, with correlations of 0.98 and 0.86, respectively. Sesquiterpenes also show a strong correlation with this factor(R=0.80). The average diurnal behavior of BVOC shows an early morning peak, because BVOC, especially monoterpenes, are often stored in vegetation and released at the start of the morning due to sunlight and slight temperature increases (Malik et al., 2023).

The fourth factor showed a good correlation with butyric acid $C_3H_5O_3^+$ (m/z 89.024) and $C_4H_5O_3^+$ (m/z 101.024), with correlation coefficients of 0.75 and 0.72, respectively. The time series of O_3 and this factor showed a good correlation during certain periods. The diurnal cycle of it exhibits a daytime peak, indicating involvement in photochemical processes. I classified it as aged VOC.

The fifth factor, biomass burning VOC, is dominated by propylene glycol $C_3H_9O_2^+$ (m/z 77.06) and orthoacetic acid $C_2H_7O_3^+$ (m/z 79.039), with strong correlations of 0.85 and 0.83, respectively. Additionally, ring fragments of oxidized syringol molecules $C_4H_7O_4^+$ (m/z 119.034), and ring fragments of oxidized guaiacol and syringol molecules $C_5H_3O_2^+$ (m/z 95.013), $C_5H_7O_4^+$ (m/z 131.034) and $C_4H_7O_3^+$ (m/z 103.04) contribute smaller fractions but display even higher correlations, with values of 0.90, 0.91, 0.92 and 0.86 (Yee et al., 2013b). Compared with the other 4 factors, the biomass burning VOC mass spectrum shows more oxidized compounds.

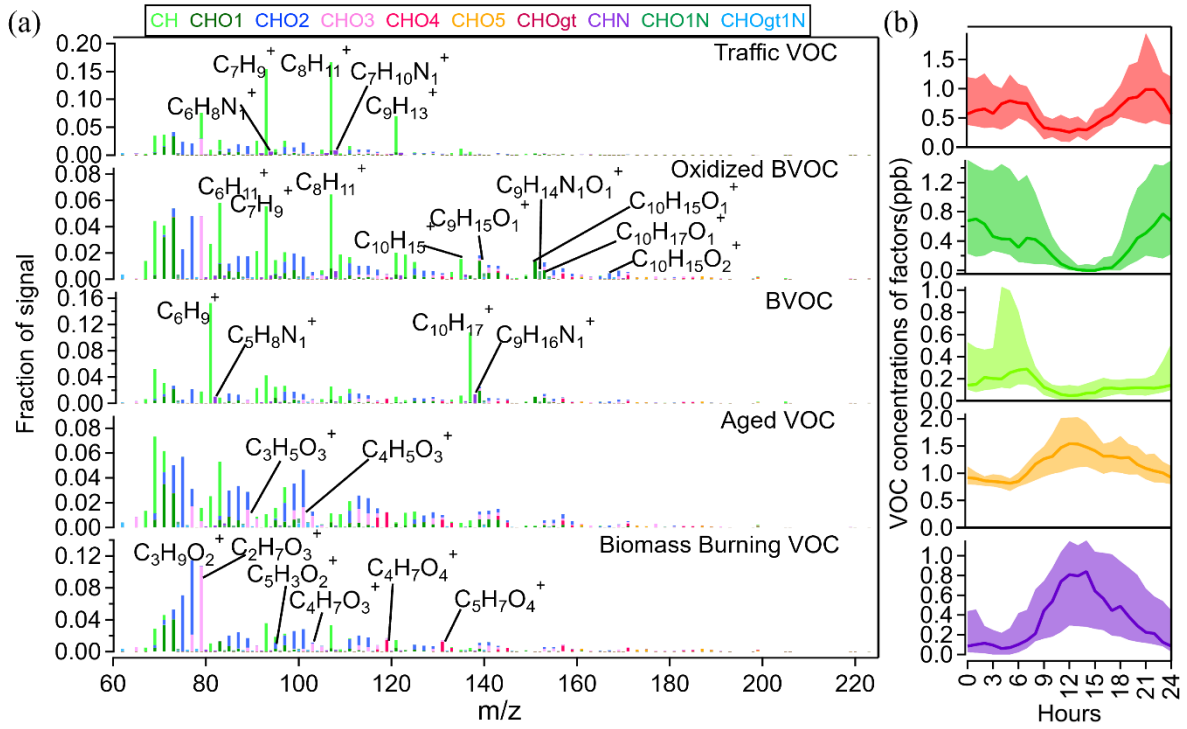

Figure 43. VOC source apportionment for summer time. (a) Normalized VOC factor mass spectra from PMF analysis and characteristic mass peaks in summer; (b) Median diurnal variations in VOC factors during summer time

In winter, the first factor was identified as traffic VOC using the same method as in summer, showing high contributions and strong correlations with aromatic hydrocarbon ions, including toluene $C_7H_9^+$ (m/z 93.07), C_9 aromatics $C_9H_{13}^+$ (m/z 121.102), and cymene $C_{10}H_{13}^+$ (m/z 133.102).

The second factor, classified as terpenes VOCs, was marked by the predominance of monoterpene $C_{10}H_{17}^+$ (m/z 137.133) and its fragment $C_6H_9^+$ (m/z 81.07) ions with correlations of 0.90 and 0.89, respectively. Sesquiterpenes also show a strong correlation (R=0.92). The diurnal variation shows both morning and evening peaks, with the morning peak being higher than the evening peak. This pattern differs from typical traffic trends. This pattern is similar to that of limonene from shower gels (Yeoman et al., 2020), which shows higher concentrations in the morning compared to the evening. It correlates with the traffic factor because people typically shower in the morning before leaving home, leading to higher detection. By the evening, the limonene has dissipated.

The third factor included a lot of smaller oxygenated VOC (OVOC) such as 1,3-propanediol $C_3H_9O_2^+$ (m/z 77.06), acetic anhydride $C_4H_7O_3^+$ (m/z 103.04), 2-furoic acid $C_5H_5O_3^+$ (m/z 113.024), maleic acid $C_4H_5O_4^+$ (m/z 117.019), succinic acid $C_4H_7O_4^+$ (m/z 119.034), benzoic acid $C_7H_7O_2^+$ (m/z 123.045) (Lemieux et al., 2004) and salicylic acid $C_7H_7O_3^+$ (m/z 139.04). They all show strong correlations (R=0.85-0.90) with this factor. Notably, $C_5H_5O_3^+$ and

$C_7H_7O_3^+$ are recognized as tracers of biomass burning VOC (Li et al., 2020b; Romanias et al., 2024). It displays a peak during the daytime, possibly due to biomass burning activities in certain areas (e.g., cooking or outdoor grilling), which increase VOC emissions and lead to a daytime peak in the VOC diurnal profile. I classify this factor as biomass burning VOC.

The fourth factor was dominated by xylene, represented by C_8-aromatic hydrocarbon $C_8H_{11}^+$ (m/z 107.086), with a correlation of 0.96. This factor also shows a strong correlation with 3-ethyl-pyridine $C_7H_{10}N_1^+$ (m/z 108.081) and the C_9-aromatic hydrocarbon VOC $C_9H_{13}^+$ (m/z 121.102), with correlations of 0.98 and 0.91, respectively. Xylene and trimethylbenzene are components of flue gases from fossil fuel combustion VOC (Niu et al., 2021). It also displays morning and evening peaks in its diurnal cycle, leading to its identification as a traffic2 VOC factor.

The fifth factor has minimal correlation with most masses, only showing a correlation of 0.73 with benzene ($C_6H_7^+$) and weak correlations with various oxygenated compounds. Therefore, this factor may originate from different low-concentration emission sources. Its diurnal variation shows a small evening peak, likely influenced by minor traffic or industrial emissions. This factor accounts for 31% (Figure 43), and as background VOC are commonly found to have a high fraction, I classify it as background VOC.

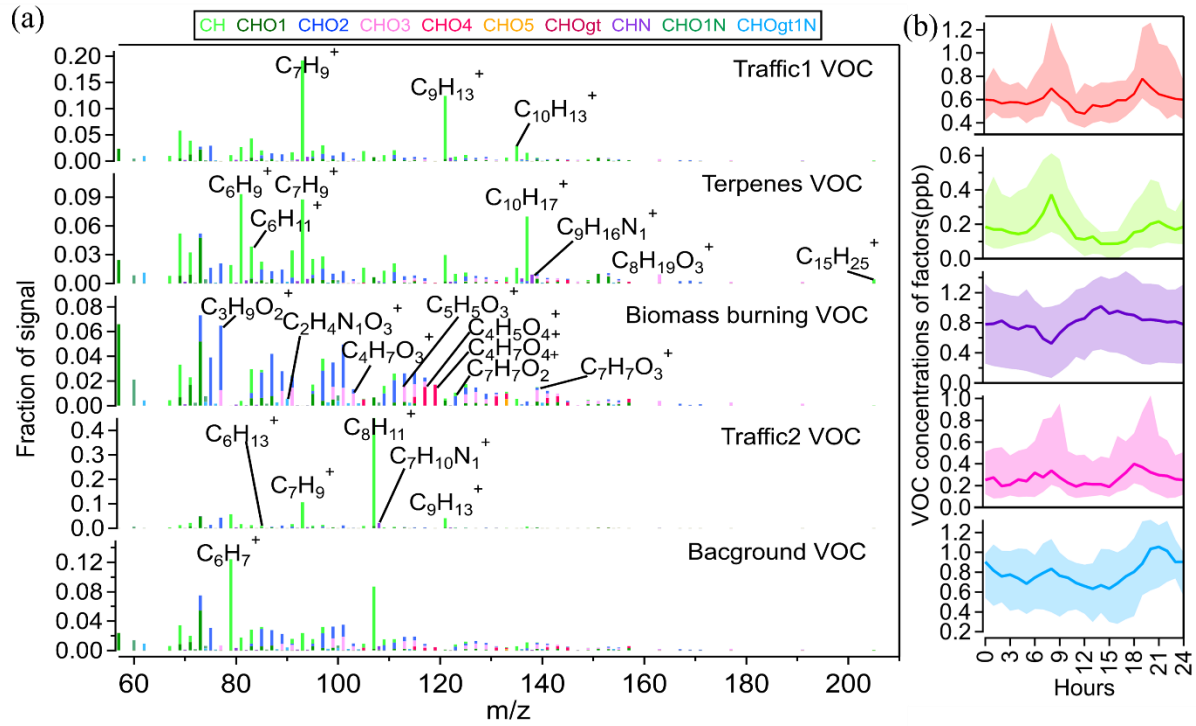

Figure 44. (a) Normalized VOC factor spectra from PMF analysis of PTR-MS data and characteristic mass/z peaks in winter; (b) Median diurnal variations in VOC factors during winter and spring time in Munich.

The source contributions of VOCs vary significantly across seasons, reflecting shifts in emission patterns and atmospheric conditions. In summer, the largest contributor is aged VOC at 42±18%, indicating the dominance of secondary pollutants formed through atmospheric photochemical processing. Traffic emissions account for 22±14%, while oxidized biogenic VOCs (BVOCs) make up 13±13%, and fresh BVOCs contribute 7±7%. Biomass burning plays a notable role at 16±15%, likely due to outdoor barbeque in warmer months. Winter exhibits a different profile, with background sources dominating at 54±9%, suggesting stable atmospheric conditions. Traffic-related emissions split into two categories—traffic1 (26±6%) and traffic2 (7±6%)—possibly reflecting different vehicle types or fuel usage patterns. Monoterpene VOCs remain low (4±4%), consistent with reduced biogenic activity and from anthropogenic source like personal care products (Wu et al., 2024), while biomass burning contributes 8±6%, potentially from residential heating. In spring, the contributions are traffic1 22±7%, monoterpene VOC increased to 9±9% as vegetation becomes more active, biomass burning VOC 33±14%, traffic2 13±8%, and background 23±16% (Figure 45). 3.4±1.0 ppb in summer, 2.1±0.7 ppb in winter, and 3.4 ±1.7 ppb in spring.

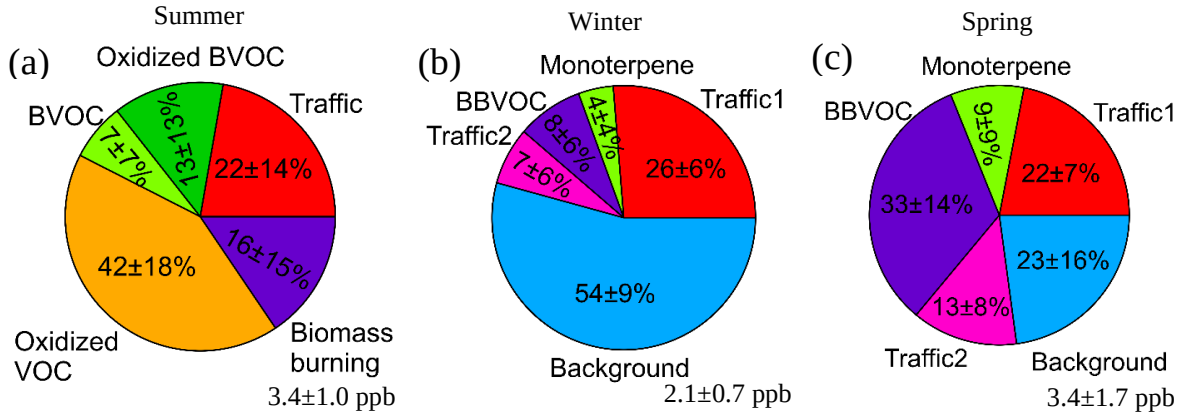

Figure 45. The relative contribution of each VOC factor to total VOC concentrations in (a) summer (traffic, biogenic, oxidized biogenic, biomass burning and oxidized VOC factors), (b) in winter and (c) in spring (traffic1, traffic2, monoterpene, biomass burning (BBVOC) and background VOC factors).

3.3.5 Extreme pollution events

In my work, I aim to investigate the influence of VOC on aerosol particles. To achieve this, I selected representative periods characterized by higher pollution events from both campaigns in Munich for a more detailed analysis. From August 10th to 25th, elevated pollution levels and several particle growth events were observed. Notably, these ultrafine particle growth events predominantly occurred for lower BLH during nighttime hours (Figure 46d and 46e). Traffic-related VOCs, BVOCs and OBVOCs all increased when BLH decreased. Especially traffic-related VOCs was stronger affected by BLH, increasing as BLH decreased. This pattern

suggests that shallow boundary layers enhance the accumulation of these VOC factors near the surface by limiting vertical dispersion. BVOCs and OBVOCs consistently peaked during ultrafine particle growth events, which exclusively occurred when BLH was already low. During these periods, traffic-related VOCs showed decreasing trends, while BBVOCs and Aged VOCs reached their daily minimum levels. This observation strongly indicates that BVOCs and OBVOCs were the dominant contributors to ultrafine particle growth. Increasing in BVOCs and OBVOCs coincide with decreasing ozone (Figure 46d), suggesting rapid reactions between monoterpenes and O_3 that drive ultrafine particle growth. In contrast, BBVOCs and aged VOCs (Figure 46c) decrease during growth events and show peaks around noon, indicating they are not associated with nighttime particle growth. The toluene/benzene and xylene/benzene ratios exhibited relatively stable trends in most cases (Figure 46a), suggesting a predominant and consistent influence from vehicular emissions. This stability aligns with findings from (Nakhjirgan et al., 2024), where similar ratio patterns were attributed to traffic-related sources. However, occasional sharp increases in these ratios were observed, particularly when the total traffic-related VOC concentration approached near-zero levels. These ratio spikes likely occurred not due to actual increases in toluene or xylene emissions, but rather because benzene concentrations dropped to extremely low levels, causing the ratios to mathematically inflate. This phenomenon could result from temporary reductions in benzene-rich emission sources (e.g., reduced traffic during specific hours) or enhanced atmospheric oxidation of benzene under daytime.

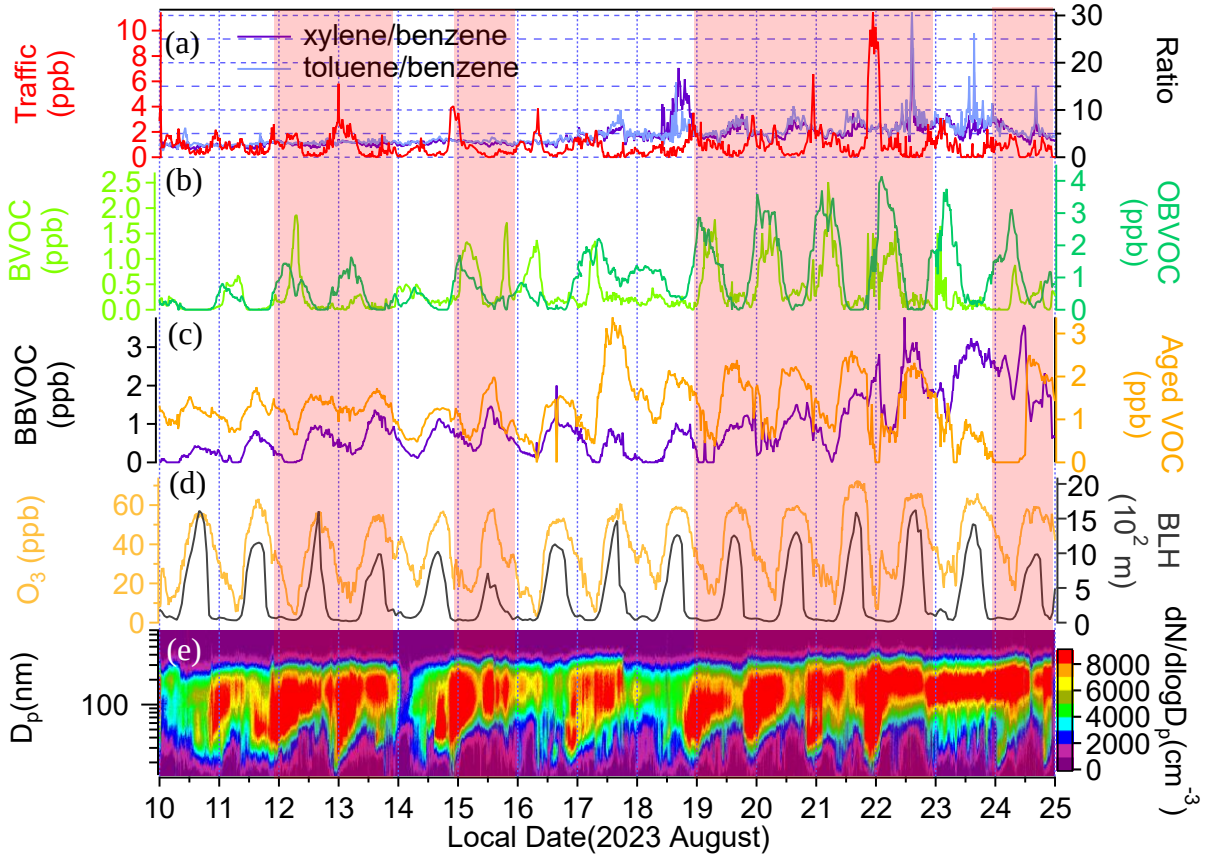

Figure 46. Traffic VOC and ratios of toluene to benzene and xylene to benzene (a), mixing ratio of isoprene, monoterpene and sesquiterpene (b), BBVOC factor (c), O_3 and BLH (d) and particle size distributions (e). (pink shaded area indicates days with particle growth events)

Table 4 Correlation (R) between VOC species and different size range ultrafine particle concentration numbers from 19th to 22nd August 2023

Correlation	7-10 nm	10-30 nm	30-50 nm	50-100 nm
Traffic	**0.91**	**0.76**	**0.82**	**0.86**
Isoprene	**0.78**	**0.54**	**0.72**	**0.80**
Isoprene oxidation products	**0.78**	**0.49**	**0.60**	**0.67**
Monoterpene	0.28	0.13	0.17	0.31
Monoterpene oxidation products	0.32	0.16	0.21	0.32
Sesquiterpene	0.56	0.36	0.40	0.55

Figure 47 and Table 4 show that traffic-related VOCs correlated with ultrafine particles, as both peak during traffic hours (Figure 47a, 47d). Similarly, isoprene and its oxidation products follow the same pattern as traffic-related VOCs, both being affected by the decreasing BLH (Figure 47e). It indicates that isoprene and its oxidation products were mostly from traffic. However, ultrafine particle growth events occur after midnight, when traffic, isoprene, isoprene oxidation products, and ultrafine particles decline. In contrast, monoterpenes, their oxidation products, and sesquiterpenes (Figure 47b, 47c) increase and peak during particle growth events. They show weak correlations with ultrafine particles due to their correlations with particle

growth, not concentrations. Thus, summer nighttime particle growth is strongly influenced by monoterpenes and their oxidation products. This is in agreement with previous in Stuttgart and near Karlsruhe (Huang et al., 2019; Song et al., 2024b).

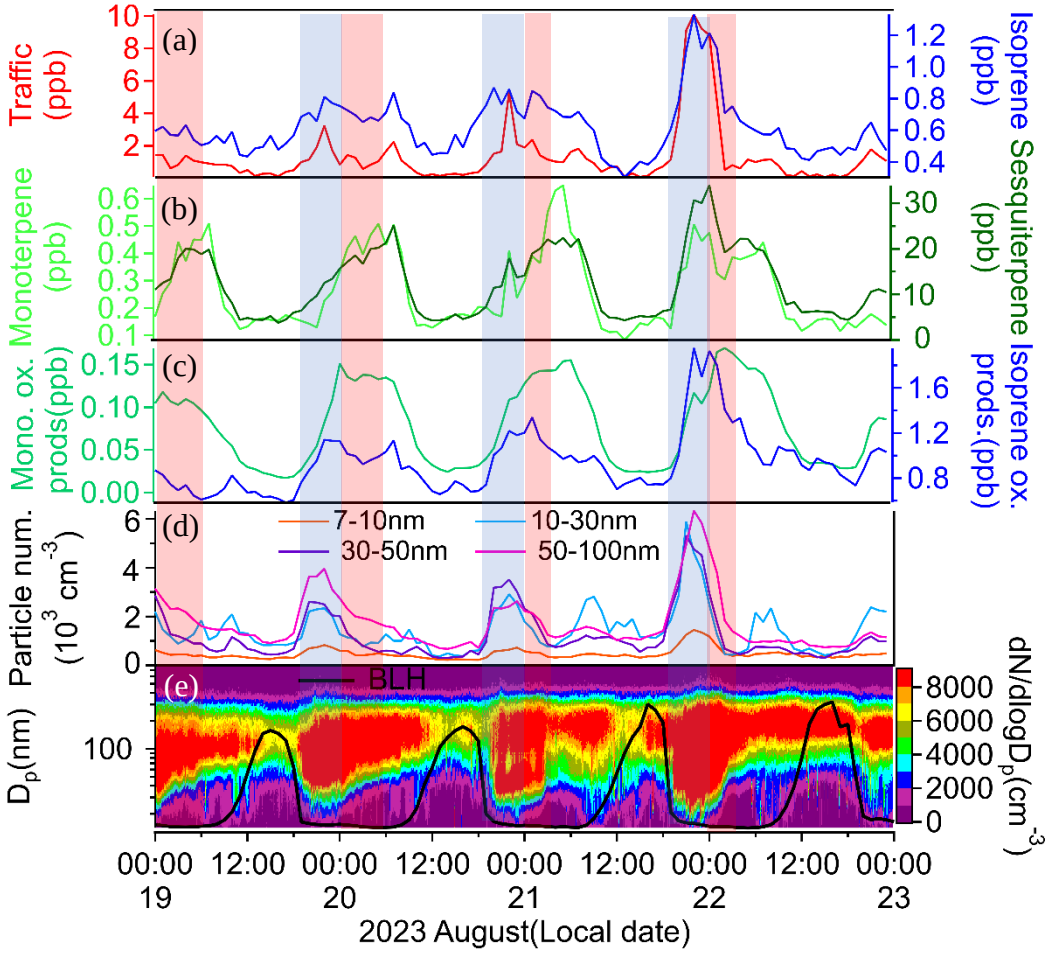

Figure 47. Traffic and isoprene concentration(a) monoterpene and sesquiterpene concentration(b) the sum of monoterpene oxidation products ($C_{10}H_{15}O_{1\text{-}3}^+$ and $C_{10}H_{17}O_{1\text{-}3}^+$) and isoprene oxidation products ($C_4H_7O_{1\text{-}4}^+$, $C_4H_9O_{1\text{-}3}^+$, $C_5H_9O_{1\text{-}4}^+$, $C_5H_{11}O_{1\text{-}3}^+$ and $C_5H_{13}O_2^+$) (c) particle numbers of 7-10nm, 10-30nm, 30-50nm and 50-100nm(d) size distribution of particle(e) from 19th to 22nd August 2023（Blue shade for ultrafine particle peak events and red shade for particle growth events）

The average toluene/benzene and xylene/benzene ratios during March 2024 were 1.8±1.1 and 2.1±1.3, respectively (Figure 48a), indicating VOC sources from aged air masses, with toluene, xylene, and trimethylbenzene primarily emitted by vehicles. Ratios exceeding 5 suggest contributions from fresh emissions (Kumar et al., 2018). Particle growth events were much less frequent in winter and spring than in summer. On March 15th, 20th, and 22nd, weak particle growth events occurred during shallow or decreasing BLH, accompanied by increasing VOC factors (Figure 48). Figure 49 and Table 5 illustrate that all tracers of the VOC factors exhibit peaks corresponding to the peaks in ultrafine particles, indicating that all of them influence

ultrafine particles in winter/spring time. But no VOC factor show any influence for the particle growth.

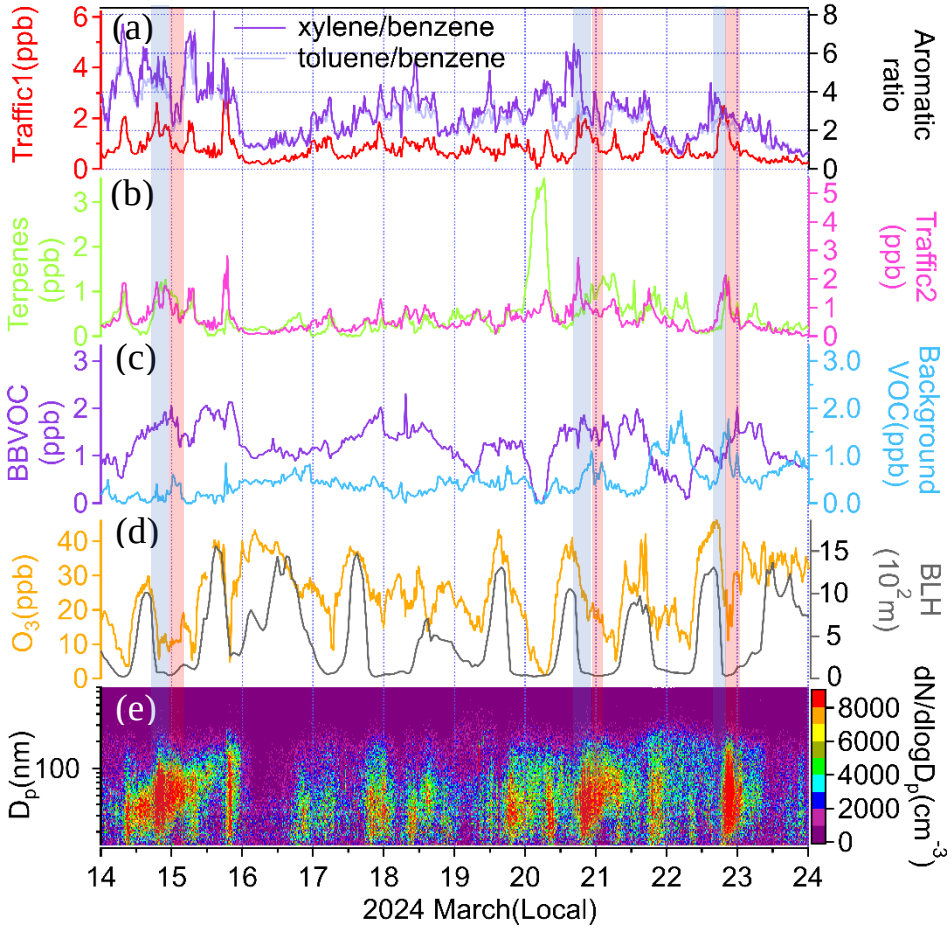

Figure 48. Evolutions of traffic VOC factor and ratio of toluene to benzene and xylene to benzene (a), mixing ratio of monoterpenes and sesquiterpenes (b), BBVOC factor (c), O3 and BLH (d) and size distribution of particle (e). (Blue shaded area indicates ultrafine particle peak events and red shaded area indicates particle growth events)

Table 5 Correlation (R) between VOC species and different size range ultrafine particle concentration numbers from 20th to 23rd March 2024

Correlation	14-30 nm	30-50 nm	50-100 nm
Toluene	**0.71**	**0.69**	**0.67**
C_9 aromatics	**0.70**	**0.66**	**0.62**
Monoterpene	0.29	0.28	0.33
Xylene	**0.66**	**0.68**	**0.65**
Salicylic acid	0.27	0.46	0.35
Benzene	0.49	0.46	0.48

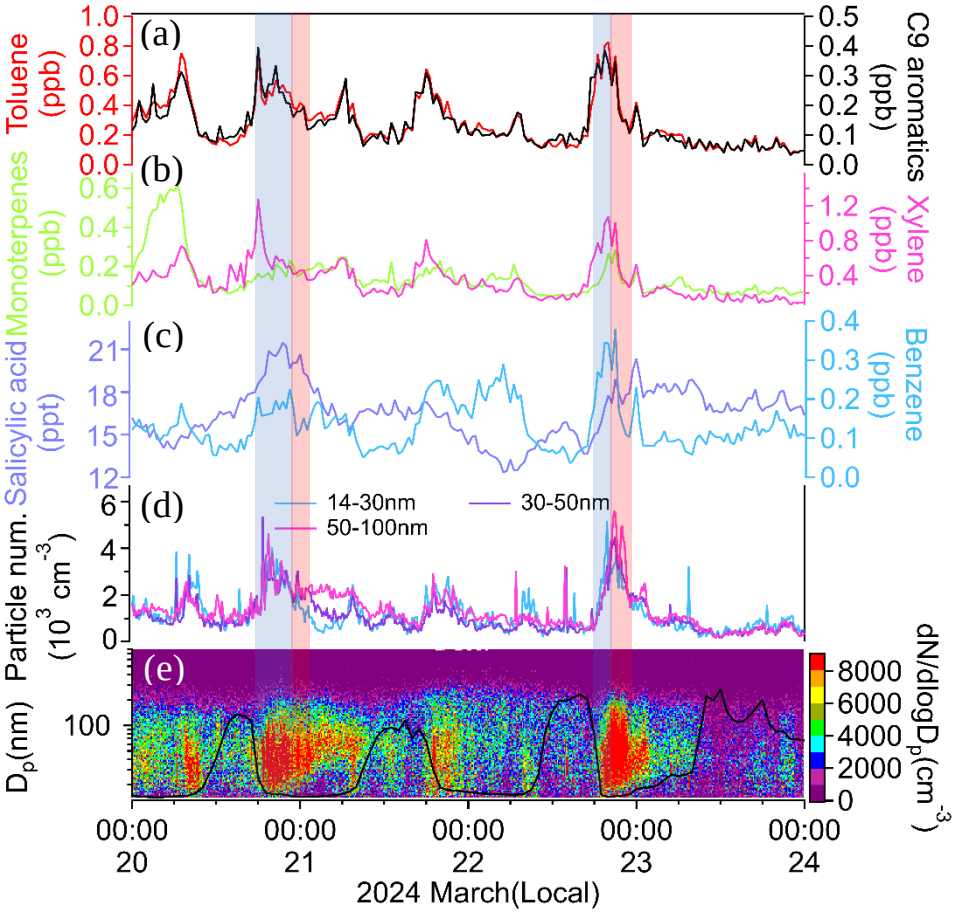

Figure 49. Traffic1 VOC factor tracers: toluene and trimethylbenzene (a) terpenes VOC factor tracer monoterpene and traffic2 tracer xylene(b) BBVOC factor tracer salicylic acid and regional background tracer benzene (c) particle numbers of 14-30nm, 30-50nm and 50-100nm(d) particle size distribution and BLH (e) from 20th to 23rd March 2024 (Blue shades indicate ultrafine particle peak events and red shades indicate particle growth events)

Figures 50 and 51 illustrate the influence of semi volatile organic aerosol (SVOA) factors on ultrafine particles during summer and spring, focusing on the same periods analyzed in Figures 47 and 49, which were selected due to their high frequency of ultrafine particle growth events. In summer, regional background, weakly oxidized monoterpene, and more oxidized monoterpene SVOAs increased during UFP growth events, suggesting that BVOCs play a role in nighttime UFP growth. In contrast, biomass burning related SVOA decreased during UFP growth events, confirming that biomass burning emissions had little influence on UFP formation in summer. In spring, only the regional background SVOA peaked during UFP growth events, reinforcing its role in particle growth. These observations highlight the seasonal shifts in dominant UFP growth sources, with biogenic and regional background SVOAs being more relevant in summer and only regional background SVOA in spring playing a more prominent role.

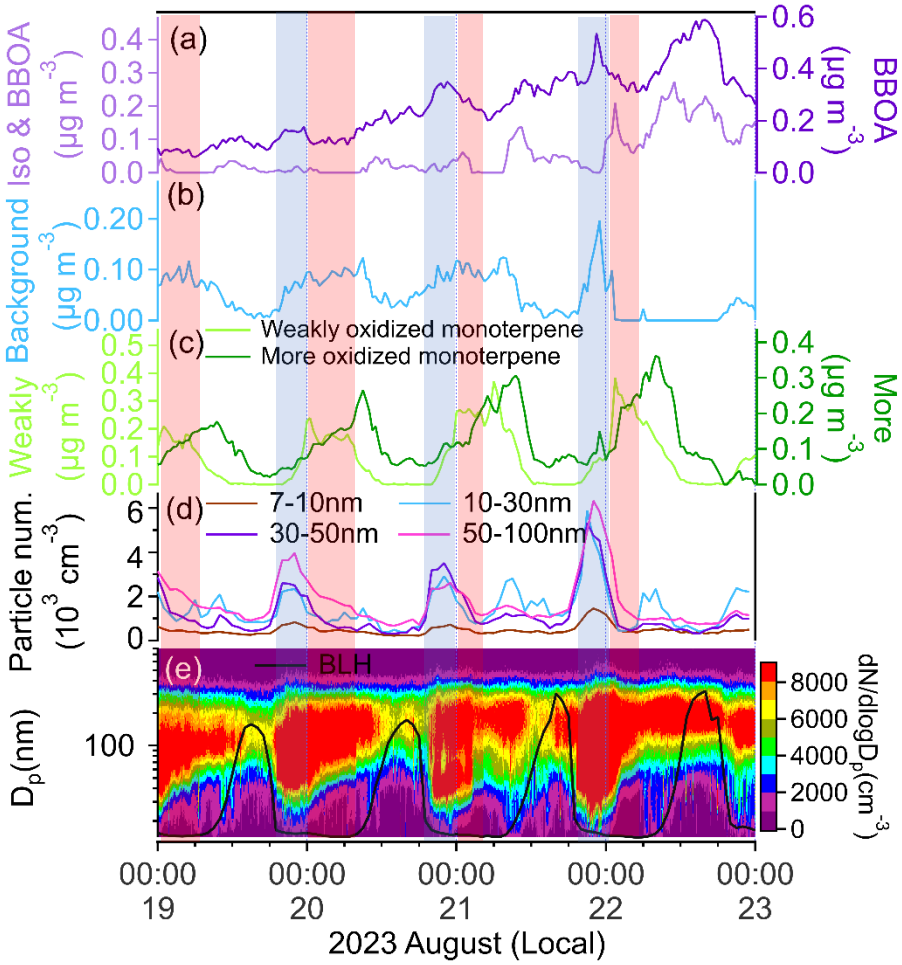

Figure 50**.** Evolution of semi-volatile organic aerosol of Iso OA & BBOA and BBOA(a), regional background (b), weakly and more oxidized monoterpene (c), particle numbers of 7-10nm, 10-30nm, 30-50nm and 50-100nm(d) size distribution of particle and BLH (e) from 19th to 22nd August 2023 (Blue shade for ultrafine particle peak events and red shade for particle growth events)

Table 6 Correlation (R) between SVOA factors and different size range ultrafine particle concentration numbers from 19th to 22nd August 2023.

Correlation	7-10 nm	10-30 nm	30-50 nm	50-100 nm
Weakly oxidized monoterpene	0.14	0.01	0.07	0.16
Iso & BBOA	-0.05	-0.11	-0.23	-0.28
BBOA	0.23	0.13	0.11	-0.02
Regional background	**0.42**	**0.41**	**0.50**	**0.55**
More oxidized monoterpene	-0.06	0.02	-0.19	-0.17

Table 7 Correlation (R) between SVOA factors and different size range ultrafine particle concentration numbers from 20th to 23rd March 2024.

Correlation	14-30 nm	30-50 nm	50-100 nm
Night-time aged BBOA	**0.59**	**0.65**	**0.64**
Cooking	**0.62**	**0.53**	**0.51**
Aged combustion	0.13	0.28	0.36
Day-time aged BBOA	0.11	-0.06	-0.03
Regional background	-0.06	0.17	0.20

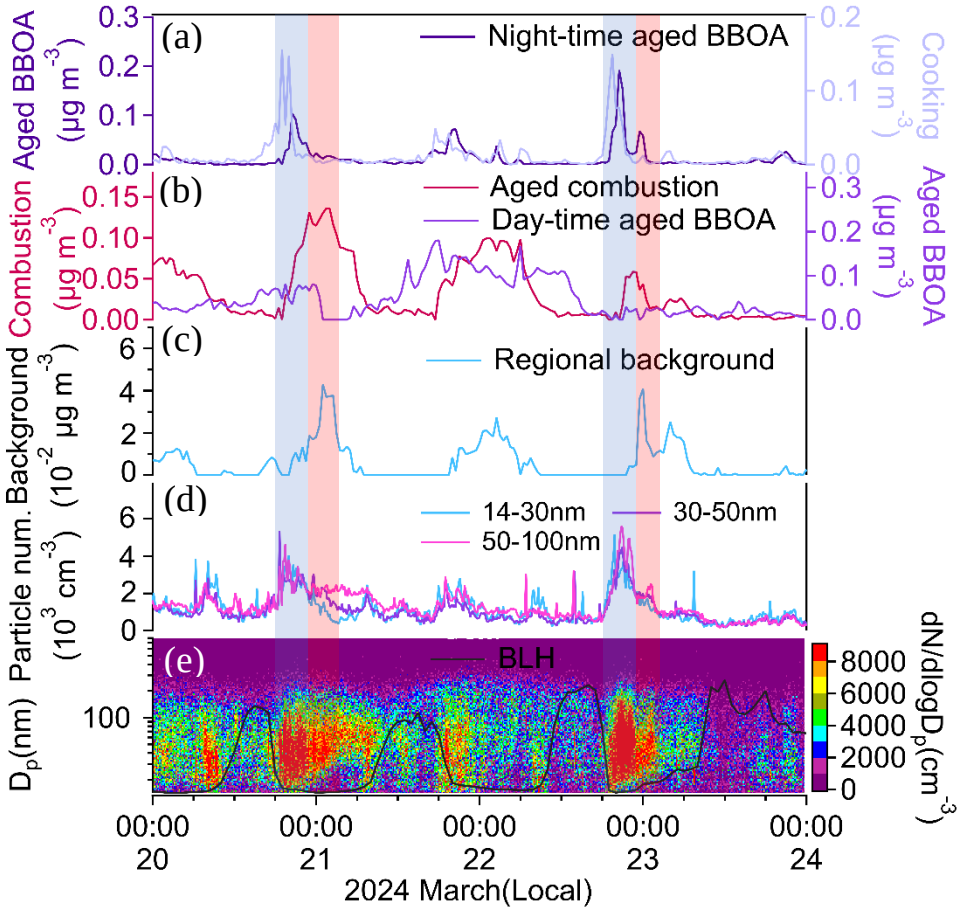

Figure 51. Evolution of semi-volatile organic aerosol of Aged BBOA and Cooking SVOA (a), Aged combustion and Day-time aged BBOA (b), Regional background SVOA (c), particle numbers of 14-30nm, 30-50nm and 50-100nm(d), and size distribution of particle and BLH (e) from 20th to 23rd March 2024（Blue shade for ultrafine particle peak and red shade for particle growth）

The analysis of SVOA-UFP correlations reveals distinct seasonal patterns in their relationships (Table 6 and 7). During summer, most SVOA factors showed weak or negative correlations with UFP concentrations across all size bins, with only the regional background factor demonstrating moderate positive correlations (0.42-0.55). These relatively low correlations suggest SVOAs played a limited role in UFP concentrations during summer, likely due to enhanced photochemical activity and atmospheric dilution reducing the influence of semi-volatile organics on particle nucleation and growth. In contrast, spring exhibited better correlations, particularly for night-time aged biomass burning SVOA (0.59-0.65 across size bins) and cooking SVOA (0.51-0.62), indicating these sources contributed more substantially to UFP concentrations. And Night-time aged biomass burning and Cooking SVOAs peaked alongside UFP concentrations, which also indicates their stronger contribution to UFP concentrations in this season (Figure 51), which also indicates their stronger contribution to UFP concentrations in this season. This seasonal difference may arise from spring's more stable

atmospheric conditions and lower BLHs, which favor the accumulation and condensation of semi-volatile organics onto particles. These observations highlight the seasonal shifts in dominant UFP sources, with biogenic and regional background SVOAs being more relevant in summer and night-time aged biomass burning, cooking and regional background SVOAs playing a more prominent role in spring. The generally low summer correlations could also reflect technical limitations, as the CHARON-PTR-MS's decreasing detection efficiency for smaller particles may have underrepresented traffic-related UFPs (<100 nm) (Piel et al., 2019; Lintusaari et al., 2023; Wang et al., 2024a), potentially explaining the absence of a distinct traffic-related SVOA factor.

Table 8 Correlation (R) between OA factors and different size range UFP concentration numbers from 19th to 22nd August 2023.

Correlation	7-10 nm	10-30 nm	30-50 nm	50-100 nm
Cooking	0.43	0.39	**0.52**	**0.50**
Traffic	**0.89**	**0.68**	**0.78**	**0.86**
BOA	0.20	0.07	0.12	0.27
Aged BBOA	**0.55**	0.34	0.31	0.35
LVOOA	**-0.42**	**-0.32**	**-0.41**	**-0.56**

Table 9 Correlation (R) between OA factors and different size range UFP concentration numbers from 20th to 23rd March 2024.

Correlation	14-30 nm	30-50 nm	50-100 nm
Traffic	**0.78**	**0.74**	**0.76**
Cooking	**0.69**	**0.72**	**0.73**
Fresh BBOA	0.43	**0.55**	**0.68**
Aged BBOA	-0.23	-0.24	-0.2
LVOOA	0.10	-0.02	0.03

Figures 52 and 53 select the same typical periods as those identified for VOC and SVOA analysis. UFP concentrations show correlations with traffic- and cooking-related OA, consistent with the source factors observed for VOC and SVOA. Cooking OA exhibits moderate correlations with 30-50 nm (R = 0.52) and 50-100 nm (R = 0.50) UFP concentrations (Table 8), while traffic OA demonstrates strong correlations (R = 0.68-0.89) across all UFP size ranges. Aged BBOA and BOA concentrations increase during periods of decreasing BLH and also peak during UFP growth events. However, aged BBOA only shows a moderate correlation (R = 0.55) with 7-10 nm UFP concentrations, suggesting that it originates from nearby primary particles. It should be noted that the observed UFP growth events occur in the 10-60 nm size range, whereas the AMS primarily detects particles between 20 nm and 2.5 µm.

As a result, OA factors derived from AMS data are more representative of larger particles and may not be directly linked to UFP growth processes. BOA shows almost no correlation with UFP concentrations. In contrast, LV-OOA, which is associated with photochemical oxidation products, exhibits a negative correlation with UFP concentrations.

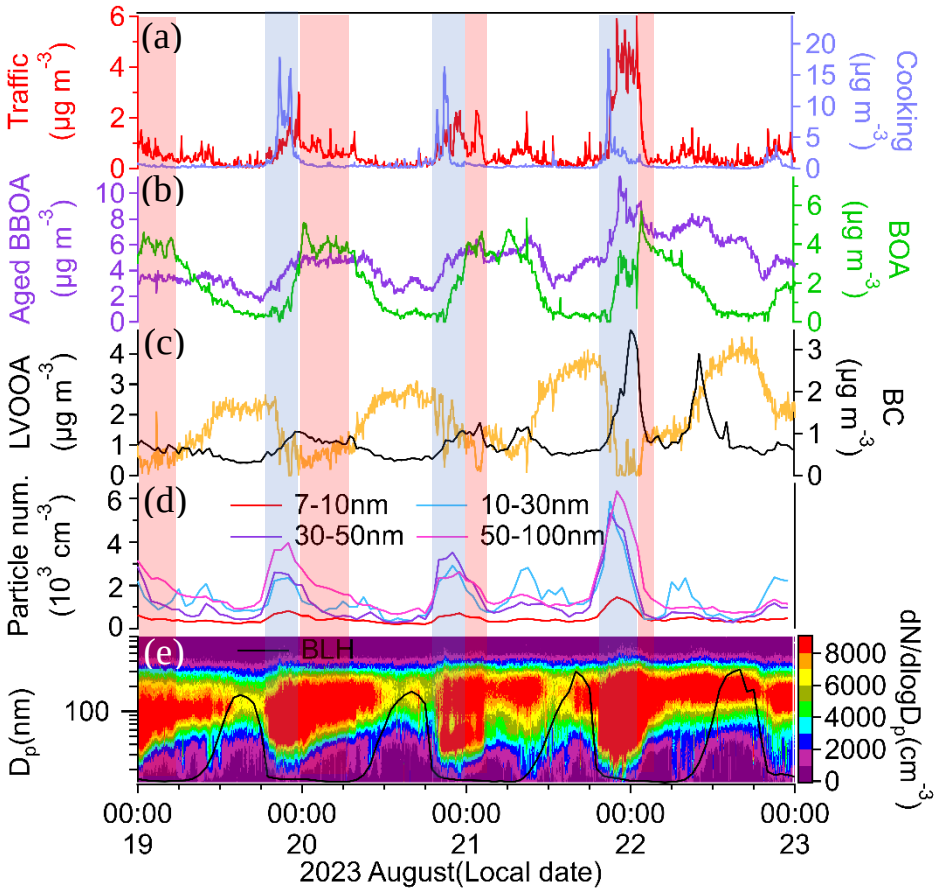

Figure 52. Evolution of organic aerosol particles of traffic and cooking (a), of aged BBOA and BOA (b), of LVOOA (c), particle numbers of 7-10nm, 10-30nm, 30-50nm and 50-100nm (d) particle size distributions (e) from 19th to 22nd August 2023 （Blue shaded area indicate ultrafine particle peak events and red shaded areas indicate particle growth events

In spring, traffic emissions, cooking-related OA, fresh BBOA, and UFP concentrations all peak simultaneously (Figure 53). Traffic-related OA shows strong correlations (R = 0.74-0.78) with UFP concentrations across all size ranges, while cooking-related OA also exhibits strong correlations (R = 0.69-0.73). Fresh BBOA displays moderate correlations (R = 0.55-0.68) with 30-50 nm and 50-100 nm UFP numbers (Table 9). In contrast, aged BBOA is negatively correlated with UFP concentrations, suggesting it originates from transported sources rather than local emissions. LV-OOA, which represents regional background aerosol, shows a weak and slightly anti-correlated relationship with UFP concentrations in spring. Notably, both fresh and aged BBOA remain at peak levels even when UFP numbers decline to their lowest concentrations. This observation confirms that aged BBOA does not contribute to UFP growth,

as it shows no correlation with UFP concentrations. In contrast, fresh BBOA likely plays a role in UFP growth, given its moderate correlation with UFP particle numbers.

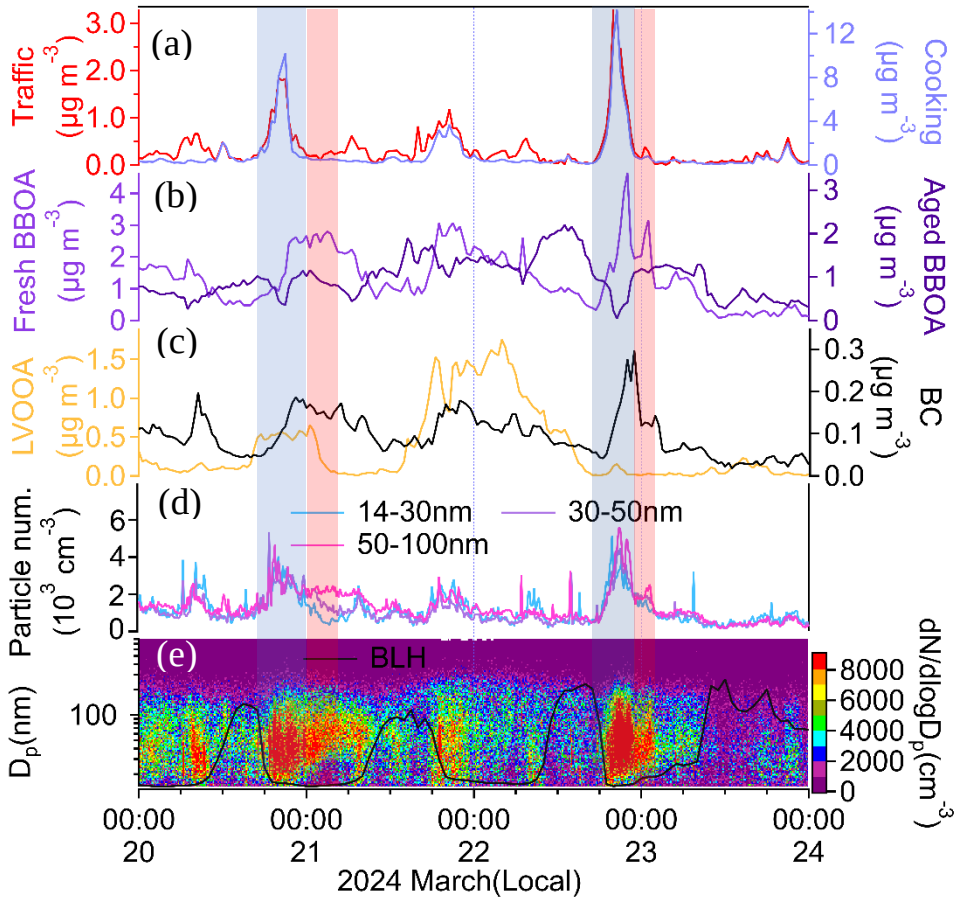

Figure 53. Evolution of traffic and cooking OA (a) fresh and aged BBOA (b) LVOOA (c) particle numbers of 14-30nm, 30-50nm and 50-100nm (d) size distribution of particle and BLH (e) from 20th to 23rd March 2024 (Blue shade for ultrafine particle peak and red shade for particle growth)

The analysis of VOC, SVOA, and OA reveals consistent contributions from traffic-related and biomass burning emissions across all three seasons. However, summer exhibits a distinct increase in biogenic influences, with higher contributions from BVOCs and oxidized BVOCs due to enhanced biogenic emissions. While monoterpene VOCs are also detected in winter, these likely originate from anthropogenic sources rather than natural processes. Monoterpene-dominated BVOCs and their oxidation products play a critical role in driving nighttime particle growth during summer. In terms of SVOA, the results highlight a significant biogenic contribution, including isoprene oxidation products, weakly oxidized monoterpenes, and more oxidized monoterpene SVOAs. In contrast, winter and spring are characterized by a stronger anthropogenic influence, with elevated contributions from aged BBOA, aged combustion aerosols, and other aerosols linked to human activities. Traffic related SVOA was not identified, likely because traffic aerosols, primarily composed of hydrocarbons, volatilized into the gas

phase, making their detection in the particle phase challenging for CHARON-PTR-MS. For total OA composition, traffic, cooking, aged BBOA, and LVOOA are present in all seasons. The difference is UFP number concentrations were surprisingly lower in winter compared to summer. Traffic-related VOCs and traffic-related OA exhibit peak concentrations at the same time as ultrafine particles, indicating that traffic has a significant influence on ultrafine particles in all the seasons.

Figures S13 and S14 present the particle number concentrations for average particles in the range of 2.5-100 nm, with average values of 8175 ± 4623 cm^{-3} in summer, 2765 ± 1197 cm^{-3} in winter, and 3131 ± 1921 cm^{-3} in spring. The corresponding fractions of 2.5-100 nm particles relative to the total particle number are 80.6 ± 8.2% in summer, 71.6 ± 8.1% in winter, and 82.0 ± 6.0% in spring. It is observed that in the colder winter months, the particle number concentrations and the fraction of ultrafine particles decreases. This agrees with higher VOC levels in summer, including especially monoterpenes, which can contribute to new particle formation and particle growth following their oxidation. Previous studies have shown that this can also occur during nighttime e.g. by reactions of NO_3 radicals with unsaturated compounds also leading to the formation of organo-nitrates (Huang et al., 2019; Song et al., 2024b).

I performed a correlation analysis between ultrafine particles, VOC factors, SVOA factors, OA factors, meteorological parameters, and trace gases. For the summer, I found a strong correlation between ultrafine particle numbers and traffic (VOC: R = 0.65; OA: R = 0.70) and NO_2 (R = 0.67), implicating the primary tailpipe. Additionally, there was a moderate correlation with cooking OA (R = 0.50) (Xiang et al., 2021). Winter/Spring UFPs retain traffic associations (VOC: R = 0.61; OA: R = 0.64) but show weaker ties to cooking-related components (SVOA/OA: R = 0.51-0.57).

According to the PMF analysis of AMS mass spectra, aged BBOA contributes 25±21% in summer, 49±21% in winter, and 64±36% in spring to the organic aerosol particle mass ($PM_{2.5}$). Figure 54 presents various BBOA tracers from CHARON-PTR-MS for four strong BBOA events, revealing similar time series patterns across the tracers. Notably, the concentrations of the fresh BBOA tracer guaiacol ($C_7H_9O_2^+$) and aged BBOA tracer ($C_7H_9O_5^+$) are significantly higher compared to other BBOA tracers. This indicates the dominance of lignin-rich biomass combustion and extensive atmospheric aging of BBOA in the studied environment. The temporal variability and short-lived spikes in BBOA tracer concentrations, especially during August events, suggest significant contribution from local or nearby biomass burning sources. Furthermore, the higher summer concentrations of BBOA tracers compared to winter/spring

suggest that, despite its greater relative contribution to OA in winter, BBOA concentrations are lower in winter. This may be due to residential wood burning for heating in winter, while summer BBOA likely originates from open flames, such as barbecues, or agricultural activities in Munich, resulting in higher summer concentrations (In 'T Veld et al., 2023).

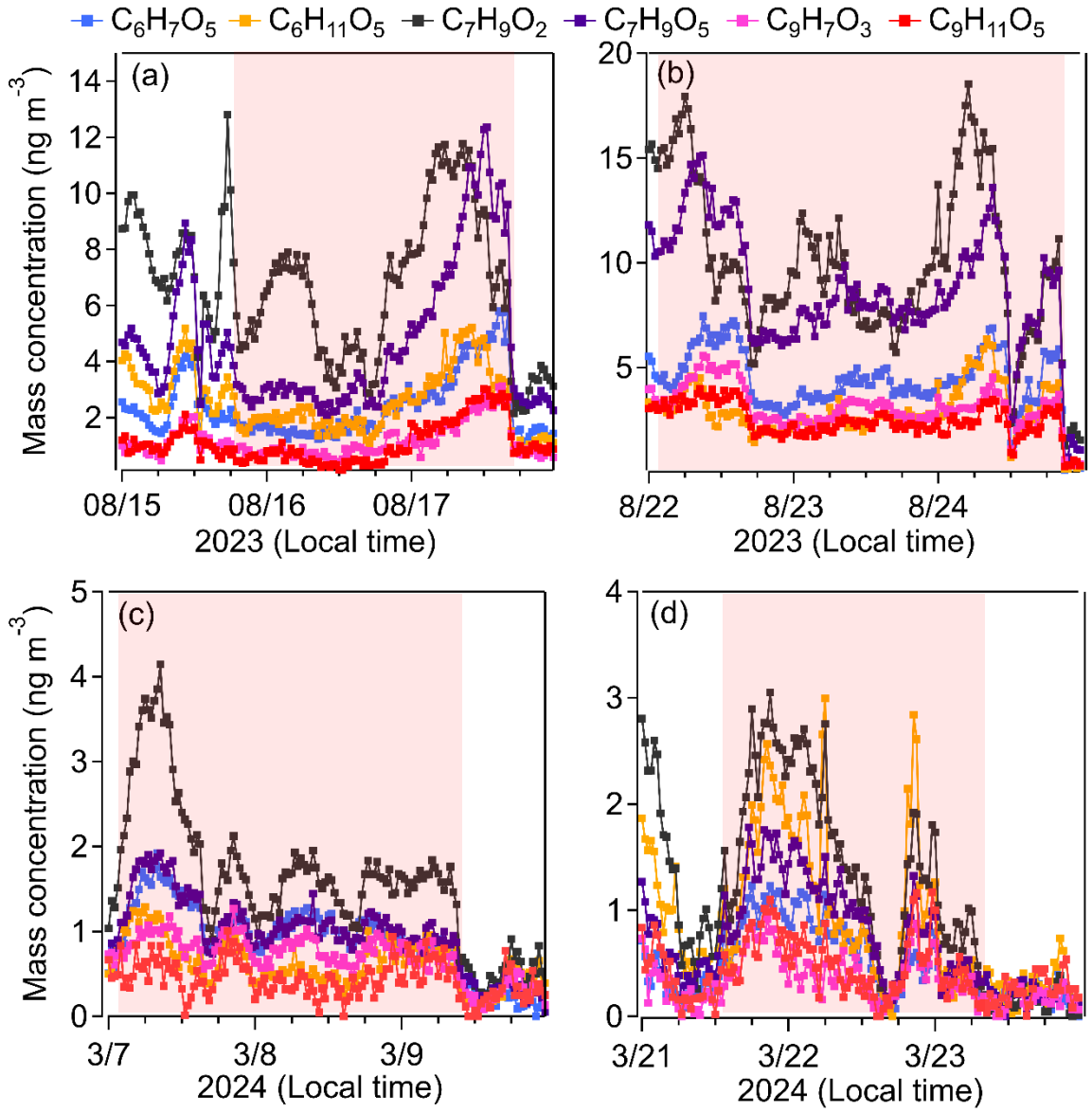

Figure 54. Evolution of fresh BBOA tracer compounds $C_7H_9O_2^+$ and $C_6H_{11}O_5^+$; of aged BBOA tracers $C_6H_7O_5^+$, $C_7H_9O_5^+$, $C_9H_7O_3^+$, and $C_9H_{11}O_5^+$, for 15th-17th August (a), 22rd-24th August (b), 07th- 09th March (c) and 21st-23rd March (d). Red shaded area for strong biomass burning events.

3.3.6 Summary of aerosol particles and VOC in downtown Munich

This study examines the sources, concentrations, and seasonal variations of VOCs, SVOA, and OA in an urban street canyon in Munich. In summer, VOCs are primarily derived from aged VOCs (42 ± 18%) and traffic emissions (22 ± 14%), with minor contributions from biogenic VOCs (BVOCs: 7 ± 7%) and oxidized biogenic VOCs (OBVOCs: 13 ± 13%). Notably,

nighttime monoterpene oxidation significantly influences particle growth, suggesting urban planners should prioritize low-monoterpene-emitting vegetation. Winter VOCs are dominated by anthropogenic combustion, particularly traffic (33 ± 12%) and background sources (54 ± 9%), while spring sees a shift toward traffic emissions (35 ± 15%) and biogenic VOCs linked to biomass burning (BBVOCs: 33 ± 14%). The rise in BBVOCs during spring is attributed to outdoor barbecuing, a popular activity in Munich. Notably, traffic-derived VOCs demonstrate a year-round influence on ultrafine particle concentrations, while biogenic VOCs, particularly terpenes, contribute significantly to nighttime particle growth during summer.

The composition of SVOA and OA also exhibits a strong seasonal dependence. Summer SVOA is characterized by oxidized monoterpenes (29 ± 31%) and a mixed source of isoprene oxidation products and biomass burning organic aerosol (BBOA: 16 ± 15%), with additional contributions from barbecue emissions. In contrast, winter and spring are dominated by BBOA, accounting for 65 ± 30% and 58 ± 37% of SVOA, respectively, primarily due to residential heating and springtime barbecue activities. Similarly, OA composition shifts seasonally: summer OA is predominantly composed of highly oxidized aerosols (LVOOA: 33 ± 20%), aged BBOA (25 ± 21%), and biogenic OA (22 ± 14%), whereas winter and spring OA are overwhelmingly influenced by BBOA, peaking at 49 ± 21% (fresh) and 64 ± 36% (aged). Tracer analysis identifies guaiacol and its oxidation products as key markers for aged BBOA, while traffic- and cooking-related OA emerge as major contributors to ultrafine particles.

To combine the different sources identified by analyzing aerosol particles and VOC I combined the main air pollution sources in a comprehensive Figure 55. Air pollution in Munich shows strong seasonal variations, with biomass burning (Aged and Fresh BBOA) dominating in winter and spring, likely due to heating and barbecue. Winter also sees high regional background pollution, possibly from stagnant atmospheric conditions. In contrast, summer is characterized by biogenic emissions and photochemical LV-OOA, driven by sunlight and plant activity, while biomass burning contributions drop. Traffic emissions peak in spring, possibly linked to weather or travel patterns, whereas cooking remains a small but steady source year-round. Aged combustion has a minor yet consistent presence across seasons.

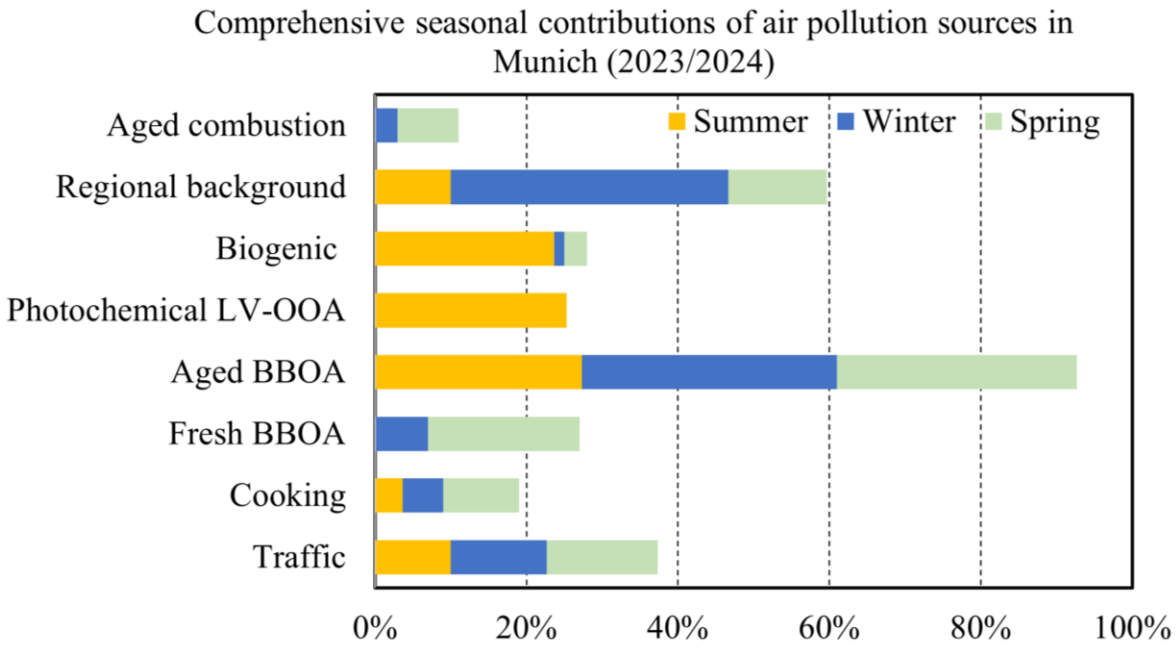

Figure 55. Comprehensive seasonal contributions of air pollution sources in Munich summer, winter and spring time.

These findings highlight the need for targeted urban air quality management strategies in Munich. Reducing emissions from traffic and outdoor barbecue activities would help mitigate ultrafine particle pollution. Additionally, careful selection of urban vegetation—prioritizing low-terpene-emitting species—could minimize secondary organic aerosol formation, particularly during summer. Such measures would contribute to improved air quality while maintaining the benefits of urban green.

4. Conclusions and outlook

4.1 Conclusions

In my doctoral research I have systematically investigated the sources, transformations, and impacts of VOC, SVOA, and OA across diverse environments—urban, industrial, and forested regions—through four targeted field campaigns. The integration of advanced analytical techniques, including CHARON-PTR-MS, aerosol mass spectrometry (AMS), and detailed statistical analysis employing PMF, has provided a robust framework for characterizing atmospheric composition, while revealing critical insights into the interplay of local emissions, long-range transport, and meteorological dynamics. The findings underscore the complexity of atmospheric processes and emphasize the need for context-specific air quality management strategies (Figure 56).

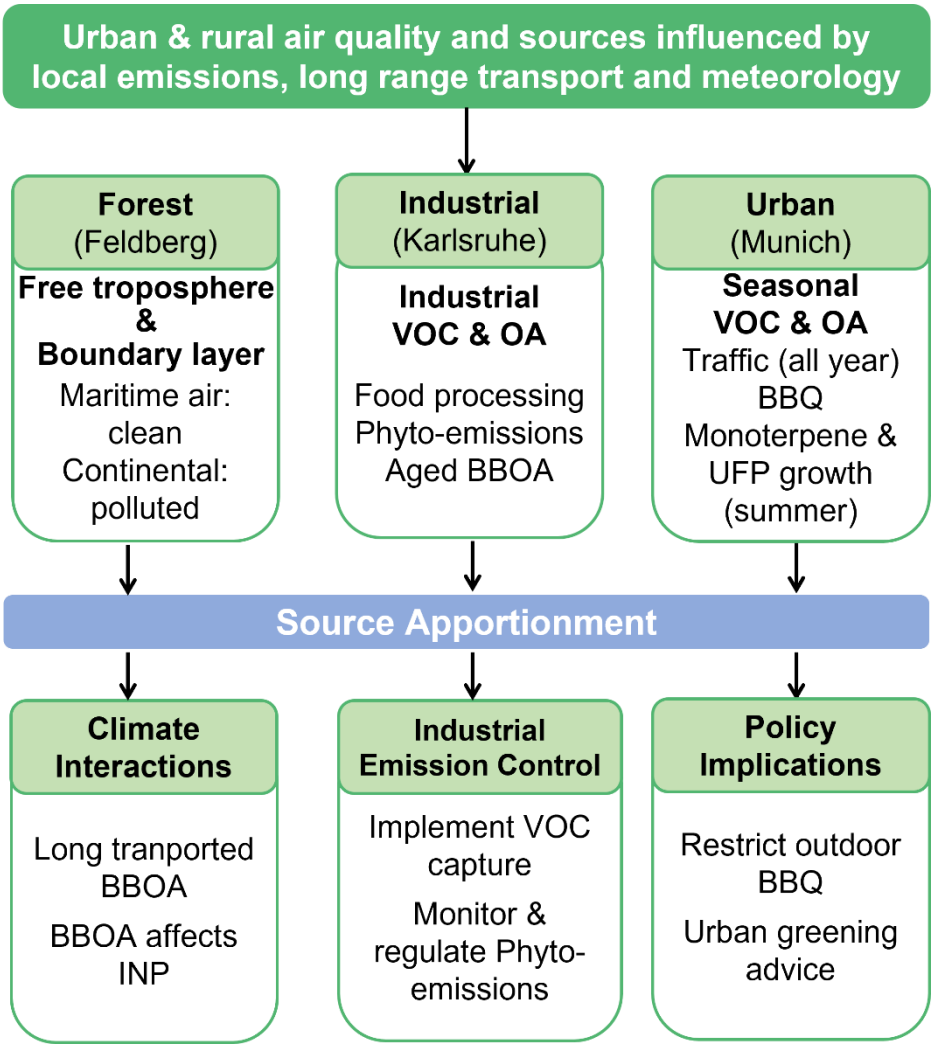

Figure 56. Schematic visualization of my main conclusions

A key revelation from this work is the dominant role of source-receptor relationships and meteorological modulation in shaping aerosol particle and VOC distributions. In the elevated forest site of Feldberg, for instance, air mass origin decided compositional shifts: marine inflows (56.3% Atlantic Ocean at 1500 m) reduced pollutant concentrations with cleaner air masses but also with more frequent wet scavenging, while continental air masses (32.8% German-French-Switzerland border at 500 m) showed elevated anthropogenic pollution from regional metropolitan areas. Probing air alternatingly in the boundary layer and free troposphere with predominant westerly wind patterns, allowed to demonstrate how boundary layer dynamics and long-range transport govern aerosol aging and mixing (Scholz et al., 2023). The organic aerosol components identified—aged biomass burning organic aerosol, regional background organic aerosol, and oxygenated organic aerosol factors (SV-OOA/LV-OOA)—highlight that even in remote areas, anthropogenic and biomass burning emissions undergo extensive atmospheric processing, blurring source signatures. Notably, episodic events like Canadian wildfires and regional pollution episodes marked by long-transport biomass burning aerosols that substantially increased organic aerosol concentrations, fine particle counts, and ice-nucleating particle number (Wang et al., 2024c). The Feldberg summit measurements revealed a remarkable atmospheric phenomenon: while BVOC were present in the gas phase as emitted from the Black Forest in the warm summer, their conversion to secondary organic aerosols was very limited due to the pristine high-altitude conditions characterized by extremely low NO_x levels that reduced oxidation pathways (Dewald et al., 2022). Furthermore, frequent clean marine air masses promoted wet aerosol scavenging, leading to a higher fraction of ultrafine particles (Andronache et al., 2006; Niu et al., 2023).

The study at Karlsruhe harbor identified three major air mass pathways, with 58% originating from regional areas, where westerly/southwesterly winds transported industrial pollutants, significantly shaping local air quality. PMF analysis highlighted industrial food processing as the dominant source, contributing 41±23% to VOC and 20±9% to organic aerosol, while industrial phyto-emissions accounted for 13±14% of VOC and 44±27% of semi-volatile organic aerosol (SVOA). More oxygenated OA (30±15%) showed strong links to industrial phyto-emissions SVOA, indicating it was from industrial phyto-emissions. During the measurement period, French wildfires (Menut et al., 2023) led to increased biomass burning contributions (VOC: 17±15%; SVOA: 26±21%). Please note, that there was still some mass spectral overlap between wildfire aerosol and landfill gas combustion emissions. Biogenic sources had minor but consistent impacts (VOC: 16±12%; SVOA: 15±14%; OA: 12±9%),

underscoring the dominance of industrial emissions at this location. Weak correlations between ultrafine particle numbers (50-90 nm) and sources like biogenic OA, landfill combustion, and industrial solvent VOC indicate highly mixed and aged aerosols (Liu et al., 2025). These observations challenge conventional assumptions about industrial point sources, emphasizing their role in sustaining regional secondary aerosol formation rather than merely emitting primary particles. Regulatory measures should be implemented to restrict these emissions through stricter operational controls or cleaner production technologies especially including secondary aerosol particle precursor emissions.

The Munich campaigns reveal distinct seasonal patterns in Munich's urban air pollution, with summer dominated by photochemical aged VOCs (42±18%) and traffic emissions (22±14%), while biogenic contributions (BVOCs: 7±7%; oxidized BVOCs: 13±13%) drive nighttime ultrafine particle growth. Winter and spring are characterized by anthropogenic sources, notably traffic (33±12% winter, 35±15% spring) and biomass burning organic aerosol (65±30% in winter, 58±37% in spring). Summer semi-volatile organic aerosol features oxidized monoterpenes (29±31%) and mixed isoprene oxidation and biomass burning SVOA (16±15%), whereas OA composition shifts from photochemical low-volatile oxygenated OA (33±20%) in summer to biomass burning OA dominated (49±21% fresh, 64±36% aged) in colder seasons. Traffic and cooking emissions persistently influence ultrafine particles (Qadir et al., 2013; Schnell, 2014; Xiang et al., 2021), while biogenic VOC enhance summer ultrafine particle growth (Song et al., 2024b). These findings underscore the need for seasonally tailored strategies: reducing traffic and barbecue emissions, and selecting vegetation with lower terpene emissions to mitigate secondary aerosols. Implementing such measures would balance air quality improvements with urban greening benefits.

Across all four field campaigns, biomass burning emerged as a dominant contributor to both VOCs and organic aerosols (Bond et al., 2004; Bhattu, 2017), with particularly pronounced impacts in Munich during both summer and winter seasons. The chemical tracers and source apportionment results consistently highlighted two major origins for these biomass burning signals: (1) regional wildfire plumes undergoing long-range transport (as evidenced during the Canadian wildfire episodes) and (2) localized emissions from residential heating and pervasive outdoor barbecue activities—a cultural staple in Munich. These findings underscore an urgent need for public awareness campaigns and regulatory measures to discourage biomass-fueled barbecuing, particularly in densely populated urban areas where such activities exacerbate ultrafine particle pollution. Transitioning to cleaner alternatives (e.g., electric grills) could

mitigate this source without compromising cultural practices. Equally critical is the discovery of nighttime particle growth events in Munich driven by monoterpene oxidation—a process accounting for 29±31% of summer SVOA and which has been observed near Karlsruhe (Song et al., 2024b). While urban greening provides ecological benefits, the data demonstrate that selecting high-terpene-emitting vegetation can inadvertently promote secondary aerosol formation. Urban planners should therefore prioritize tree species with low terpene emission potentials (e.g., Acer platanoides over Pinus sylvestris) and strategically limit their planting density near traffic corridors where NOx availability accelerates SOA production (Qadir et al., 2013). This targeted approach balances air quality goals with urban heat island mitigation and biodiversity preservation.

In my doctoral research I have achieved my objectives by systematically characterizing the sources, transformations, and impacts of VOCs and OA across urban, industrial, and forested environments. The findings significantly advance the general understanding of atmospheric aerosols by demonstrating the critical role of source-receptor relationships, meteorological, and long-range transport in shaping aerosol composition and aging processes. For instance, the dominance of BBOA in both urban (e.g., Munich barbecues) and remote regions (e.g., Canadian wildfire plumes) highlights its pervasive influence on OA budgets, aligning with recent studies emphasizing biomass burning as a key driver of SOA formation (Fang et al., 2024). The discovery of limited BVOC-to-SOA conversion at the pristine Feldberg site due to ultra-low NOx levels challenges traditional oxidation pathway assumptions, supporting emerging literature on NOx-dependent SOA yields (Pullinen et al., 2020). In urban settings, industrial emissions (e.g., Karlsruhe food processing) were shown to sustain regional SOA formation rather than just primary particles, reinforcing the need to reevaluate industrial source impacts (Zhang et al., 2024). Seasonal variations in major aerosol sources in Munich further underscored the different roles of biogenic (monoterpene oxidation contributing 29% to summer SVOA) and anthropogenic (winter heating) sources, with traffic emissions perennially driving ultrafine particle numbers and biogenic emissions driving their growth—a finding consistent with global urban aerosol studies (Sporre et al., 2020; Bessagnet et al., 2022). Collectively, this work bridges gaps between localized emissions and large-scale atmospheric processes, providing a mechanistic framework for context-specific air quality strategies while validating and expanding upon recent advances in our understanding of the role of atmospheric aerosols in air quality.

4.2 Outlook

This work has identified critical knowledge gaps that demand further investigation: (1) the climate feedback potential of biomass burning aerosols, (2) urban biogenic-anthropogenic interactions under changing NOx regimes, (3) industrial emission evolution with decarbonization policies, and (4) vertical transport mechanisms in complex terrain. The proposed outlook addresses these gaps through targeted approaches to refine predictive models and mitigation strategies.

(1) Climate-Air quality feedback mechanisms and source attribution. Future research should develop integrated modeling frameworks to quantify how climate-driven increases in wildfire activity alter aerosol chemistry, particularly the ice-nucleating potential of aged biomass burning aerosols, while incorporating advanced source-tracing methodologies to map pollution origins. This requires combining isotopic fingerprinting, high-resolution satellite detection, and chemical transport modeling to track emissions from boreal forests, urban-wildland interfaces, and transboundary transport pathways. The synthesis of these approaches through machine learning-enhanced receptor modeling will generate policy-relevant source contribution maps, elucidating both local and distant influences on air quality-climate interactions under changing environmental conditions. Field validation should focus on warming-sensitive regions where complex emission mixtures and long-range transport dominate atmospheric composition.

(2) Urban greening optimization strategies. Implement controlled city-scale experiments with low-terpene tree species while monitoring OH reactivity and SOA yields. Combine eddy-covariance flux measurements with particle-phase characterization to develop species-specific planting guidelines for climate-resilient cities.

(3) Industrial emission transformation tracking. Establish real-time VOC "fingerprinting" systems near industrial clusters to monitor changes in phyto-emissions and process gases. Particular focus on biomass burning source impacts for food/pharmaceutical emissions during winter time.

(4) Boundary layer dynamics in mountain aerosol studies. Future work should employ BLH-stratified PMF analysis at high-altitude sites to quantify how boundary layer ventilation controls biogenic aerosol formation. Day-night comparisons offer an alternative approach when BLH data is unavailable. This methodology will clarify the vertical coupling between lowland emissions and mountain aerosol composition, particularly for biogenic systems.

Reference

Abbatt, J. P. D. and Wang, C.: The atmospheric chemistry of indoor environments, Environ Sci Process Impacts, 22, 25-48, 10.1039/c9em00386j, 2020.

Aiello, A., Pepe, E., De Luca, L., Pizzolongo, F., and Romano, R.: Preliminary study on kinetics of pyroglutamic acid formation in fermented milk, International Dairy Journal, 126, 105233, https://doi.org/10.1016/j.idairyj.2021.105233, 2022.

Aiello, A., De Luca, L., Pizzolongo, F., Pinto, G., Addeo, F., and Romano, R.: Kinetics of Formation of Butyric and Pyroglutamic Acid during the Shelf Life of Probiotic, Prebiotic and Synbiotic Yoghurt, 10.3390/fermentation9080763, 2023.

Äijälä, M., Heikkinen, L., Fröhlich, R., Canonaco, F., Prévôt, A. S. H., Junninen, H., Petäjä, T., Kulmala, M., Worsnop, D., and Ehn, M.: Resolving anthropogenic aerosol pollution types – deconvolution and exploratory classification of pollution events, Atmospheric Chemistry and Physics, 17, 3165-3197, 10.5194/acp-17-3165-2017, 2017.

Aimanant, S. and Ziemann, P. J.: Chemical Mechanisms of Aging of Aerosol Formed from the Reaction of n-Pentadecane with OH Radicals in the Presence of NOx, Aerosol Science and Technology, 47, 979-990, 10.1080/02786826.2013.804621, 2013.

Allison C. Aiken, Peter F. DeCarlo, Jesse H. Kroll, Douglas R. Worsnop, J. Alex Huffman, Kenneth S. Docherty, Ingrid M. Ulbrich, Claudia Mohr, Joel R. Kimmel, Donna Sueper, Yele Sun, Qi Zhang, Achim Trimborn, Megan Northway, Paul J. Ziemann, Manjula R. Canagaratna, Timothy B. Onasch, M. Rami Alfarra, and Prevot, A. S. H.: O/C and OM/OC Ratios of Primary, Secondary, and Ambient Organic Aerosols with High-Resolution Time-of-Flight Aerosol Mass Spectrometry, Environmental Science & Technology, 42, 4237-4614, 2008.

Andronache, C., Grönholm, T., Laakso, L., Phillips, V., and Venäläinen, A.: Scavenging of ultrafine particles by rainfall at a boreal site: observations and model estimations, Atmos. Chem. Phys., 6, 4739-4754, 10.5194/acp-6-4739-2006, 2006.

Atanassova, I., Milena, H., and Banov, M.: Free Lipid Biomarkers in Anthropogenic, Soil Health Restoration and Management, 321, 2019.

Berndt, T., Herrmann, H., Sipila, M., and Kulmala, M.: Highly Oxidized Second-Generation Products from the Gas-Phase Reaction of OH Radicals with Isoprene, J Phys Chem A, 120, 10150-10159, 10.1021/acs.jpca.6b10987, 2016.

Bessagnet, B., Allemand, N., Putaud, J.-P., Couvidat, F., André, J.-M., Simpson, D., Pisoni, E., Murphy, B. N., and Thunis, P.: Emissions of Carbonaceous Particulate Matter and Ultrafine Particles from Vehicles—A Scientific Review in a Cross-Cutting Context of Air Pollution and Climate Change, 10.3390/app12073623, 2022.

Bethel, H. L., Atkinson, R., and Arey, J.: Products of the Gas-Phase Reactions of OH Radicals with p-Xylene and 1,2,3- and 1,2,4-Trimethylbenzene: Effect of NO2 Concentration, The Journal of Physical Chemistry A, 104, 8922-8929, 10.1021/jp001161s, 2000.

Bhattarai, H., Saikawa, E., Wan, X., Zhu, H., Ram, K., Gao, S., Kang, S., Zhang, Q., Zhang, Y., Wu, G., Wang, X., Kawamura, K., Fu, P., and Cong, Z.: Levoglucosan as a tracer of biomass burning: Recent progress and perspectives, Atmospheric Research, 220, 20-33, 10.1016/j.atmosres.2019.01.004, 2019.

Bhattu, D.: Air pollution and control, Primary Organic Aerosols, Springer, Singapore, https://doi.org/10.1007/978-981-10-7185-0_7, 2017.

Bi, C., Krechmer, J. E., Canagaratna, M. R., and Isaacman-VanWertz, G.: Correcting bias in log-linear instrument calibrations in the context of chemical ionization mass spectrometry, Atmos. Meas. Tech., 14, 6551-6560, 10.5194/amt-14-6551-2021, 2021.

Birdsall, A. W. and Elrod, M. J.: Comprehensive NO-Dependent Study of the Products of the Oxidation of Atmospherically Relevant Aromatic Compounds, The Journal of Physical Chemistry A, 115, 5397-5407, 10.1021/jp2010327, 2011.

Bond, T. C., Streets, D. G., Yarber, K. F., Nelson, S. M., Woo, J. H., and Klimont, Z.: A technology-based global inventory of black and organic carbon emissions from combustion, Journal of Geophysical Research: Atmospheres, 109, 10.1029/2003jd003697, 2004.

Brown, S. G., Eberly, S., Paatero, P., and Norris, G. A.: Methods for estimating uncertainty in PMF solutions: Examples with ambient air and water quality data and guidance on reporting PMF results, Science of The Total Environment, 518-519, 626-635, https://doi.org/10.1016/j.scitotenv.2015.01.022, 2015.

Brownwood, B., Turdziladze, A., Hohaus, T., Wu, R., Mentel, T. F., Carlsson, P. T. M., Tsiligiannis, E., Hallquist, M., Andres, S., Hantschke, L., Reimer, D., Rohrer, F., Tillmann, R., Winter, B., Liebmann, J., Brown, S. S., Kiendler-Scharr, A., Novelli, A., Fuchs, H., and Fry, J. L.: Gas-Particle Partitioning and SOA Yields of Organonitrate Products from NO(3)-Initiated Oxidation of Isoprene under Varied Chemical Regimes, ACS Earth Space Chem, 5, 785-800, 10.1021/acsearthspacechem.0c00311, 2021.

Bruns, E. A., Slowik, J. G., El Haddad, I., Kilic, D., Klein, F., Dommen, J., Temime-Roussel, B., Marchand, N., Baltensperger, U., and Prévôt, A. S. H.: Characterization of gas-phase organics using proton transfer reaction time-of-flight mass spectrometry: fresh and aged residential wood combustion emissions, Atmospheric Chemistry and Physics, 17, 705-720, 10.5194/acp-17-705-2017, 2017.

Cáceres, L. A., Lakshminarayan, S., Yeung, K. K. C., McGarvey, B. D., Hannoufa, A., Sumarah, M. W., Benitez, X., and Scott, I. M.: Repellent and Attractive Effects of α-, β-, and Dihydro-β- Ionone to Generalist and Specialist Herbivores, Journal of Chemical Ecology, 42, 107-117, 10.1007/s10886-016-0669-z, 2016., last access: 17th May.

Canagaratna, M. R., Jimenez, J. L., Kroll, J. H., Chen, Q., Kessler, S. H., Massoli, P., Hildebrandt Ruiz, L., Fortner, E., Williams, L. R., Wilson, K. R., Surratt, J. D., Donahue, N. M., Jayne, J. T., and Worsnop, D. R.: Elemental ratio measurements of organic compounds using aerosol mass spectrometry: characterization, improved calibration, and implications, Atmospheric Chemistry and Physics, 15, 253-272, 10.5194/acp-15-253-2015, 2015.

Canagaratna, M. R., Jayne, J. T., Jimenez, J. L., Allan, J. D., Alfarra, M. R., Zhang, Q., Onasch, T. B., Drewnick, F., Coe, H., Middlebrook, A., Delia, A., Williams, L. R., Trimborn, A. M., Northway, M. J., DeCarlo, P. F., Kolb, C. E., Davidovits, P., and Worsnop, D. R.: Chemical and microphysical characterization of ambient aerosols with the aerodyne aerosol mass spectrometer, Mass Spectrom Rev, 26, 185-222, 10.1002/mas.20115, 2007.

Canaval, E., Hyttinen, N., Schmidbauer, B., Fischer, L., and Hansel, A.: NH_4^+ Association and Proton Transfer Reactions With a Series of Organic Molecules, Front Chem, 7, 191, 10.3389/fchem.2019.00191, 2019.

Canonaco, F., Crippa, M., Slowik, J. G., Baltensperger, U., and Prévôt, A. S. H.: SoFi, an IGOR-based interface for the efficient use of the generalized multilinear engine (ME-2) for the source apportionment: ME-2 application to aerosol mass spectrometer data, Atmos. Meas. Tech., 6, 3649-3661, 10.5194/amt-6-3649-2013, 2013.

Cao, J., Zheng, W., Chen, B., Yan, Z., Tang, X., Li, J., Zhang, Z., Ang, S., Li, C., Wu, R., Wu, P., and Chen, W.-H.: Chemical Composition of Essential Oil from Citrus reticulata Blanco cv. Chachiensis (Chachi) and Its Anti-Mosquito Activity against Pyrethroid-Resistant Aedes albopictus, 10.3390/insects15050345, 2024.

Chakraborty, A., Tripathi, S. N., and Gupta, T.: Effects of organic aerosol loading and fog processing on organic aerosol volatility, Journal of Aerosol Science, 105, 73-83, 10.1016/j.jaerosci.2016.11.015, 2017.

Smoke from Canada's wildfires darkens Europe's skies, https://www.npr.org/2023/06/27/1184494482/smoke-canada-wildfire-europe-air. last access: May 19.

Chen, G., Canonaco, F., Tobler, A., Aas, W., Alastuey, A., Allan, J., Atabakhsh, S., Aurela, M., Baltensperger, U., Bougiatioti, A., De Brito, J. F., Ceburnis, D., Chazeau, B., Chebaicheb, H., Daellenbach, K. R., Ehn, M., El Haddad, I., Eleftheriadis, K., Favez, O., Flentje, H., Font, A., Fossum, K., Freney, E., Gini, M., Green, D. C., Heikkinen, L., Herrmann, H., Kalogridis, A. C., Keernik, H., Lhotka, R., Lin, C., Lunder, C., Maasikmets, M., Manousakas, M. I., Marchand, N., Marin, C., Marmureanu, L., Mihalopoulos, N., Mocnik, G., Necki, J., O'Dowd, C., Ovadnevaite, J., Peter, T., Petit, J. E., Pikridas, M., Matthew Platt, S., Pokorna, P., Poulain, L., Priestman, M., Riffault, V., Rinaldi, M., Rozanski, K., Schwarz, J., Sciare, J., Simon, L., Skiba, A., Slowik, J. G., Sosedova, Y., Stavroulas, I., Styszko, K., Teinemaa, E., Timonen, H., Tremper, A., Vasilescu, J., Via, M., Vodicka, P., Wiedensohler, A., Zografou, O., Cruz Minguillon, M., and Prevot, A. S. H.: European aerosol phenomenology - 8: Harmonised source apportionment of organic aerosol using 22 Year-long ACSM/AMS datasets, Environ Int, 166, 107325, 10.1016/j.envint.2022.107325, 2022.

Corma, A., González-Alfaro, V., and Orchillés, A. V.: Decalin and tetralin as probe molecules for cracking and hydrotreating the light cycle oil, Journal of Catalysis, 200, 34-44, 2001.

Crippa, M., El Haddad, I., Slowik, J. G., DeCarlo, P. F., Mohr, C., Heringa, M. F., Chirico, R., Marchand, N., Sciare, J., Baltensperger, U., and Prévôt, A. S. H.: Identification of marine and continental aerosol sources in Paris using high resolution aerosol mass spectrometry, Journal of Geophysical Research: Atmospheres, 118, 1950-1963, 10.1002/jgrd.50151, 2013.

Crippa, M., Canonaco, F., Lanz, V. A., Äijälä, M., Allan, J. D., Carbone, S., Capes, G., Ceburnis, D., Dall'Osto, M., Day, D. A., DeCarlo, P. F., Ehn, M., Eriksson, A., Freney, E., Hildebrandt Ruiz, L., Hillamo, R., Jimenez, J. L., Junninen, H., Kiendler-Scharr, A., Kortelainen, A. M., Kulmala, M., Laaksonen, A., Mensah, A. A., Mohr, C., Nemitz, E., O'Dowd, C., Ovadnevaite, J., Pandis, S. N., Petäjä, T., Poulain, L., Saarikoski, S., Sellegri, K., Swietlicki, E., Tiitta, P., Worsnop, D. R., Baltensperger, U., and Prévôt, A. S. H.: Organic aerosol components derived from 25 AMS data sets across Europe using a consistent ME-2 based source apportionment approach, Atmos. Chem. Phys., 14, 6159-6176, 10.5194/acp-14-6159-2014, 2014.

Crossman, Z. M., Abraham, F., and Evershed, R. P.: Stable isotope pulse-chasing and compound specific stable carbon isotope analysis of phospholipid fatty acids to assess methane oxidizing bacterial populations in landfill cover soils, Environmental Science & Technology, 38, 1359-1367, 2004.

Dada, L., Stolzenburg, D., Simon, M., Fischer, L., Heinritzi, M., Wang, M., Xiao, M., Vogel, A. L., Ahonen, L., and Amorim, A.: Role of sesquiterpenes in biogenic new particle formation, Science advances, 9, eadi5297, 2023.

Dam, M., Draper, D. C., Marsavin, A., Fry, J. L., and Smith, J. N.: Observations of gas-phase products from the nitrate-radical-initiated oxidation of four monoterpenes, Atmos. Chem. Phys., 22, 9017-9031, 10.5194/acp-22-9017-2022, 2022.

Daniel R Oros and Simoneit, B. R. T.: Identification and emission factors of molecular tracers in organic aerosols from biomass burning Part 1. Temperate climate conifers, Applied Geochemistry, 16, 1513-1544, https://doi.org/10.1016/S0883-2927(01)00021-X, 2001.

Darsih, C., Damayanti, E., Windarsih, A., Indrianingsih, A. W., Nisa, K., Rosyida, V. T., Handayani, S., Hayati, S. N., and Sujarwo, W.: Phytochemicals analysis, antioxidant, and antibacterial activities from fraction of Pneumatopteris callosa leaves extract, AIP Conference Proceedings, 2957, 060013, 10.1063/5.0183959, 2024.

Dash, P. P., Mohanty, P., Behura, R., Behera, S., Naik, S., Mishra, M., Sahoo, H., Barick, A. K., Mohapatra, P., Sahoo, S. K., and Jali, B. R.: Rapid Colorimetric and Fluorometric Discrimination of Maleic Acid vs. Fumaric Acid and Detection of Maleic Acid in Food Additives, Journal of Fluorescence, 34, 1015-1024, 10.1007/s10895-023-03330-z, 2024.

De Gouw, J. and Jimenez, J. L.: Organic Aerosols in the Earth's Atmosphere, Environmental Science & Technology, 43, 7614-7618, 10.1021/es9006004, 2009.

De Gouw, J. and Warneke, C.: Measurements of volatile organic compounds in the earth's atmosphere using proton-transfer-reaction mass spectrometry, Mass Spectrom Rev, 26, 223-257, 10.1002/mas.20119, 2007.

De Gouw, J. A., Middlebrook, A. M., Warneke, C., Goldan, P. D., Kuster, W. C., Roberts, J. M., Fehsenfeld, F. C., Worsnop, D. R., Canagaratna, M. R., Pszenny, A. A. P., Keene, W. C., Marchewka, M., Bertman, S. B., and Bates, T. S.: Budget of organic carbon in a polluted atmosphere: Results from the New England Air Quality Study in 2002, Journal of Geophysical Research: Atmospheres, 110, 10.1029/2004jd005623, 2005.

DeCarlo, P. F., Kimmel, J. R., Trimborn, A., Northway, M. J., Jayne, J. T., Aiken, A. C., Gonin, M., Fuhrer, K., Horvath, T., Docherty, K. S., Worsnop, D. R., and Jimenez, J. L.: Field-Deployable, High-Resolution, Time-of-Flight Aerosol Mass Spectrometer, Analytical Chemistry, 78, 8281-8289, 10.1021/ac061249n, 2006.

Detlev Helmig, John Ortega, Tiffany Duhl, David Tanner, Guenther, A., Peter Harley, Christine Wiedinmyer, Jana Milford, and Sakulyanontvittaya, a. T.: Sesquiterpene Emissions from Pine Trees − Identifications, Emission Rates and Flux Estimates for the Contiguous United States, Environmental Science & Technology, 41, 1545–1553, https://doi.org/10.1021/es0618907, 2007.

DeVault, M. P., Ziola, A. C., and Ziemann, P. J.: Products and Mechanisms of Secondary Organic Aerosol Formation from the NO3 Radical-Initiated Oxidation of Cyclic and Acyclic Monoterpenes, ACS Earth and Space Chemistry, 6, 2076-2092, 10.1021/acsearthspacechem.2c00130, 2022.

Dewald, P., Nussbaumer, C. M., Schuladen, J., Ringsdorf, A., Edtbauer, A., Fischer, H., Williams, J., Lelieveld, J., and Crowley, J. N.: Fate of the nitrate radical at the summit of a semi-rural mountain site in Germany assessed with direct reactivity measurements, Atmos. Chem. Phys., 22, 7051-7069, 10.5194/acp-22-7051-2022, 2022.

Docherty, K. S., Yaga, R., Preston, W. T., Jaoui, M., Reidel, T. P., Offenberg, J. H., Kleindienst, T. E., and Lewandowski, M.: Relative contributions of selected multigeneration products to chamber SOA formed from photooxidation of a range (C_{10}–C_{17}) of n-alkanes under high NOx conditions, Atmospheric Environment, 244, 117976, https://doi.org/10.1016/j.atmosenv.2020.117976, 2021.

Docherty, K. S., Aiken, A. C., Huffman, J. A., Ulbrich, I. M., DeCarlo, P. F., Sueper, D., Worsnop, D. R., Snyder, D. C., Peltier, R. E., Weber, R. J., Grover, B. D., Eatough, D. J., Williams, B. J., Goldstein, A. H., Ziemann, P. J., and Jimenez, J. L.: The 2005 Study of Organic Aerosols at Riverside (SOAR-1): instrumental intercomparisons and fine particle composition, Atmospheric Chemistry and Physics, 11, 12387-12420, 10.5194/acp-11-12387-2011, 2011.

Drinovec, L., Močnik, G., Zotter, P., Prévôt, A. S. H., Ruckstuhl, C., Coz, E., Rupakheti, M., Sciare, J., Müller, T., Wiedensohler, A., and Hansen, A. D. A.: The "dual-spot" Aethalometer: an improved measurement of aerosol black carbon with real-time loading compensation, Atmos. Meas. Tech., 8, 1965-1979, 10.5194/amt-8-1965-2015, 2015.

Drosatou, A. D., Skyllakou, K., Theodoritsi, G. N., and Pandis, S. N.: Positive matrix factorization of organic aerosol: insights from a chemical transport model, Atmos. Chem. Phys., 19, 973-986, 10.5194/acp-19-973-2019, 2019.

Du, W., Zhao, J., Dada, L., Xu, W., Wang, Y., Shi, Y., Chen, X., Kokkonen, T. V., Cai, J., Zhang, Y., Wang, Q., Cai, R., Zha, Q., Zhou, L., Li, Z., Yu, F., Fu, P., Hu, F., Wang, Z., Worsnop, D. R., Bianchi, F., Kerminen, V.-M., Kulmala, M., and Sun, Y.: Impacts of enhanced new-particle growth events above urban roughness sublayer on cloud condensation nuclei, One Earth, 8, 10.1016/j.oneear.2024.12.005, 2025.

Duan, C., Liao, H., Wang, K., and Ren, Y.: The research hotspots and trends of volatile organic compound emissions from anthropogenic and natural sources: A systematic quantitative review, Environ Res, 216, 114386, 10.1016/j.envres.2022.114386, 2023.

Eichler, P., Müller, M., D'Anna, B., and Wisthaler, A.: A novel inlet system for online chemical analysis of semi-volatile submicron particulate matter, Atmos. Meas. Tech., 8, 1353-1360, 10.5194/amt-8-1353-2015, 2015a.

Eichler, P., Müller, M., D'Anna, B., and Wisthaler, A.: A novel inlet system for online chemical analysis of semi-volatile submicron particulate matter, Atmospheric Measurement Techniques, 8, 1353-1360, 10.5194/amt-8-1353-2015, 2015b.

El Haddad, I., Marchand, N., D'Anna, B., Jaffrezo, J. L., and Wortham, H.: Functional group composition of organic aerosol from combustion emissions and secondary processes at two contrasted urban environments, Atmospheric Environment, 75, 308-320, https://doi.org/10.1016/j.atmosenv.2013.04.019, 2013.

Elser, M., Huang, R.-J., Wolf, R., Slowik, J. G., Wang, Q., Canonaco, F., Li, G., Bozzetti, C., Daellenbach, K. R., Huang, Y., Zhang, R., Li, Z., Cao, J., Baltensperger, U., El-Haddad, I., and Prévôt, A. S. H.: New insights into PM2.5 chemical composition and sources in two major cities in China during extreme haze events using aerosol mass spectrometry, Atmospheric Chemistry and Physics, 16, 3207-3225, 10.5194/acp-16-3207-2016, 2016.

European Food Safety, A., Alvarez, F., Arena, M., Auteri, D., Borroto, J., Brancato, A., Carrasco Cabrera, L., Castoldi, A. F., Chiusolo, A., Colagiorgi, A., Colas, M., Crivellente, F., De Lentdecker, C., Egsmose, M., Fait, G., Gouliarmou, V., Ferilli, F., Greco, L., Ippolito, A., Istace, F., Jarrah, S., Kardassi, D., Kienzler, A., Leuschner, R., Lava, R., Linguadoca, A., Lythgo, C., Magrans, O., Mangas, I., Miron, I., Molnar, T., Padovani, L., Parra Morte, J. M., Pedersen, R., Reich, H., Santos, M., Sharp, R., Szentes, C., Terron, A., Tiramani, M., Vagenende, B., and Villamar-Bouza, L.: Peer review of the pesticide risk assessment of the active substance pelargonic acid (nonanoic acid), EFSA Journal, 19, e06813, https://doi.org/10.2903/j.efsa.2021.6813, 2021.

Fang, Z., Lai, A., Dongmei, C., Chunlin, L., Carmieli, R., Chen, J., Wang, X., and Rudich, Y.: Secondary Organic Aerosol Generated from Biomass Burning Emitted Phenolic Compounds: Oxidative Potential, Reactive Oxygen Species, and Cytotoxicity, Environmental Science & Technology, 58, 8194-8206, 10.1021/acs.est.3c09903, 2024.

Farina, S. C., Adams, P. J., and Pandis, S. N.: Modeling global secondary organic aerosol formation and processing with the volatility basis set: Implications for anthropogenic secondary organic aerosol, Journal of Geophysical Research: Atmospheres, 115, 10.1029/2009jd013046, 2010.

Fayad, L., Coeur, C., Fagniez, T., Secordel, X., Houzel, N., and Mouret, G.: Kinetic and mechanistic study of the gas-phase reaction of ozone with γ-terpinene, Atmospheric Environment, 246, 10.1016/j.atmosenv.2020.118073, 2021.

Fleming, L. T., Lin, P., Roberts, J. M., Selimovic, V., Yokelson, R., Laskin, J., Laskin, A., and Nizkorodov, S. A.: Molecular composition and photochemical lifetimes of brown carbon chromophores in biomass burning organic aerosol, Atmospheric Chemistry and Physics, 20, 1105-1129, 10.5194/acp-20-1105-2020, 2020.

Forstner, H. J. L., Flagan, R. C., and Seinfeld, J. H.: Secondary Organic Aerosol from the Photooxidation of Aromatic Hydrocarbons: Molecular Composition, Environmental Science & Technology, 31, 1345-1358, 10.1021/es9605376, 1997.

Freney, E. J., Sellegri, K., Canonaco, F., Boulon, J., Hervo, M., Weigel, R., Pichon, J. M., Colomb, A., Prévôt, A. S. H., and Laj, P.: Seasonal variations in aerosol particle composition at the puy-de-Dôme research station in France, Atmospheric Chemistry and Physics, 11, 13047-13059, 10.5194/acp-11-13047-2011, 2011.

Frischmon, C. and Hannigan, M.: VOC source apportionment: How monitoring characteristics influence positive matrix factorization (PMF) solutions., Atmos Environ X., doi: 10.1016/j.aeaoa.2023.100230, 2023.

Froyd, K. D., Murphy, S. M., Murphy, D. M., de Gouw, J. A., Eddingsaas, N. C., and Wennberg, P. O.: Contribution of isoprene-derived organosulfates to free tropospheric aerosol mass, Proc Natl Acad Sci U S A, 107, 21360-21365, 10.1073/pnas.1012561107, 2010.

Fry, J. L., Brown, S. S., Middlebrook, A. M., Edwards, P. M., Campuzano-Jost, P., Day, D. A., Jimenez, J. L., Allen, H. M., Ryerson, T. B., Pollack, I., Graus, M., Warneke, C., de Gouw, J. A., Brock, C. A., Gilman, J., Lerner, B. M., Dubé, W. P., Liao, J., and Welti, A.: Secondary organic aerosol (SOA) yields from NO3 radical + isoprene based on nighttime aircraft power plant plume transects, Atmospheric Chemistry and Physics, 18, 11663-11682, 10.5194/acp-18-11663-2018, 2018.

Fu, P., Kawamura, K., and Miura, K.: Molecular characterization of marine organic aerosols collected during a round-the-world cruise, Journal of Geophysical Research, 116, 10.1029/2011jd015604, 2011.

Fujii, Y., Tohno, S., Amil, N., Latif, M. T., Oda, M., Matsumoto, J., and Mizohata, A.: Annual variations of carbonaceous PM2.5 in Malaysia: influence by Indonesian peatland fires, Atmospheric Chemistry and Physics, 15, 13319-13329, 10.5194/acp-15-13319-2015, 2015.

Fuzzi, S., Andreae, M. O., Huebert, B. J., Kulmala, M., Bond, T. C., Boy, M., Doherty, S. J., Guenther, A., Kanakidou, M., and Kawamura, K.: Critical assessment of the current state of scientific knowledge, terminology, and research needs concerning the role of organic aerosols in the atmosphere, climate, and global change, Atmospheric Chemistry and Physics, 6, 2017-2038, 2006.

Gao, L., Song, J., Mohr, C., Huang, W., Vallon, M., Jiang, F., Leisner, T., and Saathoff, H.: Kinetics, SOA yields, and chemical composition of secondary organic aerosol from β-caryophyllene ozonolysis with and without nitrogen oxides between 213 and 313 K, Atmos. Chem. Phys., 22, 6001-6020, 10.5194/acp-22-6001-2022, 2022a.

Gao, Y., Chu, F., Chen, W., Wang, X., and Pan, Y.: Arc-Induced Nitrate Reagent Ion for Analysis of Trace Explosives on Surfaces Using Atmospheric Pressure Arc Desorption/Ionization Mass Spectrometry, Analytical Chemistry, 94, 5463-5468, 10.1021/acs.analchem.1c05650, 2022b.

Garmash, O., Kumar, A., Jha, S., Barua, S., Hyttinen, N., Iyer, S., and Rissanen, M.: Enhanced detection of aromatic oxidation products using NO3− chemical ionization mass spectrometry with limited nitric acid, Environmental science: atmospheres, 4, 1368-1381, 2024.

George, J., Pramanik, I., Sanewski, G., Nguyen, T., Pun, S., Edwards, D., Currie, M., Møller, S., Hardner, C., Lyons, P., and Smyth, H. E.: Relationship between Key Aroma Compounds and Sensory Attributes of Australian Grown Commercial Pineapple Cultivars, Journal of Agricultural and Food Chemistry, 73, 5839-5849, 10.1021/acs.jafc.4c12482, 2025.

Gerritz, L., Schervish, M., Lakey, P. S. J., Oeij, T., Wei, J., Nizkorodov, S. A., and Shiraiwa, M.: Photoenhanced Radical Formation in Aqueous Mixtures of Levoglucosan and Benzoquinone: Implications to Photochemical Aging of Biomass-Burning Organic Aerosols, The Journal of Physical Chemistry A, 127, 5209-5221, 10.1021/acs.jpca.3c01794, 2023.

Gkatzelis, G. I., Coggon, M. M., McDonald, B. C., Peischl, J., Gilman, J. B., Aikin, K. C., Robinson, M. A., Canonaco, F., Prevot, A. S. H., Trainer, M., and Warneke, C.: Observations Confirm that Volatile Chemical Products Are a Major Source of Petrochemical Emissions in U.S. Cities, Environ Sci Technol, 55, 4332-4343, 10.1021/acs.est.0c05471, 2021.

Gkatzelis, G. I., Tillmann, R., Hohaus, T., Müller, M., Eichler, P., Xu, K.-M., Schlag, P., Schmitt, S. H., Wegener, R., Kaminski, M., Holzinger, R., Wisthaler, A., and Kiendler-Scharr, A.: Comparison of three aerosol chemical characterization techniques utilizing PTR-ToF-MS: a study on freshly formed and aged biogenic SOA, Atmospheric Measurement Techniques, 11, 1481-1500, 10.5194/amt-11-1481-2018, 2018a.

Gkatzelis, G. I., Hohaus, T., Tillmann, R., Gensch, I., Müller, M., Eichler, P., Xu, K.-M., Schlag, P., Schmitt, S. H., Yu, Z., Wegener, R., Kaminski, M., Holzinger, R., Wisthaler, A., and Kiendler-Scharr, A.: Gas-to-particle partitioning of major biogenic oxidation products: a study on freshly formed and aged biogenic SOA, Atmospheric Chemistry and Physics, 18, 12969-12989, 10.5194/acp-18-12969-2018, 2018b.

Goldstein, A. H. and Galbally, I. E.: Known and Unexplored Organic Constituents in the Earth's Atmosphere, Environmental Science & Technology, 41, 1514–1521, https://doi.org/10.1021/es072476p, 2007.

Gong, Y., Jiang, F., Li, Y., Leisner, T., and Saathoff, H.: Impact of temperature on the role of Criegee intermediates and peroxy radicals in dimer formation from β-pinene ozonolysis, Atmos. Chem. Phys., 24, 167-184, 10.5194/acp-24-167-2024, 2024.

Gray Be, A., Upshur, M. A., Liu, P., Martin, S. T., Geiger, F. M., and Thomson, R. J.: Cloud Activation Potentials for Atmospheric alpha-Pinene and beta-Caryophyllene Ozonolysis Products, ACS Cent Sci, 3, 715-725, 10.1021/acscentsci.7b00112, 2017.

Guo, H., Campuzano-Jost, P., Nault, B. A., Day, D. A., Schroder, J. C., Kim, D., Dibb, J. E., Dollner, M., Weinzierl, B., and Jimenez, J. L.: The importance of size ranges in aerosol instrument intercomparisons: a case study for the Atmospheric Tomography Mission, Atmos. Meas. Tech., 14, 3631-3655, 10.5194/amt-14-3631-2021, 2021.

Guo, J., Zhang, J., Shao, J., Chen, T., Bai, K., Sun, Y., Li, N., Wu, J., Li, R., Li, J., Guo, Q., Cohen, J. B., Zhai, P., Xu, X., and Hu, F.: A merged continental planetary boundary layer height dataset based on high-resolution radiosonde measurements, ERA5 reanalysis, and GLDAS, Earth Syst. Sci. Data, 16, 1-14, 10.5194/essd-16-1-2024, 2024.

Hafner, S. D., Howard, C., Muck, R. E., Franco, R. B., Montes, F., Green, P. G., Mitloehner, F., Trabue, S. L., and Rotz, C. A.: Emission of volatile organic compounds from silage: Compounds, sources, and implications, Atmospheric Environment, 77, 827-839, 10.1016/j.atmosenv.2013.04.076, 2013.

Hajizadeh, Y., Mokhtari, M., Faraji, M., Mohammadi, A., Nemati, S., Ghanbari, R., Abdolahnejad, A., Fard, R. F., Nikoonahad, A., Jafari, N., and Miri, M.: Trends of BTEX in the central urban area of Iran: A preliminary study of photochemical ozone pollution and health risk assessment, Atmospheric Pollution Research, 9, 220-229, 10.1016/j.apr.2017.09.005, 2018.

Hamilton, J., F., L., A. , C., C., T. J.,, Wenger, J. C., Borrás i Garcia, E., and and Muñoz, A.: Reactive oxidation products promote secondary organic aerosol formation from green leaf volatiles, Atmos. Chem. Phys., 9, 3815–3823, https://doi.org/10.5194/acp-9-3815-2009, 2009.

Hamilton, J. F., Bryant, D. J., Edwards, P. M., Ouyang, B., Bannan, T. J., Mehra, A., Mayhew, A. W., Hopkins, J. R., Dunmore, R. E., Squires, F. A., Lee, J. D., Newland, M. J., Worrall, S. D., Bacak, A., Coe, H., Percival, C., Whalley, L. K., Heard, D. E., Slater, E. J., Jones, R. L., Cui, T., Surratt, J. D., Reeves, C. E., Mills, G. P., Grimmond, S., Sun, Y., Xu, W., Shi, Z., and Rickard, A. R.: Key Role of NO(3) Radicals in the Production of Isoprene Nitrates and Nitrooxyorganosulfates in Beijing, Environ Sci Technol, 55, 842-853, 10.1021/acs.est.0c05689, 2021.

Handwerker J., Barthlott C., Bauckholt M., Belleflamme A., Böhmländer A., Borg E., Dick G., Dietrich P., Fichtelmann B., Geppert G., Goergen K., Güntner A., Hammoudeh S., Hervo M., Hühn E., Kaniyodical M., Keller J., Kohler M., Knippertz P., Kunz M., Landmark S., and Y., L.: From initiation of convective storms to their impact - the Swabian MOSES 2023 campaign in southwestern Germany, Frontiers in Earth Science, section Atmospheric Science In minor revision, 2025.

Henze, D. K., Seinfeld, J. H., Ng, N. L., Kroll, J. H., Fu, T.-M., Jacob, D. J., and and Heald, C. L.: Global modeling of secondary organic aerosol formation from aromatic hydrocarbons: high- vs. low-yield pathways, Atmos. Chem. Phys., 8, 2405–2420, https://doi.org/10.5194/acp-8-2405-2008, 2008.

Hodzic, A., Kasibhatla, P. S., Jo, D. S., Cappa, C. D., Jimenez, J. L., Madronich, S., and Park, R. J.: Rethinking the global secondary organic aerosol (SOA) budget: stronger production, faster removal, shorter lifetime, Atmospheric Chemistry and Physics, 16, 7917-7941, 10.5194/acp-16-7917-2016, 2016.

Holzinger, R., Acton, W. J. F., Bloss, W. J., Breitenlechner, M., Crilley, L. R., Dusanter, S., Gonin, M., Gros, V., Keutsch, F. N., Kiendler-Scharr, A., Kramer, L. J., Krechmer, J. E., Languille, B., Locoge, N., Lopez-Hilfiker, F., Materić, D., Moreno, S., Nemitz, E., Quéléver, L. L. J., Sarda Esteve, R., Sauvage, S., Schallhart, S., Sommariva, R., Tillmann, R., Wedel, S., Worton, D. R., Xu, K., and Zaytsev, A.: Validity and limitations of simple reaction kinetics to calculate concentrations of organic compounds from ion counts in PTR-MS, Atmos. Meas. Tech., 12, 6193-6208, 10.5194/amt-12-6193-2019, 2019.

Huang, D. D., Zhu, S., An, J., Wang, Q., Qiao, L., Zhou, M., He, X., Ma, Y., Sun, Y., Huang, C., Yu, J. Z., and Zhang, Q.: Comparative Assessment of Cooking Emission Contributions to Urban Organic Aerosol Using Online Molecular Tracers and Aerosol Mass Spectrometry Measurements, Environ Sci Technol, 55, 14526-14535, 10.1021/acs.est.1c03280, 2021.

Huang, S., Wu, Z., Poulain, L., van Pinxteren, M., Merkel, M., Assmann, D., Herrmann, H., and Wiedensohler, A.: Source apportionment of the organic aerosol over the Atlantic Ocean from 53° N to 53° S: significant contributions from marine emissions and long-range transport, Atmos. Chem. Phys., 18, 18043-18062, 10.5194/acp-18-18043-2018, 2018a.

Huang, W., Saathoff, H., Shen, X., Ramisetty, R., Leisner, T., and Mohr, C.: Seasonal characteristics of organic aerosol chemical composition and volatility in Stuttgart, Germany, Atmospheric Chemistry and Physics, 19, 11687-11700, 10.5194/acp-19-11687-2019, 2019.

Huang, W., Wu, C., Gao, L., Gramlich, Y., Haslett, S. L., Thornton, J., Lopez-Hilfiker, F. D., Lee, B. H., Song, J., Saathoff, H., Shen, X., Ramisetty, R., Tripathi, S. N., Ganguly, D., Jiang, F., Vallon, M., Schobesberger, S., Yli-Juuti, T., and Mohr, C.: Variation in chemical composition and volatility of oxygenated organic aerosol in different rural, urban, and mountain environments, Atmos. Chem. Phys., 24, 2607-2624, 10.5194/acp-24-2607-2024, 2024.

Huang, X.-F., Zou, B.-B., He, L.-Y., Hu, M., Prévôt, A. S. H., and Zhang, Y.-H.: Exploration of PM_{2.5} sources on the regional scale in the Pearl River Delta based on ME-2 modeling, Atmospheric Chemistry and Physics, 18, 11563-11580, 10.5194/acp-18-11563-2018, 2018b.

In 't Veld, M., Khare, P., Hao, Y., Reche, C., Perez, N., Alastuey, A., Yus-Diez, J., Marchand, N., Prevot, A. S. H., Querol, X., and Daellenbach, K. R.: Characterizing the sources of ambient PM(10) organic aerosol in urban and rural Catalonia, Spain, Sci Total Environ, 902, 166440, 10.1016/j.scitotenv.2023.166440, 2023.

Islam, F., Saeed, F., Imran, A., Shehzadi, U., Ali, R., Nosheen, F., Chauhan, A., Asghar, A., and Ojukwu, M.: Bio-preservatives and essential oils as an alternative to chemical preservatives in the baking industry: a concurrent review, Journal of Food Science and Technology, 61, 609-620, 10.1007/s13197-023-05762-8, 2024.

J. L. Jimenez , M. R. Canagaratna, N. M. Donahue, A. S. H. Prevot , Q. Zhang, J. H. Kroll, P. F. DeCarlo, J. D. Allan, H. Coe, N. L. Ng, A. C. Aiken, K. S. Docherty, I. M. Ulbrich, and Grieshop, A. P.: Evolution of organic aerosols in the atmosphere, Science, 326, 1525-1529, DOI: 10.1126/science.1180353, 2009.

Jain, V., Tripathi, S. N., Tripathi, N., Sahu, L. K., Gaddamidi, S., Shukla, A. K., Bhattu, D., and Ganguly, D.: Seasonal variability and source apportionment of non-methane VOCs using PTR-TOF-MS measurements in Delhi, India, Atmospheric Environment, 283, 10.1016/j.atmosenv.2022.119163, 2022.

Jakobsen, H. B. and Christensen, L. P.: Diurnal changes in the concentrations of 2-phenylethyl β-D-glucopyranoside and the corresponding volatile aglycone in the tissue and headspace of Trifolium repens L. florets, Plant, Cell & Environment, 25, 773-781, 10.1046/j.1365-3040.2002.00855.x, 2002.

Jang, M. and Kamens, R. M.: Characterization of Secondary Aerosol from the Photooxidation of Toluene in the Presence of NOx and 1-Propene, Environmental Science & Technology, 35, 3626-3639, 10.1021/es010676+, 2001.

Jiang, F., Siemens, K., Linke, C., Li, Y., Gong, Y., Leisner, T., Laskin, A., and Saathoff, H.: Molecular analysis of secondary organic aerosol and brown carbon from the oxidation of indole, Atmos. Chem. Phys., 24, 2639-2649, 10.5194/acp-24-2639-2024, 2024.

PMF-AMS Analysis Guide, https://cires1.colorado.edu/jimenez-group/wiki/index.php/Igor_Quick_Reference. last access: 18 April.

Kaltsonoudis, C., Kostenidou, E., Florou, K., Psichoudaki, M., and Pandis, S. N.: Temporal variability and sources of VOCs in urban areas of the eastern Mediterranean, Atmospheric Chemistry and Physics, 16, 14825-14842, 10.5194/acp-16-14825-2016, 2016.

Kanellopoulos, P. G., Verouti, E., Chrysochou, E., Koukoulakis, K., and Bakeas, E.: Primary and secondary organic aerosol in an urban/industrial site: Sources, health implications and the role of plastic enriched waste burning, Journal of Environmental Sciences, 99, 222-238, https://doi.org/10.1016/j.jes.2020.06.012, 2021.

Kautzman, K. E., Surratt, J. D., Chan, M. N., Chan, A. W. H., Hersey, S. P., Chhabra, P. S., Dalleska, N. F., Wennberg, P. O., Flagan, R. C., and Seinfeld, J. H.: Chemical Composition of Gas- and Aerosol-Phase Products from the Photooxidation of Naphthalene, The Journal of Physical Chemistry A, 114, 913-934, 10.1021/jp908530s, 2010.

Kelly, J. M., Doherty, R. M., O'Connor, F. M., and Mann, G. W.: The impact of biogenic, anthropogenic, and biomass burning volatile organic compound emissions on regional and seasonal variations in secondary organic aerosol, Atmospheric Chemistry and Physics, 18, 7393-7422, 10.5194/acp-18-7393-2018, 2018.

Kim, E., Hopke, P. K., Larson, T. V., Maykut, N. N., and Lewtas, J.: Factor Analysis of Seattle Fine Particles, Aerosol Science and Technology, 38, 724-738, 10.1080/02786820490490119, 2004.

Kim, M. J., Seo, Y. K., Kim, J. H., and Baek, S. O.: Impact of industrial activities on atmospheric volatile organic compounds in Sihwa-Banwol, the largest industrial area in South Korea, Environ Sci Pollut Res Int, 27, 28912-28930, 10.1007/s11356-020-09217-x, 2020.

Kim, P. S., Jacob, D. J., Fisher, J. A., Travis, K., Yu, K., Zhu, L., Yantosca, R. M., Sulprizio, M. P., Jimenez, J. L., Campuzano-Jost, P., Froyd, K. D., Liao, J., Hair, J. W., Fenn, M. A., Butler, C. F., Wagner, N. L., Gordon, T. D., Welti, A., Wennberg, P. O., Crounse, J. D., St. Clair, J. M., Teng, A. P., Millet, D. B., Schwarz, J. P., Markovic, M. Z., and Perring, A. E.: Sources, seasonality, and trends of southeast US aerosol: an integrated analysis of surface, aircraft, and satellite observations with the GEOS-Chem chemical transport model, Atmospheric Chemistry and Physics, 15, 10411-10433, 10.5194/acp-15-10411-2015, 2015.

Kittelson, D., Khalek, I., McDonald, J., Stevens, J., and Giannelli, R.: Particle emissions from mobile sources: Discussion of ultrafine particle emissions and definition, Journal of Aerosol Science, 159, 105881, https://doi.org/10.1016/j.jaerosci.2021.105881, 2022.

Koss, A. R., Sekimoto, K., Gilman, J. B., Selimovic, V., Coggon, M. M., Zarzana, K. J., Yuan, B., Lerner, B. M., Brown, S. S., Jimenez, J. L., Krechmer, J., Roberts, J. M., Warneke, C., Yokelson, R. J., and de Gouw, J.: Non-methane organic gas emissions from biomass burning: identification, quantification, and emission factors from PTR-ToF during the FIREX 2016 laboratory experiment, Atmospheric Chemistry and Physics, 18, 3299-3319, 10.5194/acp-18-3299-2018, 2018.

Kourtchev, I., Godoi, R. H. M., Connors, S., Levine, J. G., Archibald, A. T., Godoi, A. F. L., Paralovo, S. L., Barbosa, C. G. G., Souza, R. A. F., Manzi, A. O., Seco, R., Sjostedt, S., Park, J.-H., Guenther, A., Kim, S., Smith, J., Martin, S. T., and Kalberer, M.: Molecular composition of organic aerosols in central Amazonia: an ultra-high-resolution mass spectrometry study, Atmospheric Chemistry and Physics, 16, 11899-11913, 10.5194/acp-16-11899-2016, 2016.

Kuang, Y., Xu, W., Tao, J., Ma, N., Zhao, C., and Shao, M.: A Review on Laboratory Studies and Field Measurements of Atmospheric Organic Aerosol Hygroscopicity and Its Parameterization Based on Oxidation Levels, Current Pollution Reports, 6, 410-424, 10.1007/s40726-020-00164-2, 2020.

Kumar, A., Singh, D., Kumar, K., Singh, B. B., and Jain, V. K.: Distribution of VOCs in urban and rural atmospheres of subtropical India: Temporal variation, source attribution, ratios, OFP and risk assessment, Sci Total Environ, 613-614, 492-501, 10.1016/j.scitotenv.2017.09.096, 2018.

Kumar, B., Chakraborty, A., Tripathi, S. N., and Bhattu, D.: Highly time resolved chemical characterization of submicron organic aerosols at a polluted urban location, Environ Sci Process Impacts, 18, 1285-1296, 10.1039/c6em00392c, 2016.

Kundu, S., Fisseha, R., Putman, A. L., Rahn, T. A., and Mazzoleni, L. R.: Molecular formula composition of β-caryophyllene ozonolysis SOA formed in humid and dry conditions, Atmospheric Environment, 154, 70-81, 10.1016/j.atmosenv.2016.12.031, 2017.

Lalchandani, V., Kumar, V., Tobler, A., M. Thamban, N., Mishra, S., Slowik, J. G., Bhattu, D., Rai, P., Satish, R., Ganguly, D., Tiwari, S., Rastogi, N., Tiwari, S., Močnik, G., Prévôt, A. S. H., and Tripathi, S. N.: Real-time characterization and source apportionment of fine particulate matter in the Delhi megacity area during late winter, Science of The Total Environment, 770, 10.1016/j.scitotenv.2021.145324, 2021.

Lee, A., Goldstein, A. H., Kroll, J. H., Ng, N. L., Varutbangkul, V., Flagan, R. C., and Seinfeld, J. H.: Gas-phase products and secondary aerosol yields from the photooxidation of 16 different terpenes, Journal of Geophysical Research: Atmospheres, 111, 10.1029/2006jd007050, 2006.

Lee, B. H., Lopez-Hilfiker, F. D., Mohr, C., Kurtén, T., Worsnop, D. R., and Thornton, J. A.: An Iodide-Adduct High-Resolution Time-of-Flight Chemical-Ionization Mass Spectrometer: Application to Atmospheric Inorganic and Organic Compounds, Environmental Science & Technology, 48, 6309-6317, 10.1021/es500362a, 2014.

Lee, H., Romero, J., Belbase, N., Connors, S., and de Coninck, H., et al.: Climate Change 2023: Synthesis Report, Contribution of Working Groups I, II and III to the Sixth Assessment Report of the Intergovernmental Panel on Climate Change, IPCC, Geneva, Switzerland, 2023.

Leglise, J., Muller, M., Piel, F., Otto, T., and Wisthaler, A.: Bulk Organic Aerosol Analysis by Proton-Transfer-Reaction Mass Spectrometry: An Improved Methodology for the Determination of Total Organic Mass, O:C and H:C Elemental Ratios, and the Average Molecular Formula, Anal Chem, 91, 12619-12624, 10.1021/acs.analchem.9b02949, 2019.

Lemieux, P. M., Lutes, C. C., and Santoianni, D. A.: Emissions of organic air toxics from open burning: a comprehensive review, Progress in Energy and Combustion Science, 30, 1-32, 10.1016/j.pecs.2003.08.001, 2004.

Li, D., Lu, W., Liu, Y., Guo, H., Xu, S., Ming, Z., and Wang, H.: Analysis of relative concentration of ethanol and other odorous compounds (OCs) emitted from the working surface at a landfill in China, 2015.

Li, H., Riva, M., Rantala, P., Heikkinen, L., Daellenbach, K., Krechmer, J. E., Flaud, P.-M., Worsnop, D., Kulmala, M., Villenave, E., Perraudin, E., Ehn, M., and Bianchi, F.: Terpenes and their oxidation products in the French Landes forest: insights from Vocus PTR-TOF measurements, Atmospheric Chemistry and Physics, 20, 1941-1959, 10.5194/acp-20-1941-2020, 2020a.

Li, H., Canagaratna, M. R., Riva, M., Rantala, P., Zhang, Y., Thomas, S., Heikkinen, L., Flaud, P.-M., Villenave, E., Perraudin, E., Worsnop, D., Kulmala, M., Ehn, M., and Bianchi, F.: Atmospheric organic vapors in two European pine forests measured by a Vocus PTR-TOF: insights into monoterpene and sesquiterpene oxidation processes, Atmospheric Chemistry and Physics, 21, 4123-4147, 10.5194/acp-21-4123-2021, 2021.

Li, J., Li, K., Wang, W., Wang, J., Peng, C., and Ge, M.: Optical properties of secondary organic aerosols derived from long-chain alkanes under various NOx and seed conditions, Science of The Total Environment, 579, 1699-1705, https://doi.org/10.1016/j.scitotenv.2016.11.189, 2017.

Li, R., Zhang, K., Li, Q., Yang, L., Wang, S., Liu, Z., Zhang, X., Chen, H., Yi, Y., Feng, J., Wang, Q., Huang, L., Wang, W., Wang, Y., Yu, J. Z., and Li, L.: Characteristics and degradation of organic aerosols from cooking sources based on hourly observations of organic molecular markers in urban environments, Atmos. Chem. Phys., 23, 3065-3081, 10.5194/acp-23-3065-2023, 2023a.

Li, S., Liu, D., Kong, S., Wu, Y., Hu, K., Zheng, H., Cheng, Y., Zheng, S., Jiang, X., Ding, S., Hu, D., Liu, Q., Tian, P., Zhao, D., and Sheng, J.: Evolution of source attributed organic aerosols and gases in a megacity of central China, Atmos. Chem. Phys., 22, 6937-6951, 10.5194/acp-22-6937-2022, 2022.

Li, W., Wang, J., Qi, L., Yu, W., Nie, D., Shi, S., Gu, C., Ge, X., and Chen, M.: Molecular characterization of biomass burning tracer compounds in fine particles in Nanjing, China, Atmospheric Environment, 240, 10.1016/j.atmosenv.2020.117837, 2020b.

Li, X., Chen, Y., Li, Y., Cai, R., Li, Y., Deng, C., Wu, J., Yan, C., Cheng, H., Liu, Y., Kulmala, M., Hao, J., Smith, J. N., and Jiang, J.: Seasonal variations in composition and sources of atmospheric ultrafine particles in urban Beijing based on near-continuous measurements, Atmos. Chem. Phys., 23, 14801-14812, 10.5194/acp-23-14801-2023, 2023b.

Liang, C., Wang, S., Hu, R., Huang, G., Xie, J., Zhao, B., Li, Y., Zhu, W., Guo, S., Jiang, J., and Hao, J.: Molecular tracers, mass spectral tracers and oxidation of organic aerosols emitted from cooking and fossil fuel burning sources, Science of The Total Environment, 868, 161635, https://doi.org/10.1016/j.scitotenv.2023.161635, 2023.

Lim, Y. B. and Ziemann, P. J.: Effects of Molecular Structure on Aerosol Yields from OH Radical-Initiated Reactions of Linear, Branched, and Cyclic Alkanes in the Presence of NOx, Environmental Science & Technology, 43, 2328-2334, 10.1021/es803389s, 2009a.

Lim, Y. B. and Ziemann, P. J.: Chemistry of Secondary Organic Aerosol Formation from OH Radical-Initiated Reactions of Linear, Branched, and Cyclic Alkanes in the Presence of NO x, Aerosol Science and Technology, 43, 604-619, 10.1080/02786820902802567, 2009b.

Lintusaari, H., Kuuluvainen, H., Vanhanen, J., Salo, L., Portin, H., Järvinen, A., Juuti, P., Hietikko, R., Teinilä, K., Timonen, H., Niemi, J. V., and Rönkkö, T.: Sub-23 nm Particles Dominate Non-Volatile Particle Number Emissions of Road Traffic, Environmental Science & Technology, 57, 10763-10772, 10.1021/acs.est.3c03221, 2023.

Liu, B., Gu, Y., Wu, Y., Dai, Q., Song, S., Feng, Y., and Hopke, P. K.: Review of source analyses of ambient volatile organic compounds considering reactive losses: methods of reducing loss effects, impacts of losses, and sources, Atmos. Chem. Phys., 24, 12861-12879, 10.5194/acp-24-12861-2024, 2024.

Liu, C., Chen, D., and Chen, X. e.: Atmospheric Reactivity of Methoxyphenols: A Review, Environmental Science & Technology, 56, 2897-2916, 10.1021/acs.est.1c06535, 2022.

Liu, J., Zhang, F., Ren, J., Chen, L., Zhang, A., Wang, Z., Zou, S., Xu, H., and Yue, X.: The evolution of aerosol mixing state derived from a field campaign in Beijing: implications for particle aging timescales in urban atmospheres, Atmos. Chem. Phys., 25, 5075-5086, 10.5194/acp-25-5075-2025, 2025.

Liu, T., Wang, Z., Wang, X., and Chan, C. K.: Primary and secondary organic aerosol from heated cooking oil emissions, Atmospheric Chemistry and Physics, 18, 11363-11374, 10.5194/acp-18-11363-2018, 2018a.

Liu, T., Wang, Z., Huang, D. D., Wang, X., and Chan, C. K.: Significant Production of Secondary Organic Aerosol from Emissions of Heated Cooking Oils, Environmental Science & Technology Letters, 5, 32-37, 10.1021/acs.estlett.7b00530, 2018b.

Mahilang, M., Deb, M. K., and Pervez, S.: Biogenic secondary organic aerosols: A review on formation mechanism, analytical challenges and environmental impacts, Chemosphere, 262, 127771, 10.1016/j.chemosphere.2020.127771, 2021.

Malik, T. G., Sahu, L. K., Gupta, M., Mir, B. A., Gajbhiye, T., Dubey, R., Clavijo McCormick, A., and Pandey, S. K.: Environmental Factors Affecting Monoterpene Emissions from Terrestrial Vegetation, Plants (Basel), 12, 10.3390/plants12173146, 2023.

Marais, E. A., Jacob, D. J., Jimenez, J. L., Campuzano-Jost, P., Day, D. A., Hu, W., Krechmer, J., Zhu, L., Kim, P. S., Miller, C. C., Fisher, J. A., Travis, K., Yu, K., Hanisco, T. F., Wolfe, G. M., Arkinson, H. L., Pye, H. O. T., Froyd, K. D., Liao, J., and McNeill, V. F.: Aqueous-phase mechanism for secondary organic aerosol formation from isoprene: application to the Southeast United States and co-benefit of SO(2) emission controls, Atmos Chem Phys, 16, 1603-1618, 10.5194/acp-16-1603-2016, 2016.

Massoli, P., Stark, H., Canagaratna, M. R., Krechmer, J. E., Xu, L., Ng, N. L., Mauldin, R. L., Yan, C., Kimmel, J., Misztal, P. K., Jimenez, J. L., Jayne, J. T., and Worsnop, D. R.: Ambient Measurements of Highly Oxidized Gas-Phase Molecules during the Southern Oxidant and Aerosol Study (SOAS) 2013, ACS Earth and Space Chemistry, 2, 653-672, 10.1021/acsearthspacechem.8b00028, 2018.

McDonald, B. C., de Gouw, J. A., Gilman, J. B., Jathar, S. H., Akherati, A., Cappa, C. D., Jimenez, J. L., Lee-Taylor, J., Hayes, P. L., McKeen, S. A., Cui, Y. Y., Kim, S.-W., Gentner, D. R., Isaacman-VanWertz, G., Goldstein, A. H., Harley, R. A., Frost, G. J., Roberts, J. M., Ryerson, T. B., and Trainer, M.: Volatile chemical products emerging as largest petrochemical source of urban organic emissions, Science, 359, 760-764, 10.1126/science.aaq0524, 2018.

Mentes, D., Tóth, C. E., Nagy, G., Muránszky, G., and Póliska, C.: Investigation of gaseous and solid pollutants emitted from waste tire combustion at different temperatures, Waste Management, 149, 302-312, 2022.

Menut, L., Cholakian, A., Siour, G., Lapere, R., Pennel, R., Mailler, S., and Bessagnet, B.: Impact of Landes forest fires on air quality in France during the 2022 summer, Atmos. Chem. Phys., 23, 7281-7296, 10.5194/acp-23-7281-2023, 2023.

Middlebrook, A. M., Bahreini, R., Jimenez, J. L., and Canagaratna, M. R.: Evaluation of Composition-Dependent Collection Efficiencies for the Aerodyne Aerosol Mass Spectrometer using Field Data, Aerosol Science and Technology, 46, 258-271, 10.1080/02786826.2011.620041, 2012.

Milani, J. M. and Dehghan, B.: Biodegradable Polyesters for Food Packaging: An Overview on Classification, Biosynthesis, and Recent Applications, Journal of Research & Innovation in Food Science & Technology, 13, 2024.

Mohd Hanif, N., Limi Hawari, N. S. S., Othman, M., Abd Hamid, H. H., Ahamad, F., Uning, R., Ooi, M. C. G., Wahab, M. I. A., Sahani, M., and Latif, M. T.: Ambient volatile organic compounds in tropical environments: Potential sources, composition and impacts - A review, Chemosphere, 285, 131355, 10.1016/j.chemosphere.2021.131355, 2021.

Mohr, C., DeCarlo, P. F., Heringa, M. F., Chirico, R., Slowik, J. G., Richter, R., Reche, C., Alastuey, A., Querol, X., Seco, R., Peñuelas, J., Jiménez, J. L., Crippa, M., Zimmermann, R., Baltensperger, U., and Prévôt, A. S. H.: Identification and quantification of organic aerosol from cooking and other sources in Barcelona using aerosol mass spectrometer data, Atmos. Chem. Phys., 12, 1649-1665, 10.5194/acp-12-1649-2012, 2012.

Molteni, U., Bianchi, F., Klein, F., El Haddad, I., Frege, C., Rossi, M. J., Dommen, J., and Baltensperger, U.: Formation of highly oxygenated organic molecules from aromatic compounds, Atmospheric Chemistry and Physics, 18, 1909-1921, 10.5194/acp-18-1909-2018, 2018.

Montero-Montoya, R., Lopez-Vargas, R., and Arellano-Aguilar, O.: Volatile Organic Compounds in Air: Sources, Distribution, Exposure and Associated Illnesses in Children, Ann Glob Health, 84, 225-238, 10.29024/aogh.910, 2018.

Muller, M., Eichler, P., D'Anna, B., Tan, W., and Wisthaler, A.: Direct Sampling and Analysis of Atmospheric Particulate Organic Matter by Proton-Transfer-Reaction Mass Spectrometry, Anal Chem, 89, 10889-10897, 10.1021/acs.analchem.7b02582, 2017.

Müller, M., George, C., and D'Anna, B.: Enhanced spectral analysis of C-TOF Aerosol Mass Spectrometer data: Iterative residual analysis and cumulative peak fitting, International Journal of Mass Spectrometry, 306, 1-8, https://doi.org/10.1016/j.ijms.2011.04.007, 2011.

Müller, M., Eichler, P., D'Anna, B., Tan, W., and Wisthaler, A.: Direct Sampling and Analysis of Atmospheric Particulate Organic Matter by Proton-Transfer-Reaction Mass Spectrometry, Analytical Chemistry, 89, 10889-10897, 10.1021/acs.analchem.7b02582, 2017.

Müller, M., Mikoviny, T., Jud, W., D'Anna, B., and Wisthaler, A.: A new software tool for the analysis of high resolution PTR-TOF mass spectra, Chemometrics and Intelligent Laboratory Systems, 127, 158-165, 10.1016/j.chemolab.2013.06.011, 2013.

München, S.: LHM Stat. Faltkarte, https://stadt.muenchen.de/infos/statistik-stadtteilinformationen.html. 2023.

Mutzel, A., Rodigast, M., Iinuma, Y., Böge, O., and Herrmann, H.: Monoterpene SOA – Contribution of first-generation oxidation products to formation and chemical composition, Atmospheric Environment, 130, 136-144, 10.1016/j.atmosenv.2015.10.080, 2016.

Nakao, S., Clark, C., Tang, P., Sato, K., and Cocker Iii, D.: Secondary organic aerosol formation from phenolic compounds in the absence of NO_x, Atmospheric Chemistry and Physics, 11, 10649-10660, 10.5194/acp-11-10649-2011, 2011a.

Nakao, S., Clark, C., Tang, P., Sato, K., and Cocker Iii, D.: Secondary organic aerosol formation from phenolic compounds in the absence of NO_x, Atmos. Chem. Phys., 11, 10649-10660, 10.5194/acp-11-10649-2011, 2011b.

Nakhjirgan, P., Fanaei, F., Jonidi Jafari, A., Gholami, M., Shahsavani, A., and Kermani, M.: Extensive investigation of seasonal and spatial fluctuations of BTEX in an industrial city with a health risk assessment, Sci Rep, 14, 23662, 10.1038/s41598-024-74901-8, 2024.

Nareman Adeem Shnaa Aljazy and Abdulstar, A. R.: Antioxidant activity and the laxative agent of red hawthorn (Crataegus sumbollis) in jam industry, Journal of Survey in Fisheries Sciences, 10, 1257-1271, 2023.

Nimbkar, S., Leena, M. M., Moses, J. A., and Anandharamakrishnan, C.: Medium chain triglycerides (MCT): State-of-the-art on chemistry, synthesis, health benefits and applications in food industry, Comprehensive Reviews in Food Science and Food Safety, 21, 843-867, https://doi.org/10.1111/1541-4337.12926, 2022.

Niu, G., Qi, X., Chen, L., Xue, L., Lai, S., Huang, X., Wang, J., Chi, X., Nie, W., Kerminen, V. M., Petäjä, T., Kulmala, M., and Ding, A.: The variation in the particle number size distribution during the rainfall: wet scavenging and air mass changing, Atmos. Chem. Phys., 23, 7521-7534, 10.5194/acp-23-7521-2023, 2023.

Niu, Y., Yan, Y., Li, J., Liu, P., Liu, Z., Hu, D., Peng, L., and Wu, J.: Establishment and verification of anthropogenic volatile organic compound emission inventory in a typical coal resource-based city, Environ Pollut, 288, 117794, 10.1016/j.envpol.2021.117794, 2021.

Noziere, B., Kalberer, M., Claeys, M., Allan, J., D'Anna, B., Decesari, S., Finessi, E., Glasius, M., Grgic, I., Hamilton, J. F., Hoffmann, T., Iinuma, Y., Jaoui, M., Kahnt, A., Kampf, C. J., Kourtchev, I., Maenhaut, W., Marsden, N., Saarikoski, S., Schnelle-Kreis, J., Surratt, J. D., Szidat, S., Szmigielski, R., and Wisthaler, A.: The molecular identification of organic compounds in the atmosphere: state of the art and challenges, Chem Rev, 115, 3919-3983, 10.1021/cr5003485, 2015.

Ofner, J., Krüger, H. U., Grothe, H., Schmitt-Kopplin, P., Whitmore, K., and Zetzsch, C.: Physico-chemical characterization of SOA derived from catechol and guaiacol – a model substance for the aromatic fraction of atmospheric HULIS, Atmos. Chem. Phys., 11, 1-15, 10.5194/acp-11-1-2011, 2011.

Ortega, A. M., Day, D. A., Cubison, M. J., Brune, W. H., Bon, D., de Gouw, J. A., and Jimenez, J. L.: Secondary organic aerosol formation and primary organic aerosol oxidation from biomass-burning smoke in a flow reactor during FLAME-3, Atmospheric Chemistry and Physics, 13, 11551-11571, 10.5194/acp-13-11551-2013, 2013.

Paatero, P.: Least squares formulation of robust non-negative factor analysis, Chemometrics and Intelligent Laboratory Systems, 37, 23-35, https://doi.org/10.1016/S0169-7439(96)00044-5, 1997.

Paatero, P.: The Multilinear Engine—A Table-Driven, Least Squares Program for Solving Multilinear Problems, Including then-Way Parallel Factor Analysis Model, Journal of Computational and Graphical Statistics, 8, 854-888, 10.1080/10618600.1999.10474853, 1999.

Paatero, P. and Tapper, U.: Positive matrix factorization: A non-negative factor model with optimal utilization of error estimates of data values, Environmetrics, 5, 111-126, 10.1002/env.3170050203, 1994.

Pagonis, D., Sekimoto, K., and de Gouw, J.: A Library of Proton-Transfer Reactions of H3O+ Ions Used for Trace Gas Detection, Journal of the American Society for Mass Spectrometry, 30, 1330-1335, 10.1007/s13361-019-02209-3, 2019.

Panda, J., Sarkar, A., and Giri, R. K.: Atmospheric aerosols and their effects on radiation, clouds, and precipitation in different meteorological scenarios, Vayumandal, 49, 50-87, 2023.

Parshintsev, J., Nurmi, J., Kilpelainen, I., Hartonen, K., Kulmala, M., and Riekkola, M. L.: Preparation of beta-caryophyllene oxidation products and their determination in ambient aerosol samples, Anal Bioanal Chem, 390, 913-919, 10.1007/s00216-007-1755-4, 2008.

Penuelas, J., Filella, I., Stefanescu, C., and Llusia, J.: Caterpillars of Euphydryas aurinia (Lepidoptera: Nymphalidae) feeding on Succisa pratensis leaves induce large foliar emissions of methanol, New Phytol, 167, 851-857, 10.1111/j.1469-8137.2005.01459.x, 2005.

Pereira, K. L., Hamilton, J. F., Rickard, A. R., Bloss, W. J., Alam, M. S., Camredon, M., Ward, M. W., Wyche, K. P., Muñoz, A., Vera, T., Vázquez, M., Borrás, E., and Ródenas, M.: Insights into the Formation and Evolution of Individual Compounds in the Particulate Phase during Aromatic Photo-Oxidation, Environmental Science & Technology, 49, 13168-13178, 10.1021/acs.est.5b03377, 2015.

Peter F. DeCarlo, Joel R. Kimmel, Achim Trimborn, Megan J. Northway, John T. Jayne, Allison C. Aiken, Marc Gonin, Katrin Fuhrer, Thomas Horvath, Kenneth S. Docherty, Doug R. Worsnop, and Jimenez, a. J. L.: Field-Deployable, High-Resolution, Time-of-FlightAerosol Mass Spectrometer, Analytical Chemistry, 78, 8169-8575, 10.1029/2001jd001213, 2006.

Philippe Dagaut, Zahraa Dbouk , Nesrine Belhadj , Maxence Lailliau , and Benoit, R.: On the combustion of terpenes biofuels, ASME Turbo Expo 2024: Turbomachinery Technical Conference and Exposition, London, United Kingdom, DOI: 10.1115/GT2024-121549, 2024.

Piel, F., Müller, M., Mikoviny, T., Pusede, S. E., and Wisthaler, A.: Airborne measurements of particulate organic matter by proton-transfer-reaction mass spectrometry (PTR-MS): a pilot study, Atmos. Meas. Tech., 12, 5947-5958, 10.5194/amt-12-5947-2019, 2019.

Pingqing Fu, Kimitaka Kawamura, and Barrie, L. A.: Photochemical and Other Sources of Organic Compounds in the Canadian High Arctic Aerosol Pollution during Winter−Spring, Environmental Science & Technology, 43, 286–292, https://doi.org/10.1021/es803046q, 2008.

Pullinen, I., Schmitt, S., Kang, S., Sarrafzadeh, M., Schlag, P., Andres, S., Kleist, E., Mentel, T. F., Rohrer, F., Springer, M., Tillmann, R., Wildt, J., Wu, C., Zhao, D., Wahner, A., and Kiendler-Scharr, A.: Impact of NOx on secondary organic aerosol (SOA) formation from α-pinene and β-pinene photooxidation: the role of highly oxygenated organic nitrates, Atmos. Chem. Phys., 20, 10125-10147, 10.5194/acp-20-10125-2020, 2020.

Pye, H. O. T., Chan, A. W. H., Barkley, M. P., and Seinfeld, J. H.: Global modeling of organic aerosol: the importance of reactive nitrogen, Atmospheric Chemistry and Physics, 10, 11261-11276, 10.5194/acp-10-11261-2010, 2010.

Qadir, R. M., Abbaszade, G., Schnelle-Kreis, J., Chow, J. C., and Zimmermann, R.: Concentrations and source contributions of particulate organic matter before and after implementation of a low emission zone in Munich, Germany, Environ Pollut, 175, 158-167, 10.1016/j.envpol.2013.01.002, 2013.

Rattanavaraha, W., Chu, K., Budisulistiorini, S. H., Riva, M., Lin, Y. H., Edgerton, E. S., Baumann, K., Shaw, S. L., Guo, H., King, L., Weber, R. J., Neff, M. E., Stone, E. A., Offenberg, J. H., Zhang, Z., Gold, A., and Surratt, J. D.: Assessing the impact of anthropogenic pollution on isoprene-derived secondary organic aerosol formation in PM(2.5) collected from the Birmingham, Alabama, ground site during the 2013 Southern Oxidant and Aerosol Study, Atmos Chem Phys, 16, 4897-4914, 10.5194/acp-16-4897-2016, 2017.

Reinecke, T., Leiminger, M., Jordan, A., Wisthaler, A., and Muller, M.: Ultrahigh Sensitivity PTR-MS Instrument with a Well-Defined Ion Chemistry, Anal Chem, 95, 11879-11884, 10.1021/acs.analchem.3c02669, 2023.

Reyes-Villegas, E., Green, D. C., Priestman, M., Canonaco, F., Coe, H., Prévôt, A. S. H., and Allan, J. D.: Organic aerosol source apportionment in London 2013 with ME-2: exploring the solution space with annual and seasonal analysis, Atmospheric Chemistry and Physics, 16, 15545-15559, 10.5194/acp-16-15545-2016, 2016.

Reyes-Villegas, E., Bannan, T., Le Breton, M., Mehra, A., Priestley, M., Percival, C., Coe, H., and Allan, J. D.: Online Chemical Characterization of Food-Cooking Organic Aerosols: Implications for Source Apportionment, Environ Sci Technol, 52, 5308-5318, 10.1021/acs.est.7b06278, 2018.

Rios, J. C. R.: Atmospheric Chemistry of Isoprene Hydroxyhydroperoxides, The Department of Chemistry and Chemical Biology, Harvard University, 159 pp., 2018.

Riva, M., Budisulistiorini, S. H., Chen, Y., Zhang, Z., D'Ambro, E. L., Zhang, X., Gold, A., Turpin, B. J., Thornton, J. A., Canagaratna, M. R., and Surratt, J. D.: Chemical Characterization of Secondary Organic Aerosol from Oxidation of Isoprene Hydroxyhydroperoxides, Environ Sci Technol, 50, 9889-9899, 10.1021/acs.est.6b02511, 2016.

Romanias, M. N., Coggon, M. M., Al Ali, F., Burkholder, J. B., Dagaut, P., Decker, Z., Warneke, C., Stockwell, C. E., Roberts, J. M., Tomas, A., Houzel, N., Coeur, C., and Brown, S. S.: Emissions and Atmospheric Chemistry of Furanoids from Biomass Burning: Insights from Laboratory to Atmospheric Observations, ACS Earth and Space Chemistry, 8, 857-899, 10.1021/acsearthspacechem.3c00226, 2024.

Saarikoski, S., Niemi, J. V., Aurela, M., Pirjola, L., Kousa, A., Rönkkö, T., and Timonen, H.: Sources of black carbon at residential and traffic environments obtained by two source apportionment methods, Atmos. Chem. Phys., 21, 14851-14869, 10.5194/acp-21-14851-2021, 2021.

Saathoff, H., Naumann, K. H., Möhler, O., Jonsson, Å. M., Hallquist, M., Kiendler-Scharr, A., Mentel, T. F., Tillmann, R., and Schurath, U.: Temperature dependence of yields of secondary organic aerosols from the ozonolysis of α-pinene and limonene, Atmos. Chem. Phys., 9, 1551-1577, 10.5194/acp-9-1551-2009, 2009.

Saeed, S., Aslam, S., Mehmood, T., Naseer, R., Nawaz, S., Mujahid, H., Firyal, S., Anjum, A. A., and Sultan, A.: Production of Gallic Acid Under Solid-State Fermentation by Utilizing Waste from Food Processing Industries, Waste and Biomass Valorization, 12, 155-163, 10.1007/s12649-020-00980-z, 2021.

Schäfer, K., Elsasser, M., Arteaga-Salas, J. M., Gu, J., Pitz, M., Schnelle-Kreis, J., Cyrys, J., Emeis, S., Prevot, A. S. H., and Zimmermann, R.: Source apportionment and the role of meteorological conditions in the assessment of air pollution exposure due to urban emissions, Atmos. Chem. Phys. Discuss., 2014, 2235-2275, 10.5194/acpd-14-2235-2014, 2014.

Schilling Fahnestock, K. A., Yee, L. D., Loza, C. L., Coggon, M. M., Schwantes, R., Zhang, X., Dalleska, N. F., and Seinfeld, J. H.: Secondary Organic Aerosol Composition from C12 Alkanes, The Journal of Physical Chemistry A, 119, 4281-4297, 10.1021/jp501779w, 2015.

Schnell, F. I. J.: Aerosol distribution above Munich using remote sensing techniques, 2014.

Schnelle-Kreis J., Istvan Gebefügi, Gerhard Welzl, Thomas Jaensch, and Kettrup, A.: Occurrence of particle-associated polycyclic aromatic compounds in ambient air of the city of Munich, Atmospheric Environment, 35, S71-S81, https://doi.org/10.1016/S1352-2310(00)00557-4, 2001.

Scholz, W., Shen, J., Aliaga, D., Wu, C., Carbone, S., Moreno, I., Zha, Q., Huang, W., Heikkinen, L., Jaffrezo, J. L., Uzu, G., Partoll, E., Leiminger, M., Velarde, F., Laj, P., Ginot, P., Artaxo, P., Wiedensohler, A., Kulmala, M., Mohr, C., Andrade, M., Sinclair, V., Bianchi, F., and Hansel, A.: Measurement report: Long-range transport and the fate of dimethyl sulfide oxidation products in the free troposphere derived from observations at the high-altitude research station Chacaltaya (5240 m a.s.l.) in the Bolivian Andes, Atmospheric Chemistry and Physics, 23, 895-920, 10.5194/acp-23-895-2023, 2023.

Schwantes, R. H., Charan, S. M., Bates, K. H., Huang, Y., Nguyen, T. B., Mai, H., Kong, W., Flagan, R. C., and Seinfeld, J. H.: Low-volatility compounds contribute significantly to isoprene secondary organic aerosol (SOA) under high-NOx conditions, Atmospheric Chemistry and Physics, 19, 7255-7278, 10.5194/acp-19-7255-2019, 2019.

Sekimoto, K., Li, S.-M., Yuan, B., Koss, A., Coggon, M., Warneke, C., and de Gouw, J.: Calculation of the sensitivity of proton-transfer-reaction mass spectrometry (PTR-MS) for organic trace gases using molecular properties, International Journal of Mass Spectrometry, 421, 71-94, https://doi.org/10.1016/j.ijms.2017.04.006, 2017.

Setyan, A., Zhang, Q., Merkel, M., Knighton, W. B., Sun, Y., Song, C., Shilling, J. E., Onasch, T. B., Herndon, S. C., Worsnop, D. R., Fast, J. D., Zaveri, R. A., Berg, L. K., Wiedensohler, A., Flowers, B. A., Dubey, M. K., and Subramanian, R.: Characterization of submicron particles influenced by mixed biogenic and anthropogenic emissions using high-resolution aerosol mass spectrometry: results from CARES, Atmospheric Chemistry and Physics, 12, 8131-8156, 10.5194/acp-12-8131-2012, 2012.

Shi, Q., Tang, W., Kong, K., Liu, X., Wang, Y., and Duan, H.: Electrocatalytic Upgrading of Plastic and Biomass-Derived Polyols to Formamide under Ambient Conditions, Angewandte Chemie, 136, e202407580, 2024.

Shrivastava, M., Cappa, C. D., Fan, J., Goldstein, A. H., Guenther, A. B., Jimenez, J. L., Kuang, C., Laskin, A., Martin, S. T., Ng, N. L., Petaja, T., Pierce, J. R., Rasch, P. J., Roldin, P., Seinfeld, J. H., Shilling, J., Smith, J. N., Thornton, J. A., Volkamer, R., Wang, J., Worsnop, D. R., Zaveri, R. A., Zelenyuk, A., and Zhang, Q.: Recent advances in understanding secondary organic aerosol: Implications for global climate forcing, Reviews of Geophysics, 55, 509-559, 10.1002/2016rg000540, 2017.

Simoneit, B. R. T.: Biomass burning—a review of organic tracers for smoke from incomplete combustion, Applied Geochemistry, 17, 129-162, https://doi.org/10.1016/S0883-2927(01)00061-0, 2002.

Song, J., Gkatzelis, G. I., Tillmann, R., Brüggemann, N., Leisner, T., and Saathoff, H.: Characterization of biogenic volatile organic compounds and their oxidation products in a stressed spruce-dominated forest close to a biogas power plant, Atmospheric Chemistry and Physics, 24, 13199-13217, 10.5194/acp-24-13199-2024, 2024a.

Song, J., Saathoff, H., Jiang, F., Gao, L., Zhang, H., and Leisner, T.: Sources of organic gases and aerosol particles and their roles in nighttime particle growth at a rural forested site in southwest Germany, Atmospheric Chemistry and Physics, 24, 6699-6717, 10.5194/acp-24-6699-2024, 2024b.

Song, J., Saathoff, H., Gao, L., Gebhardt, R., Jiang, F., Vallon, M., Bauer, J., Norra, S., and Leisner, T.: Variations of PM2.5 sources in the context of meteorology and seasonality at an urban street canyon in Southwest Germany, Atmospheric Environment, 282, 10.1016/j.atmosenv.2022.119147, 2022.

Sporre, M. K., Blichner, S. M., Schrödner, R., Karset, I. H. H., Berntsen, T. K., van Noije, T., Bergman, T., O'Donnell, D., and Makkonen, R.: Large difference in aerosol radiative effects from BVOC-SOA treatment in three Earth system models, Atmos. Chem. Phys., 20, 8953-8973, 10.5194/acp-20-8953-2020, 2020.

Squires, F. A., Nemitz, E., Langford, B., Wild, O., Drysdale, W. S., Acton, W. J. F., Fu, P., Grimmond, C. S. B., Hamilton, J. F., Hewitt, C. N., Hollaway, M., Kotthaus, S., Lee, J., Metzger, S., Pingintha-Durden, N., Shaw, M., Vaughan, A. R., Wang, X., Wu, R., Zhang, Q., and Zhang, Y.: Measurements of traffic-dominated pollutant emissions in a Chinese megacity, Atmospheric Chemistry and Physics, 20, 8737-8761, 10.5194/acp-20-8737-2020, 2020.

Srivastava, D., Vu, T. V., Tong, S., Shi, Z., and Harrison, R. M.: Formation of secondary organic aerosols from anthropogenic precursors in laboratory studies, npj Climate and Atmospheric Science, 5, 10.1038/s41612-022-00238-6, 2022.

Stockwell, C. E., Coggon, M. M., Gkatzelis, G. I., Ortega, J., McDonald, B. C., Peischl, J., Aikin, K., Gilman, J. B., Trainer, M., and Warneke, C.: Volatile organic compound emissions from solvent- and water-borne coatings – compositional differences and tracer compound identifications, Atmos. Chem. Phys., 21, 6005-6022, 10.5194/acp-21-6005-2021, 2021.

Surratt, J. D., Chan, A. W., Eddingsaas, N. C., Chan, M., Loza, C. L., Kwan, A. J., Hersey, S. P., Flagan, R. C., Wennberg, P. O., and Seinfeld, J. H.: Reactive intermediates revealed in secondary organic aerosol formation from isoprene, Proc Natl Acad Sci U S A, 107, 6640-6645, 10.1073/pnas.0911114107, 2010.

Taiti, C., Costa, C., Figorilli, S., Billi, M., Caparrotta, S., Comparini, D., and Mancuso, S.: Volatome analysis approach for the taxonomic classification of tree exudate collection using Proton Transfer Reaction Time of Flight Mass Spectrometry, Flavour and Fragrance Journal, 33, 245-262, 10.1002/ffj.3439, 2018.

Tang, R., Wu, Z., Li, X., Wang, Y., Shang, D., Xiao, Y., Li, M., Zeng, L., Wu, Z., Hallquist, M., Hu, M., and Guo, S.: Primary and secondary organic aerosols in summer 2016 in Beijing, Atmos. Chem. Phys., 18, 4055-4068, 10.5194/acp-18-4055-2018, 2018.

Thomas, A. E., Glicker, H. S., Guenther, A. B., Seco, R., Vega Bustillos, O., Tota, J., Souza, R. A. F., and Smith, J. N.: Seasonal investigation of ultrafine-particle organic composition in an eastern Amazonian rainforest, Atmos. Chem. Phys., 25, 959-977, 10.5194/acp-25-959-2025, 2025.

Thornton, J. A., Mohr, C., Schobesberger, S., D'Ambro, E. L., Lee, B. H., and Lopez-Hilfiker, F. D.: Evaluating Organic Aerosol Sources and Evolution with a Combined Molecular Composition and Volatility Framework Using the Filter Inlet for Gases and Aerosols (FIGAERO), Acc Chem Res, 53, 1415-1426, 10.1021/acs.accounts.0c00259, 2020.

Timkovsky, J., Dusek, U., Henzing, J. S., Kuipers, T. L., Röckmann, T., and Holzinger, R.: Offline thermal-desorption proton-transfer-reaction mass spectrometry to study composition of organic aerosol, Journal of Aerosol Science, 79, 1-14, https://doi.org/10.1016/j.jaerosci.2014.08.010, 2015.

Todea, A., Deganutti, C., Spennato, M., Asaro, F., Zingone, G., Milizia, T., and Gardossi, L.: Azelaic Acid: A Bio-Based Building Block for Biodegradable Polymers, 10.3390/polym13234091, 2021.

Tong, L., Zhang, J., Xu, H., Xiao, H., He, M., and Zhang, H.: Contribution of Regional Transport to Surface Ozone at an Island Site of Eastern China, Aerosol and Air Quality Research, 18, 3009-3024, 10.4209/aaqr.2017.11.0508, 2018.

Tong, Y., Qi, L., Stefenelli, G., Wang, D. S., Canonaco, F., Baltensperger, U., Prévôt, A. S. H., and Slowik, J. G.: Quantification of primary and secondary organic aerosol sources by combined factor analysis of extractive electrospray ionisation and aerosol mass spectrometer measurements (EESI-TOF and AMS), Atmos. Meas. Tech., 15, 7265-7291, 10.5194/amt-15-7265-2022, 2022.

Tsimpidi, A. P., Scholz, S. M. C., Milousis, A., Mihalopoulos, N., and Karydis, V. A.: Aerosol Composition Trends during 2000–2020: In depth insights from model predictions and multiple worldwide observation datasets, EGUsphere, 2024, 1-66, 2024.

Ulbrich, I. M., Canagaratna, M. R., Zhang, Q., Worsnop, D. R., and and Jimenez, J. L.: Interpretation of organic components from Positive Matrix Factorization of aerosol mass spectrometric data, Atmos. Chem. Phys., 9, 2891–2918, https://doi.org/10.5194/acp-9-2891-2009, 2009.

Upshur, M. A., Be, A. G., Luo, J., Varelas, J. G., Geiger, F. M., and Thomson, R. J.: Organic synthesis in the study of terpene-derived oxidation products in the atmosphere, Nat Prod Rep, 40, 890-921, 10.1039/d2np00064d, 2023.

Vallon, M., Gao, L., Jiang, F., Krumm, B., Nadolny, J., Song, J., Leisner, T., and Saathoff, H.: LED-based solar simulator to study photochemistry over a wide temperature range in the large simulation chamber AIDA, Atmos. Meas. Tech., 15, 1795-1810, 10.5194/amt-15-1795-2022, 2022.

Verbruggen, N. and Hermans, C.: Proline accumulation in plants: a review, Amino Acids, 35, 753-759, 10.1007/s00726-008-0061-6, 2008.

Victor, A., Sharma, P., Pulidindi, I. N., and Gedanken, A.: Levulinic Acid Is a Key Strategic Chemical from Biomass, 10.3390/catal12080909, 2022.

Vita, F., Taiti, C., Pompeiano, A., Bazihizina, N., Lucarotti, V., Mancuso, S., and Alpi, A.: Volatile organic compounds in truffle (Tuber magnatum Pico): comparison of samples from different regions of Italy and from different seasons, Sci Rep, 5, 12629, 10.1038/srep12629, 2015.

Von Schneidemesser, E., Monks, P. S., and Plass-Duelmer, C.: Global comparison of VOC and CO observations in urban areas, Atmospheric Environment, 44, 5053-5064, 10.1016/j.atmosenv.2010.09.010, 2010.

Wan, X., Kawamura, K., Ram, K., Kang, S., Loewen, M., Gao, S., Wu, G., Fu, P., Zhang, Y., Bhattarai, H., and Cong, Z.: Aromatic acids as biomass-burning tracers in atmospheric aerosols and ice cores: A review, Environ Pollut, 247, 216-228, 10.1016/j.envpol.2019.01.028, 2019.

Wan, X., Kang, S., Li, Q., Rupakheti, D., Zhang, Q., Guo, J., Chen, P., Tripathee, L., Rupakheti, M., Panday, A. K., Wang, W., Kawamura, K., Gao, S., Wu, G., and Cong, Z.: Organic molecular tracers in the atmospheric aerosols from Lumbini, Nepal, in the northern Indo-Gangetic Plain: influence of biomass burning, Atmospheric Chemistry and Physics, 17, 8867-8885, 10.5194/acp-17-8867-2017, 2017.

Wang, C., Xiang, J., Austin, E., Larson, T., and Seto, E.: Quantifying the contributions of road and air traffic to ambient ultrafine particles in two urban communities, Environmental Pollution, 348, 123892, https://doi.org/10.1016/j.envpol.2024.123892, 2024a.

Wang, H., Liu, X., Wu, C., and Lin, G.: Regional to global distributions, trends, and drivers of biogenic volatile organic compound emission from 2001 to 2020, Atmos. Chem. Phys., 24, 3309-3328, 10.5194/acp-24-3309-2024, 2024b.

Wang, Q., He, X., Zhou, M., Huang, D. D., Qiao, L., Zhu, S., Ma, Y.-g., Wang, H.-l., Li, L., Huang, C., Huang, X. H. H., Xu, W., Worsnop, D., Goldstein, A. H., Guo, H., and Yu, J. Z.: Hourly Measurements of Organic Molecular Markers in Urban Shanghai, China: Primary Organic Aerosol Source Identification and Observation of Cooking Aerosol Aging, ACS Earth and Space Chemistry, 4, 1670-1685, 10.1021/acsearthspacechem.0c00205, 2020.

Wang, W., Zhang, Y., Jiang, B., Chen, Y., Song, Y., Tang, Y., Dong, C., and Cai, Z.: Molecular characterization of organic aerosols in Taiyuan, China: Seasonal variation and source identification, Sci Total Environ, 800, 149419, 10.1016/j.scitotenv.2021.149419, 2021a.

Wang, Y., Yang, L., Zhang, K., Chen, X., Wang, H., Cheng, P., and Wang, J.: Untargeted metabolomics analysis of different grape varieties and different parts of wine grape using gas chromatography and mass spectrometry technique, Journal of Biobased Materials and Bioenergy, 15, 459-471, 2021b.

Wang, Y. Q.: An Open Source Software Suite for Multi-Dimensional Meteorological Data. Computation and Visualisation, Journal of Open Research Software, 7, 10.5334/jors.267, 2019.

Wang, Z., Wang, Z., Sun, J., Wang, Y., Sun, Z., Ma, K., and Wei, L.: Investigation of oxygen-enriched atmosphere combustion of oily sludge: Performance, mechanism, emission of the S/N-containing compound, and residue characteristics, Journal of Cleaner Production, 378, 10.1016/j.jclepro.2022.134233, 2022.

Wang, Z., Wang, Z., Zou, Z., Chen, X., Wu, H., Wang, W., Su, H., Li, F., Xu, W., Liu, Z., and Zhu, J.: Severe Global Environmental Issues Caused by Canada's Record-Breaking Wildfires in 2023, Advances in Atmospheric Sciences, 41, 565-571, 10.1007/s00376-023-3241-0, 2024c.

Warneke, C., McKeen, S. A., de Gouw, J. A., Goldan, P. D., Kuster, W. C., Holloway, J. S., Williams, E. J., Lerner, B. M., Parrish, D. D., Trainer, M., Fehsenfeld, F. C., Kato, S., Atlas, E. L., Baker, A., and Blake, D. R.: Determination of urban volatile organic compound emission ratios and comparison with an emissions database, Journal of Geophysical Research: Atmospheres, 112, 10.1029/2006jd007930, 2007.

Wennberg, P. O., Bates, K. H., Crounse, J. D., Dodson, L. G., McVay, R. C., Mertens, L. A., Nguyen, T. B., Praske, E., Schwantes, R. H., Smarte, M. D., St Clair, J. M., Teng, A. P., Zhang, X., and Seinfeld, J. H.: Gas-Phase Reactions of Isoprene and Its Major Oxidation Products, Chem Rev, 118, 3337-3390, 10.1021/acs.chemrev.7b00439, 2018.

Williams, L. R., Gonzalez, L. A., Peck, J., Trimborn, D., McInnis, J., Farrar, M. R., Moore, K. D., Jayne, J. T., Robinson, W. A., Lewis, D. K., Onasch, T. B., Canagaratna, M. R., Trimborn, A., Timko, M. T., Magoon, G., Deng, R., Tang, D., de la Rosa Blanco, E., Prévôt, A. S. H., Smith, K. A., and Worsnop, D. R.: Characterization of an aerodynamic lens for transmitting particles greater than 1 micrometer in diameter into the Aerodyne aerosol mass spectrometer, Atmospheric Measurement Techniques, 6, 3271-3280, 10.5194/amt-6-3271-2013, 2013.

Wu, T., Müller, T., Wang, N., Byron, J., Langer, S., Williams, J., and Licina, D.: Indoor Emission, Oxidation, and New Particle Formation of Personal Care Product Related Volatile Organic Compounds, Environmental Science & Technology Letters, 11, 1053-1061, 10.1021/acs.estlett.4c00353, 2024.

Wyche, K. P., Monks, P. S., Ellis, A. M., Cordell, R. L., Parker, A. E., Whyte, C., Metzger, A., Dommen, J., Duplissy, J., Prevot, A. S. H., Baltensperger, U., Rickard, A. R., and Wulfert, F.: Gas phase precursors to anthropogenic secondary organic aerosol: detailed observations of 1,3,5-trimethylbenzene photooxidation, Atmos. Chem. Phys., 9, 635-665, 10.5194/acp-9-635-2009, 2009.

Xiang, J., Hao, J., Austin, E., Shirai, J., and Seto, E.: Characterization of cooking-related ultrafine particles in a US residence and impacts of various intervention strategies, Science of The Total Environment, 798, 149236, https://doi.org/10.1016/j.scitotenv.2021.149236, 2021.

Yáñez-Serrano, A. M., Filella, I., Llusià, J., Gargallo-Garriga, A., Granda, V., Bourtsoukidis, E., Williams, J., Seco, R., Cappellin, L., Werner, C., de Gouw, J., and Peñuelas, J.: GLOVOCS - Master compound assignment guide for proton transfer reaction mass spectrometry users, Atmospheric Environment, 244, 117929, https://doi.org/10.1016/j.atmosenv.2020.117929, 2021.

Ye, C., Yuan, B., Lin, Y., Wang, Z., Hu, W., Li, T., Chen, W., Wu, C., Wang, C., Huang, S., Qi, J., Wang, B., Wang, C., Song, W., Wang, X., Zheng, E., Krechmer, J. E., Ye, P., Zhang, Z., Wang, X., Worsnop, D. R., and Shao, M.: Chemical characterization of oxygenated organic compounds in the gas phase and particle phase using iodide CIMS with FIGAERO in urban air, Atmos. Chem. Phys., 21, 8455-8478, 10.5194/acp-21-8455-2021, 2021.

Yee, L. D., Craven, J. S., Loza, C. L., Schilling, K. A., Ng, N. L., Canagaratna, M. R., Ziemann, P. J., Flagan, R. C., and Seinfeld, J. H.: Effect of chemical structure on secondary organic aerosol formation from C_{12} alkanes, Atmos. Chem. Phys., 13, 11121-11140, 10.5194/acp-13-11121-2013, 2013a.

Yee, L. D., Kautzman, K. E., Loza, C. L., Schilling, K. A., Coggon, M. M., Chhabra, P. S., Chan, M. N., Chan, A. W. H., Hersey, S. P., Crounse, J. D., Wennberg, P. O., Flagan, R. C., and Seinfeld, J. H.: Secondary organic aerosol formation from biomass burning intermediates: phenol and methoxyphenols, Atmospheric Chemistry and Physics, 13, 8019-8043, 10.5194/acp-13-8019-2013, 2013b.

Yee, L. D., Isaacman-VanWertz, G., Wernis, R. A., Meng, M., Rivera, V., Kreisberg, N. M., Hering, S. V., Bering, M. S., Glasius, M., Upshur, M. A., Gray Bé, A., Thomson, R. J., Geiger, F. M., Offenberg, J. H., Lewandowski, M., Kourtchev, I., Kalberer, M., de Sá, S., Martin, S. T., Alexander, M. L., Palm, B. B., Hu, W., Campuzano-Jost, P., Day, D. A., Jimenez, J. L., Liu, Y., McKinney, K. A., Artaxo, P., Viegas, J., Manzi, A., Oliveira, M. B., de Souza, R., Machado, L. A. T., Longo, K., and Goldstein, A. H.: Observations of sesquiterpenes and their oxidation products in central Amazonia during the wet and dry seasons, Atmospheric Chemistry and Physics, 18, 10433-10457, 10.5194/acp-18-10433-2018, 2018.

Yeoman, A. M., Shaw, M., Carslaw, N., Murrells, T., Passant, N., and Lewis, A. C.: Simplified speciation and atmospheric volatile organic compound emission rates from non-aerosol personal care products, Indoor Air, 30, 459-472, 10.1111/ina.12652, 2020.

Ylisirniö, A., Buchholz, A., Mohr, C., Li, Z., Barreira, L., Lambe, A., Faiola, C., Kari, E., Yli-Juuti, T., Nizkorodov, S. A., Worsnop, D. R., Virtanen, A., and Schobesberger, S.: Composition and volatility of secondary organic aerosol (SOA) formed from oxidation of real tree emissions compared to simplified volatile organic compound (VOC) systems, Atmos. Chem. Phys., 20, 5629-5644, 10.5194/acp-20-5629-2020, 2020.

Yuan, B., Koss, A. R., Warneke, C., Coggon, M., Sekimoto, K., and de Gouw, J. A.: Proton-Transfer-Reaction Mass Spectrometry: Applications in Atmospheric Sciences, Chem Rev, 117, 13187-13229, 10.1021/acs.chemrev.7b00325, 2017.

Zhang, B., Zhang, D., Dong, Z., Song, X., Zhang, R., and Li, X.: The variations in volatile organic compounds based on the policy change for Omicron in the traffic hub of Zhengzhou, Atmos. Chem. Phys., 24, 13587-13601, 10.5194/acp-24-13587-2024, 2024.

Zhang, P., Huang, J., Shu, J., and Yang, B.: Comparison of secondary organic aerosol (SOA) formation during o-, m-, and p-xylene photooxidation, Environmental Pollution, 245, 20-28, https://doi.org/10.1016/j.envpol.2018.10.118, 2019.

Zhang, Q., Jimenez, J. L., Canagaratna, M. R., Ulbrich, I. M., Ng, N. L., Worsnop, D. R., and Sun, Y.: Understanding atmospheric organic aerosols via factor analysis of aerosol mass spectrometry: a review, Analytical and Bioanalytical Chemistry, 401, 3045-3067, 10.1007/s00216-011-5355-y, 2011a.

Zhang, Q., Jimenez, J. L., Canagaratna, M. R., Ulbrich, I. M., Ng, N. L., Worsnop, D. R., and Sun, Y.: Understanding atmospheric organic aerosols via factor analysis of aerosol mass spectrometry: a review, Anal Bioanal Chem, 401, 3045-3067, 10.1007/s00216-011-5355-y, 2011b.

Zhang, R., Song, W., Zhang, Y., Wang, X., Fu, X., and Li, S.: Particulate nitrated aromatic compounds from corn straw burning: Compositions, optical properties and potential health risks, Environmental Pollution, 323, 121332, https://doi.org/10.1016/j.envpol.2023.121332, 2023.

Zhao, J., Mickwitz, V., Zhang, J., Alton, M., Canagaratna, M., Graeffe, F., Schobesberger, S., Worsnop, D., and Ehn, M.: Comparison of Gaseous and Particulate Highly Oxygenated Organic Molecules from the Ozonolysis of Terpenes, ACS ES&T Air, 1, 1294-1303, 10.1021/acsestair.4c00121, 2024.

Zhu, J., Wang, Q., Han, L., Zhang, C., Wang, Y., Tu, K., Peng, J., Wang, J., and Pan, L.: Effects of caprolactam content on curdlan-based food packaging film and detection by infrared spectroscopy, Spectrochimica Acta Part A: Molecular and Biomolecular Spectroscopy, 245, 118942, https://doi.org/10.1016/j.saa.2020.118942, 2021.

Appendix A

Supplement for the results and discussion in the dissertation

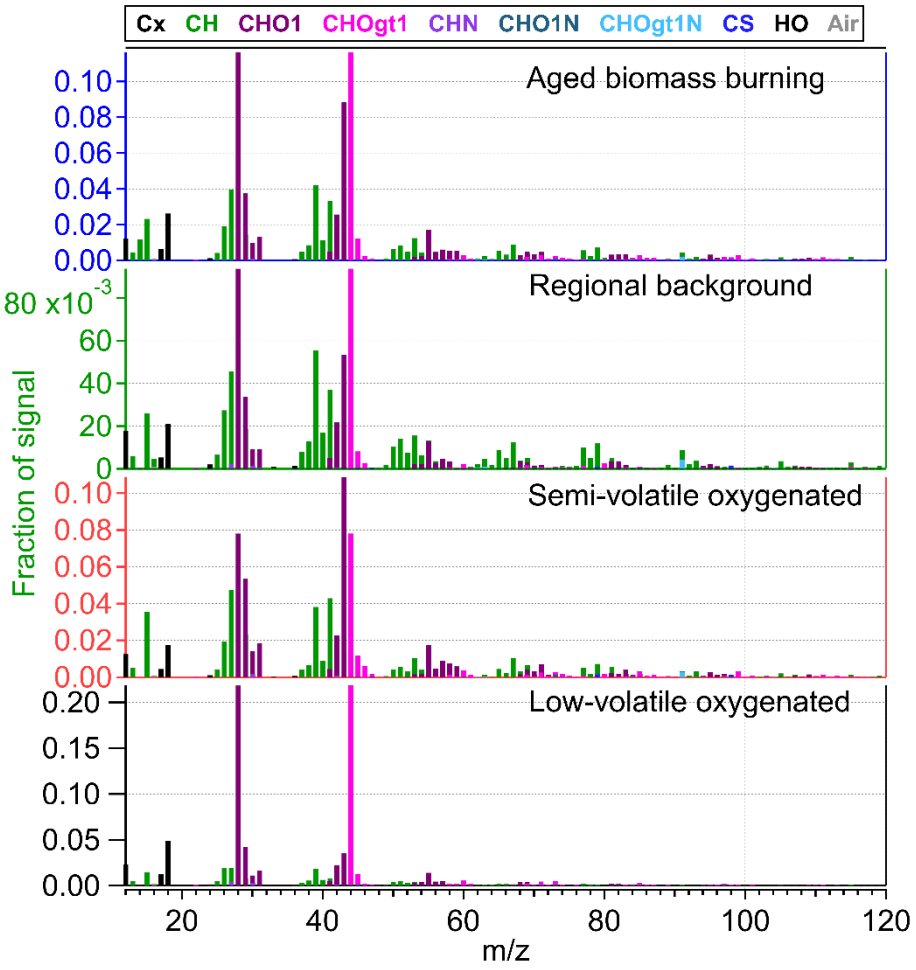

Figure S1 Source apportionment of OA measured by the AMS. Mass spectra of OA factors – Aged, Regional transported factor, Semi-Volatile oxygenated organic aerosol (SV-OOA) and Low-Volatile oxygenated organic aerosol (LV-OOA).

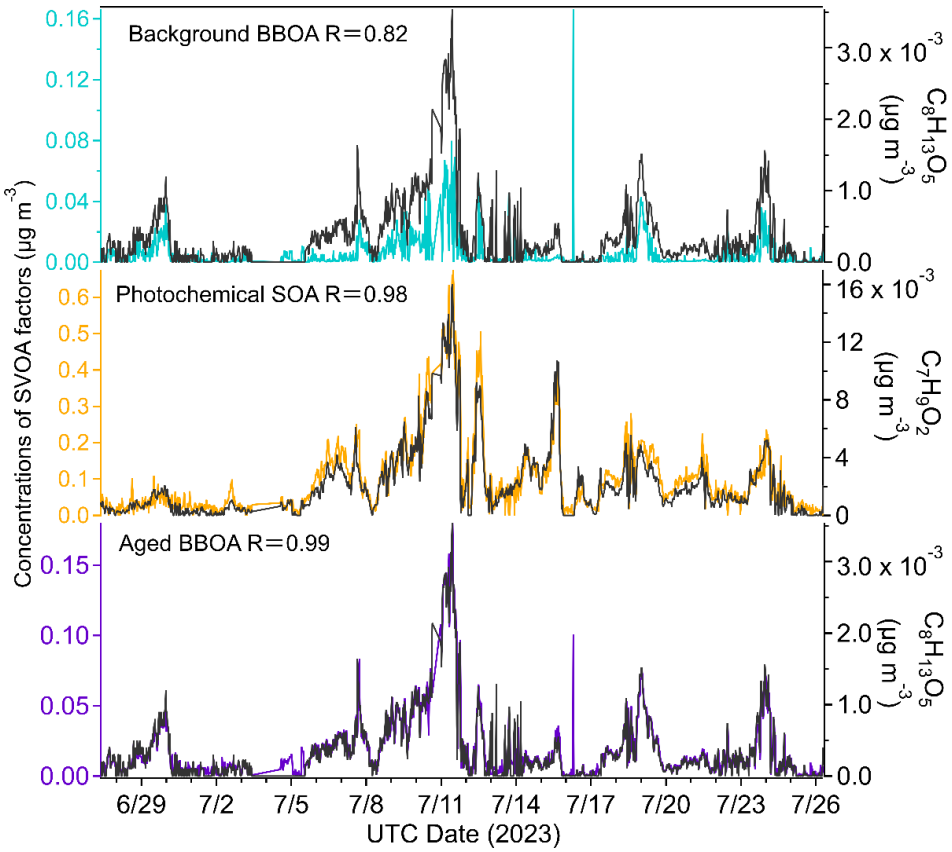

Figure S2. Time series of the three SVOA factors (Background BBOA, Photochemical SOA, and Aged BBOA) along with selected molecular marker compounds ($C_8H_{13}O_5^+$ for Background BBOA and Aged BBOA, and $C_7H_9O_2^+$ for Photochemical SOA). Correlation coefficients (R) between each factor and its respective marker compound are also shown, indicating strong associations between factor concentrations and tracer species

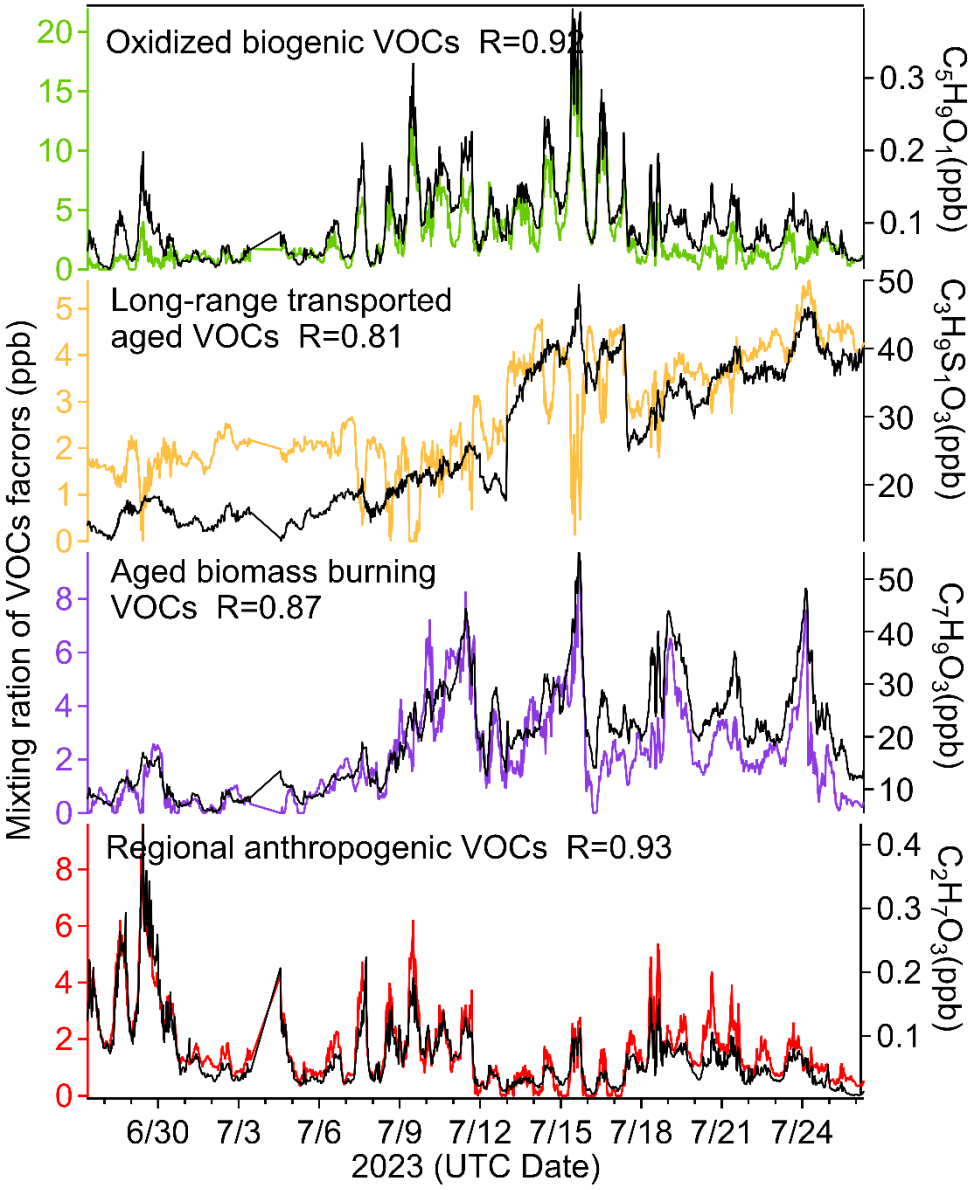

Figure S3. Temporal variation of four VOC factors and associated tracer compounds, highlighting strong correlations (R) between each VOC factor and its representative molecular markers.

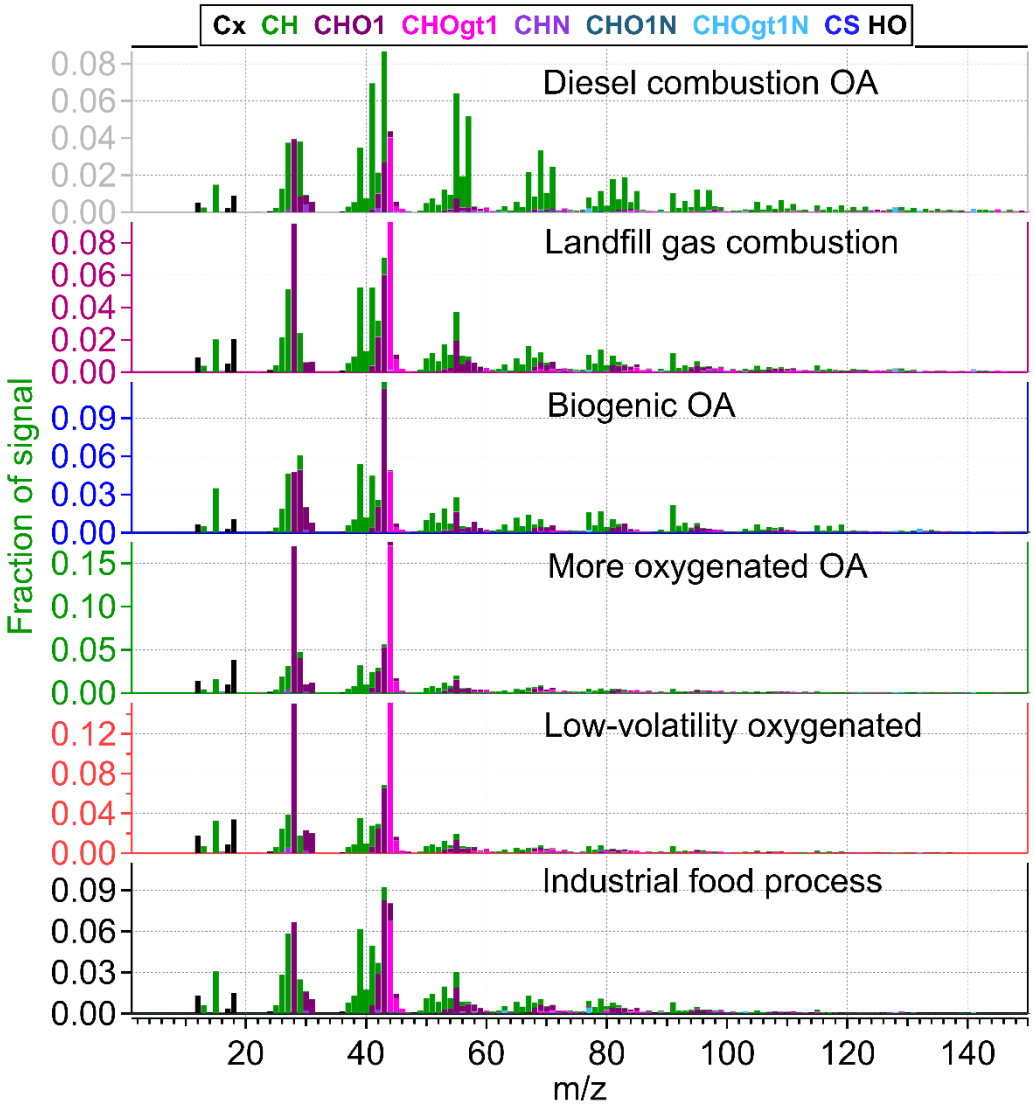

Figure S4 Source apportionment of OA measured by the AMS. Mass spectra of OA factors – Diesel combustion OA, Landfill gas combustion OA, Biogenic OA, More oxygenated OA, Low-volatility oxygenated OA and Industrial food process OA.

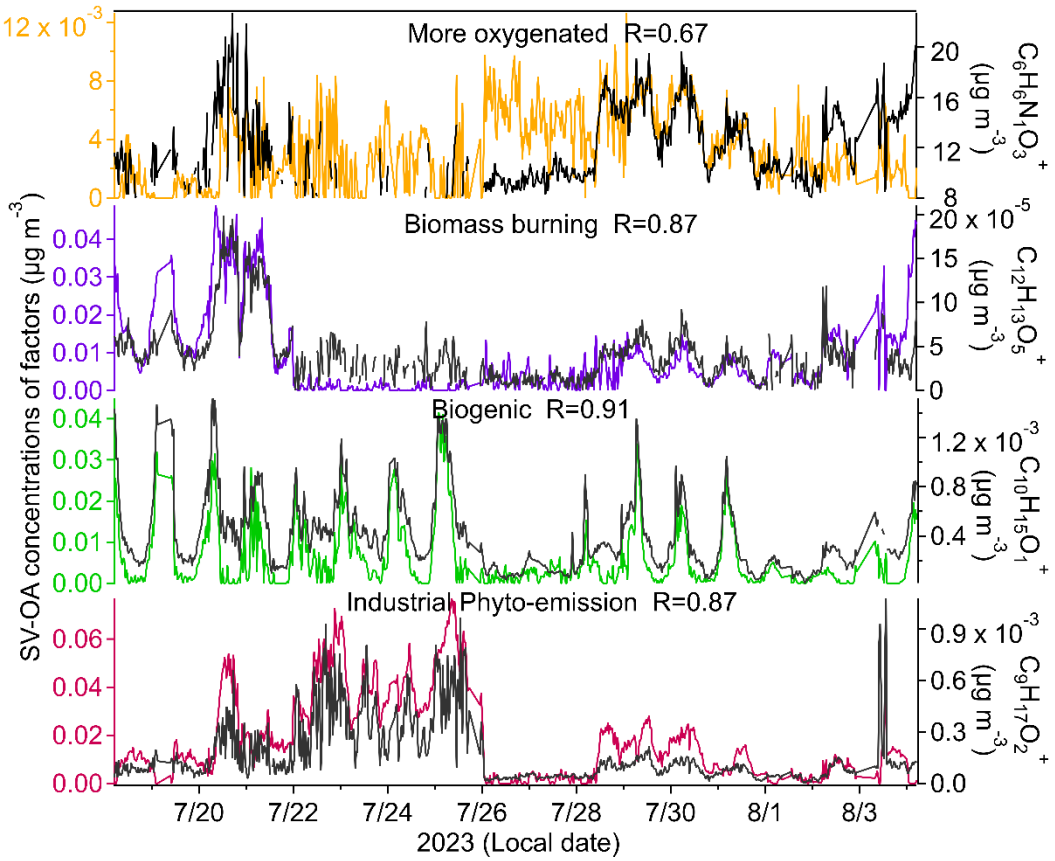

Figure S5 Time series of SV-OA factors and their tracer ions. The black lines show the concentrations of four resolved SV-OA factors: More oxygenated, Biomass burning, Biogenic, and Industrial food process SV-OA. Colored lines indicate time series of representative tracer ions: $C_6H_6N_1O_3^+$ for More oxygenated (yellow), $C_{12}H_{13}O_5^+$ for Biomass burning (purple), $C_{10}H_{15}O_1^+$ for Biogenic (green), and $C_9H_{17}O_2^+$ for Industrial Phyto-emission SV-OA (magenta). The good temporal correlations highlight the factor-specific chemical markers.

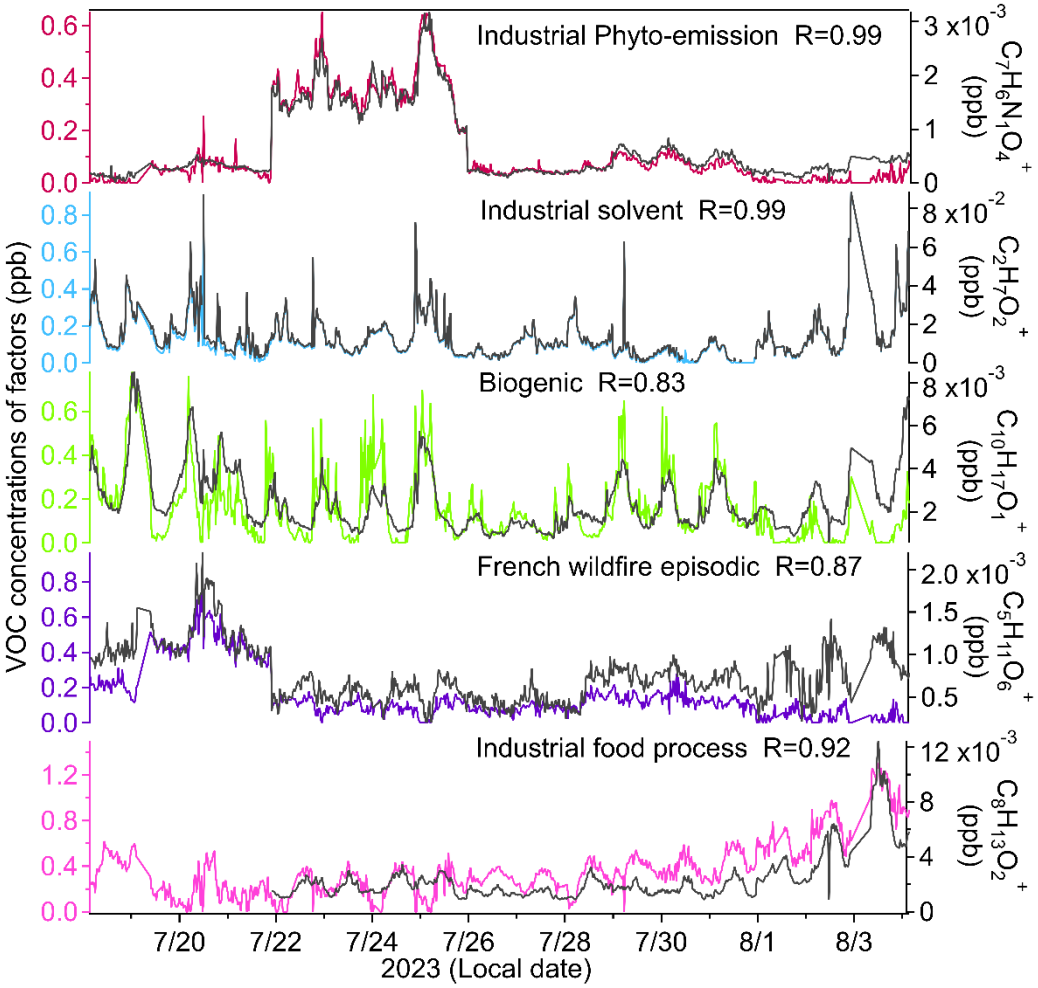

Figure S6. Time series of VOC factor concentrations (colored lines, ppb) and selected marker ions (black lines, ppb) from 19 July to 4 August 2023. Five factors are shown: Industrial Phyto-emission, Industrial solvent, Biogenic, French wildfire episodic, and Industrial food process VOC. Each panel includes the Pearson correlation coefficient (R) between the VOC factor and its representative ion, indicating the degree of temporal coherence.

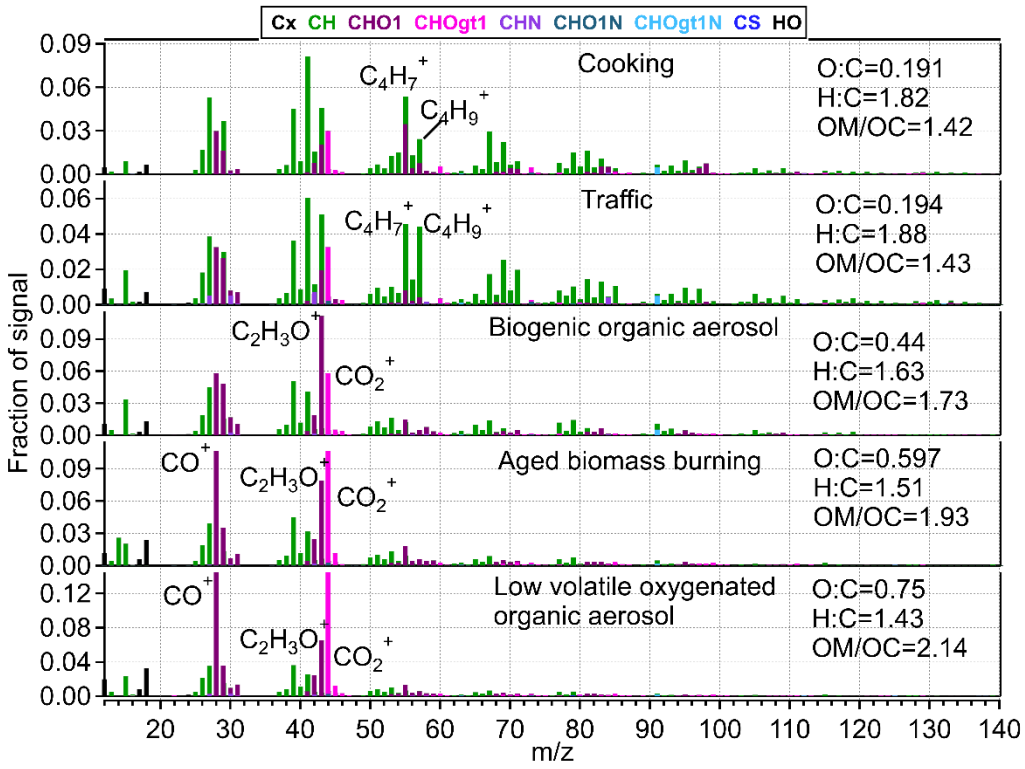

Figure S7 Source apportionment of OA in summer measured by the AMS. (a) Mass spectra of OA factors – cooking OA(COA), hydrocarbon-like OA (HOA), biogenic secondary OA(BOA), aged biomass burning aerosol (BBOA), and low-volatility oxygenated OA (LV-OOA).

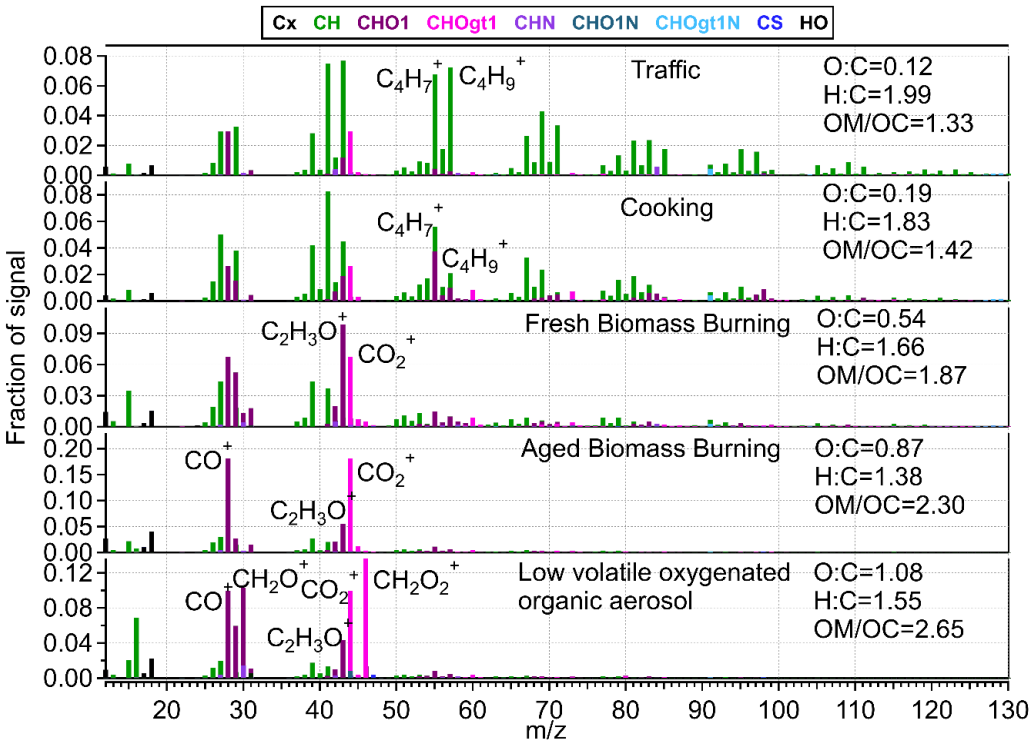

Figure S8 (a) Mass spectra of OA factors in winter– HOA, COA, fresh BBOA, aged BBOA, and LV-OOA.

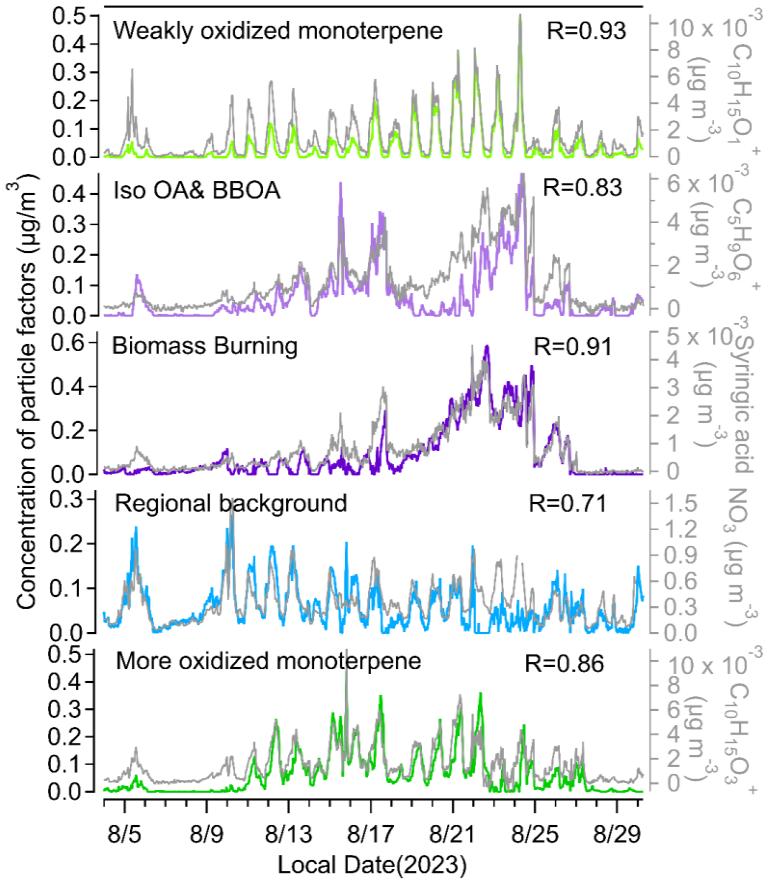

Figure S9 Time series of SVOA factors including oxidized terpene, iso OA & BBOA, BBOA, background, and more oxidized BOA identified by PMF during winter 2024. Gray lines represent selected tracer compounds (e.g., $C_{10}H_{15}O_1^+$, $C_5H_9O_6^+$, syringic acid, NO_3 and $C_{10}H_{15}O_3^+$), with correlation coefficients (R) indicating the agreement between factors and corresponding tracers.

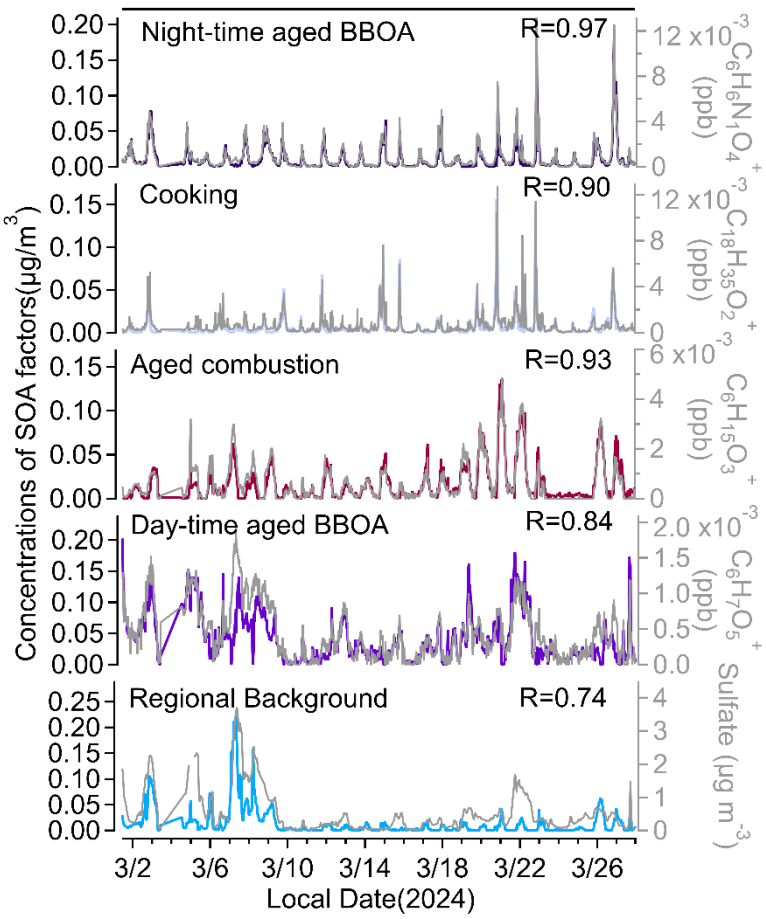

Figure S10 Time series of SVOA factors including oxidized Night-time aged BBOA, Cooking, Aged combustion, Day-time aged BBOA and Regional background identified by PMF during winter 2024. Gray lines represent selected tracer compounds (e.g., $C_6N_6N_1O_4^+$, $C_{18}H_{35}O_2^+$, $C_6H_{15}O_3^+$, $C_6H_7O_5^+$, and Sulfate), with correlation coefficients (R) indicating the agreement between factors and corresponding tracers.

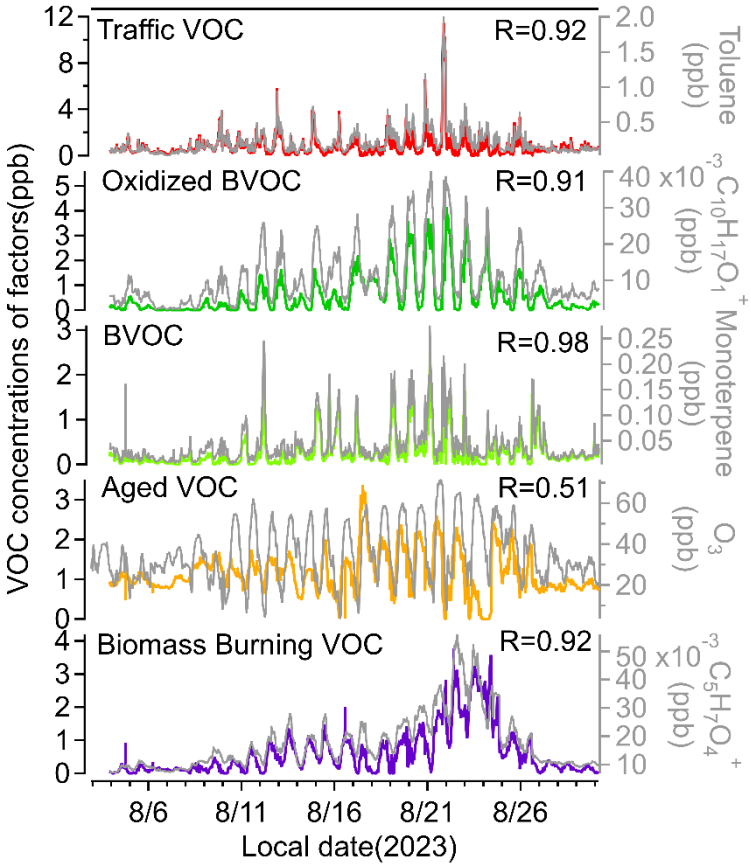

Figure S11. Time series of VOC factors identified by PMF during summer 2023, including traffic-related VOC, oxidized BVOC, fresh BVOC, aged VOC, and biomass burning VOC. Gray lines represent selected tracer compounds (e.g., toluene, monoterpenes, ozone, and $C_5H_8O_4^+$), with correlation coefficients (R) indicating the agreement between factors and corresponding tracers.

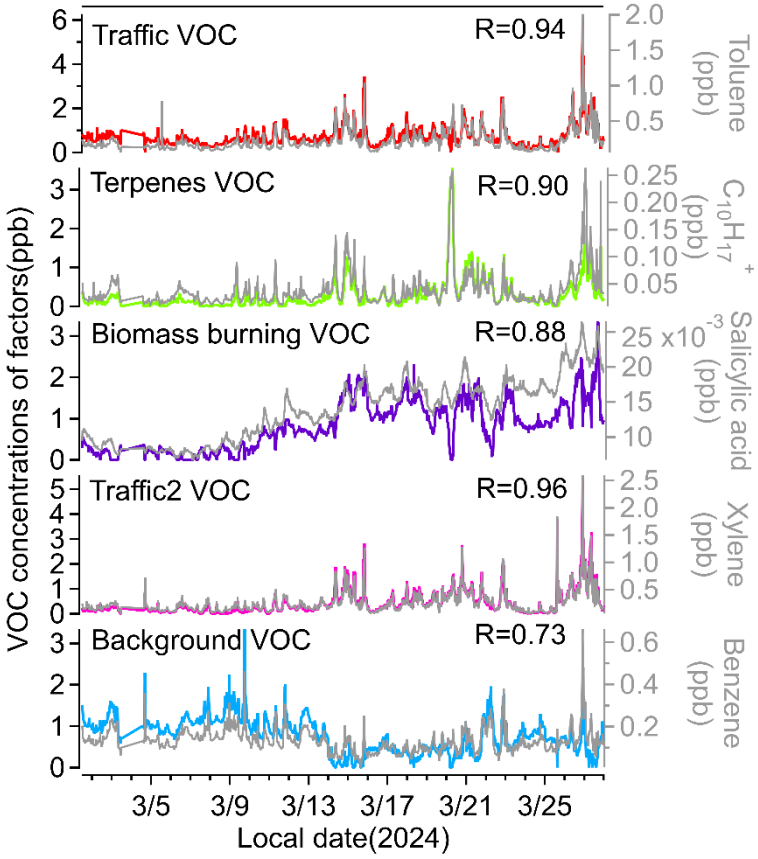

Figure S12 Time series of VOC factors identified by PMF during summer 2023, including traffic, Terpenes, Biomass burning, Traffic2, and Background VOC. Gray lines represent selected tracer compounds (e.g., toluene, $C_{10}H_{17}^+$, salicylic acid, xylene, and benzene, with correlation coefficients (R) indicating the agreement between factors and corresponding tracers.

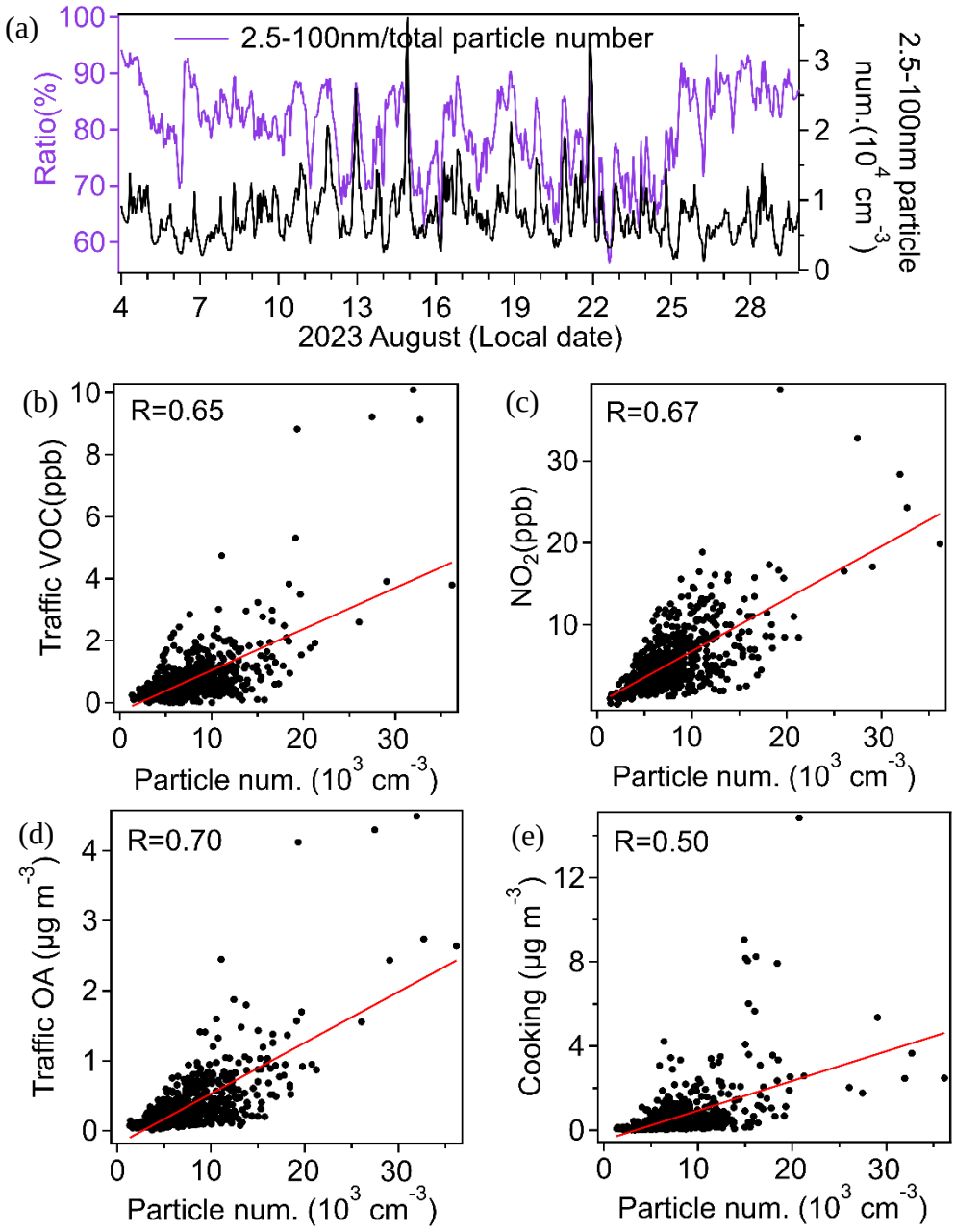

Figure S13 The ratio of 2.5-100nm particles number to total particle numbers and 2.5-100nm particle number (a), the correlation of traffic VOC(b), NO_2(c), traffic OA(d) and cooking OA(e) with 2.5-100nm particle number

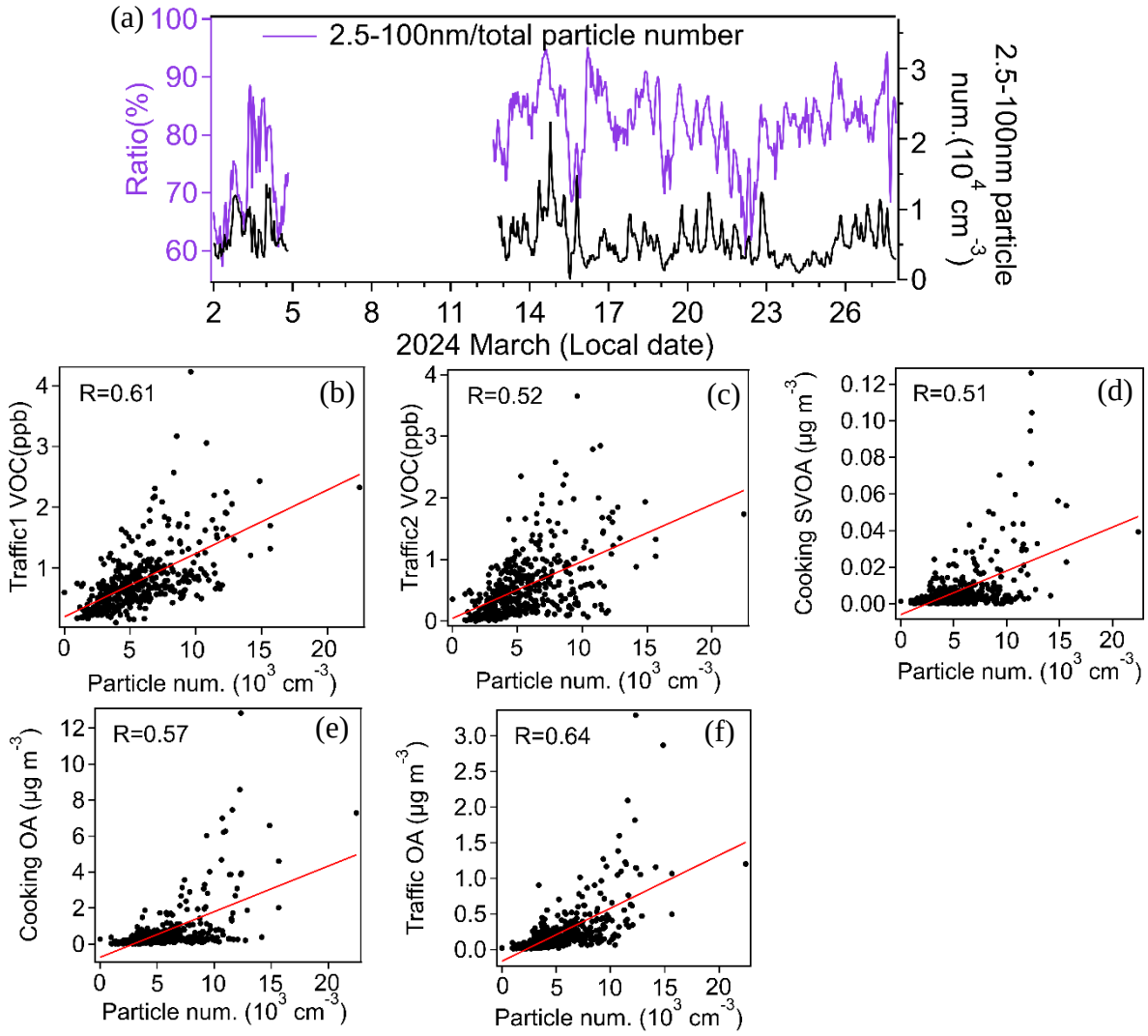

Figure S14 The ratio of 2.5-100nm particles number to total particle numbers and 2.5-100nm particle number (a), the correlation of traffic1 VOC (b), traffic2 (c), cooking SVOA (d), cooking OA (e), and traffic OA (f) with 2.5-100nm particle number

Table S1: Major mass peaks correlated to the four aerosol related source factors

PMF factor related	Mass peak (m/z)	Tentative ion	Tentative compound	Correlation to PMF factor
Aged BBOA (correlated with compounds from CHARON-PTR-MS measured)		Organic aerosol	AMS measured	0.89
	185.081	$C_9H_{13}O_4^+$ (gas)	Syringic alcohol	0.87
	171.066	$C_8H_{11}O_4^+$	oxidation products of ethylbenzene	0.81
	187.061	$C_8H_{11}O_5^+$ (CHARON)	guaiacylglycerol or vanillic acid derivative	0.86
	157.050	$C_7H_9O_4^+$	oxidation products of ethylbenzene	0.85
	171.066	$C_8H_{11}O_4^+$	guaiacylglycerol or vanillic acid derivative	0.85
	173.060	$C_7H_9O_5^+$	oxidation products of guaiacol	0.85
	153.055	$C_8H_9O_3^+$	methyl salicylate; vanillin	0.84
Regional transported (correlated with gas from PTR-MS measured)	33.034	$C_1H_5O^+$	formaldehyde	0.76
	84.045	$C_4H_6N_1O_1^+$	cyanoacetic Acid	0.75
	99.012	$C_1H_7S_1O_3^+$	unsaturated Keto Acids	0.73
	86.024	$C_3H_4N_1O_2^+$	cyano acetic acid	0.71
	171.029	$C_7H_7O_5^+$	aromatic polyacids	0.69
	105.070	$C_8H_9^+$	styrene	0.68
	151.043	$C_5H_{11}S_1O_3^+$	organosulfates	0.68
	83.050	$C_5H_7O_1^+$	methylfuran	0.67
SVOOA		Nitrate	AMS measured	0.82
		Ammonium	AMS measured	0.76
LVOOA	104.050	$C_7H_6N_1^+$ (gas)	benzonitrile	0.70

Table S2: Major mass peaks correlated to the three SVOA related source factors

PMF factor related	Mass peak (m/z)	Tentative ion	Tentative compound	Correlation to PMF factor
Background BBOA	189.076	$C_8H_{13}O_5^+$	Syringic acid derivative / Methoxybenzenetriol isomers	0.82
	187.061	$C_8H_{11}O_5^+$	Syringol dicarboxylic acid derivative	0.76
	171.066	$C_8H_{11}O_4^+$	Syringaldehyde	0.76
	173.060	$C_7H_9O_5^+$	Multi-oxidized guaiacol, marker of aging BBOA	0.76
	157.050	$C_7H_9O_4^+$	Hydroxy-vanillic acid, product of guaiacol aging	0.75
	153.055	$C_8H_9O_3^+$	Vanillic acid	0.75
	173.060	$C_7H_9O_5^+$	Multi-oxidized guaiacol, marker of aging BBOA	0.75
	161.045	$C_6H_9O_5^+$	Highly oxidized furan derivatives (e.g., levoglucosan oxidation product)	0.75
Photochemical SOA	127.076	$C_7H_{11}O_2^+$	Pinonic acid	0.98
	129.055	$C_6H_9O_3^+$	Norpinonic acid	0.98
	125.060	$C_7H_9O_2^+$	Cresol isomers	0.98
	139.076	$C_8H_{11}O_2^+$	Dimethylphenol isomers	0.98
	71.050	$C_4H_7O_1^+$	Crotonaldehyde	0.98
	127.040	$C_6H_7O_3^+$	Trihydroxybenzene	0.97
	111.045	$C_6H_7O_2^+$	Hydroquinone, catechol	0.97
	111.081	$C_7H_{11}O_1^+$	Ketone or aldehyde	0.97
	143.071	$C_7H_{11}O_3^+$	Hydroxy-dicarboxylic acid	0.97
	103.040	$C_4H_7O_3^+$	Malic acid	0.97
	99.045	$C_5H_7O_2^+$	Methylhydroquinone	0.97
Aged BBOA	189.076	$C_8H_{13}O_5^+$	Syringic acid derivative / Methoxybenzenetriol isomers	0.99
	171.066	$C_8H_{11}O_4^+$	Syringaldehyde	0.97
	187.061	$C_8H_{11}O_5^+$	Syringol dicarboxylic acid derivative	0.97
	153.055	$C_8H_9O_3^+$	Vanillic acid	0.97
	161.045	$C_6H_9O_5^+$	Highly oxidized furan derivatives (e.g., levoglucosan oxidation product)	0.97
	157.050	$C_7H_9O_4^+$	Hydroxy-vanillic acid, product of guaiacol aging	0.96
	173.060	$C_7H_9O_5^+$	Multi-oxidized guaiacol, marker of aging BBOA	0.96
	185.081	$C_9H_{13}O_4^+$	Syringic alcohol	0.96
	155.071	$C_8H_{11}O_3^+$	Syringol	0.95
	175.061	$C_7H_{11}O_5^+$	aged guaiacol/syringol	0.95
	201.076	$C_9H_{13}O_5^+$	Highly oxidized syringol derivatives	0.94

Table S3: Major mass peaks correlated to the three VOC related source factors

PMF factor related	Mass peak (m/z)	Tentative ion	Tentative compound	Correlation to PMF factor
Oxidized biogenic VOCs	97.065	$C_6H_9O_1^+$	2, 4-Hexadienal, Dimethylfuran	0.92
	85.065	$C_5H_9O_1^+$	Oxidation product of isoprene	0.92
	111.081	$C_7H_{11}O_1^+$	2,3-dimethyl-2-cyclopentenone	0.91
	101.097	$C_6H_{13}O_1^+$	Cis-3-hexenol	0.90
	87.081	$C_5H_{11}O_1^+$	Oxidation product of isoprene	0.89
	99.081	$C_6H_{11}O_1^+$	Hexenal	0.89
	101.06	$C_5H_9O_2^+$	Oxidation product of isoprene	0.88
	87.045	$C_4H_7O_2^+$	Oxidation product of isoprene	0.88
	115.076	$C_6H_{11}O_2^+$	3,5-Dimethyldiidro-2(3 h)-furanone	0.86
	113.06	$C_6H_9O_2^+$	Oxidation product of terpene	0.86
	123.081	$C_8H_{11}O_1^+$	Ethylphenol	0.86
	125.097	$C_8H_{13}O_1^+$	Oxidation product of terpene	0.86
	73.065	$C_4H_9O_1^+$	Oxidation product of isoprene	0.85
Long-range transported aged VOCs	130.014	$C_4H_4N_1O_4^+$	Maleimide derivative / Nitro-substituted pyrrole	0.84
	145.014	$C_5H_5O_5^+$	Pentahydroxyfuranone	0.82
	125.027	$C_3H_9S_1O_3^+$	Methanesulfonic acid derivative	0.81
	153.022	$C_4H_9S_1O_4^+$	Alkylsulfonic acid or similar sulfate-organic species	0.81
	141.022	$C_3H_9S_1O_4^+$	Methanesulfonic acid-related species	0.80
	117.019	$C_4H_5O_4^+$	Maleic acid	0.78
Aged biomass burning VOCs	77.024	$C_2H_5O_3^+$	Glycolic acid / Hydroxyacetic acid	0.91
	99.045	$C_5H_7O_2^+$	Pentenoic acid	0.89
	83.05	$C_5H_7O_1^+$	Pentenal / Furanone	0.87
	141.055	$C_7H_9O_3^+$	Methoxyphenol	0.87
	113.024	$C_5H_5O_3^+$	Furancarboxylic acid	0.86
	155.071	$C_8H_{11}O_3^+$	Methoxy-substituted aromatics	0.85
	125.06	$C_7H_9O_2^+$	Cresol	0.85
	165.092	$C_{10}H_{13}O_2^+$	Guaiacol derivatives	0.84
	153.092	$C_9H_{13}O_2^+$	Alkylguaiacol	0.84
	157.05	$C_7H_9O_4^+$	Methoxyphenol	0.83
	127.076	$C_7H_{11}O_2^+$	Cresol derivatives	0.81
	158.045	$C_6H_8N_1O_4^+$	Nitrohydroxybenzene	0.81
	171.066	$C_8H_{11}O_4^+$	Syringic acid	0.81
	143.071	$C_7H_{11}O_3^+$	Aromatic acid derivatives	0.81
	151.076	$C_9H_{11}O_2^+$	Guaiacol	0.79
	123.045	$C_7H_7O_2^+$	Benzaldehyde derivatives	0.79
Transported anthropogenic VOCs	77.06	$C_3H_9O_2^+$	Hydroxypropyl fragment	0.94
	79.04	$C_2H_7O_3^+$	Ethylene glycol monoformate ion	0.93
	63.044	$C_2H_7O_2^+$	Ethoxy fragment ion (from ethanol derivatives, solvents)	0.93

Table S4: Major mass peaks correlated to the six aerosol related source factors

PMF factor related	Mass peak (m/z)	Tentative ion	Tentative compound	Correlation to PMF factor
Diesel combustion OA (correlated with gas compounds from PTR-MS measured)	189.149	$C_{10}H_{21}O_3^+$	Hydroxy-fatty acid	0.67
	161.133	$C_{12}H_{17}^+$	Dodecatriene or Alkylbenzene	0.55
	NO_2			0.55
	BC			0.53
Landfill gas combustion (correlated with gas compounds from PTR-MS measured)	141.070	$C_{11}H_9^+$	Acenaphthylene	0.80
	173.154	$C_{10}H_{21}O_2^+$	Decanoic acid	0.79
	255.2324	$C_{16}H_{31}O_2^+$	Palmitoleic acid/Hexadecenoic acid	0.74
	46.0293	$C_1H_4N_1O_1^+$	Formamide	0.74
	70.029	$C_3H_4N_1O_1^+$	Cyanoacetylene	0.72
	73.029	$C_3H_5O_2^+$	Acrylic acid	0.72
	159.139	$C_9H_{19}O_2^+$	Nonanoic acid	0.71
	201.185	$C_{12}H_{25}O_2^+$	Dodecanoic acid (Lauric acid)	0.70
	139.112	$C_9H_{15}O_1^+$	Cyclononanone	0.70
Biogenic OA (correlated with particle compounds from CHARON-PTR-MS measured)	135.117	$C_{10}H_{15}^+$	Sesquiterpenes fragments (e.g., β-caryophyllene)	0.92
	136.097	$C_5H_{14}NO_3^+$	Nitrated organics	0.90
	151.097	$C_{10}H_{15}O_1^+$	Oxygenated monoterpenes	0.90
	123.117	$C_9H_{15}^+$	unsaturated hydrocarbons	0.89
	105.070	$C_8H_9^+$	Indene	0.86
	81.070	$C_6H_9^+$	Monoterpenes fragments	0.85
	153.128	$C_{10}H_{17}O_1^+$	Oxygenated monoterpenes	0.84
More oxygenated OA (correlated with particle compounds from CHARON-PTR-MS measured)	173.045	$C_7H_9O_5^+$	Multi-oxidized guaiacol, marker of aging BBOA	0.90
	187.061	$C_8H_{11}O_5^+$	Syringol dicarboxylic acid derivative	0.88
	201.076	$C_9H_{13}O_5^+$	Highly oxidized syringol derivatives	0.88
	143.034	$C_6H_7O_4^+$	Malic acid-like	0.87
	161.045	$C_6H_9O_5^+$	Highly oxidized furan derivatives (e.g., levoglucosan oxidation product)	0.86
	213.076	$C_{10}H_{13}O_5^+$	Sesquiterpene SOA	0.86
Low-volatile oxygenated OA (correlated with AMS)	Sulfate			0.57
	Ammonia			0.51
Industrial food process OA (correlated with gas and particle	143.034	$C_6H_7O_4^+$_Gas	Methylmalonic acid / Maleic acid	0.83
	133.032	$C_5H_9SO_2^+$	3-(Methylthio)propionic acid	0.75
	112.076	$C_6H_{11}NO^+$	Caprolactam / Aminohexanoic acid	0.73
	109.050	$C_3H_8O_4^+$	Glyceric acid	0.67

compounds from CHARON-PTR-MS measured)	122.061	$C_7H_9NO^+$	Methylbenzamide / Acetaminophen	0.67
	145.050	$C_6H_9O_4^+$	Itaconic acid / Mesaconic acid	0.64
	112.040	$C_5H_5NO_2^+$	Pyroglutamic acid	0.64
	169.086	$C_9H_{14}O_3^+$	Nonanedioic acid (Azelaic acid)	0.64
	155.107	$C_9H_{15}O_2^+$_CHARON	Fatty acid esters	0.77
	167.053	$C_9H_{11}S_1O_1^+$	Benzothiophene derivatives	0.74
	98.061	$C_5H_8N_1O_1^+$	Nitropyrroles	0.74
	96.996	$CH_5SO_3^+$	Methanesulfonic acid	0.73

Table S5: Major mass peaks correlated to the four semi-volatile aerosol related source factors (correlated with particle compounds from CHARON-PTR measured)

PMF factor related	**Mass peak (m/z)**	**Tentative ion**	**Tentative compound**	**Correlation to PMF factor**
More oxygenated SV-OA	140.035	$C_6H_6N_1O_3^+$	Nitrobenzene	0.67
	167.144	$C_{11}H_{19}O_1^+$	Undecanal	0.65
Biomass burning SV-OA	237.076	$C_{12}H_{13}O_5^+$	4-hydroxy-3-methoxybenzoic acid	0.87
	151.04	$C_8H_7O_3^+$	Methyl-1,4-benzoquinone or 2,3-dihydroxybenzaldehyde	0.85
	237.185	$C_{15}H_{25}O_2^+$	Farnesyl acetate or β-Caryophyllene oxide	0.84
	209.139	$C_9H_{21}O_5^+$	1,6-anhydro-β-D-glucopyranose fragment	0.83
	114.019	$C_4H_4N_1O_3^+$	Maleimide (1H-pyrrole-2,5-dione)	0.82
	125.097	$C_8H_{13}O_1^+$	Phenylacetaldehyde or Myrtenal	0.82
	137.097	$C_9H_{13}O_1^+$	Acetophenone	0.81
	95.086	$C_7H_{11}^+$	Norbornadiene	0.80
	147.084	$C_7H_{15}S_1O_1^+$	3-methylthietane 1-oxide	0.80
	153.055	$C_8H_9O_3^+$	Vanillin	0.80
	Landfill gas combustion OA			0.66
Biogenic SV-OA	152.107	$C_9H_{14}N_1O_1^+$	Tyramine	0.94
	108.081	$C_7H_{10}N_1^+$	Toluidine	0.92
	151.097	$C_{10}H_{15}O_1^+$	Carvacrol	0.91
	107.086	$C_8H_{11}^+$	Ethylbenzene	0.90
	94.066	$C_6H_8N_1^+$	Aniline	0.90
	110.097	$C_7H_{12}N_1^+$	Cyclohexylamine	0.89
	136.097	$C_5H_{14}N_1O_3^+$	Choline	0.87
	93.07	$C_7H_9^+$	Toluene	0.85
	153.128	$C_{10}H_{17}O_1^+$	Pinonaldehyde	0.83
	Biogenic OA			0.85
Industrial phyto-emission SV-OA	157.123	$C_9H_{17}O_2^+$	Nonanoic acid (Pelargonic acid)	0.87
	129.074	$C_7H_{13}S_1^+$	3-Mercaptohexanol	0.87
	98.061	$C_5H_8N_1O_1^+$	Pyroglutamic acid	0.85
	156.102	$C_8H_{14}N_1O_2^+$	Methyl 2-aminobenzoate	0.84
	115.076	$C_6H_{11}O_2^+$	Sorbic acid	0.84

	155.107	$C_9H_{15}O_2^+$	α-Ionone / β-Ionone	0.83
	141.055	$C_7H_9O_3^+$	Protocatechuic acid	0.82
	197.081	$C_{10}H_{13}O_4^+$	Coniferyl alcohol	0.81
	199.061	$C_9H_{11}O_5^+$	Gallic acid	0.81
	169.05	$C_8H_9O_4^+$	Vanillic acid	0.80
	96.996	$CH_5SO_3^+$	Methanesulfonic acid	0.79
	183.066	$C_9H_{11}O_4^+$	Ferulic acid	0.79
	187.061	$C_8H_{11}O_5^+$	Dihydroxybenzoic acid glucoside	0.78
	More oxygenated OA			0.80

Table S6: Major mass peaks correlated to the five VOC related source factors

PMF factor related	Mass peak (m/z)	Tentative ion	Tentative compound	Correlation to PMF factor
Industrial Phyto-emission VOC (correlated with gas compounds from PTR-MS measured)	168.030	$C_7H_6N_1O_4^+$	Nitrobenzoic acid	0.99
	102.019	$C_3H_4N_1O_3^+$	Nitroxy-acrolein	0.94
	143.144	$C_9H_{19}O_1^+$	Nonanal or other aldehydes	0.93
	96.987	$CH_5S_1O_3^+$	Methanesulfonic acid (MSA)	0.92
	223.170	$C_{14}H_{23}O_2^+$	Terpenoid acids	0.91
	115.112	$C_7H_{15}O_1^+$	Heptanol isomers	0.90
	129.128	$C_8H_{17}O_1^+$	Octanal	0.89
	152.035	$C_7H_6N_1O_3^+$	Nitrosalicylic acid	0.88
	117.055	$C_5H_9O_3^+$	Levulinic acid or keto-acids	0.85
	199.064	$C_6H_{15}SO_5^+$	Sulfated sugar derivatives	0.83
	77.060	$C_3H_9O_2^+$	Isopropanol	0.83
	Industrial Phyto-emission SVOA			0.87
	More oxygenated OA			0.54
Industrial solvent VOC (correlated with gas compounds from PTR-MS measured)	47.050	$C_2H_7O_1^+$	Ethanol	0.99
	142.050	$C_6H_8N_1O_3^+$	Nitrobenzene	0.98
	257.248	$C_{16}H_{33}O_2^+$	Palmitic acid	0.97
	100.076	$C_5H_{10}N_1O_1^+$	Pyrrolidone	0.97
	57.070	$C_4H_9^+$	Butane fragment	0.94
	219.196	$C_{12}H_{27}O_3^+$	Hydroxy fatty acid	0.92
Biogenic VOC (correlated with gas compounds from PTR-MS measured)	133.102	$C_{10}H_{13}^+$	Monoterpenes (e.g., α-phellandrene)	0.96
	136.113	$C_9H_{14}N_1^+$	Indole derivatives	0.93
	120.081	$C_8H_{10}N_1^+$	Methylpyridines	0.91
	134.097	$C_9H_{12}N_1^+$	Skatole (3-methylindole)	0.91
	135.117	$C_{10}H_{15}^+$	Sesquiterpenes fragments	0.90
	108.081	$C_7H_{10}N_1^+$	Pyrrolines	0.90
	94.066	$C_6H_8N_1^+$	Pyridine derivatives	0.89
	122.097	$C_8H_{12}N_1^+$	Phenethylamine	0.88
	121.102	$C_9H_{13}^+$	Cymene isomers	0.88
	107.086	$C_8H_{11}^+$	Dimethylstyrenes	0.88
	151.112	$C_{10}H_{15}O_1^+$	Nopol or myrtenol	0.86
	161.133	$C_{12}H_{17}^+$	Retene or abietadiene	0.85
	147.102	$C_7H_{15}O_3^+$	Heptanetriol derivatives	0.84

	153.128	$C_{10}H_{17}O_1^+$	Linalool / Pinocamphone	0.83
	Biogenic SV-OA			0.72
	Biogenic OA			0.71
French wildfire episodic VOC (correlated with gas compounds from PTR-MS)	77.006	$C_2H_5S_1O_1^+$	Ethylene sulfoxide	0.92
	167.056	$C_5H_{11}O_6^+$	Xylonic acid	0.87
	141.070	$C_{11}H_9^+$	Methylnaphthalene	0.83
	151.043	$C_5H_{11}S_1O_3^+$	Dimethyl sulfone ($DMSO_2$)	0.83
	105.019	$C_3H_5O_4^+$	Glyceric acid fragments	0.81
	Biomass burning SV-OA			0.65
	Landfill gas combustion OA			0.63
Industrial food process VOC (correlated with gas compounds from PTR-MS measured)	141.097	$C_8H_{13}O_2^+$	Octenone/Octenoic acid	0.92
	111.045	$C_6H_7O_2^+$	Methylfuranone	0.89
	125.060	$C_7H_9O_2^+$	Methylbenzoquinone	0.87
	97.065	$C_6H_9O_1^+$	Cyclohexenone	0.87
	115.076	$C_6H_{11}O_2^+$	Hexenoic acid	0.86
	101.060	$C_5H_9O_2^+$	Levulinic acid fragment	0.85
	128.108	$C_7H_{14}N_1O_1^+$	Heptenamide	0.85
	135.029	$C_4H_7O_5^+$	Malic acid fragment	0.84
	155.107	$C_9H_{15}O_2^+$	Nonadienoic acid	0.81
	112.076	$C_6H_{10}N_1O_1^+$	Caprolactam derivative	0.81
	125.027	$C_3H_9S_1O_3^+$	Dimethyl sulfone	0.81
	Industrial process food OA			0.41

Table S7: OA, SVOA and OA sources correlate with 11-20nm, 20-50nm, 50-90nm particle number and ultrafine particle fraction

PMF factor correlated	**11-20nm**	**20-50nm**	**50-90nm**	**UFP fraction (<100 nm)**
Diesel combustion OA	0.18	0.13	0.29	-0.04
Landfill gas combustion OA	0.22	0.11	**0.45**	-0.36
Biogenic OA	0.18	0.05	**0.49**	-0.24
More oxygenated OA	-0.06	-0.09	0.15	-0.44
Low-volatile oxygenated OA	-0.20	-0.17	-0.34	-0.01
Industrial food process OA	-0.11	-0.18	-0.01	-0.38
More oxygenated SVOA	-0.12	-0.19	-0.32	-0.04
Biomass burning SVOA	-0.01	-0.02	0.23	-0.24
Biogenic SVOA	0.03	0.02	0.36	-0.09
Industrial food process SVOA	-0.05	0.02	0.17	-0.22
Biofuel VOC contribution VOC	0.04	0.02	0.12	-0.07
Industrial solvent VOC	0.17	0.19	**0.44**	-0.06
Biogenic VOC	0.09	0.09	0.42	-0.09
Biomass burning VOC	-0.08	-0.02	0.17	-0.22
Industrial food process VOC	-0.02	-0.06	-0.19	-0.18
Black carbon	-0.05	0.06	**0.40**	-0.26

Table S8: Major mass peaks correlated to the five SVOA related source factors in summer

PMF factor related	Mass peak(m/z)	Tentative ion	Tentative compound	Correlation to PMF factor
Weakly oxidized monoterpene	108.08	$C_7H_{10}N_1^+$	3-ethyl-pyridine	0.99
	152.11	$C_9H_{14}N_1O_1^+$	alcohols or aldehydes with nitrogen groups	0.98
	166.09	$C_9H_{12}N_1O_2^+$	alcohols or aldehydes with nitrogen groups	0.93
	135.10	$C_6H_{15}O_3^+$	dimethyl carbitol	0.93
	107.07	$C_4H_{11}O_3^+$	trimethoxy methane	0.93
	151.11	$C_{10}H_{15}O_1^+$	oxidized molecules of monoterpenes	0.93
	216.09	$C_9H_{14}N_1O_5^+$	fragments of monoterpene-derived organic nitrates	0.91
	137.10	$C_9H_{13}O_1^+$	p-cumenol	0.91
	93.06	$C_3H_9O_3^+$	1,2,3-propanetriol	0.90
	153.13	$C_{10}H_{17}O_1^+$	oxidized molecules of monoterpenes	0.89
	153.09	$C_9H_{13}O_2^+$	4-ethyl guiacol	0.85
Oxidized Isoprene & BBOA	123.04	$C_7H_7O_2^+$	benzoic acid	0.95
	105.02	$C_3H_5O_4^+$	originates from the oxidation of ISOPOOH	0.85
	191.06	$C_7H_{11}O_6^+$	oxidation of o-cresol	0.84
	161.05	$C_6H_9O_5^+$	oxidation product of benzene	0.84
	165.04	$C_5H_9O_6^+$	oxidized molecules of isoprene	0.83
	189.08	$C_8H_{13}O_5^+$	oxidized molecules of monoterpenes	0.83
	149.02	$C_8H_5O_3^+$	phthalic anhydride	0.83
	117.06	$C_5H_9O_3^+$	oxidized molecules of isoprene	0.82
BBOA	167.03	$C_8H_7O_4^+$	fragment of vanillic acid	0.96
	163.04	$C_9H_7O_3^+$	fragment of syringic acid	0.95
	199.06	$C_9H_{11}O_5^+$	syringic acid	0.91
	159.03	$C_6H_7O_5^+$	oxidation products of guaiacol	0.90
	147.03	$C_5H_7O_5^+$	2-oxopentanedioic acid	0.89
	189.04	$C_7H_9O_6^+$	oxidation of o-cresol	0.88
	169.05	$C_8H_9O_4^+$	vanillic acid	0.88
	89.02	$C_3H_5O_3^+$	pyruvic acid	0.87
	173.05	$C_7H_9O_5^+$	oxidation products of guaiacol	0.86
	135.03	$C_4H_7O_5^+$	pentanedioic acid	0.86
	161.04	$C_6H_9O_5^+$	2-oxoadipic acid	0.85
Regional background		AMS-NO_3	Nitrate	0.71
More oxidized monoterpene	183.10	$C_{10}H_{15}O_3^+$	oxidized molecules of monoterpenes	0.86
	199.10	$C_{10}H_{15}O_4^+$	oxidized molecules of monoterpenes	0.85
	215.09	$C_{10}H_{15}O_5^+$	oxidized molecules of monoterpenes	0.84
	155.07	$C_8H_{11}O_3^+$	syringol	0.83
	169.09	$C_9H_{13}O_3^+$	Methylsyringol	0.81
	141.09	$C_8H_{13}O_2^+$	oxidized molecules of monoterpenes	0.81
	173.08	$C_8H_{13}O_4^+$	oxidized molecules of monoterpenes	0.80
	177.08	$C_7H_{13}O_5^+$	diacetin	0.79

Table S9 presents the correlations between the five SVOA factors and their main ions in winter time

PMF factor related	Mass peak(m/z)	Tentative ion	Tentative compound	Correlation to PMF factor
Night-time aged BBOA	156.03	$C_6H_6N_1O_4^+$	4-nitrocatechol	0.97
	170.05	$C_7H_8N_1O_4^+$	4-nitroguaiacol	0.97
	186.04	$C_7H_8N_1O_5^+$	unknown	0.87
	184.02	$C_7H_6N_1O_5^+$	fragments of $C_7H_8N_1O_5^+$	0.85
	201.04	$C_8H_9O_6^+$	unknown	0.75
	198.05	$C_9H_{10}O_5^+$	syringic acid	0.70
Cooking	283.26	$C_{18}H_{35}O_2^+$	oleic acid	0.90
	247.11	$C_{18}H_{15}O_1^+$	unknown	0.88
	275.26	$C_{16}H_{35}O_3^+$	$C_{16}H_{33}O_2(H_2O)^+$	0.88
	285.28	$C_{18}H_{37}O_2^+$	stearic acid (fatty acid)	0.73
	257.25	$C_{16}H_{33}O_2^+$	corresponding to palmitic acid	0.54
	239.24	$C_{16}H_{31}O_1^+$	fragments of $C_{16}H_{33}O_2^+$	0.54
Aged combustion	108.08	$C_7H_{10}N_1^+$	3-ethyl-pyridine; 2,3-dimethyl-pyridine	0.94
	135.10	$C_6H_{15}O_3^+$	dimethyl carbitol	0.93
	153.13	$C_{10}H_{17}O_1^+$	oxidized molecules of monoterpenes	0.86
	137.10	$C_9H_{13}O_1^+$	p-cumenol	0.82
	166.09	$C_9H_{12}N_1O_2^+$	benzocaine	0.80
	93.07	$C_7H_9^+$	toluene	0.79
Day-time aged BBOA	105.02	$C_3H_5O_4^+$	propanedioic acid	0.88
	131.03	$C_5H_7O_4^+$	methylene butanedioic acid	0.87
	90.02	$C_2H_4N_1O_3^+$	oxamic acid	0.86
	132.03	$C_4H_6N_1O_4^+$	iminoaspartic acid	0.85
	129.06	$C_6H_9O_3^+$	sotolone; 2,5-di-(hydroxymethyl)furan	0.84
	89.02	$C_3H_5O_3^+$	butyric acid	0.84
	101.02	$C_4H_5O_3^+$	pentanedione	0.84
	143.03	$C_6H_7O_4^+$	hydroxy maltol	0.84
	147.03	$C_5H_7O_5^+$	2-oxopentanedioic acid	0.83
	102.02	$C_3H_4N_1O_3^+$	methyl isocyanatoformate	0.83
	116.03	$C_4H_6N_1O_3^+$	3-methyl-2,5-oxazolidine-dione	0.83
	159.03	$C_6H_7O_5^+$	tricarballylic anhydride	0.83
	129.02	$C_5H_5O_4^+$	methanetetracarbaldehyde	0.83
	173.05	$C_7H_9O_5^+$	oxidation products of guaiacol	0.83
	103.04	$C_4H_7O_3^+$	propylene carbonate	0.82
	161.04	$C_6H_9O_5^+$	2-oxoadipic acid	0.82
Regional background	285.28	$C_{18}H_{37}O_2^+$	stearic acid (fatty acid)	0.95
	275.26	$C_{16}H_{35}O_3^+$	$C_{16}H_{33}O_2(H_2O)^+$	0.91
	247.11	$C_{18}H_{15}O_1^+$	unknown	0.90
	259.11	$C_{19}H_{15}O_1^+$	unknown	0.88
	283.26	$C_{18}H_{35}O_2^+$	oleic acid; fragment of stearic acid (fatty acid)	0.88
	107.07	$C_4H_{11}O_3^+$	trimethoxy methane	0.82
		AMS-SO_4^{2-}	sulfate	0.74
		AMS-NH_4^+	Ammonium	0.54

Table S10: Major VOC mass peaks correlated to the five VOC factors in summer

PMF factor related	Mass peak (m/z)	Tentative ion	Tentative compound	Correlation to PMF factor
Traffic	121.10	$C_9H_{13}^+$	C_9 aromatics trimethylbenzene	0.95
	107.09	$C_8H_{11}^+$	xylene	0.93
	93.07	$C_7H_9^+$	toluene	0.92
Oxidized BVOC	152.11	$C_9H_{14}N_1O_1^+$	alcohols or aldehydes with nitrogen groups	0.97
	167.11	$C_{10}H_{15}O_2^+$	oxidized molecules of monoterpenes	0.93
	149.10	$C_{10}H_{13}O_1^+$	carvone	0.93
	151.11	$C_{10}H_{15}O_1^+$	oxidized molecules of monoterpenes	0.93
	153.13	$C_{10}H_{17}O_1^+$	oxidized molecules of monoterpenes	0.91
	139.11	$C_9H_{15}O_1^+$	myrcenol	0.87
BVOC	137.13	$C_{10}H_{17}^+$	monoterpene	0.98
	138.13	$C_9H_{16}N_1^+$	unknown	0.90
	81.07	$C_6H_9^+$	fragment of monoterpenes	0.86
	82.07	$C_5H_8N_1^+$	unknown	0.81
	205.20	$C_{15}H_{25}^+$	sesquiterpenes	0.80
Aged VOC	89.02	$C_3H_5O_3^+$	butryic acid	0.75
	101.02	$C_4H_5O_3^+$	pentanedione	0.72
		O_3		0.51
Biomass burning VOC	131.03	$C_5H_7O_4^+$	fragment of oxidized guaiacol molecules	0.92
	95.01	$C_5H_3O_2^+$	fragment of oxidized guaiacol molecules	0.91
	119.03	$C_4H_7O_4^+$	fragment of oxidized guaiacol molecules	0.90
	103.04	$C_4H_7O_3^+$	fragment of oxidized guaiacol molecules	0.86
	77.06	$C_3H_9O_2^+$	1,3-propanediol	0.85
	79.04	$C_2H_7O_3^+$	orthoacetic acid	0.83

Table S11: Major VOC mass peaks correlated to the five VOC source factors in winter

PMF factor related	Mass peak(m/z)	Tentative ion	Tentative compound	Correlation to PMF factor
Traffic	121.10	$C_9H_{13}^+$	C_9 aromatics trimethylbenzene	0.96
	93.07	$C_7H_9^+$	toluene	0.94
	133.10	$C_{10}H_{13}^+$	cymenene	0.86
Terpenes VOC	138.13	$C_9H_{16}N_1^+$	triallylamine	0.98
	205.2	$C_{15}H_{25}^+$	sesquiterpenes	0.92
	137.13	$C_{10}H_{17}^+$	monoterpene	0.90
	81.07	$C_6H_9^+$	fragment of monoterpenes	0.89
	163.13	$C_8H_{19}O_3^+$	diethyl carbitol	0.76
Oxidized VOC	103.0	$C_4H_7O_3^+$	acetic anhydride	0.89
	139.04	$C_7H_7O_3^+$	salicylic acid	0.88
	77.06	$C_3H_9O_2^+$	1,3-propanediol	0.87
	113.02	$C_5H_5O_3^+$	furoic acid	0.86
	90.02	$C_2H_4N_1O_3^+$	oxamic acid	0.86
	123.04	$C_7H_7O_2^+$	benzoic acid	0.86
	117.02	$C_4H_5O_4^+$	maleic acid	0.85
	119.03	$C_4H_7O_4^+$	butanedioic acid	0.85
Fossil fuel combustion	108.08	$C_7H_{10}N_1^+$	3-ethyl-pyridine	0.98
	107.09	$C_8H_{11}^+$	C8 aromatics xylenes	0.96
	121.10	$C_9H_{13}^+$	C_9 aromatics trimethylbenzene	0.91
	93.07	$C_7H_9^+$	toluene	0.91
	85.10	$C_6H_{13}^+$	methyl cyclopentane	0.90
Background	79.0	$C_6H_7^+$	benzene	0.73